IPP-Report

MAX-PLANCK-INSTITUT
FÜR PLASMAPHYSIK

A. Mutzke, U. von Toussaint, W. Eckstein, R. Dohmen, K. Schmid

SDTrimSP Version 7.00

IPP 2024-06
März 2024

SDTrimSP Version 7.00

A. Mutzke[a], U. von Toussaint[b],
W. Eckstein[b], R. Dohmen[b], K. Schmid[b]

[a] Max-Planck-Institut für Plasmaphysik, Greifswald, Germany
[b] Max-Planck-Institut für Plasmaphysik, Garching, Germany

Abstract

SDTrimSP version 7.00 simulates designed for atomic collisions in amorphous targets. It calculates ranges, reflection coefficients and sputtering yields as well as more detailed information like depth distributions of implanted and energy distributions of back-scattered and sputtered atoms. The program is based on the binary collision approximation and uses the same physics as its predecessors TRIM.SP and TRIDYN, but the structure of the new program has been completely changed. It runs on all sequential and parallel platforms with a F90 compiler. Table lookup is applied for all available atomic data needed for input, and different integration schemes for several interaction potentials are provided. Several examples are given to show the wide range of possible applications.

This report replaces the previous version (IPP Report 2019-02).

Contents

1. Introduction

In the last 50 years many computer simulation programs have been developed to describe the interactions of ions bombarding solid, liquid and gaseous targets. Many of these programs were based on the binary-collision approximation (BCA) dealing with crystalline and amorphous targets. Examples of programs dealing with amorphous targets are the static Monte-Carlo program TRIM and the corresponding dynamic version TRIDYN which were successful in describing collision effects in solids for many examples [1]. Many versions of these two programs evolved to handle specific physical problems. This triggered the idea to combine both programs in a new version SDTrimSP (where S stands for static and D for dynamic) with all possible output capabilities used in the past like sputtering, back-scattering and transmission. This offered the opportunity to introduce at the same time a modular structure, to have a more flexible output and to provide a higher portability. The program is suited equally well for all sequential architectures and for all parallel architectures, for which a Fortran 90 (F90) compiler and the MPI (Message Passing Interface) communication library are available. The new program also includes features which were used in the past, but were not incorporated in most versions of TRIM.SP and TRIDYN.

The extensions for SDTrimSP version 7.00 are described. The main new features are the inclusion of new modules for surface-binding-models, inelastic energy-loss and crystal-structure. The models of out-gasing for noble gas ions and chemical erosion of carbon have been improved and adapted.
Outlook:Based on the principles of SDTrimSP 7.00 also code versions for 2D- and 3D-problems have been derived [56],[57] , which however are described in separate upcoming reports.

2. Physical basis

The new program SDTrimSP is based on TRIM.SP [2] and TRIDYN [3, 4]. Both programs, the static TRIM.SP and the dynamic TRIDYN, are described in [1]. The basic physics in the program SDTrimSP is the same as in the former versions. SDTrimSP is a Monte Carlo program, which assumes an amorphous (randomized) target structure at zero temperature (ie. static target atoms $|\vec{v}| = 0$) and infinite lateral size.
The target in SDTrimSP is one dimensional (Fig. 1). The target is divided into layers. Y and Z direction are taken as infinite. In the static mode the target is fixed. In the dynamical mode the thickness of layers is changed, [26]. The polar (α) and azimuthal (β) angles show Fig. 2.

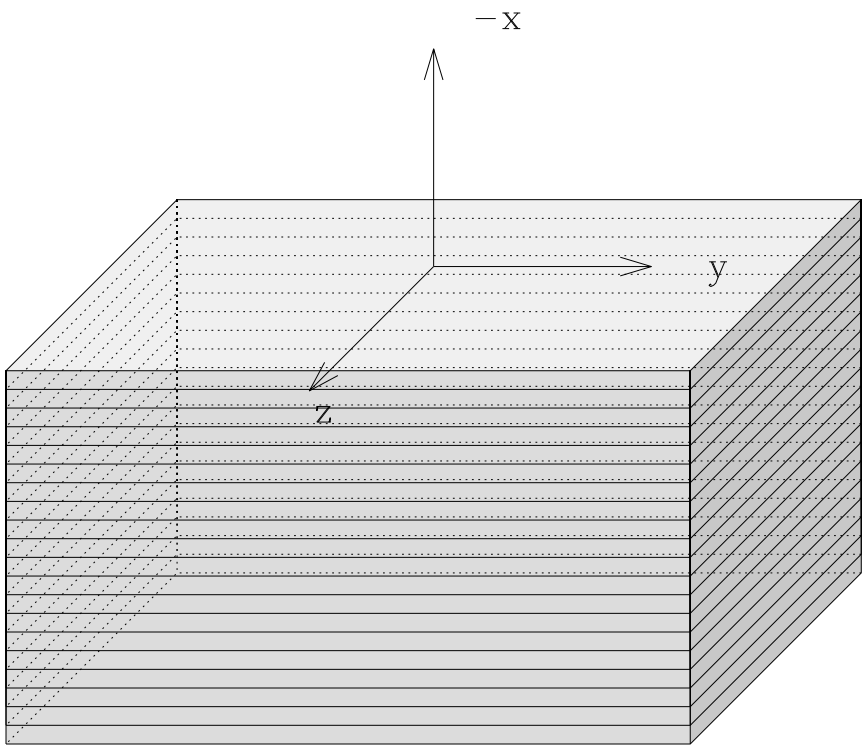

Figure 1: Geometry of the one dimensional target

The binary collision approximation is used to handle the atomic (nuclear) collisions. This means, that the change in flight direction due to the collision is given by the asymptotes of the real trajectory.
For this evaluation an interaction potential has to be chosen (usually purely repulsive and only dependent on the distance between the colliding atoms) to determine the scattering

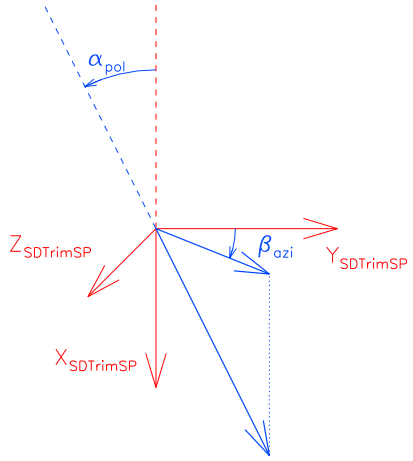

Figure 2: Definition of polar α and azimuthal β angle

angle of the moving atom and the recoil angle of the atom, which is set into motion. Then the energy loss (nuclear) of the moving atom and the energy gain of the recoil can be calculated. In addition, a moving atom looses energy to target electrons (electronic or inelastic energy loss). The program also provides the possibility to include simultaneous weak collisions, but strictly in the binary collision approximation. The program follows projectiles (incident atoms) and target recoil atoms three-dimensionally until their energy falls below some preset value or if they have left the target (back-scattering, transmission, sputtering). Besides a more modular structure many new features are included in the program. Most data needed for a calculation is taken from a database in form of tables: atomic numbers and masses of elements, densities of solid and liquid elements, surface binding energies (heat of sublimation). Displacement energies are taken from Table 6.1 in [1]; one table provides isotopic masses of elements; two other tables give the constants for the inelastic energy loss of hydrogen [5] and helium [6]. Different interaction potentials as KrC [7], ZBL [8], Molière [9], Nakagawa-Yamamura [19] , power potentials and a special Si-Si potential [10] can be chosen as well as different integration methods of the scattering integral as Magic [11], Gauß-Mehler [12], and Gauß-Legendre [13]. Magic is faster than the Gauß-Mehler and the Gauß-Legendre procedure, but is only available for KrC, ZBL and Molière. Evaluation of the accuracy [14] of the integration procedure Magic shows a maximum relative error of the scattering angle in the center-of-mass system of about 1 % nearly independent of the relative impact parameter (impact parameter/screening length). For the Gauß-Mehler procedure the corresponding error is increasing with an increasing relative impact parameter and depends on the number of pivots [14]. According to Robinson [15], the Gauss-Mehler method is generally more accurate than the Gauss-Legendre method in evaluating the scattering angle integral, but less accurate for the time integral.

3. Structure of the code

The code SDTrimSP treats the bombardment of incident ions on different target structures. Besides mono-atomic targets, layer structures, fixed and variable composition target structures are allowed. The kind of projectiles and/or target atoms is not limited. Both incident ions and recoil atoms are treated as series of subsequent collisions. There are two general cases in the code:

- static case: the target composition is fixed during the whole simulation
- dynamic case: modifications of the target caused by the ion bombardment are taken into account; in this case the target is updated at regular intervals, i.e. after a certain number NR$\geq$ 1 of projectiles and corresponding showers. NR has to be specified as a parameter in the input file.

The atoms are distinguished in projectiles (incident atoms) and recoils (target atoms). For each traced atom important physical quantities, as energy, spatial coordinates, direction of motion, are recorded along its path using general data structures. Moreover, the path length and the number of collisions are stored for the projectiles, while for the recoils the collision number in which they are generated is stored (generation). Besides the information about the single projectile there are also quantities integrated over all projectiles to save memory. For projectiles, the inelastic (electronic) energy loss and the total elastic and the elastic loss larger than the displacement energy are stored. Other values derived from these basic quantities can be determined, if of interest.
The structure of the program is depicted in Fig. 3. In the projectile loop, groups of NR projectiles are followed from collision to collision. The recoils generated along the projectile trajectories of the NR incident ions are collected and treated in a separate loop, the recoil loop. After finishing the calculation of the NR projectiles and generated recoils the target is updated in the case of the dynamic mode. In the static mode no target update is necessary, and it can be continued with the next group of projectiles until the total number NH of projectiles (number of histories) is reached. Finally, the output section is entered.
In the input file the target and incident particles are specified. A flag determines the static or dynamic mode. In the dynamic case the total fluence for a calculation has to be given in units of 10^{16}atoms/cm^2. The energy of the incident particles, the angles of incidence, the interaction potential and the inelastic energy loss model have to be chosen. The energy and angle of incidence of the projectile can be chosen fixed or by a given distribution. The input file is organized as a F90 namelist file and described in detail in the documentation delivered with the program package.
The output was designed in a very flexible manner allowing to store all important values of individual particles and offering at the same time the possibility to limit the output in order to save memory and computing time. By conditioning the different output sections in the code the user can switch on or off the different sections with corresponding flags and variables in the input file. Moreover, the output is structured in such a way that the user can insert own output sections in an obvious manner.

The general, obligatory output gives the reflection and sputtering coefficients, atomic fractions and densities as a function of depth, and the yield versus the generation. In the dynamic case the change of target thickness and atomic fractions and densities as a function of fluence is given. This minimal output has a size of some kBytes only. Optional output concerns trajectory information (evolution of spatial coordinates, directions of motion, energy, time), particle information (energy, number of collisions, path length, starting point and final coordinate), matrices (absolute frequency distributions of reflected, transmitted and sputtered particles in discrete levels of energy and exit angles). Note, that the amount of output can increase rapidly to hundreds of MBytes for the trajectory and particle output, especially when the incident energy is high. Especially for problems with a large number of reflected, transmitted and sputtered particles, the usage of matrices output is advantageous as it helps to save memory. There are several post processing programs concerning the matrix output and the visualization of calculated data by means of IDL.

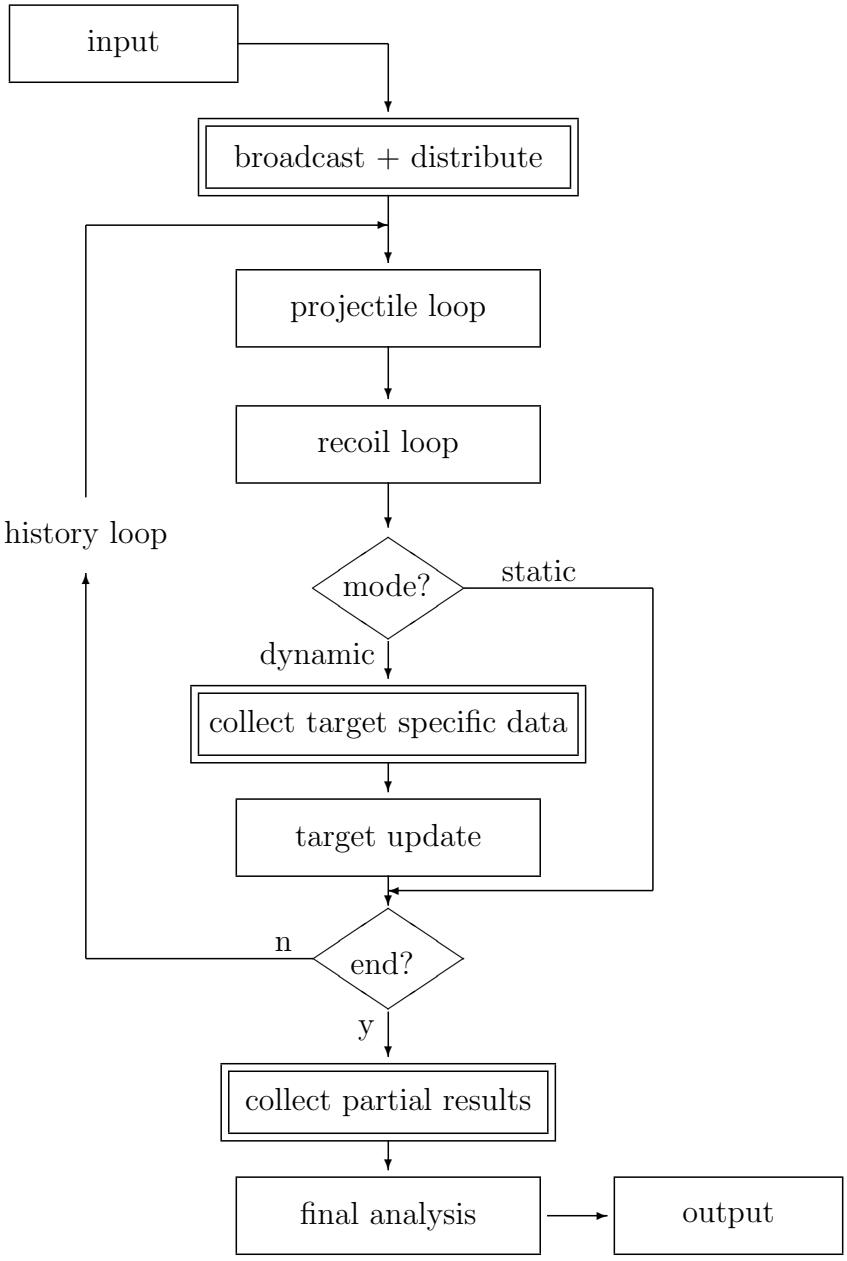

Figure 3: Main block flow chart of the program SDTrimSP. The double blocks indicate additional work necessary in the parallel mode. These parts are skipped in the sequential mode. Target updates include diffusion and chemical reactions.

4. Implementation

The program SDTrimSP is implemented in Fortran 90. The work flow depicted in Fig. 3 is transferred into a modular structure of the code. The characteristic quantities belonging to larger data units like trajectories, particle states and other data blocks are combined in F90 user-defined structures to make data handling easier.
The code is drawn up to work in different modes and on different architectures. Basically, there are two modes:

1. the sequential mode for execution on any sequential architecture with a F90 and a C compiler,

2. the parallel mode for execution on any distributed-memory parallel architecture with a F90 and a C compiler and the MPI communication library available. In this version, the NR particle showers are distributed over the processors.

Both modes are included in the same source code, the different modes are distinguished by use of preprocessor directives. The user selects the mode at compile time by choosing the respective macro in the Makefile.
In the sequential mode the course of the program is as shown in blocks with simple boxes of Fig. 3. In the parallel mode some additional work as specified blocks with double boxes in Fig. 3 is necessary to distribute data structures and computational load and to summarize the results. The parallel algorithm works as follows: The target data is replicated on all processors (broadcast in Fig. 3), while the NR incident ions between two target updates are distributed over np processors (NR $\rightarrow$ NR/np). Furthermore, each processor has to be provided with an appropriate seed for the random number generator (see below). The ions and corresponding showers are simulated independently on the processors, each processor using a dedicated sequence of random numbers. The effects caused by the particles are recorded in processor private variables. This concerns target data, ion specific data and recoil specific data. In the dynamical case, the target data has to be summed up over the processors and made known to each processor in order to perform the target update. The target update is carried out quasi-sequentially on all processors and as a result each processor has a replicate of the new target data and can continue with the next group of ions and so on. In the static case the target update and the global sums are not necessary for the calculation and the summation of the target data is postponed to the end of the program where in any case all particle information gathered locally on the processors has to be collected and printed out. That means the static program is embarrassingly parallel with nearly no communication, while the amount of communication in the dynamic case can be considerable. Depending on the application the computing time may be rather long, therefore restart files can be written at regular time intervals.
The communication is based on the Message Passing Interface (MPI). By this the algorithm is portable between different parallel architectures. Special care has been taken for the generation of random numbers. By choosing the linear congruential random number

generator from Cray's Scientific Library we have a true parallel random number generator having the advantage that the sequence of 2^{32} values can be divided into chunks of equal size so that each processor has its own sequence which is not correlated to the sequences of all other processors. To facilitate debugging and providing reproducible results there is also the possibility to associate each particle with its own, determined seed so that the result of a computation with a certain number of incident particles is always the same irrespective of how many processors are involved. One must, however, be aware that this method of using reproducible random numbers does not yield reliable results in the sense of good statistics. Again, the mode of random number generation is controlled via preprocessor directives in the code and corresponding macros in the Makefile.

The calculation steps in the program SDTrimSP are determined by NR and NH. NR is number of projectiles between target updates, NH is the number of histories. In the dynamic case the target is relaxed after each history step.

Note that the structure of the whole package SDTrimSP is designed in such a way that the same source code, Makefile and run-time commands are used for all modes and architectures and distinctions are made via preprocessor and environment variables . The object code is kept in different directories for the different architectures to facilitate the simultaneous usage of different architectures. A detailed description of the code with a list of all input and output variables and a description of all subroutines with references to the corresponding literature is provided. The code is available for free for non-commercial use. (contact mail-address: SDTrimSP@ipp.mpg.de).

5. Performance

The program was tested on several sequential and parallel architectures, as e. g. IBM SP machines, IBM Power4 and Power5 systems, Cray T3E, NEC SX5, and Linux clusters with AMD or Intel processors, and is running in production mode for several years now with great success. For large, time-consuming applications it is advisable to use the parallel version of the code. In this case, the choice of the parameter NR, which is the number of incident particles and corresponding showers between two target updates, is decisive to have good performance, while in the sequential version, this parameter is of no relevance. The reason is that NR is a quantity closely related to the granularity of the parallel algorithm, as each processor has to treat NR/np incident particles together with their recoils, where np is the number of processors. That means, NR must not be less than np, and the larger NR, the better the efficiency of the parallel program, as the ratio between communication and computation decreases. On the other hand, NR has also a physical meaning, as it determines somehow the frequency of target updates. Therefore an investigation of the influence of NR and NH on the accuracy of the results has been carried out.

5.1. Influence of NR and NH on the accuracy of the results

A physical interpretation of NR and NH is that a larger number NR improves the statistical relevance of the target update, while a larger number of histories NH means a smaller fluence step (because the fluence step is the total fluence divided by NH) and by this improves the overall statistics. In the static case, the statistics depends only on the product of NR and NH, and NR has no physical meaning.
With the following example of a dynamic case it is shown that the accuracy of the results depends merely on the product of NR and NH over a certain range of values for NR. The chosen example is a 1 keV bombardment of Fe on TaC with a fluence of 10^{17} atoms/cm^2. The results for different values of NR with $\mathrm{NR} \cdot \mathrm{NH} = \mathit{constant}$ are shown in Table 1 and Figs. 4 and 5 at the example of typical quantities. It shows that the plots and values differ only to the same extent as they would differ when using another seed for the random numbers. That means, the number NR may be increased to achieve a better parallel efficiency, while decreasing at the same time the number of histories. For statistical reasons it makes no sense to choose very small values of NH in the dynamic case. The fluence step (total fluence/NH) should of the order of 0.01 (10^{14} atoms/cm^2) to ensure that the target composition change is small in a fluence step.

NR	NH	change of thickness	qu(Fe)	qu(Ta)	qu(C)
1	1000000	4.47 nm	0.559	0.302	0.139
10	100000	4.51 nm	0.557	0.303	0.140
100	10000	4.50 nm	0.557	0.304	0.139
1000	1000	4.49 nm	0.558	0.303	0.139

Table 1: Change of thickness and atomic fraction (qu) of the surface composition with different numbers of NR and NH for the example of Fe $\rightarrow$ TaC ($\mathrm{NR} \cdot \mathrm{NH} = \mathit{constant}$)

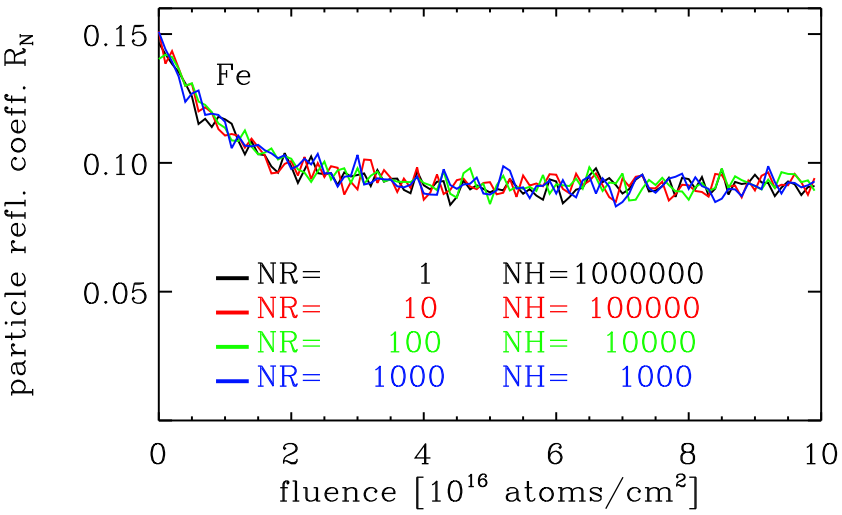

Figure 4: Particle reflection coefficient for different numbers of NR and NH ($NR \cdot NH = constant$) in the case of 1 keV Fe atoms impinging at normal incidence onto a TaC target

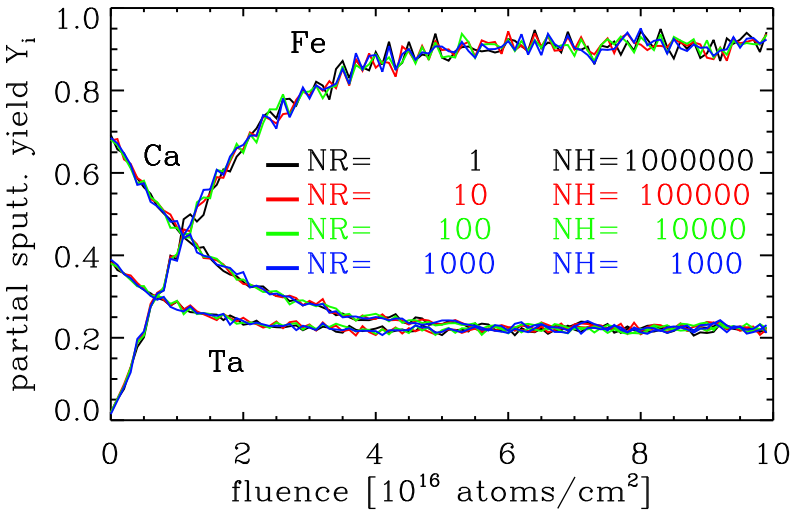

Figure 5: Partial sputtering yield for different numbers of NR and NH ($NR \cdot NH = constant$) in the case of 1 keV Fe atoms impinging at normal incidence onto a TaC target

5.2. Number of incident particles

In a Monte Carlo code the number of test particles defines the accuracy of the results. Fig. 6 shows the value of the sputtering yield for D on Be at normal incidence for three different energies as a function of the number of incident D particles. Fig. 7 shows the relative error of the yields for this example. In this particular case the number of incident projectiles should be more than 10^6 particles to obtain sufficiently good statistic estimates.

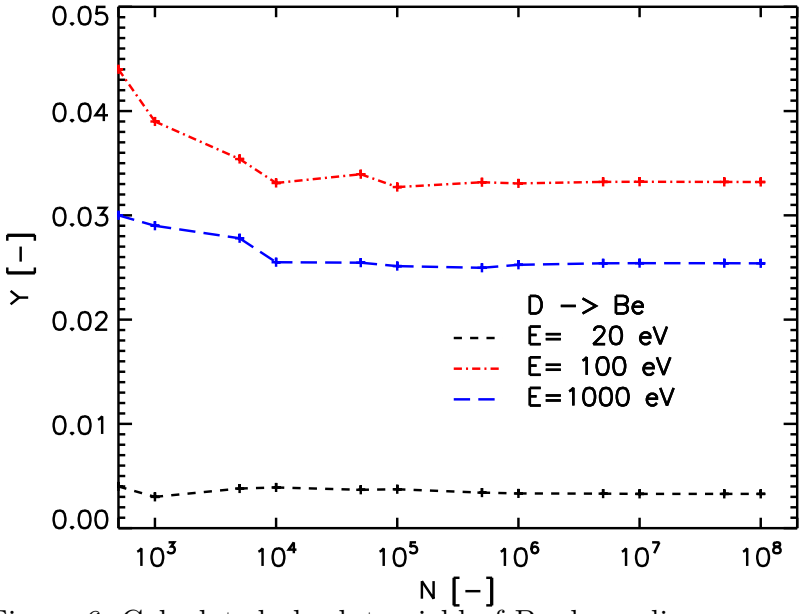

Figure 6: Calculated absolute yield of Be depending on number of incident particles of D on a Be target at normal incidence for three different energies.

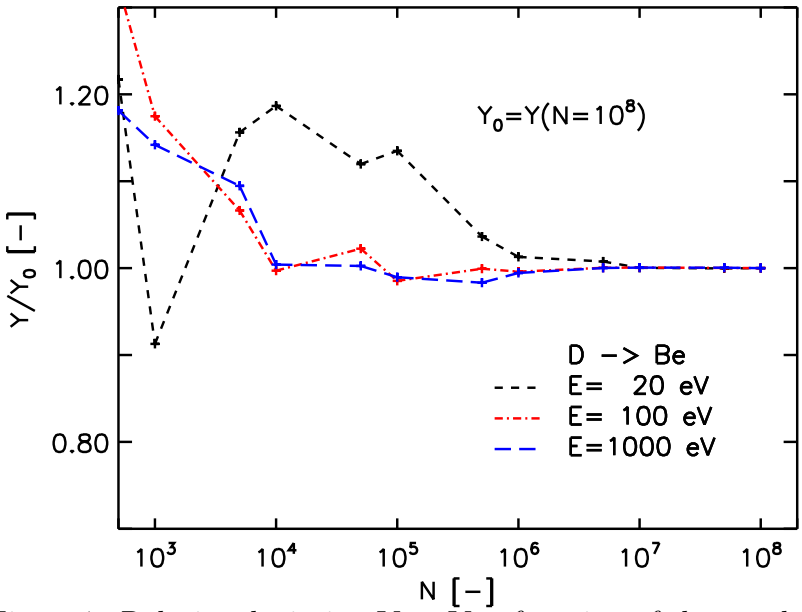

Figure 7: Relative deviation Y to Y_0 a function of the number of incident D particles on a Be target at normal incidence for three different energies

5.3. Parallel efficiency

As already pointed out the performance of the program depends strongly on the mode and on the choice of NR on the one hand, but on the other hand on the characteristics of the used architecture. When working on a single-processor system, i. e. using the sequential version, it is mainly the clock rate of the processor which determines the computing time, irrespective of whether using the static or dynamic mode. The choice of NR is not of great importance. In the dynamic case, however, the code is rather communication-intensive, and the performance depends heavily on the choice of NR.
These dependencies are demonstrated at the example of 1 keV Fe bombardment on TaC at normal incidence with a fluence of 10^{16} atoms/cm^2. The benchmark has been carried out on two different parallel architectures, an IBM 1.3-GHz-Power4 (Regatta) system and a Linux cluster with Intel 2.8-GHz processors. The Regatta system is provided with a fast communication network with Federation switch, while the nodes of the Linux cluster are connected via Gigabit Ethernet. For these benchmarks the option of minimum output was used, the parameters NR and NH have been chosen as NR = 512 and NH = 20000 which allows to use up to 512 processors in the parallel mode.
The execution times and parallel efficiencies obtained for the static mode on the two architectures are shown in Table 2. As expected the parallel efficiency of the code is very good on both architectures, because the amount of communication is very low and consists mainly in broadcasting the data at the beginning of the calculation and summing up the partial results of the processors at the end of the calculation. This is also reflected in the corresponding speedup curves, cf. the solid lines in Fig. 8(b).
Table 3 and the dashed lines in Fig. 8(b) show the corresponding behavior for the dynamic case. There is a clear difference in the performance for the two architectures. The parallel efficiency obtained with the IBM Regatta is very good up to 64 processors. This is due to the fast communication achieved by the strong Federation switch of the Regatta system and the MPI implementation on top of the shared memory architecture of the Regatta. In contrast, the parallel efficiency on the Linux cluster is not that good. This is due to the fact that the communication network of the Linux cluster is rather slow compared to the processor performance and cannot cope with the amount of communication. The speedup curves demonstrate the somewhat poorer scaling and show that the Linux cluster is not specially suited for parallel calculations with more than 16 processors in the dynamic mode. Up to 16 processors, however, the performance of the Linux cluster is quite satisfactory, at least for the chosen value of NR = 512. It should be noted that the single-processor performance of the Linux cluster is much better than that of the IBM Regatta.
To conclude, the mode of the calculation, the choice of different parameters and the characteristics of the parallel architecture determine the efficiency of the calculation. To improve the performance in the dynamic mode it is advisable to reduce the communication by using a small number of NH and a large number of NR.

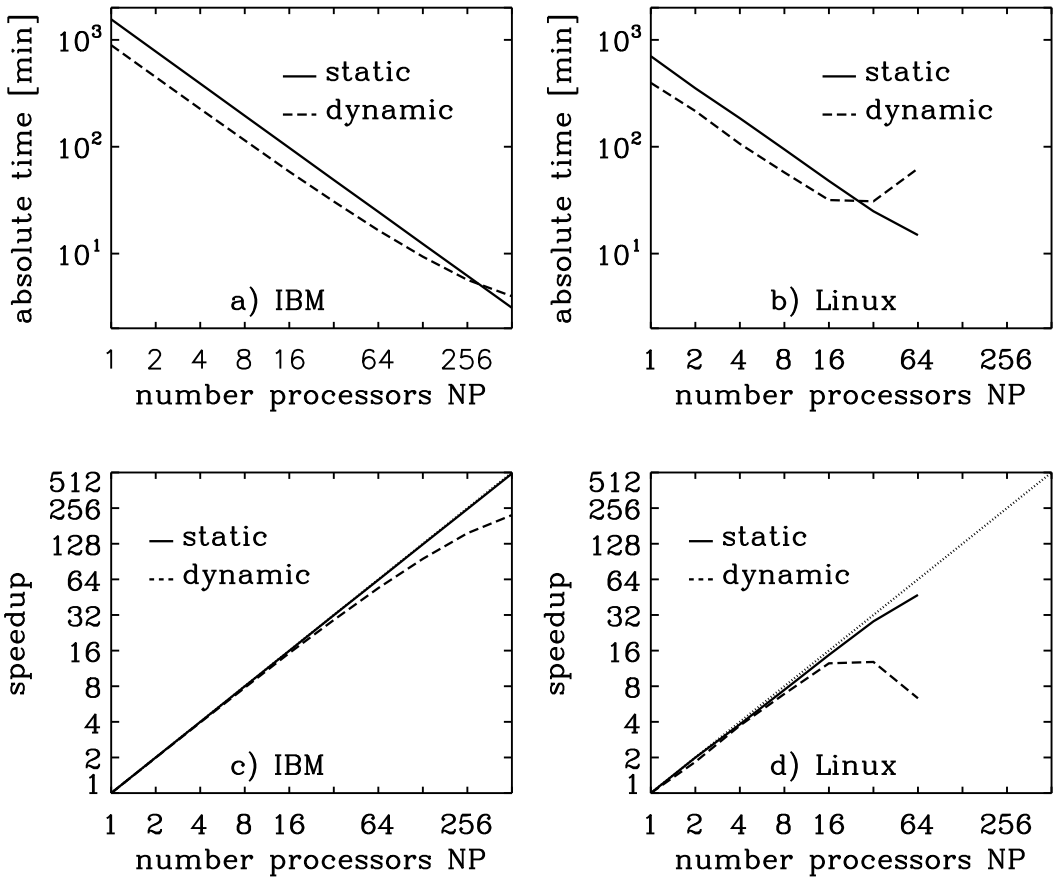

Figure 8: a, b) Absolute time and c, d) speedup of the static and dynamic cases in dependence of the number of processors for the IBM Regatta (IBM) and an Intel Linux cluster (Linux)

	IBM Regatta 1.3 GHz		Linux cluster 2.8 GHz (Intel)	
	execution time	parallel efficiency	execution time	parallel efficiency
np	[min]		[min]	
1	1557.38	1.000	703.84	1.000
2	778.61	1.000	352.47	0.998
4	389.96	0.998	184.78	0.952
8	194.81	0.999	94.40	0.931
16	97.65	0.996	47.86	0.919
32	48.87	0.995	24.90	0.883
64	24.86	0.989	14.89	0.738
128	12.31	0.988		
256	6.20	0.981		
512	3.11	0.978		

Table 2: Execution time and parallel efficiency of the static mode of SDTrimSP on the IBM Regatta and on an Intel Linux cluster for the example of 1 keV Fe atoms impinging at normal incidence onto TaC with NR = 512, NH = 20000 (10240000 particles)

	IBM Regatta 1.3 GHz		Linux cluster 2.8 GHz (Intel)	
	execution time	parallel efficiency	execution time	parallel efficiency
np	[min]		[min]	
1	891.90	1.000	395.90	1.000
2	448.17	0.995	215.72	0.917
4	225.84	0.987	106.48	0.929
8	114.77	0.971	57.46	0.861
16	58.47	0.953	31.69	0.780
32	30.72	0.907	30.85	0.401
64	16.51	0.844	62.58	0.098
128	9.35	0.745		
256	5.68	0.613		
512	3.99	0.436		

Table 3: Execution time and parallel efficiency of the dynamic mode of SDTrimSP on the IBM Regatta and on an Intel Linux cluster for the example of 1 keV Fe atoms impinging at normal incidence onto TaC with NR = 512, NH = 20000 particles

6. Special applications

6.1. Static mode (idrel $\neq$ 0)

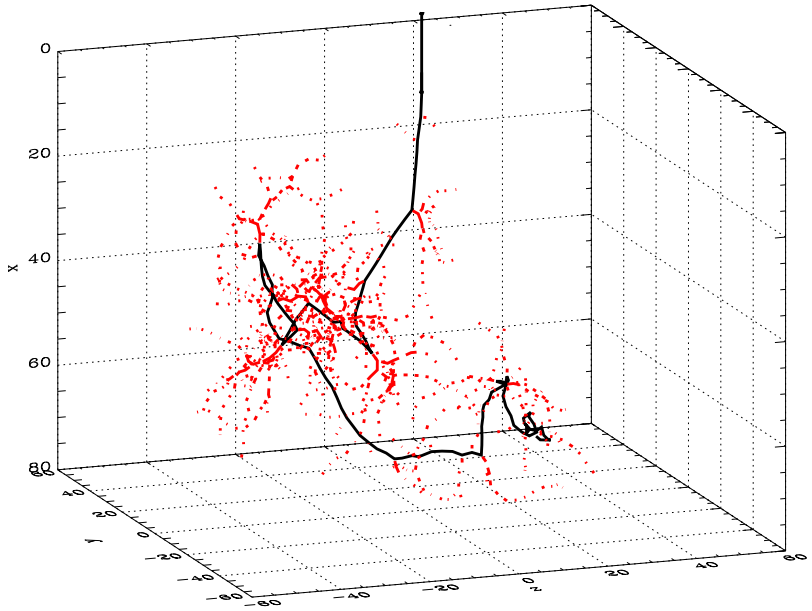

Figure 9: Trajectory of a 2 keV He atom penetrating a Ni target at normal incidence. The color indicates the projectile (black) and the recoils (red).

A typical trajectory of a 2 keV He atom in a mono-atomic Ni target is shown, see Fig. 9. The path of the incident He atom, the projectile, is black and the paths of all recoils are red (output-files: trajec_stop_p.dat + trajec_back_p.dat + trajec_back_p.dat + trajec_stop_p.dat or trajec_all.dat).
The decreasing energy of the atom along its path through the solid is indicated by the color, Fig. 10(a). The atom is stopped if its energy is smaller than the cutoff energy which is chosen to be 1.0 eV. In Fig. 10(b) the same trajectory as in the preceding figure is shown together with the generated Ni recoils. The recoils of the first generation are indicated in red, the recoils of the second generation in blue.

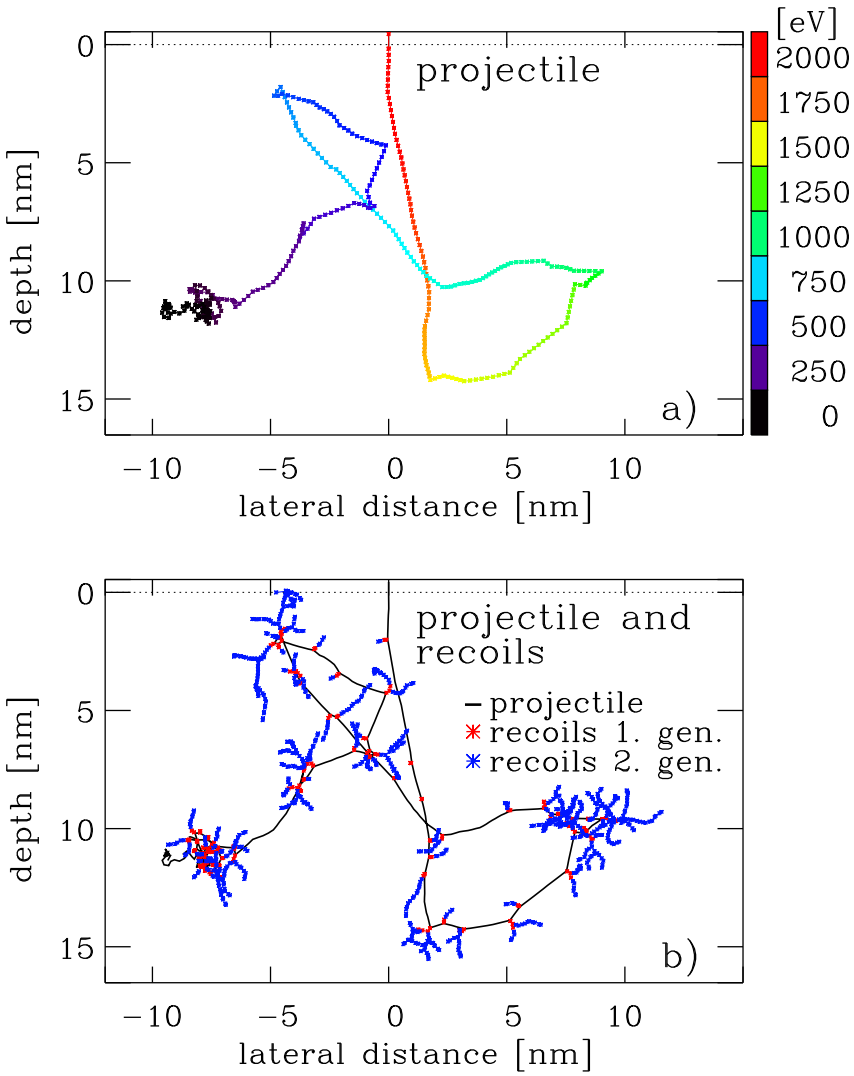

Figure 10: Trajectory of a 2 keV He atom penetrating a Ni target at normal incidence. a) The color indicates the decreasing energy of the He atom along its trajectory. b) In addition to the He trajectory also the generated recoils are shown. The color indicates the recoils of first generation (red) and the recoils of the second generation (blue).

Angular distribution of scattered and sputtered atoms

Here, we consider the bombardment of an Ni target with 1 keV Ar at $\alpha = 60°$ and $\beta = 30°$. The contour plots for the angular distributions of the reflection coefficient and of the yield per solid angle are shown in Fig.11 (output-files: meagb_p.dat and meagb_s.dat). The largest coefficient for the back-scattered particles is reached in the forward direction at a polar angle of about 75°, whereas for the back-sputtered atoms a high-intensity ridge appears in the forward direction at a polar angle of 45°. The lowest coefficients are in the backward direction for both kinds of particles.

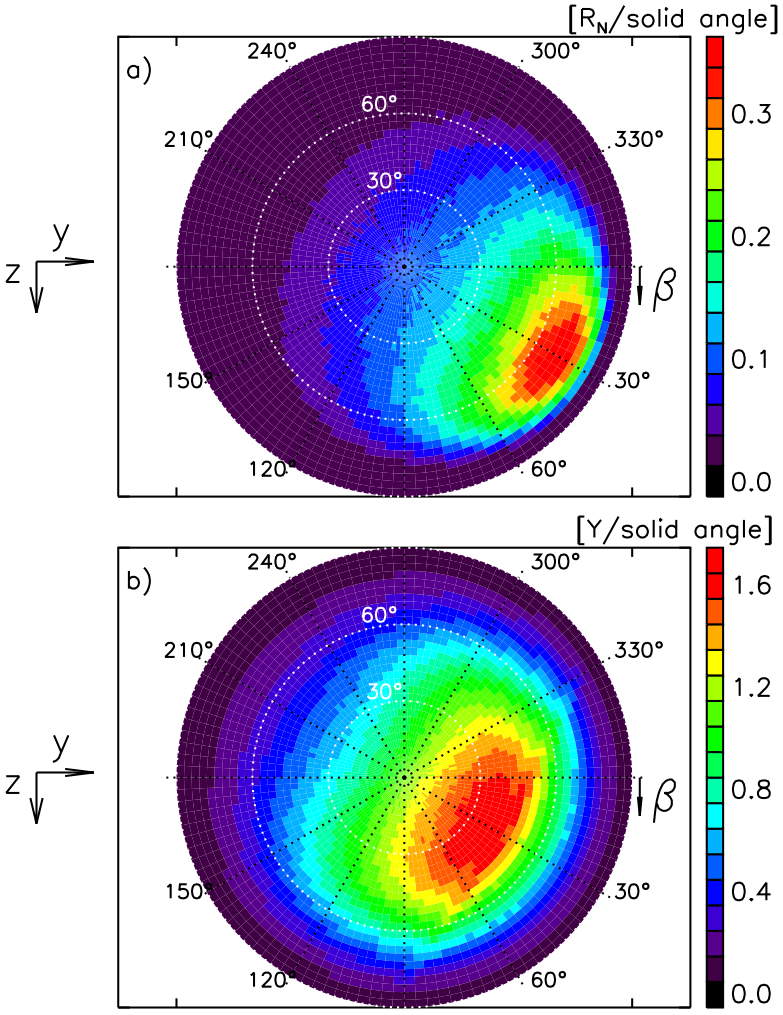

Figure 11: Contour plot of the angular distribution of the coefficient per solid angle of a) back-scattered Ar atoms and b) sputtered Ni atoms.
A Ni target is bombarded with 6400000 1 keV Ar atoms at $\alpha = 60°$ and $\beta = 30°$. The intensity is indicated by the color.

6.2. Dynamic mode (idrel=0)

back-scattering coefficient, sputtering yield and atomic fraction: back-scattering coefficient, sputtering yield and atomic fraction Fig. 12 shows the fluence dependence of the particle back-scattering coefficient, R_N, and the partial sputtering yields, Y_i, for the bombardment of the compound target WC with 10 keV Ni at normal incidence. At a fluence of about 10^{17} atoms/cm^2 R_N and Y_i become constant, which means that steady state or equilibrium is reached. The back-scattering coefficient of Ni is decreasing with increasing fluence because some of the heavy W atoms are replaced by the lighter Ni atoms. This can be seen in Fig. 13, where the atomic fractions of the three species are shown versus depth at different fluences. The partial yield of Ni is increasing from zero (pure WC target) to a constant value. At steady state the amount of Ni in the target is not changing any more with fluence which means that $R_N + Y_{\mathrm{Ni}}$ must be unity. It can also be noted from Fig. 13, that the depletion of C in the target is larger than that of W. It is a well-known fact, that in many cases the lighter element in a multi-component target is preferentially sputtered. It should be remembered that diffusion and segregation effects are not included in the calculations.

Dynamic changes of the target composition: Another interesting case is the bombardment of a target consisting of light atoms by heavy ions, in this case the bombardment of C by W at normal incidence. At the beginning of the bombardment, the target swells (positive value of surface position). This is a result of the deposition of W into the carbon target, which is larger than the sputtering of C. The composition of the target is changed particularly after a fluence of $5 \cdot 10^{16}$ atoms/cm^2. Therefore, the sputtering and reflection of W starts and the target shrinks (negative value of surface position), see Fig. 14(a). The values of back-scattering and sputtering change quasi-periodically according to the composition of the target, see Fig. 14(d). The peak of the partial yield of W (Y_{Si}) appears when the peak of the W implantation profile reaches the surface; the self-sputtering of W is much larger than the sputtering of C by W. The occurrence of further peaks is caused by the generation of further implantation profiles of W until they die out. After a fluence of $30 \cdot 10^{16}$ atoms/cm^2 a static state or equilibrium is reached and the coefficients R_N and Y_i get constant, see Fig. 14(b,c). The calculated results for atomic fraction of W show good agreement with experimental data [27], see Fig. 15.

Target composition: The program allows also layered target structures. As an example a target with several Si and Ta layers on Si is chosen, which is bombarded at normal incidence with 3 keV Ar.The oscillatory behavior of R_N and Y_i originates from the layered structure. For R_N the reason for the maxima is the higher reflection coefficient of Ar from Ta compared to that from Si due to the different mass ratio of target atom to incident ion. The peak of Y_{Si} at a fluence of about $5 \cdot 10^{17}$ atoms/cm^2 originates from the higher back-scattering of Ar from the underlying Ta. Fig. 16 shows the broadening of the depth profile, the atomic mixing and the recoil implantation in the target. Again, in this example the lighter target element, Si, is preferentially sputtered. In this run, the implantation of Ar into the target is neglected.

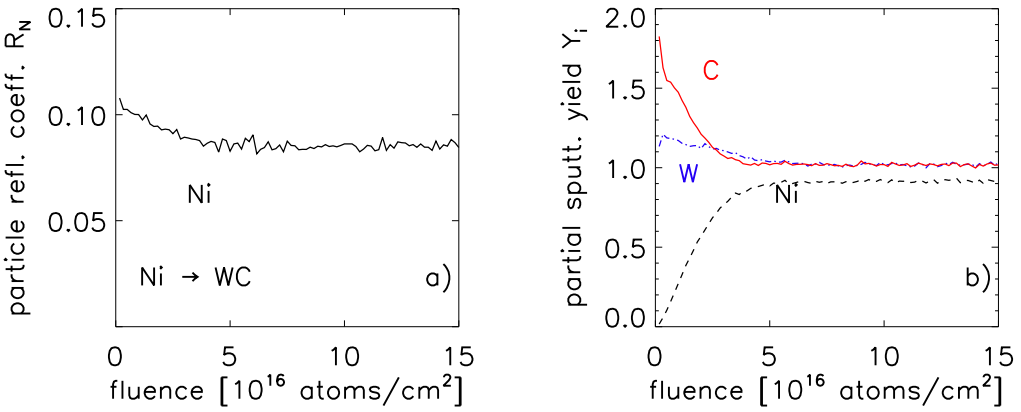

Figure 12: Fluence dependence of a) the particle reflection coefficient, R_N, and b) the partial sputtering yields, Y_i, by Ni on WC at normal incidence. A WC target is bombarded with 10 keV Ni (.

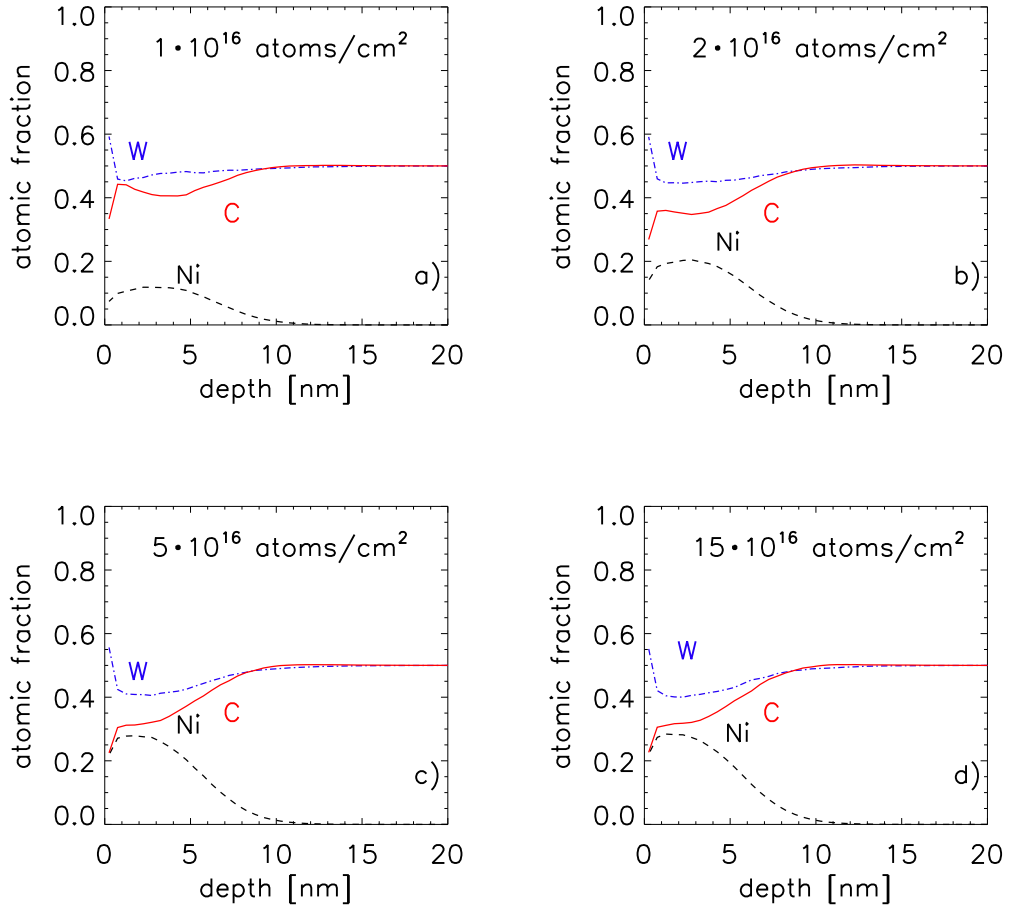

Figure 13: Atomic fraction of C, Ni and W versus depth dependent on fluence. A WC target is bombarded with 10 keV Ni at normal incidence.

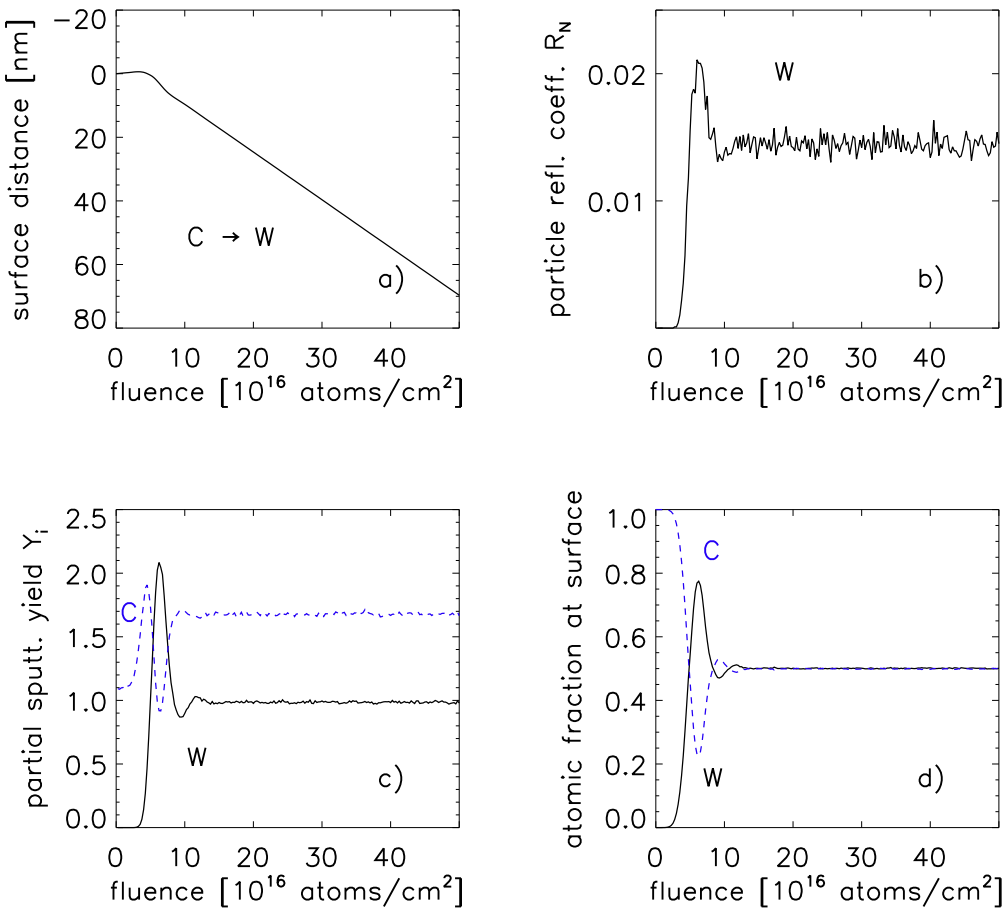

Figure 14: a) Surface distance, b) Particle reflection coefficient, R_N, of W, c) partial sputtering yields, Y_i, of C and W and d) atomic fractions of W and C for the bombardment of a C target at normal incidence with 5 keV W atoms.

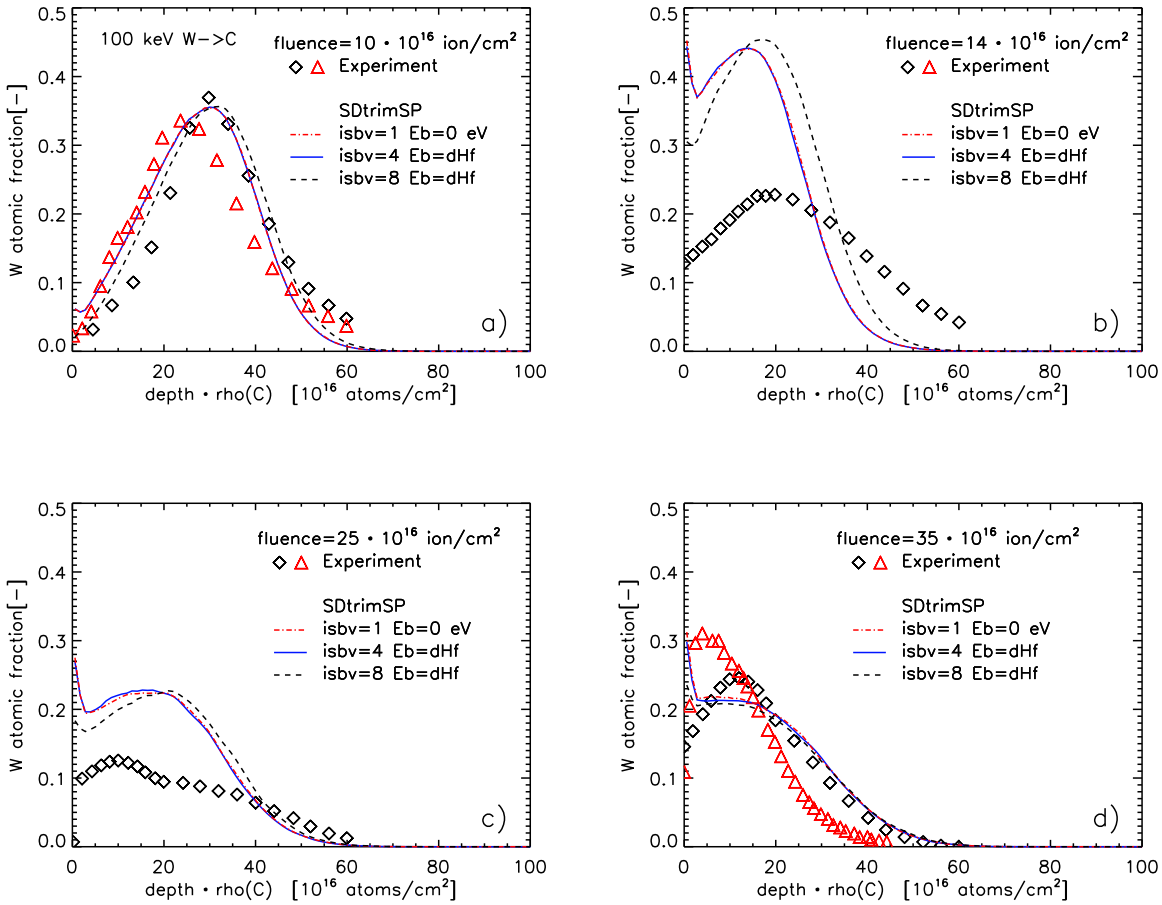

Figure 15: Comparison of the calculated atomic fractions of W with measurements [27] for four different fluences for the bombardment of a C target at normal incidence with 100 keV W atoms.

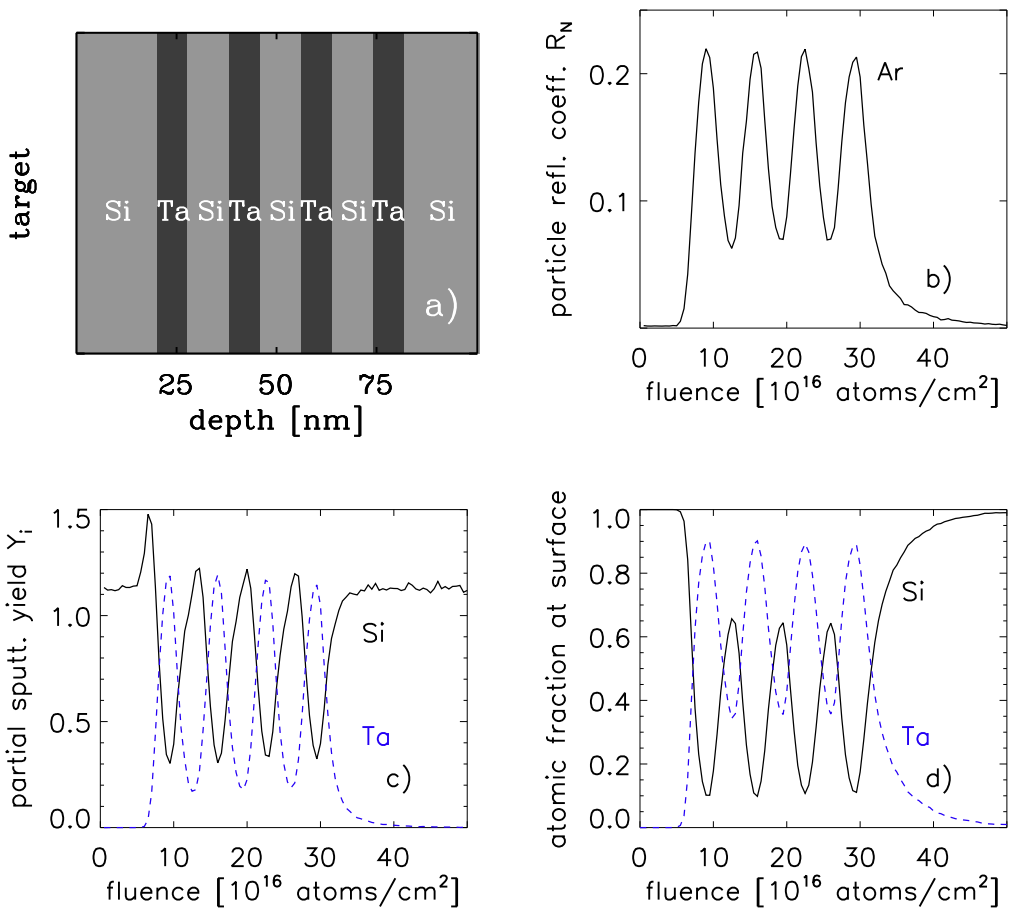

Figure 16: A Si(20 nm)[Ta(7.5 nm)Si(10.5 nm)]$_3$Ta(7.5 nm)Si target is bombarded by 3 keV Ar at normal incidence. a) Initial target composition, b) fluence dependence of the particle reflection coefficient, R_N, c) the partial sputtering yields, Y_i and d) the atomic fraction of Si and Ta at the surface (depth 0 - 0.5 nm).

6.3. Displacement-energy (irc0)

The user can choose whether he wants to take into account the displacement-energy.
default: **irc0 =-1**

If variable **irc0 < 0** then the displacement-energy is not considered. The movement of all recoils with a transfer-energy greater than cutoff- and bulk-binding-energy are calculated, i.e. all recoils can leave their old places.

If **irc0>0** then the displacement-energy is considered (threshold). All movements of recoils with a transfer-energy larger than the cutoff- and bulk-binding-energy are calculated. But at the end the recoil may be reseted, i.e. the recoils with a start-energy less then the displacement-energy can not leave their old place. This is important for the consistent calculation of damages. If the transfer-energy is less then the displacement-energy no damage is produced.
This procedure (move also if the transfer-energy is less than the displacement-energy) is necessary because this threshold (displacement-energy) looses its validity near surface.

6.4. Transport of non-bounded particles (outgasing of noble gas ions)

The implantation of atoms in the target changes the density and the composition inside the solid and therefore has an influence on the collision cascade, on the depth profile and on sputtering. Due to the low binding energy of gas atoms (nearly zero for noble gases) they can get easily sputtered. Therefore, the gas concentration near the surface is lower than in deeper layers. The sputtering happens almost exclusively in the near-surface layers, so the sputtering-yield differs only slightly from static calculations. Another effect of the low binding energy is the possible out-gasing of noble gas atoms. The descriptions of the escape of noble gas atoms from targets in TRIM and SDTrimSP (versions 4.14) are inadequate. The effect of out-gasing in these programs was realized by the re-emission of gas atoms, namely the removal of atoms from the target without any transport of these atoms through the surface. In this case the knowledge of the maximum atomic fraction qu_max of the noble gas content in the solid is required for their removal. This introduction of an upper limit for the concentration of gas atoms, which must not be exceeded, does not describe the process itself and does not calculate profiles of gas atoms in the target, representing to the correct physical situation. Fig. 17 and 18 show the areal density and profiles without out-gasing (blue dashed-line) and the red dashed-lines show the calculated results with $qu\_max = 0.1051$. The problem is the determination of the value qu_max.
A first attempt to describe the out-gasing in the SDTrimSP using a gas transport model yields very good agreement of the fluence-dependent areal density values for energies larger than 10 keV, [21]. However, as shown in [22], the maximum of the atomic fraction as a function of the energy of the incident atoms and the stationary profiles of Xe are

not reproduced correctly. Also the physical explanation of a constant gas transport is difficult to provide.
To develop a model, that reproduces the steady-state profiles, areal density values and maxima of the atomic fraction, the following assumptions are used: The implanted gas atoms are not bounded in the target and cannot diffuse through a defect free lattice. The measured noble gas profiles after the bombardment of Xe on Si are the same as those produced during the bombardment. The implantation of gas atoms lead to a swelling of the target, so that a pressure arises, which is only gradually removed through relaxation. This pressure is responsible for local transport.
Only the presence of defects are cause a local diffusion. The damage is created during the collision-cascade and exists only temporarily. The diffusion depends on the concentration of damage and the number density of the unbounded gas atoms. The total transport of gas atoms can happen only within the range of the depth of penetration and is composed of two parts, the pressure-driven transport and the damage-driven diffusion.
The input (option) variable is **loutgas**.
default: **loutgas** = **.false.**

6.4.1. Damage-driven diffusion, DDF

According to Fick's diffusion law the flux J is:

$$J = -\frac{\partial(\eta(z) \cdot n(z))}{\partial z} \quad \text{, with} \tag{6.1}$$

η the diffusion coefficient, n the concentration (number density) and z denoting the depth. The fluence-dependent equation is:

$$\frac{\partial n}{\partial \phi} = -\frac{\partial(\eta(z) \cdot \frac{\partial n(z)}{\partial z})}{\partial z} \tag{6.2}$$

Although the atoms (Xe, Ar) are not bounded, however they cannot diffuse freely. Only due to the collision damage (like damage diffusion) the atoms can move in the target. The relative probability for the diffusion is P_{dam}. Therefore the diffusion-coefficient can be express as:

$$\eta(z) = \eta_0 \cdot P_{dam} \tag{6.3}$$

A series of calculations has shown that the probability depends on both the number of the damage as well as the concentration of the particles. N_{dam} is the number density of damage in a layer and $qu(z)$ the atomic fraction. The area in which diffusion occurs is the range of the defect profile. Therefore the relative probability for diffusion is given by:

$$P_{dam} = \frac{N_{dam}(z)}{max[N_{dam}]} \cdot qu(z) \tag{6.4}$$

The input variable of η_0 is **diff_koeff1**.
default: **diff_koeff1(:)=0.0**
An example for the variation of η or $P_{dam} = \eta(z)/\eta_0$ is displaces in Fig. 20 (red dashed line).

6.4.2. Pressure-driven transport, PDT

The pressure is generated by the particles coming from the outside. A high pressure is created at the implantation position. The target responds by expansion and the pressure reduces after a certain period. But before the target relaxes fully, this pressure generate a transport non bounded particles (Xe, Ar) towards the surface. The flux J, is:

$$J = -K(z) \cdot n(z) \tag{6.5}$$

K is the transport coefficient, n is the concentration (number density) and z is the depth. ϕ is the fluence. The fluence-dependent equation is:

$$\frac{\partial n}{\partial \phi} = \frac{\partial (K(z) \cdot n(z))}{\partial z} \tag{6.6}$$

The range of the transport is limited by the range of the implanted profile z_{max}. Therefore the transport-coefficient is:

$$K(z \leq z_{max}) = K_0 \tag{6.7}$$
$$K(z > z_{max}) = 0 \tag{6.8}$$

The flux increases monotonically with the number of particles and the flux dependent on the form of the profile.
The input variable of K_0 is **diff_koeff2**.
default: **diff_koeff2(:)=0.0**
An example for the variation of K is provided in Fig. 20 (blue dot dashed line).

6.4.3. Results

The comparison between measured depth profiles and calculated profiles are shown in Fig. 19 and 20. The agreements of calculated areal density and maximum of atomic fraction with the measured values are very good, see Fig. 21 and 22.

The coefficients η_0 (diff_koeff1) and K_0 (diff_koeff2) for Xe and Ar are:

$$\begin{aligned} \eta_0(Xe) &= 1.65 \cdot 10^6 \ \mathring{A}^4/ion \\ K_0(Xe) &= 95 \ \mathring{A}^3/ion \\ \eta_0(Ar) &= 1.65 \cdot 10^5 \ \mathring{A}^4/ion \\ K_0(Ar) &= 15 \ \mathring{A}^3/ion \end{aligned}$$

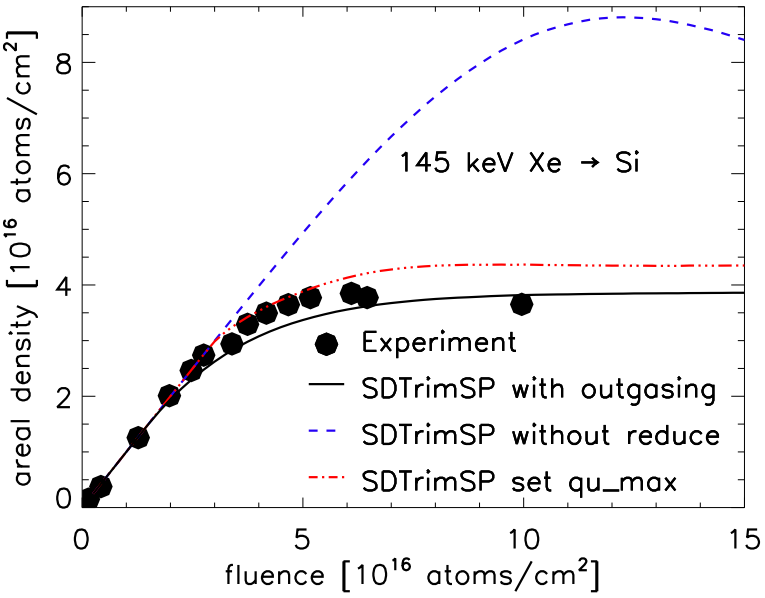

Figure 17: Comparison of experimental results [24] with calculated areal density 145 keV Xe on Si with and without transport of unbounded particles and for $qu\_max = 0.1051$

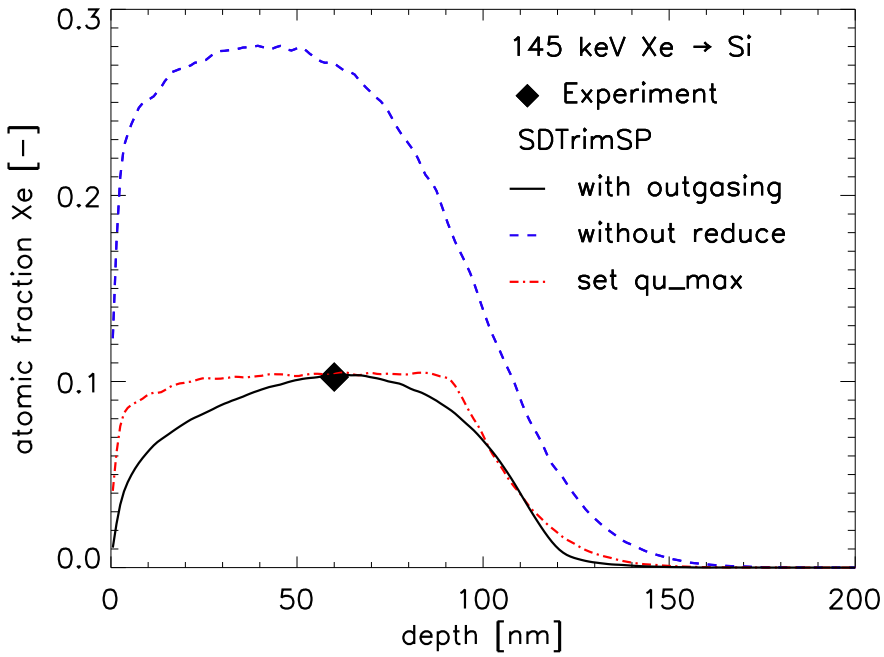

Figure 18: Comparison of the experimental maximum of atomic fraction [24] with calculated profiles for 145 keV Xe on Si with and without transport of unbounded particles and for $qu\_max = 0.1051$

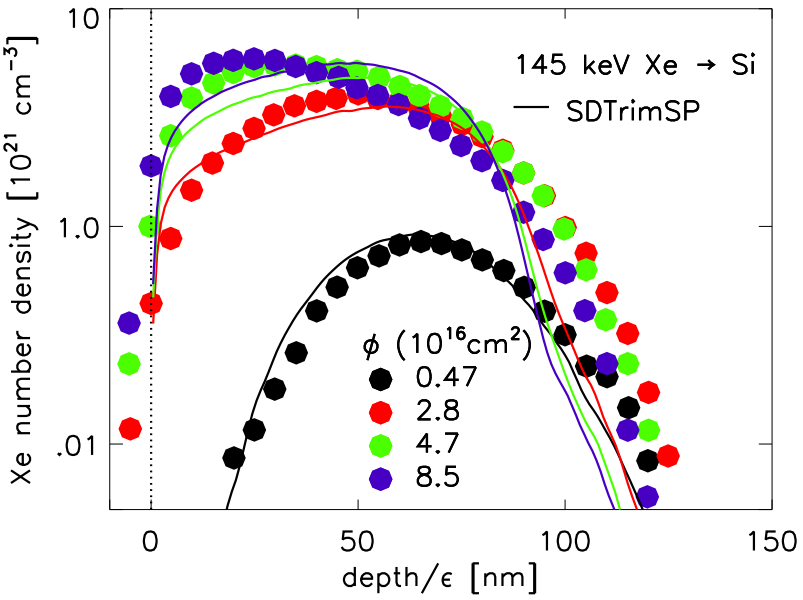

Figure 19: Comparison of experimental results [24] with calculated number density for 145 keV Xe on Si dependent on different fluences

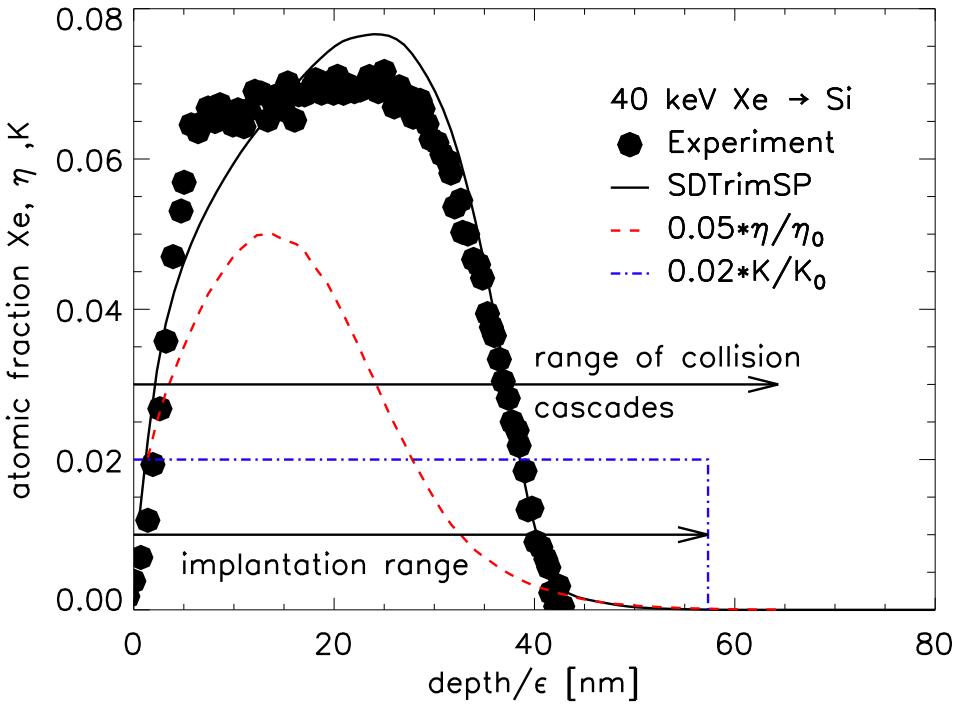

Figure 20: Compare of experimental results [23] with calculated atomic fraction for 40 keV Xe on Si with transport- and diffusion-coefficient

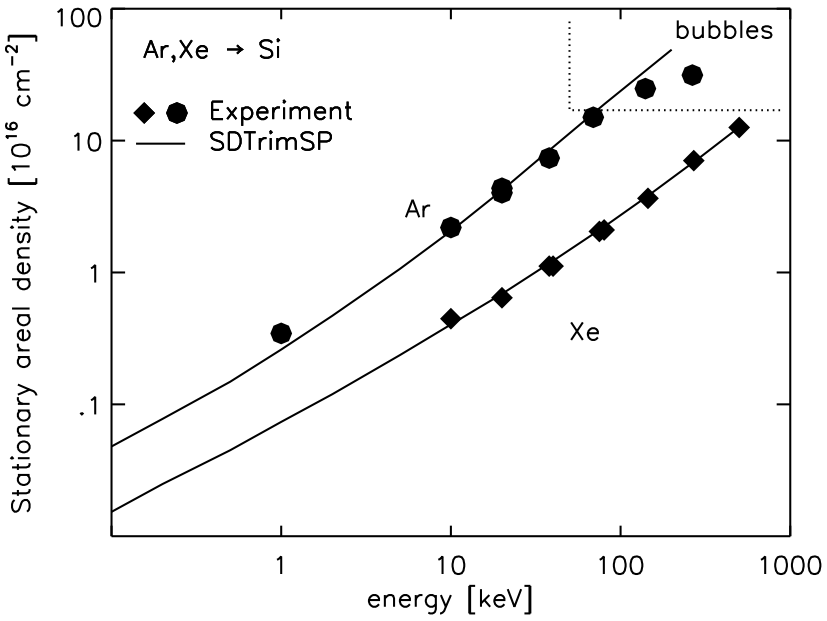

Figure 21: Calculated steady state areal density of implanted Xe versus the incident energy of Xe on a Si target at normal incidence compared with experimental data [22]

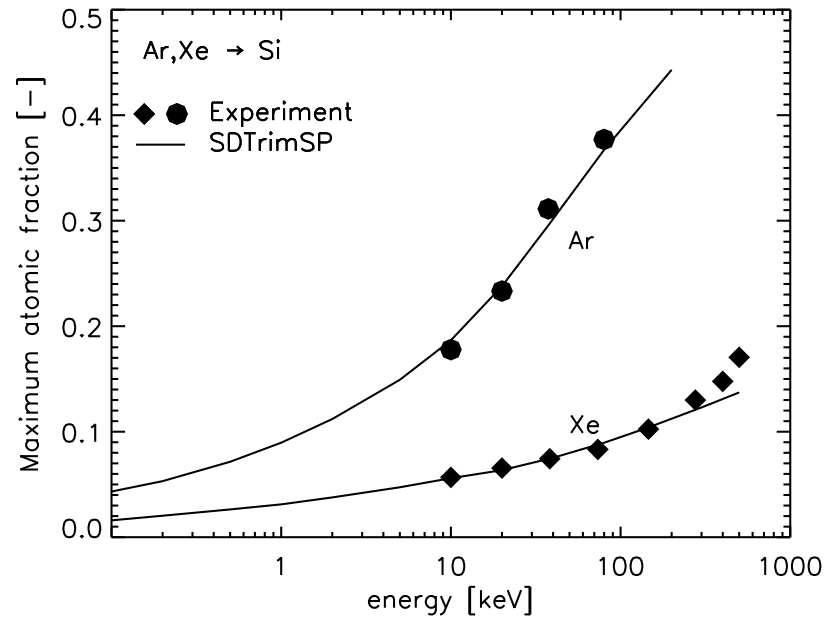

Figure 22: Calculated steady state maximum atomic fraction of implanted Xe versus the incident energy of Xe on a Si target at normal incidence compared with experimental data [22]

6.5. Chemical erosion of carbon

The total methane erosion yield (Y_{CH_4}) is calculated as a sum of a kinetic contribution Y_0 at $T_0 = 300K$ and a temperature-dependent thermal contribution Y_T, [36].

$$Y_{CH_4} = \quad Y_0(E, T_0, sp^3, sp^x_{CH}) \quad + Y_T(E, T, sp^3, sp^x_{CH}) \tag{6.9}$$

E is the energy of incident particles. sp^3 and sp^x_{CH} are carbon hybridization states.

The option is : **lchem_ch=.true.**,
default is: **lchem_ch=.false.**

Introduction of different carbon hybridization states
In the version of SDTrimSP without chemical erosion carbon atoms were simulated as a single species, C_g. For simulation of chemical erosion one needs to distinguish carbon atoms of different hybridization states as different species. Therefore, the chemistry module describes an a–C:H film in terms of three carbon species namely, sp^2 (carbon with double bonds), sp^3 (carbon with single bonds and not bonded to H atom) and sp^3_H (sp^3 carbon with a bonded H atom).

The chemical binding energy of C-C is 3.60 eV and of C=C 6.35 eV. The necessary energy to break the double-bond (C=C) to a single bond (C-C) is 2.75 eV. If the transfer-energy is greater than this value the carbon-hybrid sp^2 is changed to sp^3.
To change a sp^3-hybrid to methane (break the bond of C-C) an energy greater than 3.00 eV is used in the program (3.60 eV do not work for incident-energies less then 20 eV). The chemical binding energy of C-H is 4.3 eV. It may be that this released energy reduces the energy necessary to break the single bonds.

The code has been enhanced to include the following chemical reactions:

1. If an impinging ion transfers more than a critical value of energy, ie. the energy-transfer $\geq$ 2.75 eV to a sp^2 carbon then the double bond is broken and a sp^3 carbon is created.

2. Since there is an upper limit of 1/3 on H atoms bonded to C for typical C:H film, this was used as a limit, *ie.*,
   - if the concentration of H (n_H) or sp^3 (n_{sp^3}) exceeds the concentration of sp^3_H ($n_{sp^3_H}$), sp^3 carbon is changed to sp^3_H.
   - if n_H or n_{sp^3} is less than $n_{sp^3_H}$, sp^3_H is transferred to sp^3.

3. The maximum concentration of carbon centers in sp^3 hybridization state (sp^3, sp^3_H) is controlled (as a feedback mechanism) by the values calculated by the Mech model [35] (sp^3,sp^3_H,sp^3_{CH}) and is dependent on the temperature. For example, at a given temperature, if the total concentration of carbon centers in sp^3 hybridization state calculated from SDTrimSP ($n_{sp^3} + n_{sp^3_H}$) is greater than the corresponding value predicted by the Mech model, then sp^3_H will be changed into sp^2 carbon.

Contribution from the kinetic part

The calculation of the kinetic part, $Y_0(E, T_0)$, of the erosion yield is based on the mechanism proposed by Hopf [34]. Let's say Y_{BB} represents the number of bond breaks of sp^3_H caused by an impinging ion and $Y_{H_{stop}}$ gives the yield of the H atom implantation. These stopped or implanted H atoms can be bonded to free open carbon bonds.
For hydrocarbon formation both open carbon bonds and hydrogen atoms must be available. In order to include this effect the minimum of Y_{BB} and Y_{Hstop} is taken. For the out–diffusion probability of a hydrocarbon molecule from a depth x the kinetic part of the chemical erosion yield $Y_0(E, T_0)$ is given by

$$Y_0(E, T_0) = \int_0^d a_0 \cdot min[Y_{BB}, 2 \cdot Y_{H_{stop}}] \cdot e^{(-x/\lambda)}\, dx \qquad E > 3.0\ eV \tag{6.10}$$

Here, λ (= 0.4 nm) is the typical range of out-diffusion for hydrocarbon and d is the depth of the sample. If the whole sample is divided into k strips or depth intervals parallel to the surface as in SDTrimSP

$$Y_0(E, T_0) = \sum_0^k a_0 \cdot min[Y_{BB}(k), 2 \cdot Y_{H_{stop}}(k)] \cdot e^{(-x(k)/\lambda)}. \tag{6.11}$$

The minimum condition $min[Y_{BB}(k), 2{\cdot}Y_{H_{stop}}(k)]$ expresses the fact that chemical erosion only happens when sufficient number of open bonds ($Y_{BB}(k)$) and sufficient number of hydrogen ($Y_{H_{stop}}(k)$) are available. Therefore, the minimum of both will limit the production of hydrocarbons. The value of the coefficient a_0 ranges from 0.04 to 1.0 and was obtained by the comparison of measurements and simulation results.

$$a_0 = min[1.0,\ 0.04 + 0.0075 \cdot \frac{Y_{H_{stop}}(k)}{Y_{BB}(k)}] \tag{6.12}$$

Contribution from the thermal part

The temperature dependent part of the chemical erosion yield, $Y_T(E, T, \Phi_0)$, in the code is based on the Mech model [35].

$$Y_{TMech}(E, T, \Phi_0) = \varrho \cdot sp^x_{CH} \frac{Ex}{\Phi} \quad \text{, where} \tag{6.13}$$

ϱ is the surface density of carbon atoms: $\varrho = 6.0 \cdot 10^{19}\ atoms/m^2$.

$$Y_T(E, T, \Phi_0) = \sum_1^n a_T \cdot Y_{T\_Mech}(E, T, \Phi_0) \cdot e^{(-x/\lambda)} \qquad E > 3.0\ eV \tag{6.14}$$

$$a_T = 1/(sp^3 + sp^x_{CH})^{0.7} \tag{6.15}$$

Here n is the total number of collisions between ions and sp^3_H. A depth dependent out–diffusion probability after the hydrocarbon formation $e^{(-x/\lambda)}$ is added. The term $Y_{T\_Mech}(E, T, \Phi_0)$ is the yield of chemical erosion at a flux of ($\Phi_0 = 10^{18}\, m^{-2} s^{-1}$).

Flux dependence of chemical erosion
It is observed that the kinetic part of the erosion yield is flux independent. Therefore, in order to implement the correct flux dependence the thermal contribution (Y_{therm}) to the erosion has to be flux dependent. A flux interpolation is done with the help of Roth's formula [33].
The erosion yield given by the Mech model is correct only for a flux of $10^{18} m^{-2} s^{-1}$ (this is kept as the reference level flux Φ_0). It has been observed that with increasing flux, the temperature for which the yield is maximum ($T_{max}(E, \Phi)$) and the absolute value of the yield ($Y_{max}(E, \Phi)$) are increasing. It is assumed that $T_{max}(E, \Phi)$ as predicted by the Roth model is correct (although $Y_{max}(E, \Phi)$ is not). Then in order to calculate the flux dependent erosion yield for a given flux Φ and energy E, one proceeds as follows:

1. First the ΔT from Roth's formula (see Fig. 23) is computed

$$\Delta T = T_{max}(E, \Phi) - T_{max}(E, \Phi_0) \tag{6.16}$$

2. then the erosion yield from the Mech model at $T - \Delta T, \Phi_0$ is calculated

$$Y_{T\_Mech}(E, T - \Delta T, \Phi_0) \tag{6.17}$$

3. the corrected flux dependent erosion yield is given by

$$Y_{Tcor}(E, T, \Phi) = Y_{T\_Mech}(E, T - \Delta T, \Phi_0) \cdot \frac{max[Y_{Roth}(E, T, \Phi)]}{max[Y_{Roth}(E, T, \Phi_0)]} \tag{6.18}$$

If the sample is composed of n layers, then the total flux dependent thermal erosion yield is

$$Y_T(E, T, \Phi) = \sum_1^n a_\Phi \cdot Y_{Tcor}(E, T, \Phi) \cdot e^{(-x/\lambda)} \tag{6.19}$$

$$a_\Phi = 1/(sp^3 + sp^x_{CH})^{0.7} \quad . \tag{6.20}$$

Finally the total erosion yield of carbon is:

$$Y = Y_{physical}(E) + Y_0(E, T_0) + Y_T(E, T, \Phi) \quad . \tag{6.21}$$

In the following part of this section the general algorithm in the simulation and its technical implementation is presented, [36].
A pre–calculated number of energetic particles, depending on the fluence, are incident on the target. The target is divided into 1D layers and during each fluence step the incident particles initiate a collision cascade in the target. At the end of each fluence step the sputtering yield (chemical and physical), the scattering coefficient, and the implantation is calculated and then the sample is updated accordingly.

Depending upon the incident particle and target combination it is checked after each collision whether some thermal chemical reactions are possible or not. If yes, then the chemistry module is used to process the reactions. Then the depth dependent out–diffusion probability of the reactions products is also calculated and this is used to calculate the thermal part of the erosion yield.
During the cascade the number of broken bonds is calculated for each layer. During the collision with the target atoms the incident particles loose their energy and at the end of the collision cascade they get implanted into the target. The number of the implanted hydrogen atoms are calculated for each layer. At the end of the fluence step the total number of implanted hydrogen atoms and broken bonds are used for the calculation of the kinetic part of the erosion yield.
The maximum amount of bonded hydrogen has an upper limit of 1/3. At the end of each fluence step the relative concentration of the bonded hydrogen is calculated and if it exceeds the upper limit the surplus hydrogen is treated as freely moving. This hydrogen can then diffuse through the target and leave the system. The corresponding interchange among the different carbon hybridization states is also calculated simultaneously.
The surface binding energy (SBE) used for the pure carbon target (mainly sp^2) is 6.35 eV. If a sample of pure carbon is bombarded then sp^2 is created. The surface binding energy (SBE) of sp^2 is 3.60 eV.
Finally all the counters for the bond breaking and hydrogen implantation in each layer are reset to zero after calculation step.

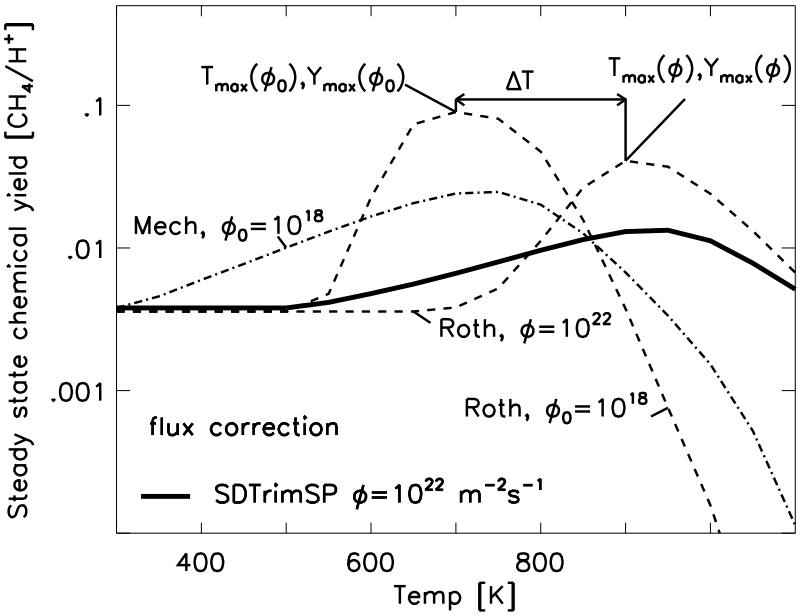

Figure 23: Correction of the thermal erosion yield of Mech [35] by a H flux $\Phi = 10^{18}\, m^{-2}s^{-1}$ to values for $\Phi = 10^{22}\, m^{-2}s^{-1}$ (SDTrimSP) using the analytical formula by Roth [33].

Comparison of calculated results of chemical erosion with experimental data

Fig. 24 shows a comparison of calculated results of H on C target with measurements at three different temperatures (T=300 K, 700 K and 800 K) as a function of the energy. The agreement of the calculated values with the experimental data is very good.
Fig. 25-27 shows a comparison of calculated methane yield of H on C target with measurements versus temperature at different energy and fluxes. The agreement is very good.
Fig. 28 provides a comparison of the calculated methane yield of 1000 eV H on a C target with measurements versus fluxes at different temperatures.

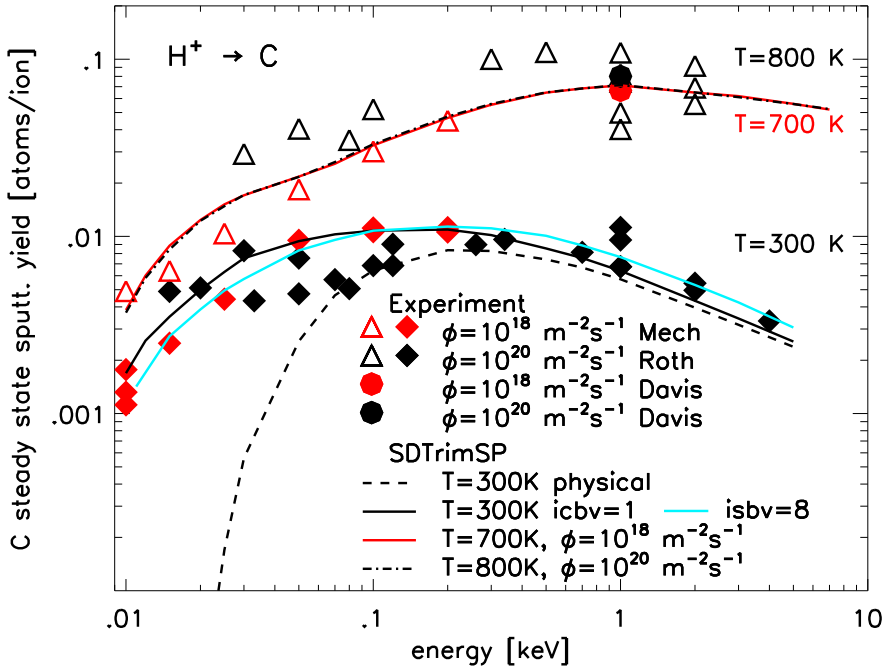

Figure 24: Calculated steady state sputtering yields of C versus the incident energy of H on a C target at normal incidence compared with experimental data [33], [35], [37].

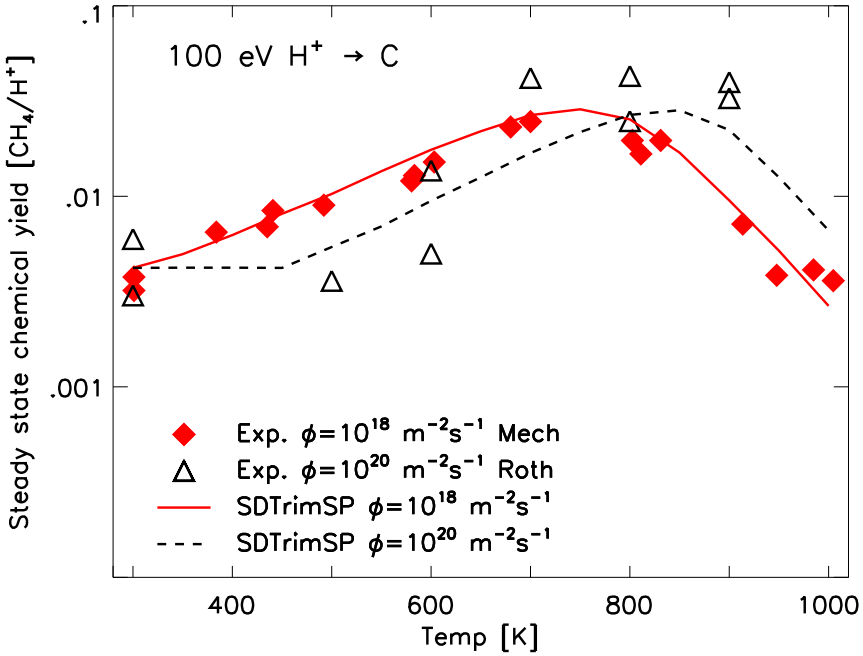

Figure 25: Calculated steady state sputtering yields of methane versus the temperature for 100 eV H on a C target at normal incidence for two different fluxes compared with experimental data [33], [35].

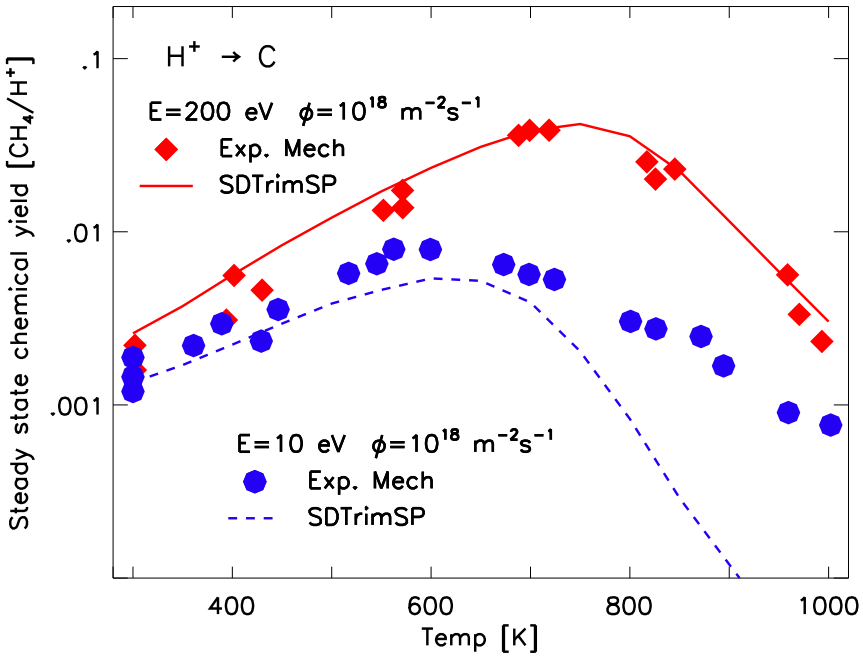

Figure 26: Calculated steady state sputtering yields of methane versus the temperature for 10 and 200 eV H on a C target at normal incidence compared with experimental data [35].

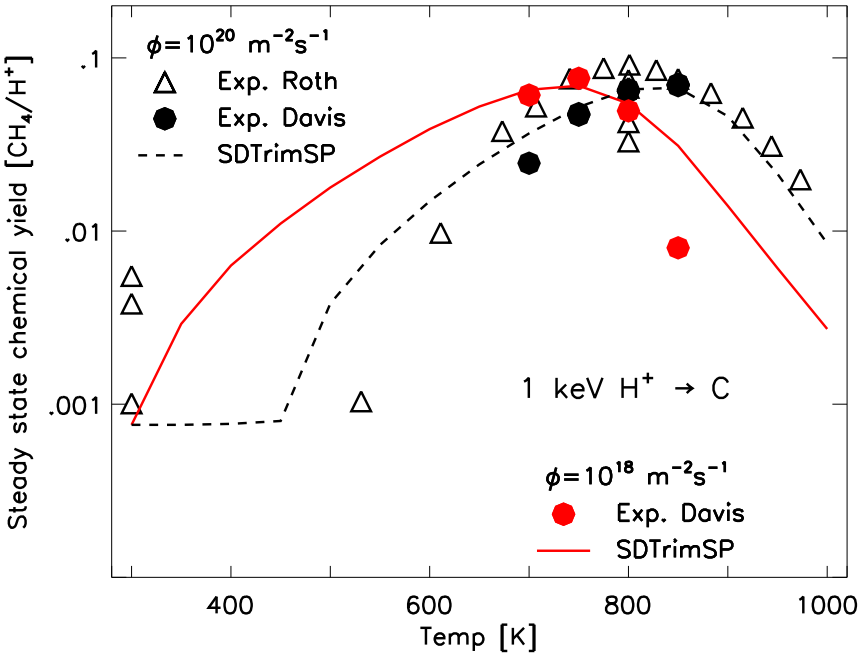

Figure 27: Calculated steady state sputtering yields of methane versus the temperature for 1000 eV H on a C target at normal incidence for two different fluxes compared with experimental data [33], [35], [37].

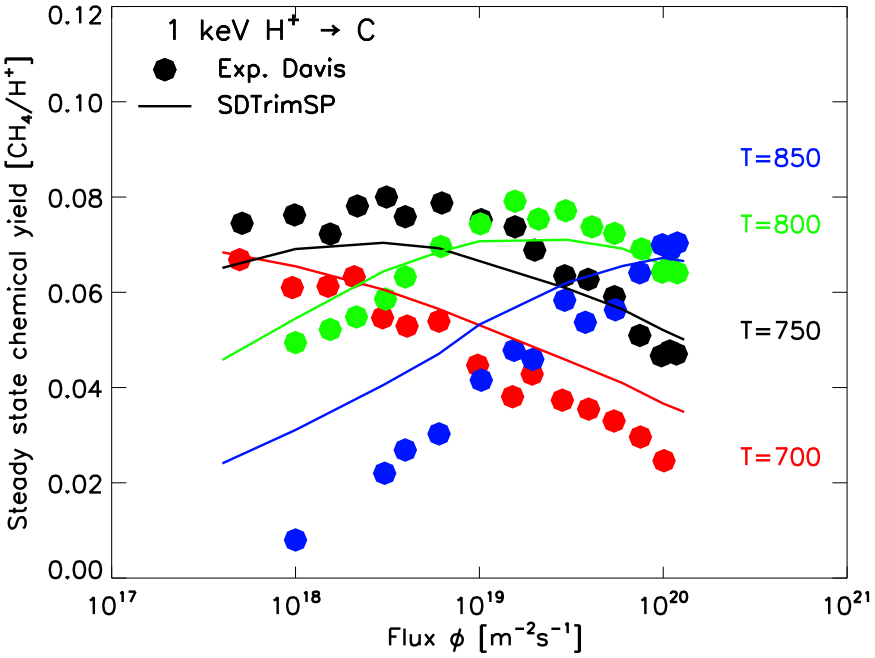

Figure 28: Calculated steady state sputtering yields of methane versus flux for 1000 eV H on a C target at normal incidence compared with experimental data [37].

Fig. 29 shows a comparison of calculated results of D on C target with measurements at two different temperatures as a function of the energy. Although the calculated results at room temperature are at the lower limit, the agreement is very good.

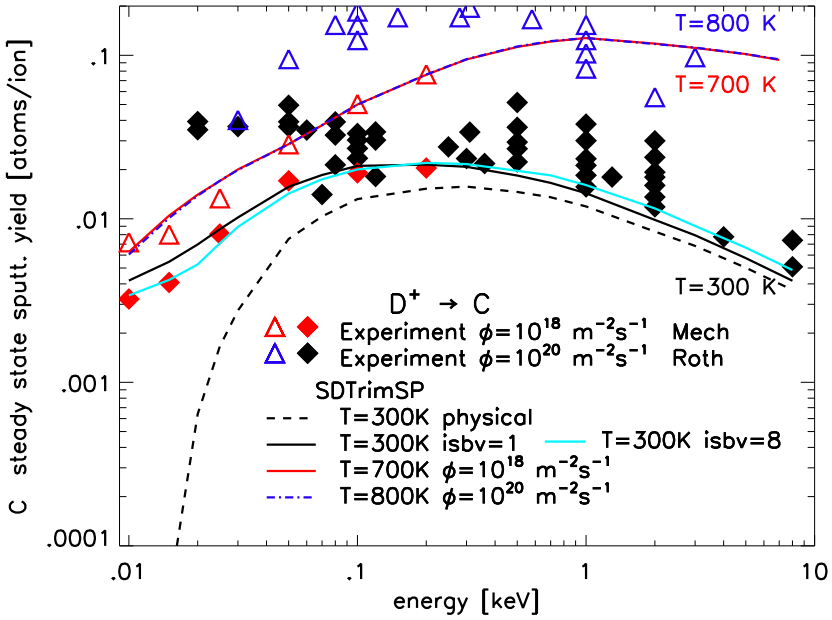

Figure 29: Calculated steady state sputtering yields of C versus the incident energy of D on a C target at normal incidence compared with experimental data [33].

6.6. Thermal diffusion (lterm_dif, a_0, e_act)

There the solid-state diffusion within the target is modelled (not outgasing). It typically matters only for high temperatures and low impinging fluxes. It is assumed that the diffusion flux is proportional to the concentration gradient.
The thermal diffusion depends on the temperature T, the time t, the atomic fraction qu and coefficients a_0 and e_act. The coefficients a_0 and e_act are matrices, which depend on the species in the target. The diffusion equation

$$\frac{\partial n(x,i)}{\partial t} = \frac{\partial(\eta(i) \cdot \frac{\partial n(x,i)}{\partial x})}{\partial x}$$

with the defusion coefficient $\eta(i)$ given by

$$\eta(i) = a\_0(i,i) \cdot e^{-e\_act(i,i)/kT}$$

The boundary condition at the surface is:

$$\frac{\partial n}{\partial x}|_{x-0} = 0$$

The time t needed for a fluence step Δflc depends on the flux of projectiles and is given by

$$t = \frac{\Delta flc}{flux}$$

The flag for diffusion is lterm_dif and the names of the input-files are "a0_tdiff.inp" and "eact_tdiff.inp", see appendix.
default: **lterm_dif=.false., a_0(:,:)=0.0, e_act_0(:,:)=0.0**

The method is controlled with flag i_diff_algo, see appendix.
default: **i_diff_algo=2**

i_diff_algo	=0 : simple diffusion
	=1 : explicit algorithm (lambda_cn=0)
	=2 : implicit algorithm (lambda_cn=1)
	=3 : Crank-Nicolson (lambda_cn=0.5)
	=4 : Crank-Nicolson with lambda_cn=0...1

The full implicit algorithm for diffusion equation is slightly faster and stable than the Crank-Nicolsen thus the recommended setting.

An example of the full coefficient-matrix for a C-W target found in [38]. All diffusion-coefficients (C in W, C in C, W in C and W in W) are same.

$$a\_0 = \begin{pmatrix} 8.91 & 8.91 \\ 8.91 & 8.91 \end{pmatrix} \cdot 10^{-6}\ [m^2/s]$$

$$e\_act = \begin{pmatrix} 2.32 & 2.32 \\ 2.32 & 2.32 \end{pmatrix}\ [eV]$$

In this version of program is for one species (for example C) no distinction between C in W or C in C. This means only the values from the diagonal are used.

$$a\_0 = \begin{pmatrix} 8.91 & 0.00 \\ 0.00 & 8.91 \end{pmatrix} \cdot 10^{-6}\ [m^2/s]$$

$$e\_act = \begin{pmatrix} 2.32 & 0.00 \\ 0.00 & 2.32 \end{pmatrix}\ [eV]$$

Fig. 30 shows the time dependent profile of a C-layer in a W-target.

Another example of the coefficient-matrix is a bombardment of a Fe-W target with D, see Fig. 31. Only Fe and W can diffuse.

$$a\_0 = \begin{pmatrix} 0.00 & 0.00 & 0.00 \\ 0.00 & 1.5e-2 & 0.00 \\ 0.00 & 0.00 & 1.5e-6 \end{pmatrix}\ [m^2/s]$$

$$e\_act = \begin{pmatrix} 0.00 & 0.00 & 0.00 \\ 0.00 & 2.97 & 0.00 \\ 0.00 & 0.00 & 2.97 \end{pmatrix}\ [eV]$$

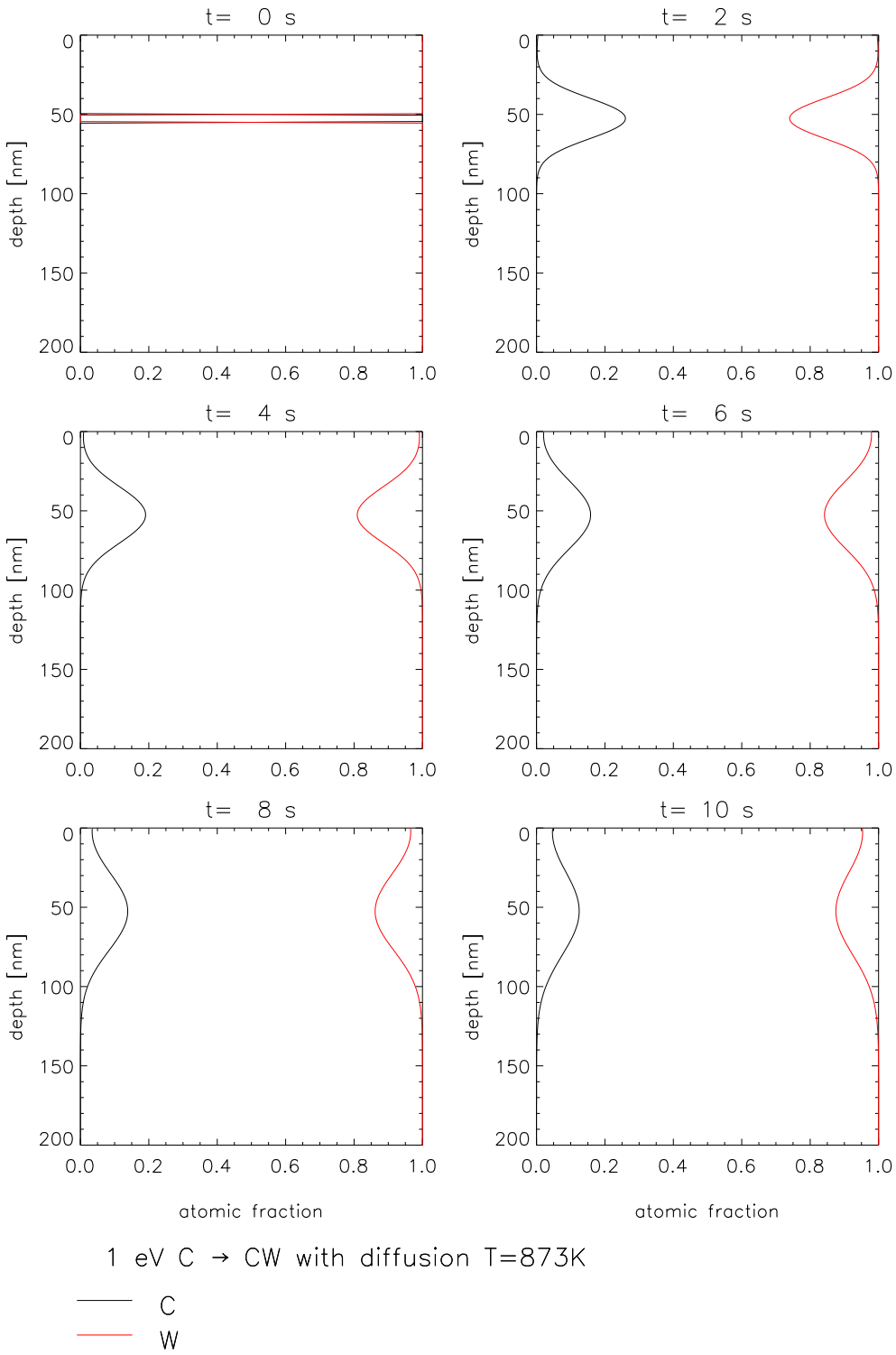

Figure 30: Calculated thermal diffusion of a thin C-layer in a W target.

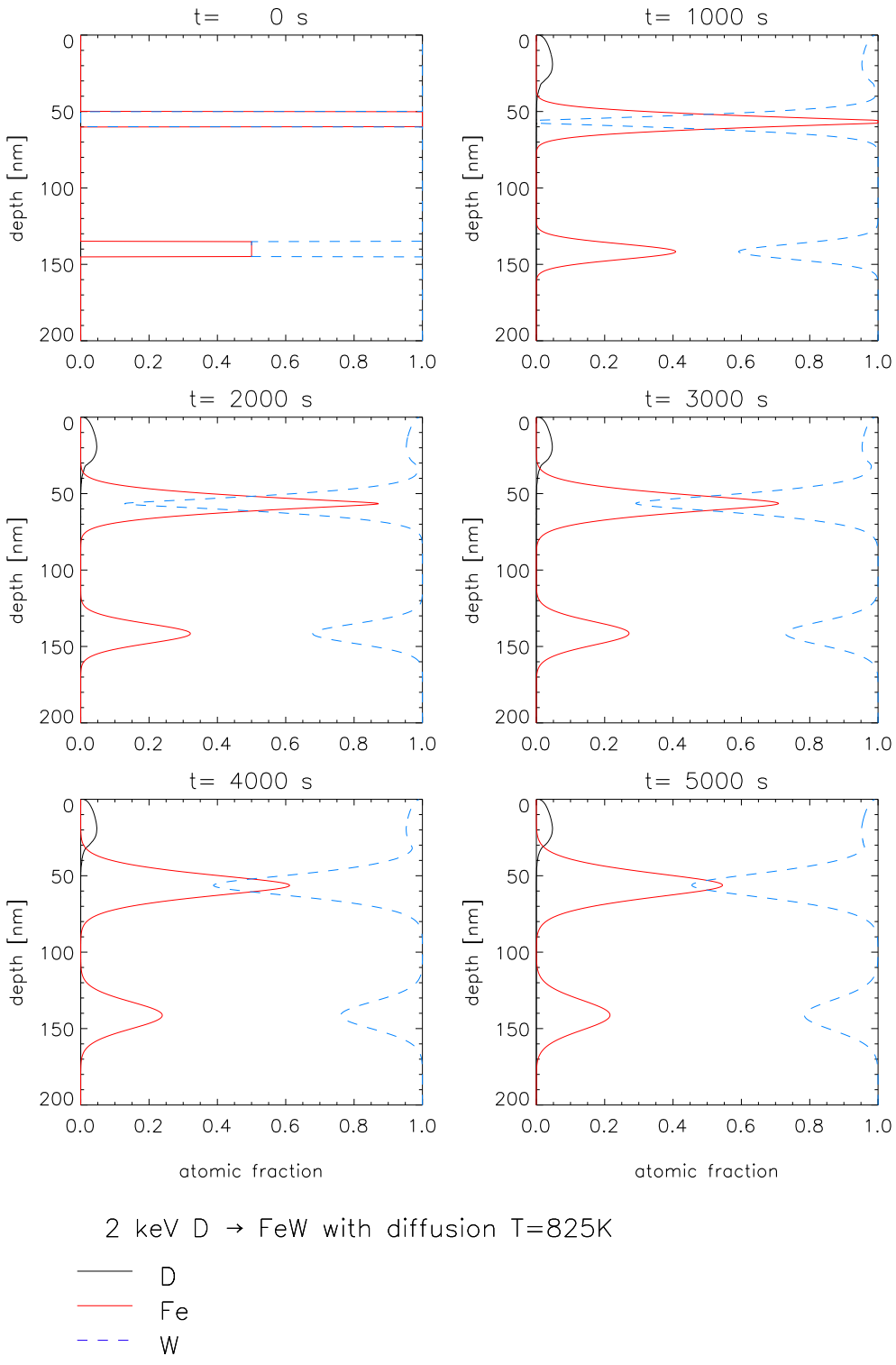

Figure 31: Calculated thermal diffusion of thin Fe-layers in a W target.

6.7. Integration methods (iintegral)

The scattering angle ϑ in the center-of-mass system [1] is determined by:

$$\vartheta = \pi - 2p \int_R^\infty r^{-2} g(r)^{-1} dr \tag{6.22}$$

$$g(r) = \sqrt{1 - \frac{p^2}{r^2} - \frac{V(r)}{E_r}} \ , \quad g(R) = 0 \tag{6.23}$$

where p is the impact parameter, R is the distance of closest approach of the two collision partners, $V(r)$ is the interaction potential and E_r is the energy in the center-of-mass system.

The other important integral is the time-integral τ

$$\tau = \sqrt{r^2 - p^2} - \int_R^\infty g(r)^{-1} - f(r)^{-1} dr \tag{6.24}$$

$$f(r) = \sqrt{1 - \frac{p^2}{r^2}} \tag{6.25}$$

The numerical solution of the integrals 6.22 and 6.24 is possible with the Gauss-Mehler quadrature [12], the Gauss-Legendre quadrature [13] or the 'MAGIC' algorithm from Biersack [11]. The results of the different integration methods are shown in Fig. 32 and Fig. 33.
All calculation were made with the '$Kr - C$' Potential and surface-binding-model one. The difference between the integration methods of Gauss-Mehler and Gauss-Legendre is small.

The method 'MAGIC' is only an approximate method and it agrees well only for high energy ranges. It should be avoided and is provided for backward compatibility used.

Default is the use of the integral-method Gauss-Legendre-Quadrature: **iintegral=2**
This method use a number of pivot-coefficients. Default is: **ipivot=8**

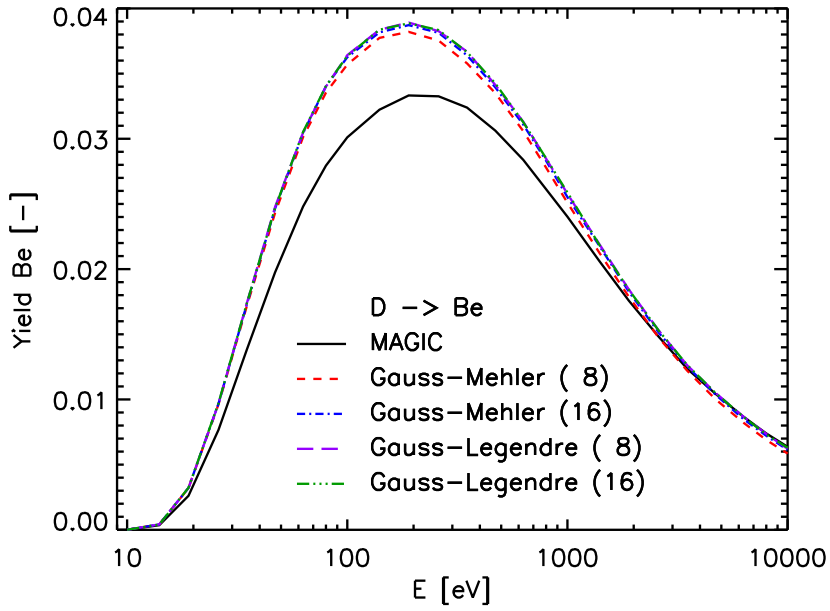

Figure 32: Calculated sputtering yield Y D on a Be target for three different integration methods. Gauss-Mehler and Gauss-Legendre were calculated with 8 and 16 numbers of integration-steps (ipivot).

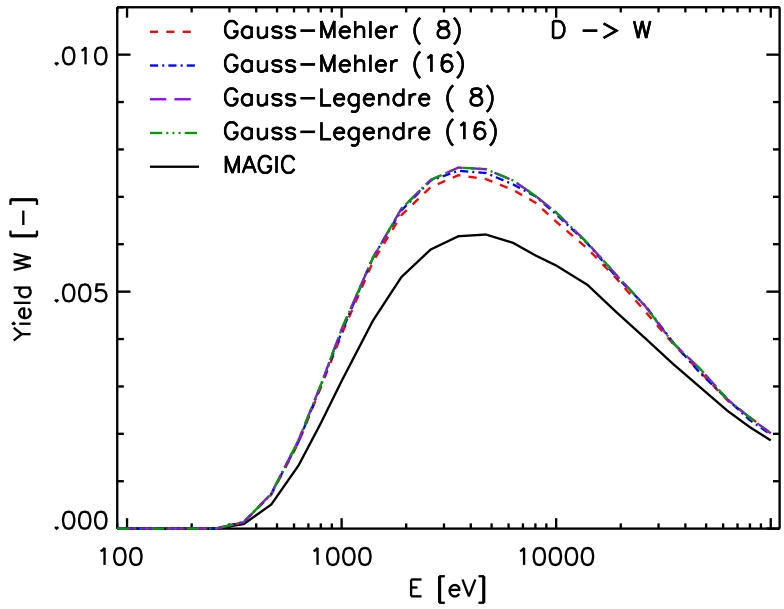

Figure 33: Calculated sputtering yield Y for D on a W target for three different integration methods. Gauss-Mehler and Gauss-Legendre were calculated with both 8 and 16 numbers of integration-step (ipivot).

6.8. Screened coulomb potentials (ipot)

The reduced energy ε is:

$$\varepsilon = a \cdot \frac{M_2}{Z_1 \cdot Z_2 \cdot e^2 \cdot (M_1 + M_2)} \cdot E \tag{6.26}$$

with M_1 relative atomic mass of projectile, M_2 relative atomic mass of target atom.
It is often used for calculation of ε the screening length a following Lindhard-Scharff, see [1].

$$a = a_{LS} = ab_{bohr} \cdot \frac{p_{const}}{Z_1^{2/3} + Z_2^{2/3})^{-1/2}} \qquad \text{(Lindhard-Scharff)} \tag{6.27}$$

The screened coulomb potentials $V(r)$, see [1], can be written in the form

$$V(r) = \frac{Z_1 \cdot Z_2 \cdot e^2}{r} \cdot \Phi(\frac{r}{a}) \tag{6.28}$$

with Z_1 atomic number of projectile, Z_2 atomic number of target atom, a the screening length and r the distance between the two atoms.

The equation for different interaction potential are given below:
for the **Krypton-carbon** potential (ipot=1):

$$\Phi(\frac{r}{a}) = 0.191 \cdot e^{-0.278r/a} + 0.474 \cdot e^{-0.637r/a} + 0.335 \cdot e^{-1.919r/a} \tag{6.29}$$

$$a = a_F = ab_{bohr} \cdot \frac{p_{const}}{\sqrt{Z_1} + \sqrt{Z_2})^{2/3}} \qquad \text{(Firsow)} \tag{6.30}$$

for the **Moliere potential (ipot=2)**:

$$\Phi(\frac{r}{a}) = 0.35 \cdot e^{-0.3r/a} + 0.55 \cdot e^{-1.2r/a} + 0.10 \cdot e^{-6.0r/a} \tag{6.31}$$

$$a = a_F = ab_{bohr} \cdot \frac{p_{const}}{\sqrt{Z_1} + \sqrt{Z_2})^{2/3}} \qquad \text{(Firsow)} \tag{6.32}$$

for the **ZBL** potential (ipot=3):

$$\begin{aligned} \Phi(\frac{r}{a}) &= 0.028171 \cdot e^{-0.20162r/a} + 0.28022 \cdot e^{-0.4029r/a} \\ &+ 0.50986 \cdot e^{-0.94229r/a} + 0.18175 \cdot e^{-3.1998r/a} \end{aligned} \tag{6.33}$$

$$a = a_{ZBL} = ab_{bohr} \cdot \frac{p_{const}}{(Z_1^{0.23} + Z_2^{0.23})} \qquad \text{(Ziegler,Biersack,Littmark: ZBL)} \tag{6.34}$$

for the **Nakagava-Yamamura** potential (ipot=4):

$$\Phi(\frac{r}{a}) = e^{(-A\cdot(r/a)+B\cdot(r/a)^{1.5}-C\cdot(r/a)^2)} \tag{6.35}$$

with:

$$\begin{aligned} A &= 1.51 \\ B &= 0.763 * (Z_1^{0.169} + Z_2^{0.169})/(Z_1^{0.307} + Z_1^{0.307}) \\ C &= 0.191 * ((Z_1^{0.0481} + Z_2^{0.0481})/(Z_2^{0.307} + Z_2^{0.307}))^{4./3.} \end{aligned} \tag{6.36}$$

$$a = a_{NY} = ab_{bohr} \cdot \frac{p_{const}}{(Z_1^{0.307} + Z_2^{0.307})^{2/3}} \qquad \text{(Nakagava-Yamamura)} \tag{6.37}$$

Name	value	unit	
ab_{bohr}	0.52917725	[Å]	Bohr radius
p_{const}	0.885341377	[-]	$(9 \cdot \pi^2/128)^{1/3}$
e^2	14.399651	[eV Å]	

Table 4: Values of constants

Fig. 34 and Fig. 37 show the results of calculation of four different potentials. It is hard to say which potential is the best. The Kr-C potential seems good for all examples. All calculations were done with Gauss-Legendre integration method, surface-binding-model one ($isbv = 1$) and inelastic loss model ($inel0 = 4(D)$, $5(He)$ or $7(other)$). The difference between the potentials is relatively small.

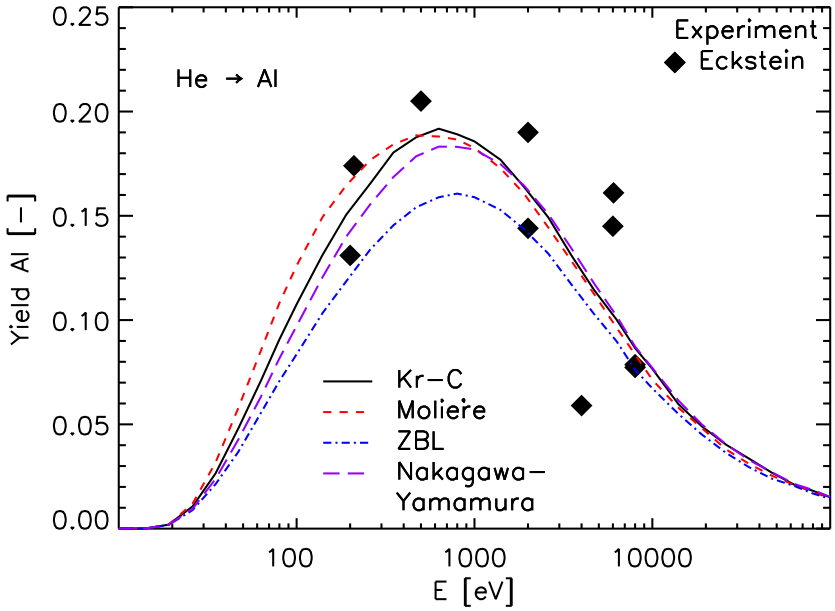

Figure 34: Calculated and measured sputtering yield Y of Al [28], He on a Al target for four different potentials.

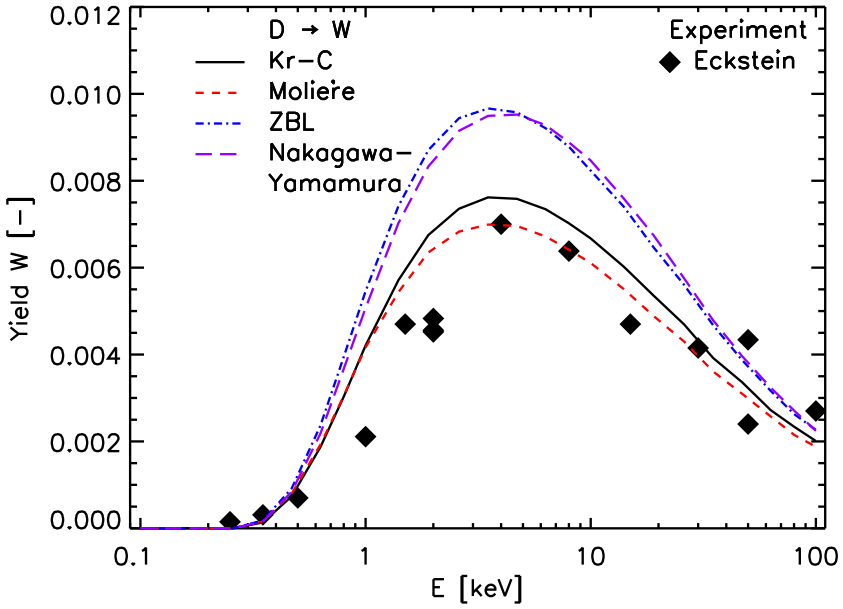

Figure 35: Calculated and measured sputtering yield Y of W [28], D on a W target for four different potentials.

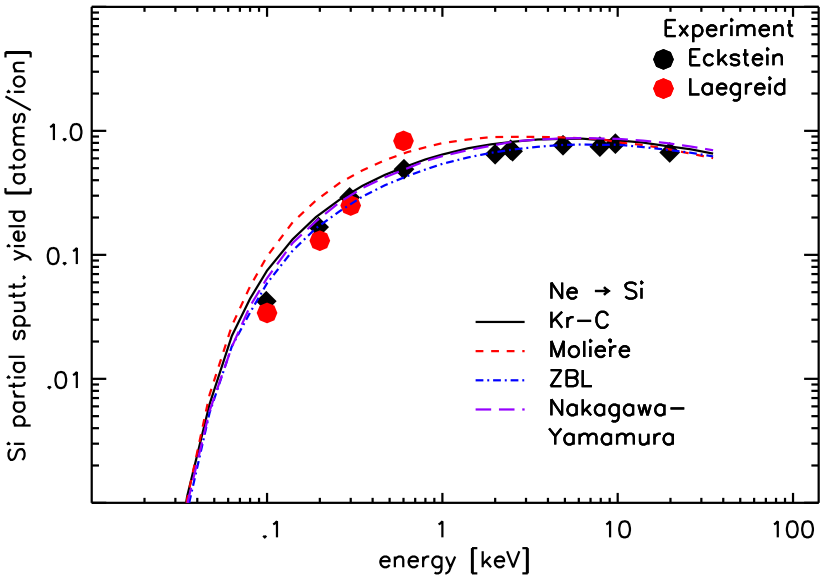

Figure 36: Calculated and measured sputtering yield Y of Si [28], Ne on a Si target for four different potentials.

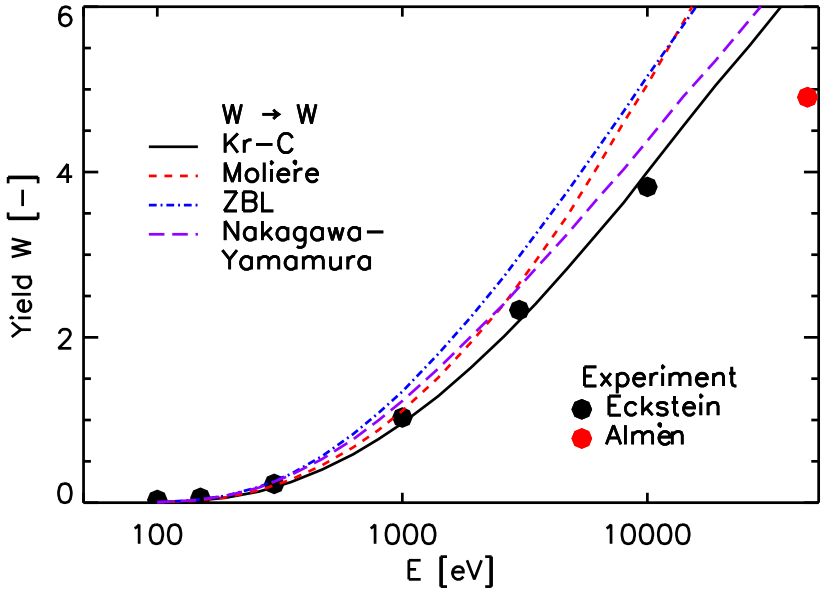

Figure 37: Calculated and measured sputtering yield Y of W [28], [51], W on a W target for four different potentials.

6.9. Two compound target (l_two_comp)

6.9.1. Calculation of density in mix target

The formula of the molecule is:

$$An_1Bn_2 \tag{6.38}$$

Parameters of the components example Ta_2O_5 are:

$$\begin{aligned} n_1 &= 2 \\ n_2 &= 5 \\ A &= \text{"}Ta\text{"} \\ B &= \text{"}O\text{"} \end{aligned}$$

Given molecule density or atomic density of Ta_2O_5 :

$$\begin{aligned} d_{mol}(Ta_2O_5) &= 0.50281\ molecule/A^3 \\ d_m(Ta_2O_5) &= 0.07183\ atoms/A^3 \end{aligned} \tag{6.39}$$

Density d of elements:

$$\begin{aligned} d_1(Ta) &= 0.04291\ atoms/A^3 \\ d_2(O) &= 0.05543\ atoms/A^3 \end{aligned} \tag{6.40}$$

Calculation of atomic fraction qu (N...number of atoms):

$$qu_1(Ta) = \frac{N_1}{N_1+N_2} \tag{6.41}$$

$$qu_2(O) = \frac{N_2}{N_1+N_2} \tag{6.42}$$

$$qu_t(Ta,O) = \frac{N_t}{N_1+N_2} = \frac{N_2+N_2}{N_1+N_2} = qu_1+qu_2 = 1 \tag{6.43}$$

Calculation of the volume V and density of target d_t:

$$V_t(target) = V_1(Ta)+V_2(O) \tag{6.44}$$

$$\frac{N_t}{d_t} = \frac{N_1}{d_1}+\frac{N_2}{d_2} \tag{6.45}$$

$$\frac{1}{d_t} = \frac{qu_1}{d_1}+\frac{qu_2}{d_2} \tag{6.46}$$

Example: Ta_2O5

$$\begin{aligned} qu_1 &= 2/7 \\ qu_2 &= 5/7 \\ d_t &= 0.05116\ atoms/A^3 \end{aligned} \tag{6.47}$$

The calculated density of target d_t (6.47) with the help of the atomic density (6.46) is **not** the density of compound d_m (6.39).

6.9.2. Calculation density of compound, example: $Ar \rightarrow Ta_2O_5$

New option in tri.inp: **l_two_comp=.true.**

assumption:
The target consists of unbound atoms (Ta, O) and bound atoms (Ta_b, O_b).

$$Ar \rightarrow Ta, O, Ta_b, O_b \tag{6.48}$$

chemical reaction:

$$An_1Bn_2 \longleftrightarrow n_1 \cdot A + n_2 \cdot B \tag{6.49}$$

or

$$Ta_2O_5 \longleftrightarrow 2 \cdot Ta + 5 \cdot O \qquad n_1 = 2 \;\; n_2 = 5$$

Number of all atoms in a layer or volume:

$$\begin{aligned} A_1(Ta) &= N(Ta) + N(Ta_b) = N_1(Ta) + N_3(Ta_b) \\ A_2(O) &= N(O) + N(O_b) \quad = N_2(O) \; + N_4(O_b) \end{aligned} \tag{6.50}$$

Number of molecules N_{mol} in a layer or volume:

$$N_{mol}(Ta_2O_5) = min(A_1/n_1, A_2/n_2) \tag{6.51}$$

Number atoms of molecules N_m (bound atoms):

$$N_m(Ta_2O_5) = N_{mol} \cdot n_1 + N_{mol} \cdot n_2 = N_3(Ta_b) + N_4(O_b) \tag{6.52}$$

Number of unbound (or free) atoms:

$$\begin{aligned} F_1(Ta) &= A_1 - N_{mol} \cdot n_1 \\ F_2(O) &= A_2 - N_{mol} \cdot n_2 \end{aligned} \tag{6.53}$$

numerical example: after bombardment we have following atoms in a layer:

$$\begin{aligned} N_0(Ar) &= 2 \\ N_1(Ta) &= 5 \\ N_2(O) &= 20 \\ N_3(Ta_b) &= 21 \\ N_4(O_b) &= 54 \end{aligned}$$

Given densities:

$$\begin{aligned} d_0(Ar) &= 0.02080 \; atoms/A^3 \\ d_1Ta) &= 0.05543 \; atoms/A^3 \\ d_2(O) &= 0.04994 \; atoms/A^3 \\ d_3(Ta_b) &= 0.07183 \; atoms/A^3 \\ d_4(O)_b) &= 0.07183 \; atoms/A^3 \\ d_m(Ta_2O_5) &= 0.07183 \; atoms/A^3 \end{aligned} \tag{6.54}$$

Number of all atoms in a layer or volume (6.50):

$$\begin{aligned} N_0(Ar) &= 2 \\ A_1(Ta) &= 26 \\ A_2(O) &= 74 \end{aligned}$$

Number of molecules (6.51):

$$N_{mol}(Ta_2O_5) = 13$$

Number atoms of molecules N_m (bound atoms)(6.52):

$$\begin{aligned} N_3(Ta_b) &= N_{mol} \cdot n_1 = 26 \\ N_4(O_b) &= N_{mol} \cdot n_2 = 65 \end{aligned}$$

Number atoms unbound atoms (6.53):

$$\begin{aligned} N_1(Ta) &= F_1 = 0 \\ N_2(O) &= F_2 = 9 \end{aligned}$$

Atomic fraction qu:

$$\begin{aligned} qu_0(Ar) &= \frac{N_0}{N_0 + N_1 + N_2 + N_3 + N_4} \\ qu_1(Ta) &= \frac{N_1}{N_0 + N_1 + N_2 + N_3 + N_4} \\ qu_2(O) &= \frac{N_2}{N_0 + N_1 + N_2 + N_3 + N_4} \\ qu_3(Ta_b) &= \frac{N_3}{N_0 + N_1 + N_2 + N_3 + N_4} \\ qu_4(O_b) &= \frac{N_4}{N_0 + N_1 + N_2 + N_3 + N_4} \end{aligned}$$

symbol	atoms N	atomic fraction qu
Ar	2	0.01961
Ta	0	0.00000
O	9	0.08824
Ta_b	26	0.25490
O_b	65	0.63725

Table 5: Number atoms and atomic fraction qu

target-density d_t:

$$\begin{aligned} \frac{1}{d_t} &= \frac{qu_0}{d_0} + \frac{qu_1}{d_1} + \frac{qu_2}{d_2} + \frac{qu_3}{d_3} + \frac{qu_4}{d_4} \\ d_t &= 0.06609\ atoms/A^3 \end{aligned} \tag{6.55}$$

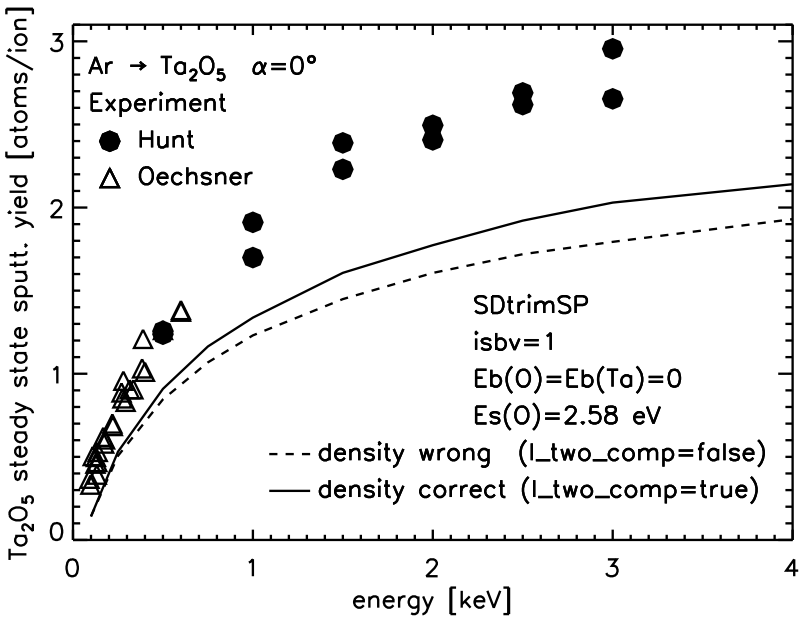

Figure 38: Comparison of sputtered yields calculated without and with considered of compound-density and experimental results [41], [60], Ar on Ta_2O_5.

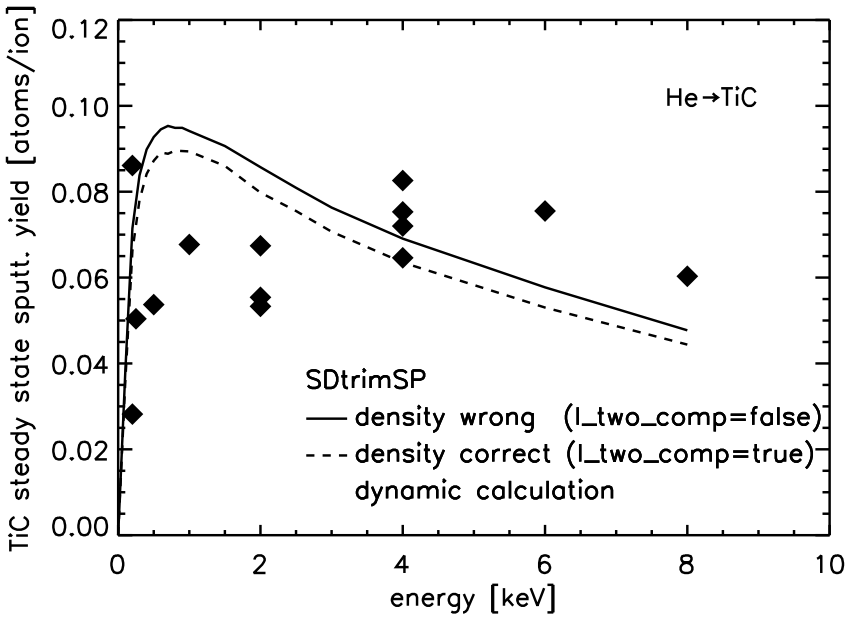

Figure 39: Comparison of sputtered yields calculated without and with considered of compound-density and experimental results [28], He on TiC.

6.10. Surface binding model (isbv)

6.10.1. Overview of models

The user can choose from 6 methods ($isbv = 1, 2, 3, 4, 6, 8$) to calculate all binding energies of each species. *sbv* is the currently surface binding energy at surface.
E_S is the atomic surface binding energy of element. E_B the bulk binding energy in the whole target, q the atomic fraction at surface and E_C the cutoff-energy, value at which the moving atom is stopped.
ΔH_{sub} is the sublimation enthalpy of element. For some elements (noble-gas:) ΔH_{sub} is replaced by 0.0 eV. For di-atomic gas ($H_2, N_2, O_2, F_2, Cl_2, Br_2, I_2$) ΔH_{sub} is replaced by dissociation enthalpy ΔH_{diss} ($E_S = 0.5 \cdot \Delta H_{diss}$) or $1eV$.
ΔH_f is the enthalpy of formation of binary compound. nm number of atoms in a two-component molecule.

	SB	SB-C	BB	BB-C	HB-C
E_S	ΔH_{sub}	ΔH_{sub}	0	0	ΔH_{sub}
E_{Bf}	0	0	ΔH_{sub}	ΔH_{sub}	0
E_{Bb}	-	0	-	$\Delta H_{sub} + \Delta H_f/nm$	$\Delta H_f/nm$
ρ_f	atomic	atomic	atomic	atomic	atomic
ρ_b	-	compound	-	compound	compound
E_C	$< \Delta H_{sub}$	$< \Delta H_{sub}$	$\Delta H_{sub}/3$	$\Delta H_{sub}/3$	$< \Delta H_{sub}$
$isbv$	1	1	8	8	4

Table 6: Overview of the main binding-models (1,4,8)
Note short forms:SB surface binding model; BB bulk binding model; HB Hybrid binding Model; SB-C, BB-C, HB-C models with compound;
E_S surface binding energy; E_B bulk binding energy;E_C cutoff energy;ρ density; f ('free') chemical unbound atom; b ('bound') chemical bound atom

The values of parameters can be taken from tables automatically or entered individually in the input-file 'tri.inp'. ,see chapter. B

The parameters in program are:

heat of dissociation (ΔH_{diss}) use for E_S
heat of sublimation (ΔH_{sub}): use for E_S
surface binding energy (E_S): e_surfb
bulk binding energy (E_B): e_bulkb
cutoff energy (E_C): e_cutoff
atomic density (ρ): dns0
heat of formation (ΔH_f): deltahf

6.10.2. Example Rn K on M

An example is K on pure Mo target (static mode).
Values are:

$$\begin{aligned} q_1 &= q(K) = 0 \\ q_2 &= q(Mo) = 1 \\ Es_1 &= \Delta H_{sub}(K) \quad = 0.93\ eV \\ Es_2 &= \Delta H_{sub}(Mo) = 6.82\ eV \\ Es_{1,2} &= Es_{2,1} = 0.5 \cdot (H_{sub}(K) + H_{sub}(Mo)) = 0.5 \cdot (0.93 + 6.82) = 3.875\ eV \end{aligned}$$

$$\begin{aligned} \textbf{model 1: } (isbv = 1)\ sbv(K) &= Es_1 = 0.93\ eV \\ sbv(Mo) &= Es_2 = 6.82\ eV \\ E_b(K) = E_b(Mo) &= 0.00 \\ E_c(K) = E_c(Mo) &= < min(Es_1, Es_2) = 0.92\ eV \end{aligned} \tag{6.56}$$

$$\begin{aligned} \textbf{model 2: } (isbv = 2)\ sbv(K) &= q_1 \cdot Es_1 + q_2 \cdot Es_2 = 6.82\ eV \\ sbv(Mo) &= q_1 \cdot Es_1 + q_2 \cdot Es_2 = 6.82\ eV \\ E_b(K) = E_b(Mo) &= 0.00 \\ E_c(K) = E_c(Mo) &= < min(Es_1, Es_2) = 0.92\ eV \end{aligned} \tag{6.57}$$

$$\begin{aligned} \textbf{model 3: } (isbv = 3)\ sbv(K) &= q_1 \cdot Es_1 + q_2 \cdot Es_{1,2} = 3.875\ eV \\ sbv(Mo) &= q_1 \cdot Es_{2,1} + q_2 \cdot Es_2 = 6.82\ eV \\ E_b(K) = E_b(Mo) &= 0.00 \\ E_c(K) = E_c(Mo) &= < min(Es_1, Es_2) = 0.92\ eV \end{aligned} \tag{6.58}$$

$$\begin{aligned} \textbf{model 6: } (isbv = 6)\ Es_1, Es_2, Es_{1,2}, Es_{2,1} &= input(mat\_surfb.inp) \\ sbv(K) &= q_1 \cdot Es_1 + q_2 \cdot Es_{1,2} \\ sbv(Mo) &= q_1 \cdot Es_{2,1} + q_2 \cdot Es_2 \\ E_b(K) = E_b(Mo) &= 0.00 \\ E_c(K) = E_c(Mo) &= < min(Es_1, Es_2) \end{aligned} \tag{6.59}$$

$$\begin{aligned} \textbf{model 8: } (isbv = 8)\ sbv(K) = sbv(Mo) &= 0 \\ E_b(K) &= Es_1 = 0.93\ eV \\ E_b(Mo) &= Es_2 = 6.82\ eV \\ E_c(K) &= Es_1/3 = 0.31\ eV \\ E_c(Mo) &= Es_2/3 = 2.273\ eV \end{aligned} \tag{6.60}$$

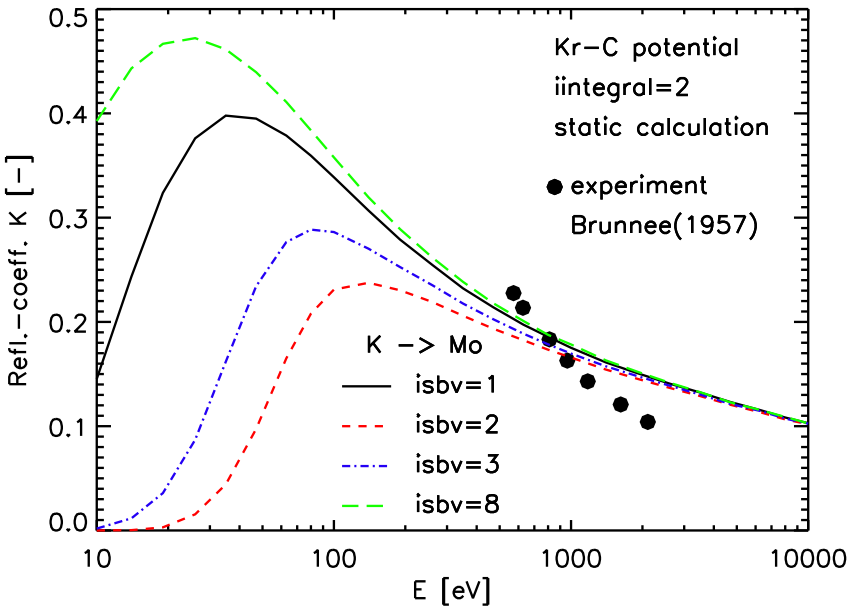

Figure 40: Calculated reflection coefficient depending on surface binding model of K on a Mo target at normal incidence in static mode (because small fluence) with measurements measurement [59]

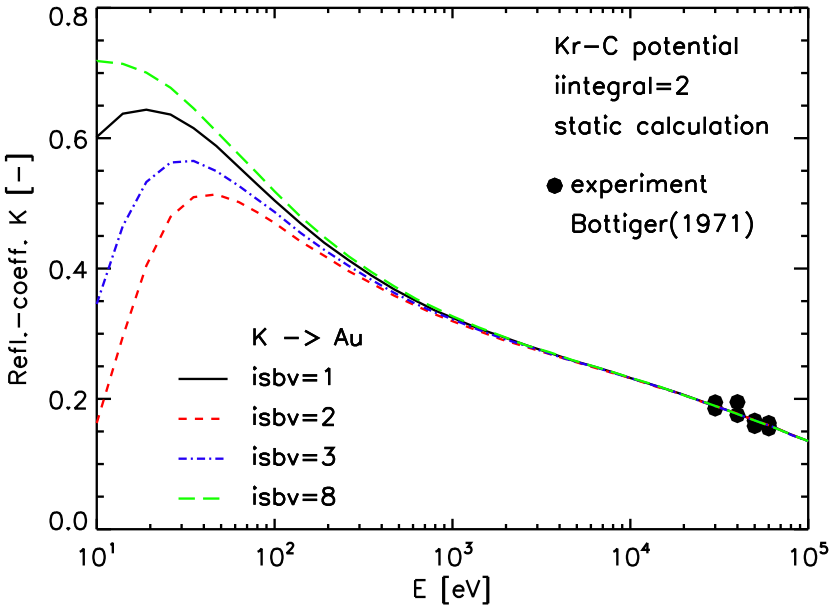

Figure 41: Calculated reflection coefficient depending on surface binding model of K on an Au target at normal incidence in static mode (because small fluence) with measurement measurement [58]

If it is used mode 'static' and model 1, 2 or 3 only the surface-binding energy of K is dependent on atomic fraction at surface. Therefore only the scattering coefficient is shown, see Fig. 40 and Fig. 41. Because we have no compound, model 4 is the same as model 1.
All calculations used the '$Kr - C$' potential and the integration-method of 'Gauss-Legendre'.

6.10.3. Example Rn D on W

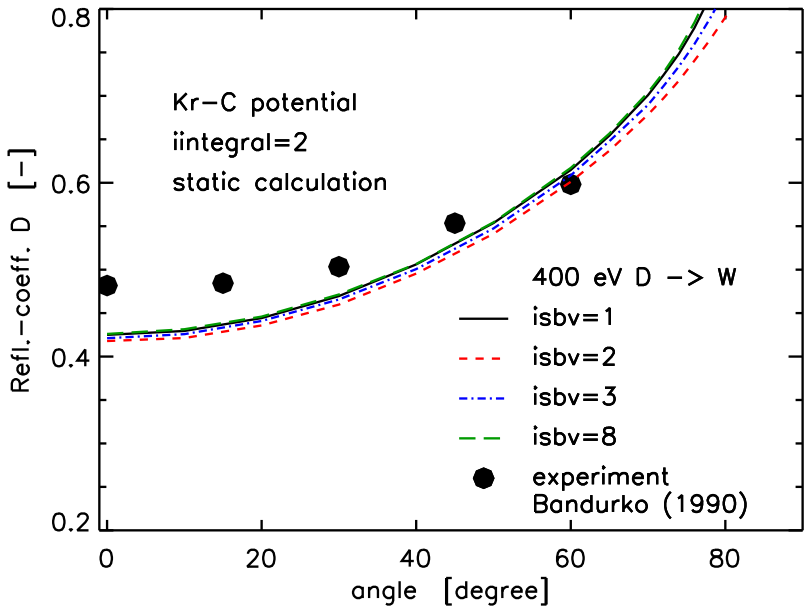

Figure 42: Calculated reflection coefficient depending on surface binding model of D on a W target at normal incidence in static mode (because small fluence) with measurements measurement [70]

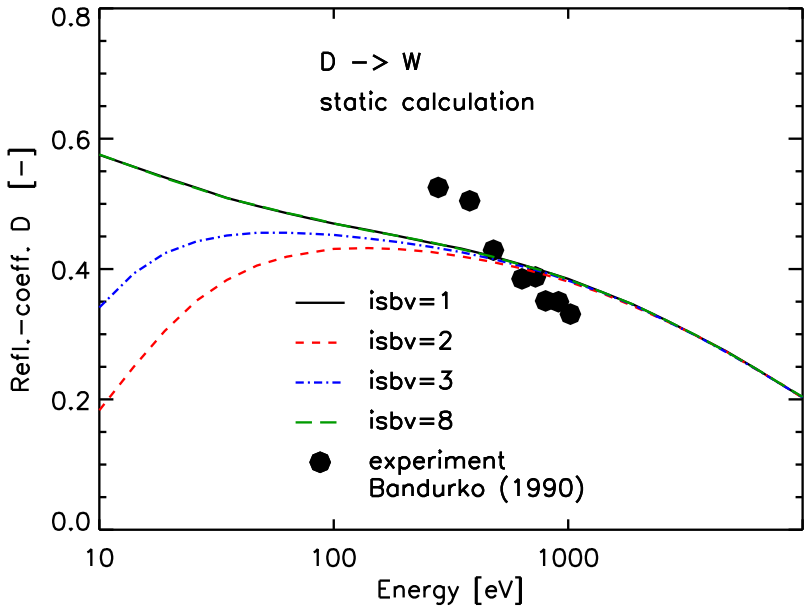

Figure 43: Calculated reflection coefficient depending on surface binding model of D on an W target at normal incidence in static mode (because small fluence) with measurement measurement [70]

6.10.4. Example Y D on W

An example is D on pure W at $fluence = 10 \cdot 10^{-16} atoms/cm^2$ target (dynamic mode). Values are:

$$
\begin{aligned}
q_1(start) &= q(D) = 0 \\
q_2(start) &= q(W) = 1 \\
E_s(D) &= 1.10\ eV \\
E_b(D) &= 0.00\ eV \\
E_c(D) &= 8.50\ eV \\
Es(W) &= \Delta H_{sub}(W) = 8.79\ eV \\
E_b(W) &= 0.00\ eV \\
E_c(W) &= 8.50\ eV
\end{aligned}
$$

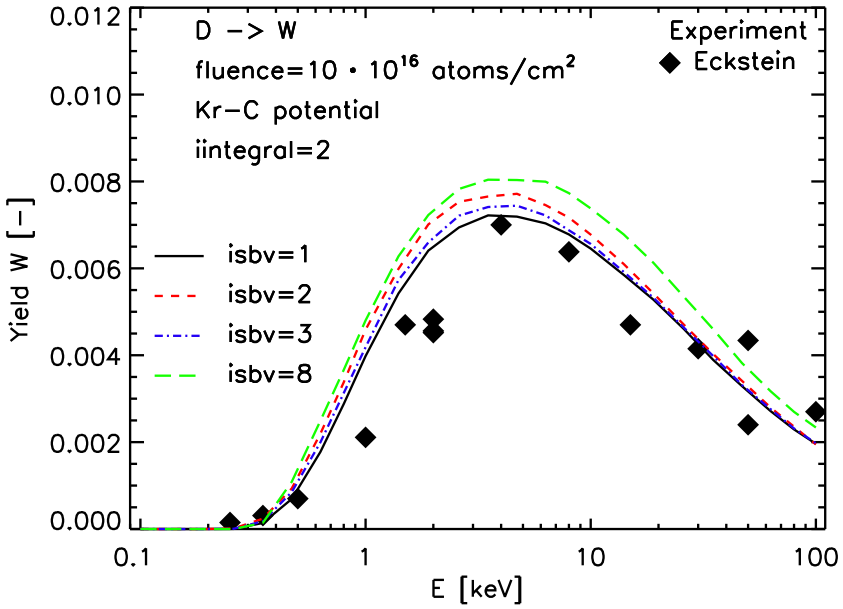

Figure 44: Comparison of sputtered yields of W calculated with Different surface binding models and experimental results [28], D on W.

6.10.5. Example Y Ar on Ta_2O_5

An example for compound is Ar on Ta_2O_5 target.
Values are:

$$\begin{aligned} sbv(Ar) &= 0.00\ eV \\ E_b(Ar) &= 0.00\ eV \\ E_c(Ar) &= 0.50\ eV \\ \Delta H_{diss}(O_2) &= 5.164\ eV \\ \Delta H_{sub}(Ta) &= 8.10\ eV \\ \Delta H_f(Ta_2O_5) &= 21.2053\ eV \quad (model\ 4,8) \\ mn(Ta_2O_5) &= 7 \end{aligned}$$

density of Ta, O and Ta_2O_5: see 6.54

$$\begin{aligned} Es(O) &= \Delta H_{diss}/2 = 2.58\ eV \quad (model\ 1,2,3) \\ Es(O) &= 1.00\ eV \quad (model\ 4) \\ Es(Ta) &= \Delta H_{sub} = 8.10\ eV \\ ... &\ f \quad not\ chemical\ bounded \\ ... &\ b \quad chemical\ bounded \end{aligned}$$

model 1,2,3:
$$\begin{aligned} sbv(Ta_f) &= sbv(Ta_b) = f(q, Es(Ta), Es(O)) \\ sbv(O_f) &= sbv(O_b) = f(q, Es(Ta), Es(O)) \\ E_b(Ta_f) &= E_b(O_f) = E_b(Ta_b) = E_b(O_b) = 0.00\ eV \end{aligned}$$

model 4:
$$\begin{aligned} sbv(Ta_f) &= sbv(Ta_b) = 8.10\ eV \\ sbv(O_f) &= sbv(O_b) = 1.00\ eV \\ E_b(Ta_f) &= E_b(O_f) = 0.00\ eV \\ E_b(Ta_b) &= E_b(O_b) = H_f(Ta_2O_5)/mn \end{aligned}$$

model 8:
$$\begin{aligned} sbv(Ta_f) &= sbv(O_f) = sbv(Ta_b) = sbv(O_b) = 0.00\ eV \\ E_b(Ta_f) &= Es(Ta) \\ E_b(O_f) &= Es(O) \\ E_b(Ta_b) &= Es(Ta) + H_f(Ta_2O_5)/mn \\ E_b(O_b) &= Es(O) + H_f(Ta_2O_5)/mn \end{aligned}$$

all model :
$$\begin{aligned} E_c(Ta_f) &= E_c(Ta_b) = Es(Ta) \cdot 2/3 \\ E_c(O_f) &= E_c(O_b) = Es(O) \cdot 1/3 \end{aligned}$$

Fig. 45 and 46 show the comparison of different surface-binding-models *isbv* with measurements by bombardment of Ta_2O_5 with Ar. The target in this example is a solid-gas compound. Because oxygen is a gas and usually the heat of dissociation ΔH_{diss} for Es, one can set the surface-binding energy of oxygen to 1eV. The best methods are the model 1,4 and 8 (black, green and purple line). For all calculations is used the '$Kr-C$' potential, the integration-method of 'Gauss-Legendre' and the 'dynamical mode'.

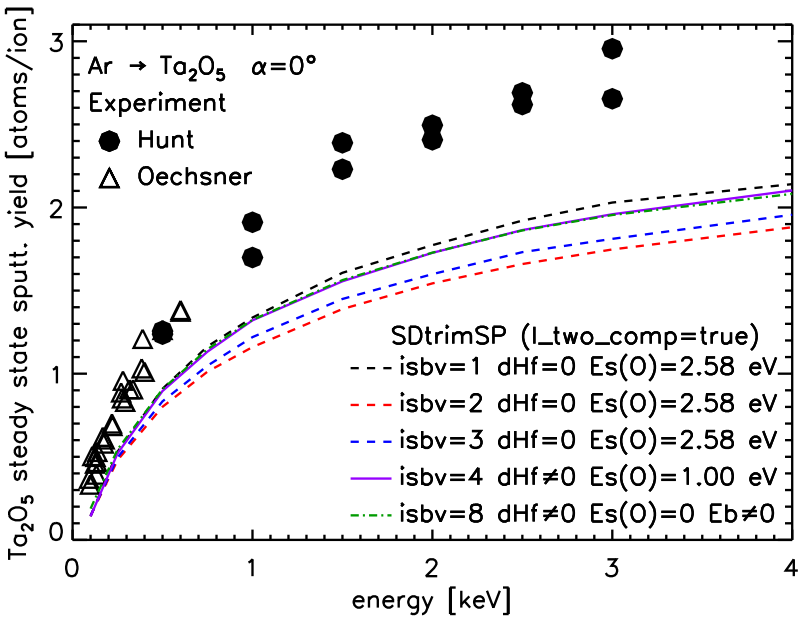

Figure 45: Comparison of sputtered yields of compound calculated with Different surface binding models with reduced Es of O and experimental results [41], [60], Ar on Ta_2O_5.

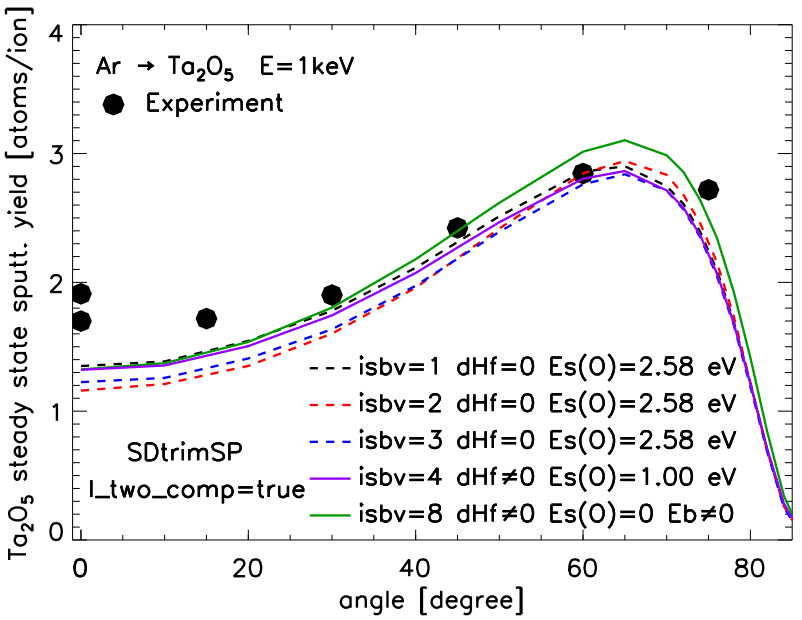

Figure 46: Comparison of sputtered yields of compound calculated with Different surface binding models with reduced Es of O and experimental results [28], Ar on Ta_2O_5.

6.10.6. Example Y D on TaC

An other example for compound is D on TaC target. For all calculations are used the '$Kr-C$' potential, the integration-method of 'Gauss-Legendre' and the 'dynamical mode'.
Values are:

$$\begin{aligned}
\Delta H_{diss}(D_2) &= 4.518\ eV \quad not\ used \\
E_s(D) &= 1.10\ eV \\
E_b(D) &= 0.00\ eV \\
E_c(D) &= 0.50\ eV \\
\Delta H_{sub}(C) &= 7.37\ eV \quad not\ used \\
Es(C) &= 4.50\ eV \\
E_c(C) &= 2.45\ eV \\
\Delta H_{sub}(Ta) &= 8.10\ eV \\
E_c(Ta) &= 5.40\ eV \\
\Delta H_f(TaC) &= 1.4935 \quad (model\ 4, 8) \\
mn(TaC) &= 2
\end{aligned}$$

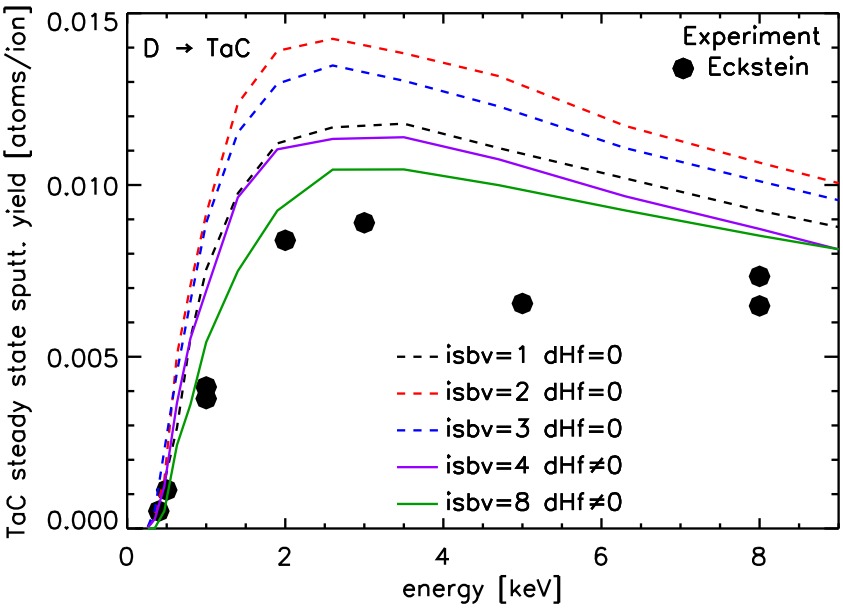

Figure 47: Comparison of sputtered yields of compound calculated with Different surface binding models and experimental results [28], D on TaC.

6.11. Inelastic loss model (inel0)

6.11.1. Electric loss model: Lindhard-Scharff (LS)

$$E_{electr} = dl \cdot d_t \cdot LS_{fak} \cdot \sqrt{E} \tag{6.61}$$

E_{electr} is the electronic-energy-loss, d_t is the atomic density of target, see 6.46 and 6.55 and dl is the moving distant of projectile dl_1 or dl_2, see Fig. 48.

$$LS_{fak} = kfac_{1,2} \cdot q_2 + kfac_{2,1} \cdot q_1$$

$$kfac_{1,2} = 1.212 \cdot \frac{Z_1^{7/6} \cdot Z_2}{(Z_1^{2/3} + Z_2^{2/3})^{3/2} \cdot \sqrt{M_1}}$$

$$kfac_{2,1} = 1.212 \cdot \frac{Z_2^{7/6} \cdot Z_1}{(Z_2^{2/3} + Z_1^{2/3})^{3/2} \cdot \sqrt{M_2}}$$

M is the atomic mass in amu and Z the atomic number.

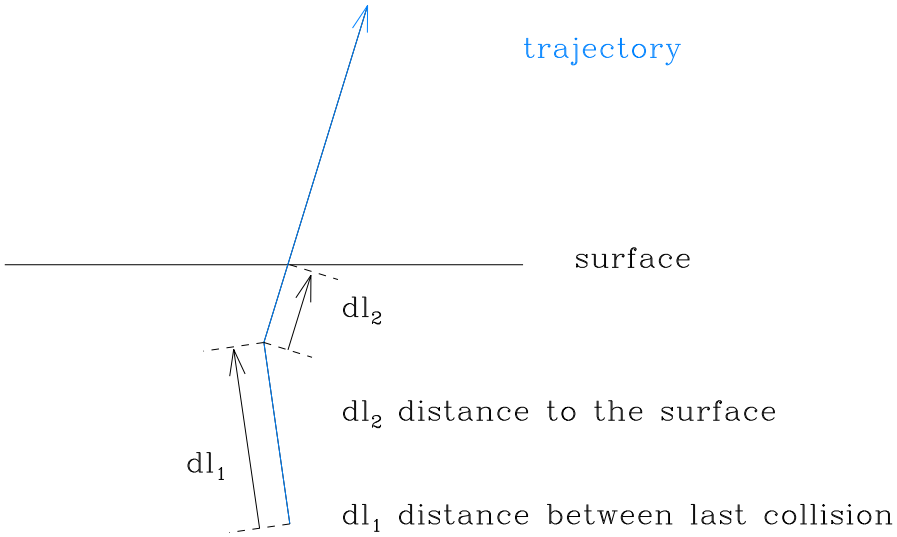

Figure 48: Distance dl between moving points of the two last collisions near surface

Version 6.05 and higher also consider the distance between last collision and surface of target. The last electronic loss of sputtered particle for model LS is:

$$E_{electr} = dl_1 \cdot d_t(x) \cdot rk23 \cdot \sqrt{E} + dl_2 \cdot d_t(x) \cdot rk23 \cdot \sqrt{E}$$

6.11.2. Electric loss model: Oen-Robenson (OR)

Inelastic loss models from Oen-Robenson [15] is:

$$E_{electr} = \sum_{ring=1}^{3} e_{loc} \tag{6.62}$$

$$e_{loc} = kor_{1,2} \cdot \sqrt{E} \cdot exp(-0.278 \cdot \frac{r}{a})$$

$$kor_{1,2} = \frac{-0.278^2}{2} \cdot \frac{kfac_{1,2}}{\pi \cdot a^2}$$

r from equation of potential calculation:

$$0 = \sqrt{1 - \frac{V(r)}{\varepsilon} - \frac{p^2}{r^2}}$$

6.11.3. Electric loss model: Ziegler-Biersack (ZB)

$$E_{electr} = dl \cdot d_t \cdot S_e \tag{6.63}$$

for H

$$S_e = A_1\Big(\frac{E_1}{M_1}\Big)^{0.5} \quad 1 \le E_1 \le 10keV \tag{6.64}$$

$$S_e = S_{low} * S_{high}/(S_{low} + S_{high}) \quad 10KeV \le E_1 \le 1MeV \tag{6.65}$$

$$\begin{aligned} S_{low} &= A_2\Big(\frac{E_1}{M_1}\Big)^{0.45} \\ S_{high} &= A_3\Big(\frac{M_1}{A_1}\Big) ln\Big(1 + A_4\Big(\frac{M_1}{A_1}\Big) + A_5\Big(\frac{E_1}{M_1}\Big)\Big) \end{aligned}$$

$$S_e = f(A_6, A_7, A_8, A_9, A_{10}, A_{11}, A_{12}, v_1, c, W_1, M_1) \quad 1MeV \le E_1 \le 100MeV \tag{6.66}$$

for He

$$S_e = S_{low} * S_{high}/(S_{low} + S_{high}) \quad 1KeV \le E_1 \le 10MeV \tag{6.67}$$

$$\begin{aligned} S_{low} &= A_1 E_1^{A_2} \\ S_{high} &= \Big(\frac{A_3}{E_1/1000}\Big) ln\Big(1 + \Big(\frac{A_4}{E_1/1000}\Big) + A_5\Big(\frac{E_1}{1000}\Big)\Big) \end{aligned}$$

$$S_e = f(A_6, A_7, A_8, A_9, E_1) \quad E_1 \ge 10MeV,\ E_1\ in\ MeV \tag{6.68}$$

for other

$$S_{low} = A_1\Big(\frac{E_1}{M_1}\Big)^{A_2} + A_3\Big(\frac{E_1}{M_1}\Big)^{A_4} \quad \frac{E_1}{M_1} > 25keV/amu \tag{6.69}$$

$$S_{high} = A_5 ln\Big(A_7\Big(\frac{M_1}{E_1}\Big) + A_8\Big(\frac{E_1}{M_1}\Big)\Big)/(\frac{E_1}{M_1})^{A_6} \quad \frac{E_1}{M_1} > 25keV/amu \tag{6.70}$$

6.11.4. Electric loss model: SDTrimSP (LZ7) $inel0 = 7$

$$E_{electr} = dl \cdot d_t \cdot S_e \tag{6.71}$$

$$S_e = S_{low} * S_{high}/(S_{low} + S_{high}) \tag{6.72}$$

$$S_{low} = ck_{elec} \cdot LS_{fak} \cdot E^{a_2} \tag{6.73}$$
$$S_{low} = LS_{fak} \cdot E^{0.5} \quad (if\ a_1\ and\ ck_{elec}\ unknown) \tag{6.74}$$

$$S_{high} = a_3/Em \cdot ln(1. + a_4/Em + a_5 \cdot Em) \tag{6.75}$$
$$S_{high} = s_{high}(ZB) \quad (if\ a_3 - a_5\ unknown) \tag{6.76}$$

$$Em = E/M_1 \cdot 10^{-6} \qquad [E] = eV \tag{6.77}$$

The correction of variable ck_{elec}, a_2 - a_5 is written in tables: 'table7_ck' and 'table7_a3a4a5'.

6.11.5. Inelastic loss models in SDTrimSP, parameter inel0=1...7

Inelastic loss model (parameter: $inel0$) are:

inel0 = 1: LS (eq. 6.61, Linhard-Scharff [61])
inel0 = 2: OR (eq. 6.62, Oen-Robenson [15])
inel0 = 3: $0.5 \cdot (LS + OR)$
inel0 = 4: for hydrogen (H, D, T) (eq. 6.63 - 6.65, Andersen-Ziegler [62])
inel0 = 5: for helium (He_3, He) (eq. 6.63, 6.67, 6.68, Ziegler [63])
inel0 = 6: ZB (eq. 6.63, 6.69, 6.70, Ziegler-Biersack [64])
inel0 = 7: $LZ7$ (combination of LS and ZB with correction eq. 6.71 - 6.77

The comparisons of calculated value with measurements chow that the agreement not ever good for using inelastic loss models 1, 2 or 6. Therefore it is used in the new version of SDTrimSP following inelastic loss models and surface-binding-energy Es :

element	inel0	new Es
H, D, T	4	
He_3, He	5	
B	7	3.75 eV
C	7	4.50 eV
Ti	7	5.60 eV
all other	7	

Table 7: Used model of inelastic loss (inel0) and surface-binding-energy (Es) dependent on element

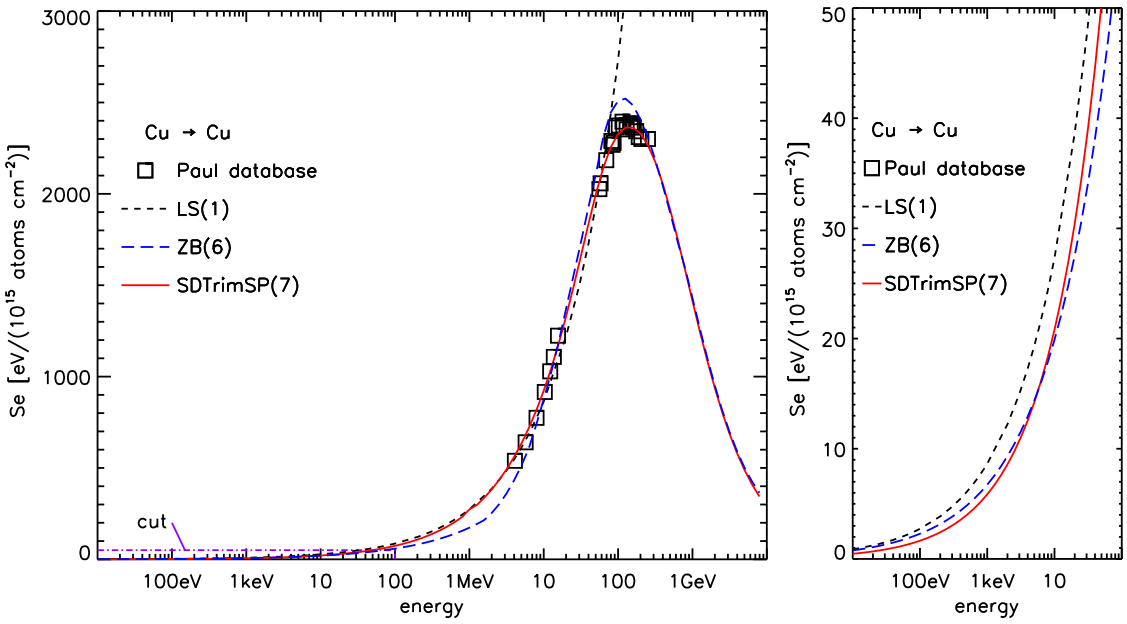

Figure 49: Electronic stopping power dependent on energy Cu on Cu with measurements [65], Correction-factors for inel0=7 are $ck_{elec} = 0.45$, $a_2 = 0.55$, $a_3 = 10701.7$, $a_4 = 3.55817$, $a_5 = 0.606379$ (right: cut of left)

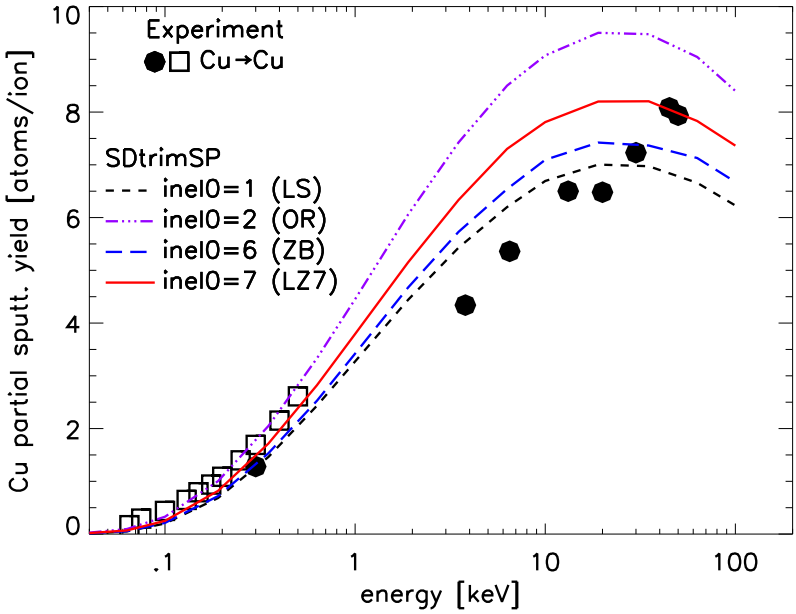

Figure 50: Comparison of yield dependent on energy Cu on Cu-target calculated with different electronic lost models and experimental results [51], [67]

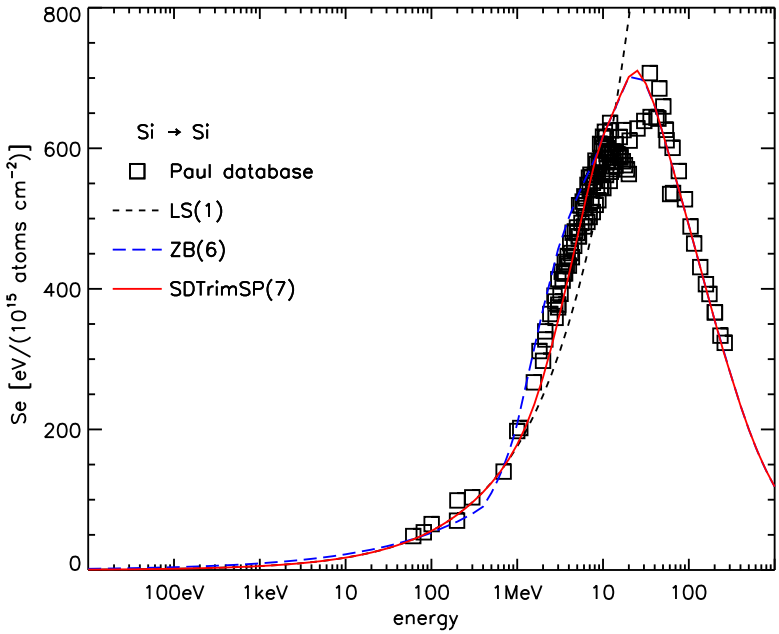

Figure 51: Electronic stopping power dependent on energy Si on Si with measurements [65]

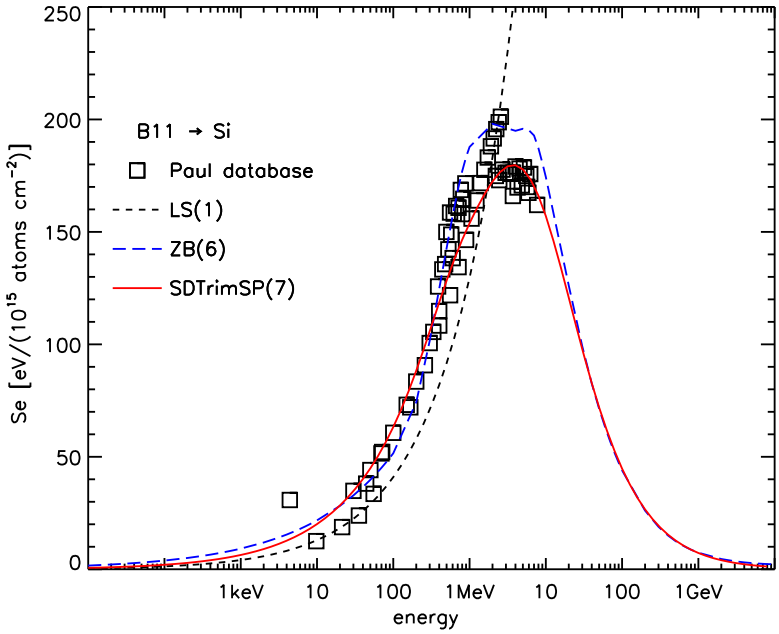

Figure 52: Electronic stopping power dependent on energy B11 on Si with measurements [65], $ck_{elec} = 1.50$, $a_2 = 0.5$, $a_3 = 105.928$, $a_4 = 0.0237644$, $a_5 = 5.46061$

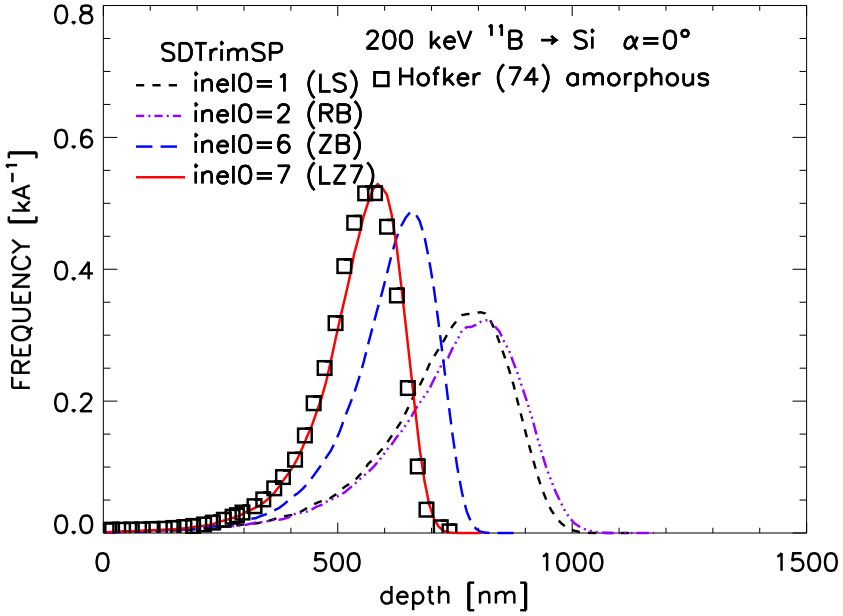

Figure 53: Comparison of implantation profiles of 200 keV B in Si calculated with different electronic lost models and experimental results [68]

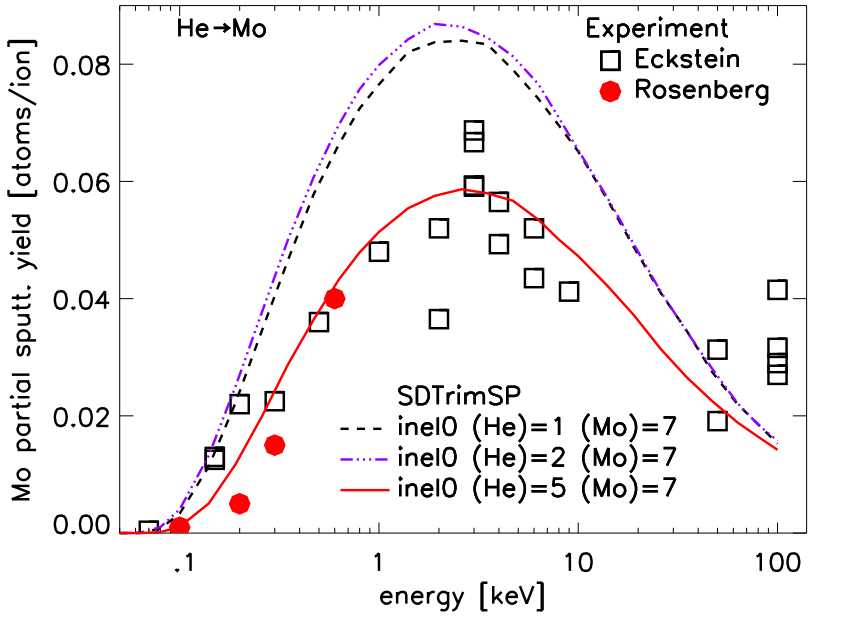

Figure 54: Comparison of yield dependent on energy He on Mo calculated with different electronic lost models and experimental results [28], [67]

6.12. Stop position of replacement or substitution and parameter irc0

If after collision from particle Z_1 on target-particle Z_2 the energy of Z_1 less then the displacement-energy Ed:

$$E(Z_1) < Ed(Z_1) \;\; and \;\; E(Z_2) > Ed(Z_2) \;\; and \;\; Z_1 = Z_2 \;\; \rightarrow replacement$$

$$E(Z_1) < Ed(Z_1) \;\; and \;\; E(Z_2) > Ed(Z_2) \;\; and \;\; Z_1 \neq Z_2 \;\; \rightarrow substitution$$

The stop-position of Z_1 is the start position of recoil Z_2.

$$\begin{aligned} x_{stop}(Z_1) &= x_{start}(Z_2) \\ y_{stop}(Z_1) &= y_{start}(Z_2) \\ z_{stop}(Z_1) &= z_{start}(Z_2) \end{aligned}$$

The output-file are depth_recoil.dat and depth_damage.dat, see chapter. D.4

The default value for parameter $irc0$

$$irc0 = 1$$

If after collision from particle Z_1 on target-particle Z_2 the energy of Z_2 less then the displacement-energy Ed:

$$E_{start}(Z_2) < Ed(Z_2) \;\; and \;\; irc0 = 1 \quad \rightarrow self \; replacement$$

The stop-position of recoil Z_2 is the start position of recoil Z_2.

$$\begin{aligned} x_{stop}(Z_2) &= x_{start}(Z_2) \\ y_{stop}(Z_2) &= y_{start}(Z_2) \\ z_{stop}(Z_2) &= z_{start}(Z_2) \end{aligned}$$

7. Crystal

7.1. New parameter $l\_crystal$ and new program-modules

A crystalline target need a list of atom positions. This positions are static and the thermal vibrations is used to find the actual positions at given temperature. In this case the program SDTrimSP becomes to a grid program and is no longer a Monte Carlo program.

New subprograms for crystal calculation:
sub_crystal.F90
recoil_c.F90
projectile_c.F90

Programs with included crystal calculation:
SDTrimSP.F90
init_all.F90
histories.F90

New parameters:
$l\_crystal$ ... calculate crystal
$l\_crystal\_dyn$ ... calculate amorphization
$miller\_ind$ ... miller index for example [1,1,1]

The default value for parameters:

$$\begin{aligned} l\_crystal &= .false. \\ l\_crystal\_dyn &= .false. \\ miller\_ind &= 1.0,\ 0.0,\ 0.0 \end{aligned}$$

7.2. New Inputfile *crystal.inp*

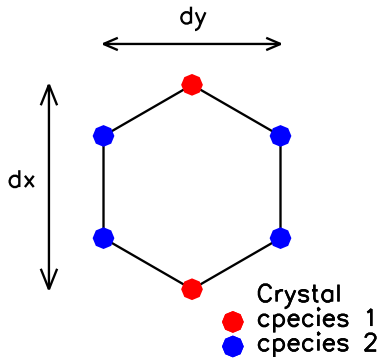

Figure 55: Example of crystal, note: x is the depth of target

Surface-area of one crystal is period into y,z-direction. There are different possibilities to input the same crystal-structure.

Inputfile '*crystal.inp*', see var1:

```
A-B-crystal    name of crystal
1              lattice_id
2              number of species like tri.inp
"A"            first species
"B"            second species
60.0 0.0 0.0       base vector a1 : dx,dy,dz [A]
0.0 50.0 0.0       base vector a2 : dx,dy,dz [A]
0.0 0.0 50.0       base vector a3 : dx,dy,dz [A]
3      number of atoms
0.0000 0.5000 0.0000 1    relative x,y,z, number of species (red)
0.3333 0.0000 0.0000 2    relative x,y,z, number of species (blue)
0.6666 0.0000 0.0000 2    relative x,y,z, number of species (blue)
0                      p_max of crystal 0...calculate in program
60.0 50.0              dy_beam dz_beam if =0 dx_beam=dy dz_beam=dz
3                      matrix_id = 5...5x5x5    = 3...3x3x3
```

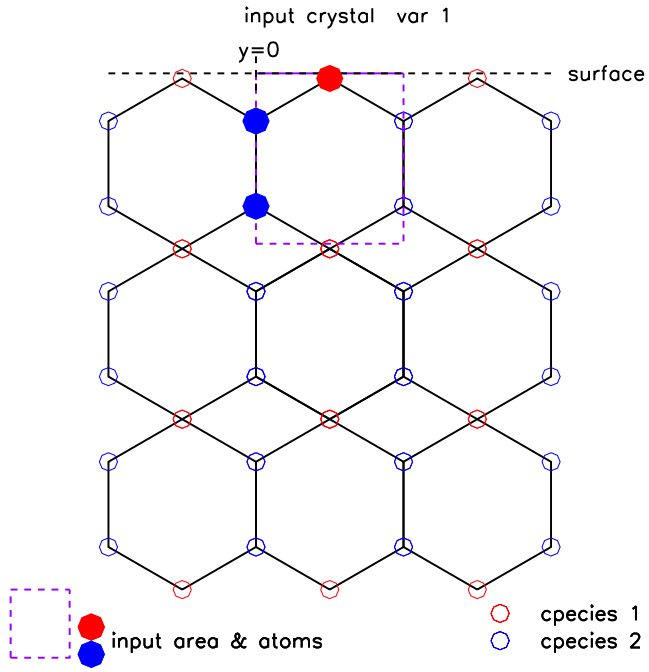

Figure 56: Example of crystal A-B input var1 (dash line), note: x is the depth of target

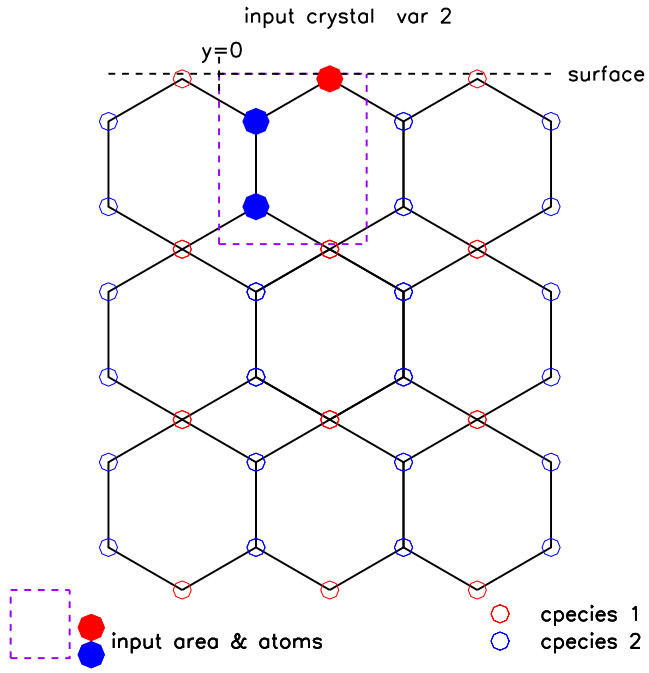

Figure 57: Example of crystal A-B input var2 (dash line), note: x is the depth of target

7.3. Simple test-example 2000 eV Cu on Cu

7.3.1. Geometry and input-file

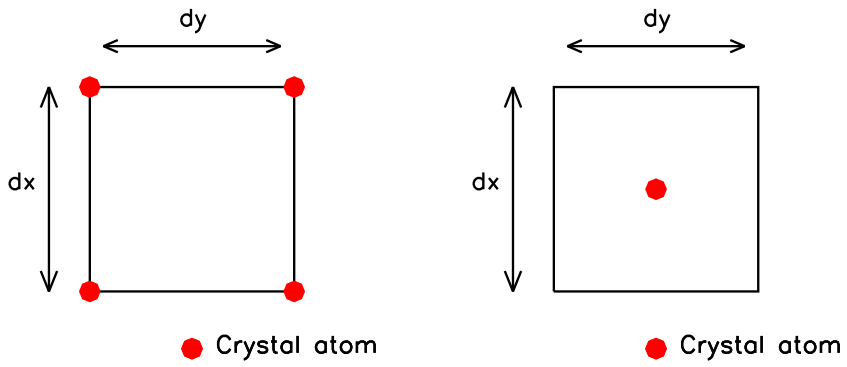

Figure 58: Two presentation of the same example of simple crystal, see also Fig. 59

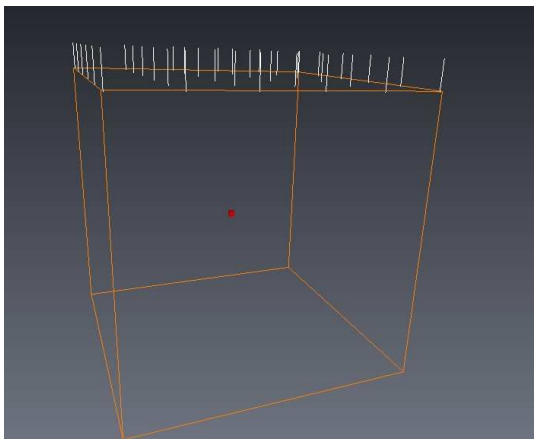

Figure 59: Example of simple crystal (white lines are the possible trajectories from outside)

Inputfile '*crystal.inp*':

test-crystal	name of crystal
1	lattice_id
1	number of species like tri.inp
"Cu"	species
2.2756 0.0 0.0	base vector a1 : dx,dy,dz [A]
0.0 2.2756 0.0	base vector a2 : dx,dy,dz [A]
0.0 0.0 2.2756	base vector a3 : dx,dy,dz [A]
1	number of atoms
0.5 0.5 0.5	relative x,y,z, number of species (red)
3.5	p_max of crystal
2.2756 2.2756	dy_beam dz_beam if =0 dx_beam=dy dz_beam=dz
3	matrix_id =5...5x5x5 =3...3x3x3

7.3.2. Field of nearest target-atoms (3x3x3) or (5x5x5)

The start-point to find the next collision partner is in the center of a 3x3x3 or 5x5x5 field of nearest target-atoms Fig. 60 and Fig. 63 of simple crystal atom Fig. 59.

The consideration of the neighboring atoms (red points in Fig. 61) is important for the calculation of the yield. The use of a 3x3x3 and also a 4x4x4 field of target-atoms is not sufficient to validate this fact, Fig. 62.
Therefore a 5x5x5 crystal-schema (Fig. 63) is used for simulation of a Cu-crystal.

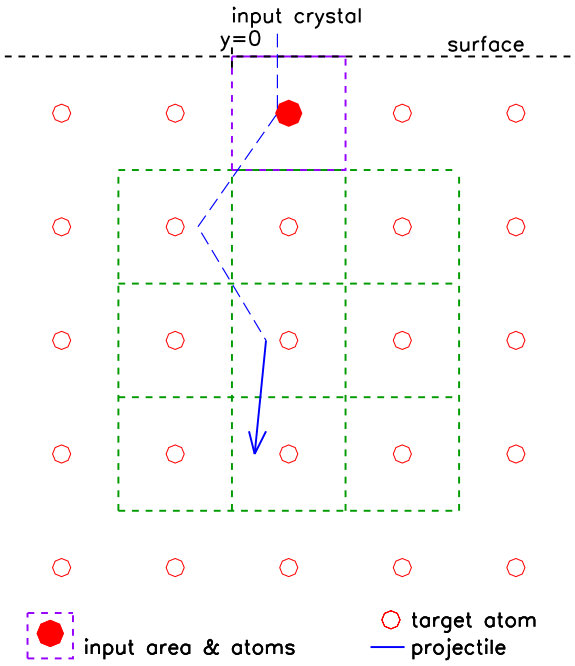

Figure 60: Example of simple crystal with the input area (dash purple). It is used a 3x3x3 field of target-atoms (here see only x-cut: 3x3 matrix, dash green) for next collision-calculation (blue solid line (or arrow). The trajectory of incident projectile is the blue line.

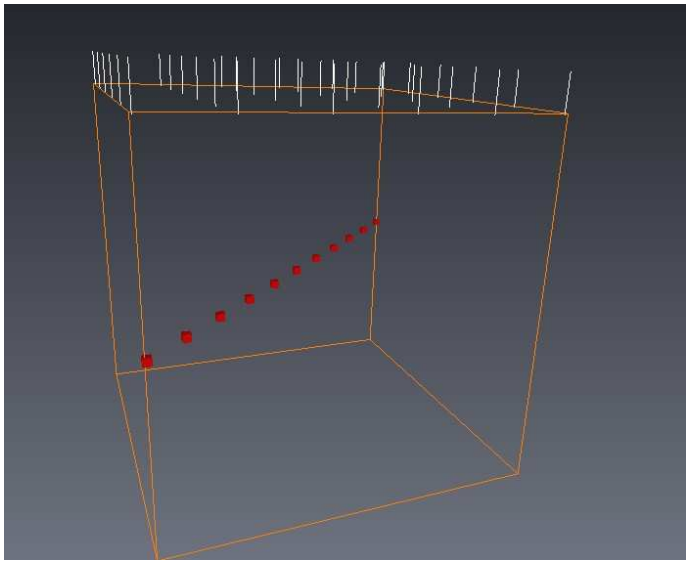

Figure 61: Variation of then input-position of crystal-atom (red) inside the crystal-area (white lines: the start positions of projectiles

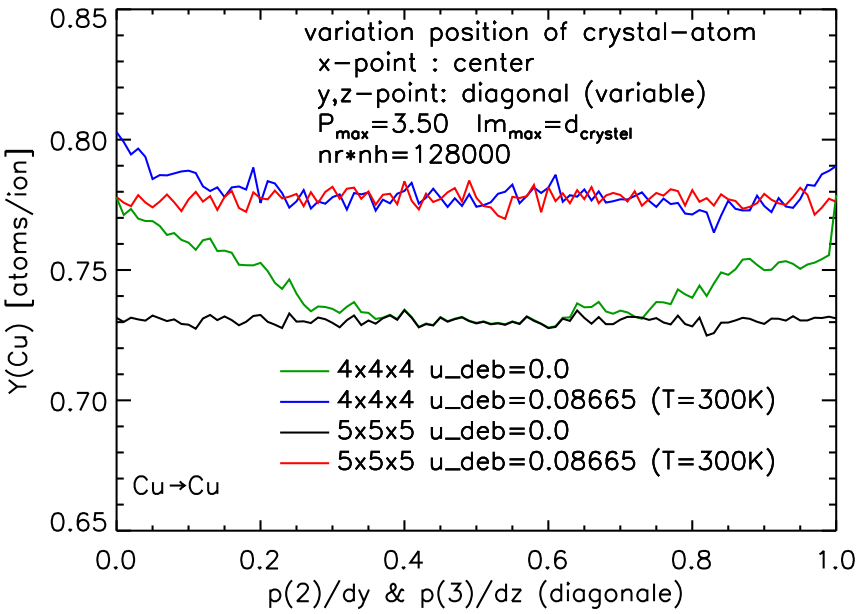

Figure 62: Calculated yield dependent on the position of a single crystal-atom inside the crystal-area by different used of the field of neighbor target-atoms

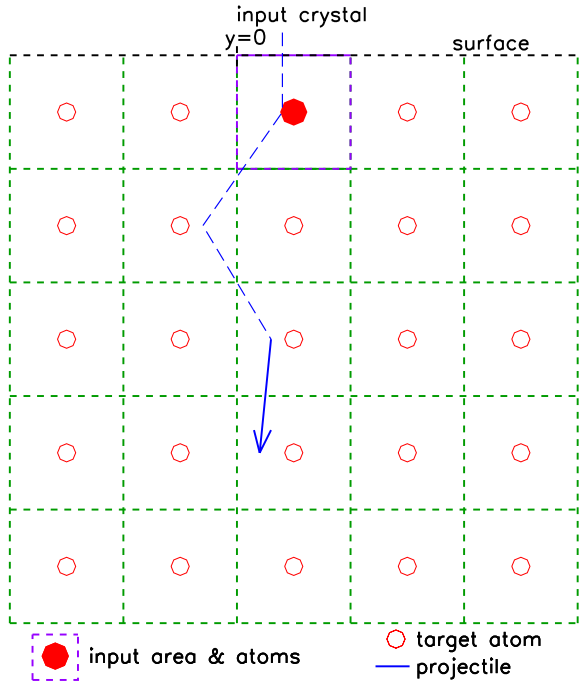

Figure 63: Example of simple crystal with the area input crystal (dash purple). It is used a 5x5x5 matrix (dash green) for the next collision-calculation (blue solid line (or arrow). The trajectory of incident projectile is the blue line

7.4. Thermal vibration, mean free paths and impact-parameter

7.4.1. Thermal vibration

A good approximation of amplitude of the Debye-Waller theory [1] dependent on temperature T, atomic mass M and Debye temperature Θ is:

$$u_{deb} = \sqrt{\frac{145.52539}{M \cdot \Theta} \cdot \left(\frac{1}{4} + \frac{T}{\Theta}\right)} \qquad T >= \Theta/2 \tag{7.78}$$

$$u_{deb} = \sqrt{\frac{145.52539}{M \cdot \Theta} \cdot \left(\frac{1}{4} + \frac{\Pi^2}{6} \cdot \frac{T^2}{\Theta^2}\right)} \quad T < \Theta/2 \tag{7.79}$$

We use a Gaussian distribution of u_{deb} to simulate the thermal vibration in program. The calculated yield dependent on uncorrelated lattice vibrations (Debye-Waller amplitude u_{deb}) show Fig. 67.
The results are inexplicable when using the impact-parameter $P_{max} = 2.22A$ (this is the values for simultaneous weak collision of 3 rings) for the calculation of yields. Fig. 68 shows the yield dependent on P_{max} for Cu. The influence of neighboring atoms up to a distance of 3.0 A must be taken into account. Only if used a impact-parameter P_{max} of 3.0 A the calculated yield dependent on uncorrelated lattice vibrations show good results , see Fig. 67 (black lines).

7.4.2. mean free path length (lm)

In the amorphous model lm is the straight mean free path between the collisions. The length lm is fixed for a given atomic density of target Fig. 64

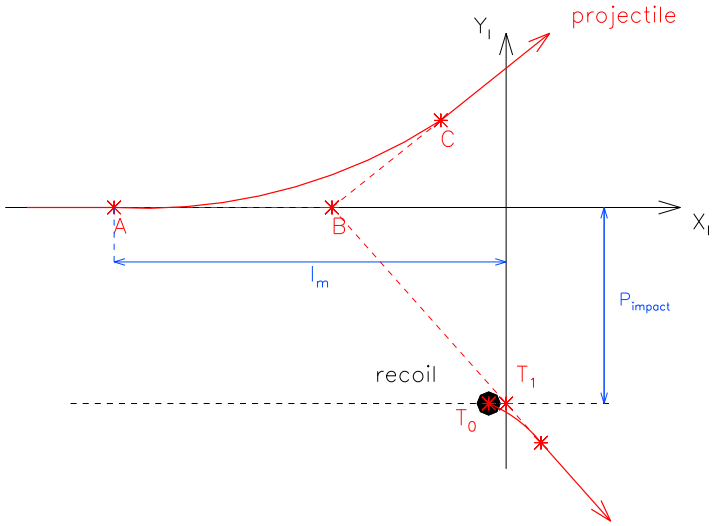

Figure 64: Free path length lm in the amorphous model

There are two possibilities to define lm in a lattice-model (see also Fig. 65):

$$1.\ lm_{max} = lm\Big(P_{Impact} = min(P_{Impact})\Big) \quad lm = 0\ ...\ d_{crystal} \tag{7.80}$$

$$2.\ lm_{max} = d_t^{-1/3} \quad d_t\ ...\ atomic\ density\ of\ crystal \tag{7.81}$$

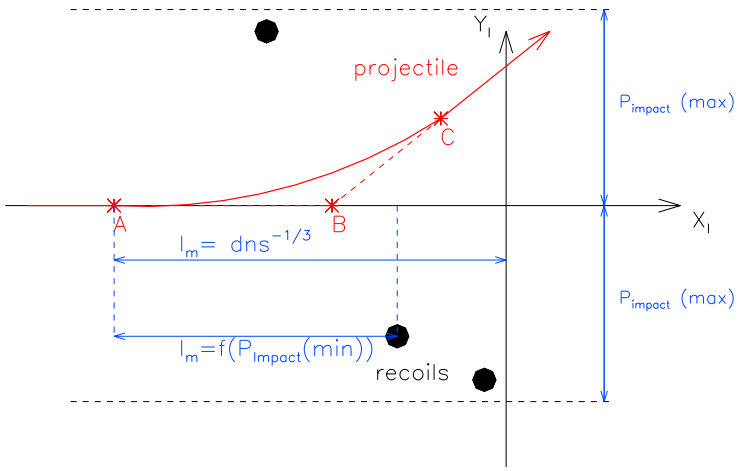

Figure 65: Free path length lm in a lattice-model, here with three recoils

The different of yields between two possibilities of lm_{max} is big, see Fig. 67 - 69 and Fig. 71. Therefore SDTrimSP use only the first definition of lm_{max}, see eq. 7.80

7.4.3. impact-parameter P_{max}

In the amorphous model P_{max} is:

$$P_{max} = 1/(d_t^{1/3}\sqrt{\pi})$$

For a crystal the value may be bigger.

7.5. Example of 2000 eV Cu on Cu fcc crystal

Inputfile '*crystal.inp*' for a face centered cubic (fcc) crystal:

```
Cu crystal fcc
1          lattice_id
1          number of species like tri.inp
"Cu"       first species
3.6150 0.0 0.0      base vector a1 : dx,dy,dz [A]
0.0 3.6150 0.0      base vector a2 : dx,dy,dz [A]
0.0 0.0 3.6150      base vector a3 : dx,dy,dz [A]
4                   number of atoms
0.0   0.0   0.0 1     relative x,y,z, number of species (red)
0.0   0.5   0.5 1     relative x,y,z, number of species (red)
0.5   0.0   0.5 1     relative x,y,z, number of species (red)
0.5   0.5   0.0 1     relative x,y,z, number of species (red)
3.0                 p_max of crystal
3.6150 3.6150       dy_beam dz_beam if =0 dx_beam=dy dz_beam=dz
3                   matrix_id =5...5x5x5    =3...3x3x3
```

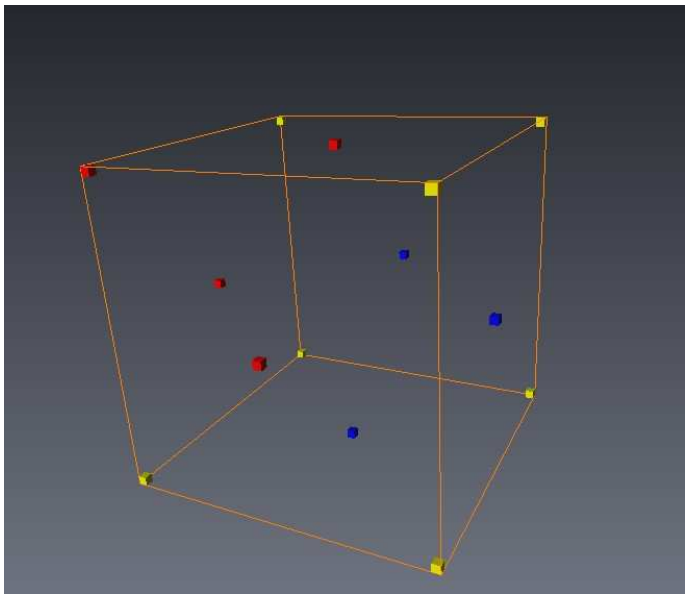

Figure 66: Atom-positions of a face centered cubic (fcc) crystal, corner atoms (yellow/red), surface atoms (blue/red), input of inputfile '*crystal.inp*' (red)

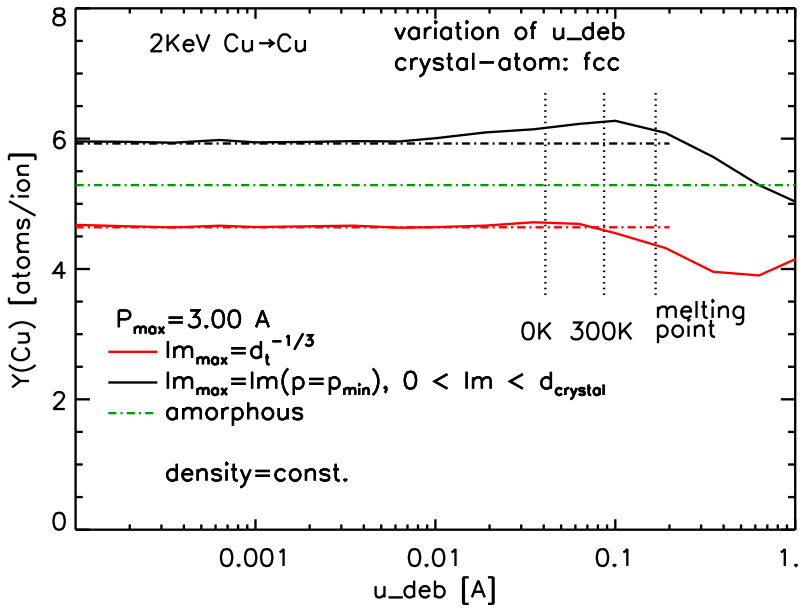

Figure 67: Calculated yield dependent on Debye-Waller amplitude u_{deb} (the positions of fcc-crystal-atoms see Fig. 66)

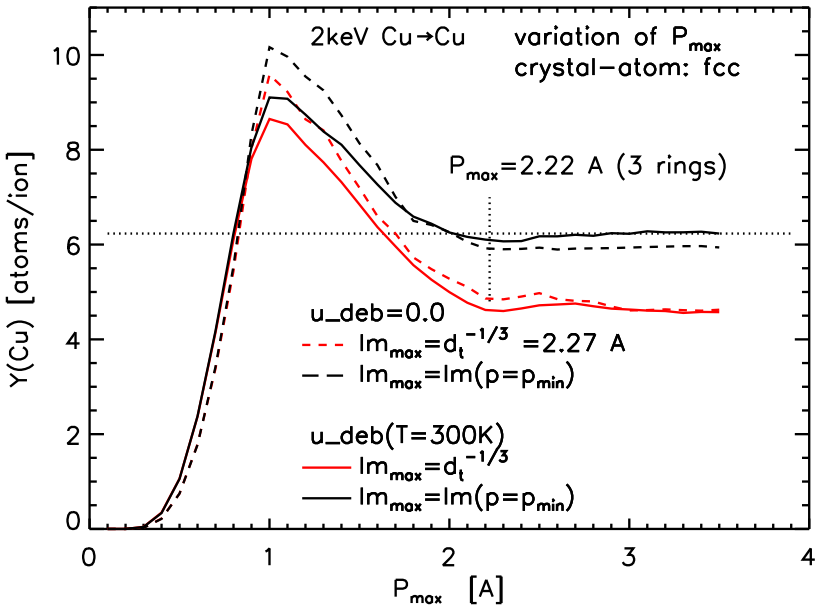

Figure 68: Calculated yield dependent on P_max (the position of fcc-crystal-atom see Fig. 66)

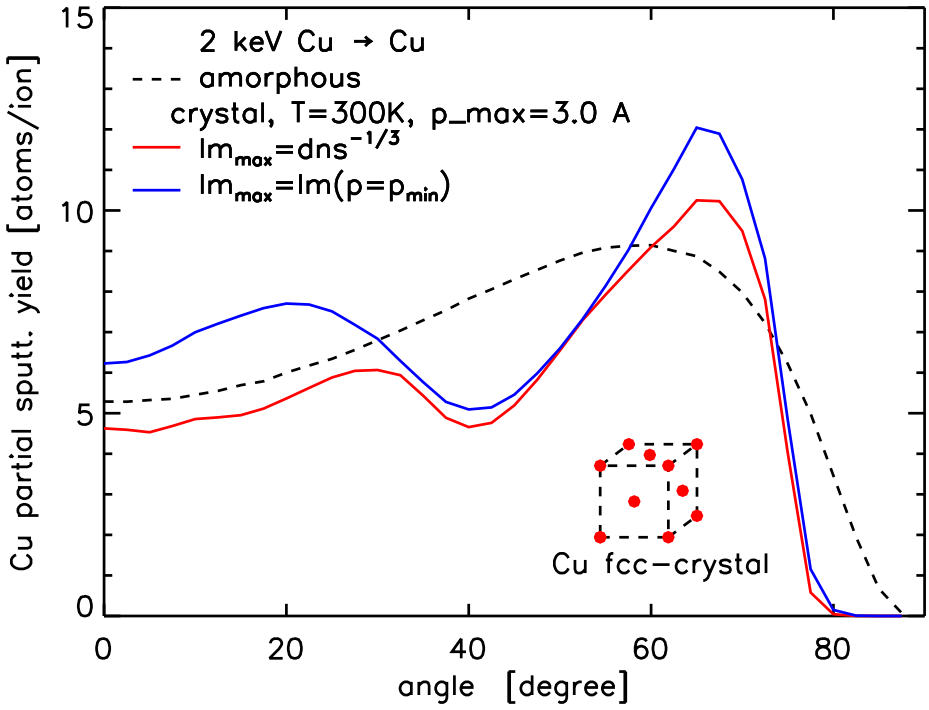

Figure 69: Yield dependent on incident angle, amorphous and crystalline $u_{deb}(T = 300\ K)$, see Fig. 66

7.6. Compare calculated Rn and Rt with MARLOW of a Cu fcc-crystal

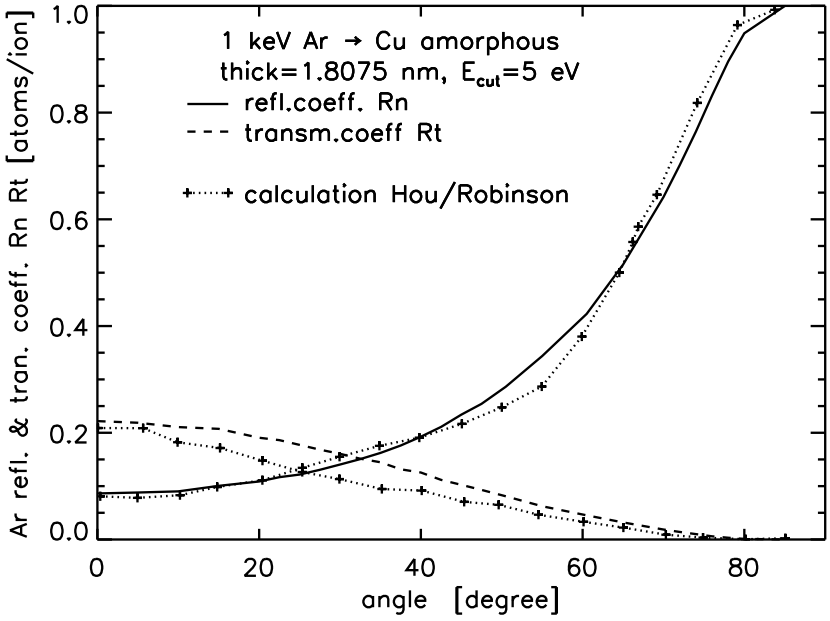

Figure 70: Compare with calculated reflection and transmitted coefficient SDTrimSP and MARLOW [66] Ar on thin amorphous Cu target (18.075 A) dependent on incident angle

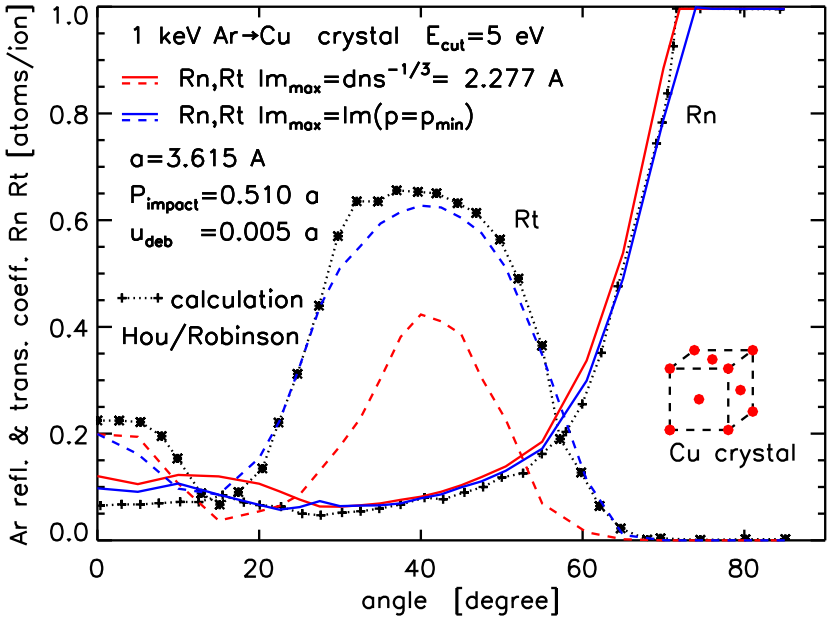

Figure 71: Compare with calculated reflection and transmitted coefficient SDTrimSP and MARLOW [66] Ar on thin crystalline Cu target ($thick = 18.075\ A = 5 \cdot a$) dependent on incident angle, length of the crystal-cube $a = 3.615\ A$, $u_{deb} = 0.005 \cdot a$

7.7. Rotation and direction fcc-crystal

$\vec{m}$ is the Miller Indices, for example $m = [1, 0, 0]$. The crystal rotates around the z-axis with the angle φ and around the y-axis with the angle ϑ.

$$\begin{aligned} \vec{a} &= \frac{\vec{m}}{\sqrt{\vec{m} \cdot \vec{m}}} \quad \text{(normalization)} \\ r &= \sqrt{a(1)^2 + a(2)^2} \\ sin(\varphi) &= a(2)/r \qquad cos(\varphi) = a(1)/r \\ sin(\vartheta) &= a(3) \qquad cos(\vartheta) = r \end{aligned}$$

The rotation-matrix is:

$$\vec{a} = \begin{bmatrix} cos(\varphi) * cos(\vartheta) & sin(\varphi) * cos(\vartheta) & sin(\vartheta) \\ -sin(\varphi) & cos(\varphi) & 0.0 \\ -cos(\varphi) * sin(\vartheta) & -sin(\varphi) * sin(\vartheta) & cos(\vartheta) \end{bmatrix}$$

7.7.1. Axis and projection of a fcc crystal

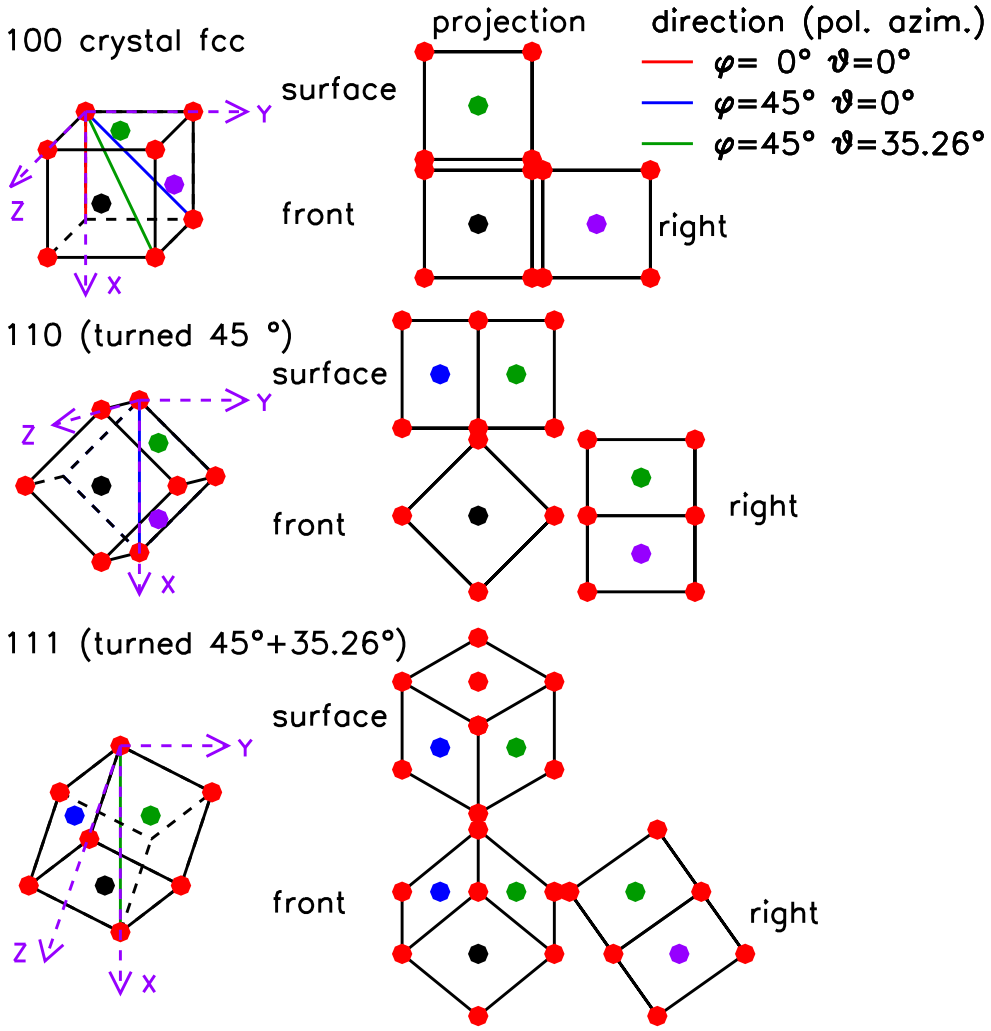

Figure 72: Axis [100], [110], [111] and projection of a fcc crystal and angle in SDTrimSP

7.7.2. fcc crystal [100]

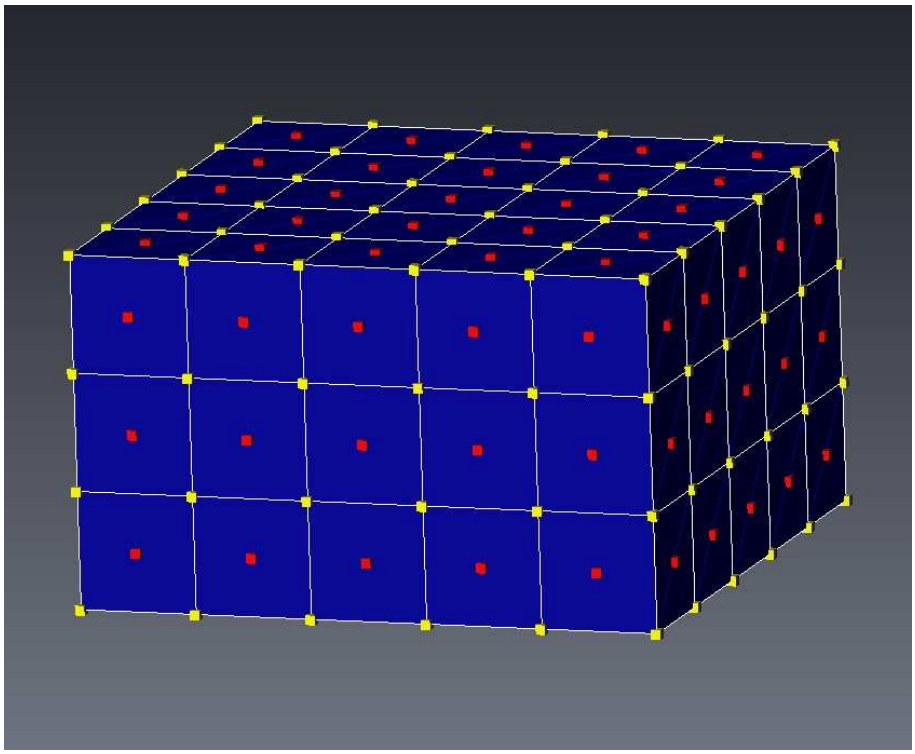

Figure 73: 3D fcc crystal [100], smooth surface

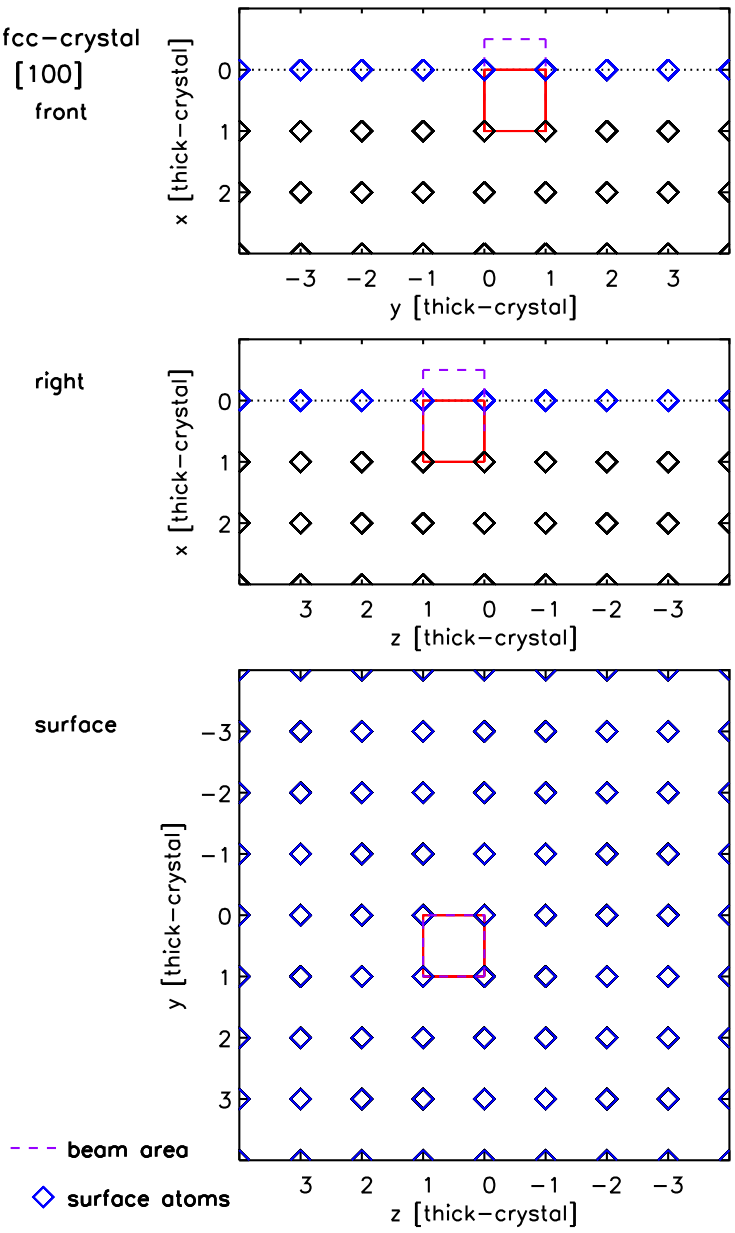

Figure 74: Projection of vertices fcc crystal [100] with beam-area for calculation

7.7.3. fcc crystal [110]

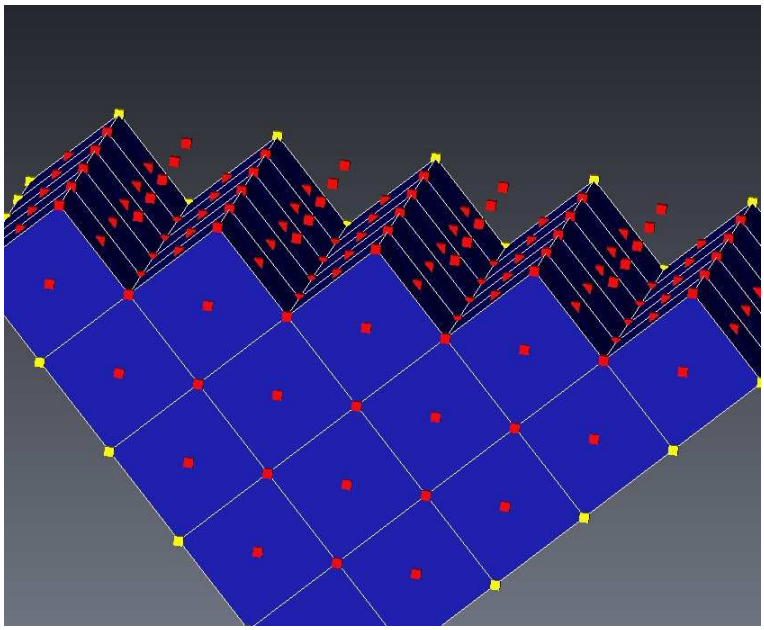

Figure 75: Cutout of fcc crystal [110 a] with smooth surface

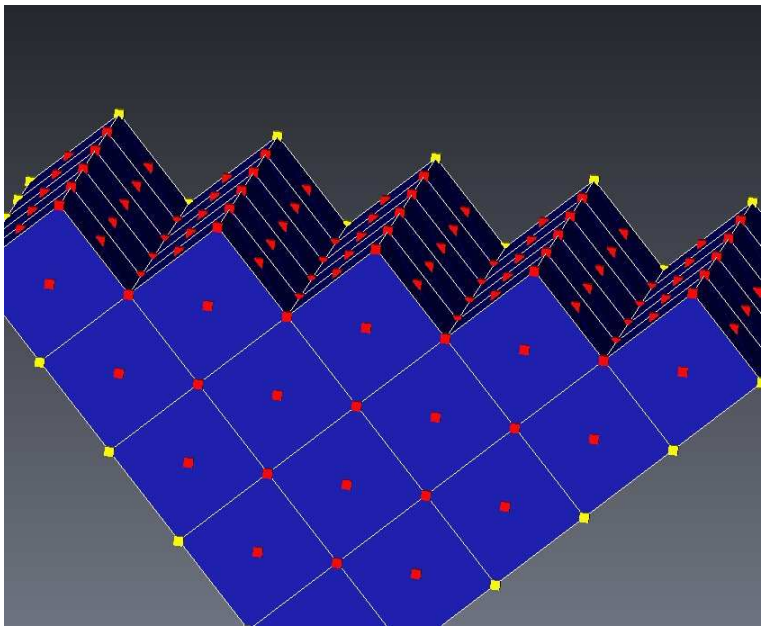

Figure 76: Cutout of fcc crystal [110 b] with rough surface (only atoms of full crystal)

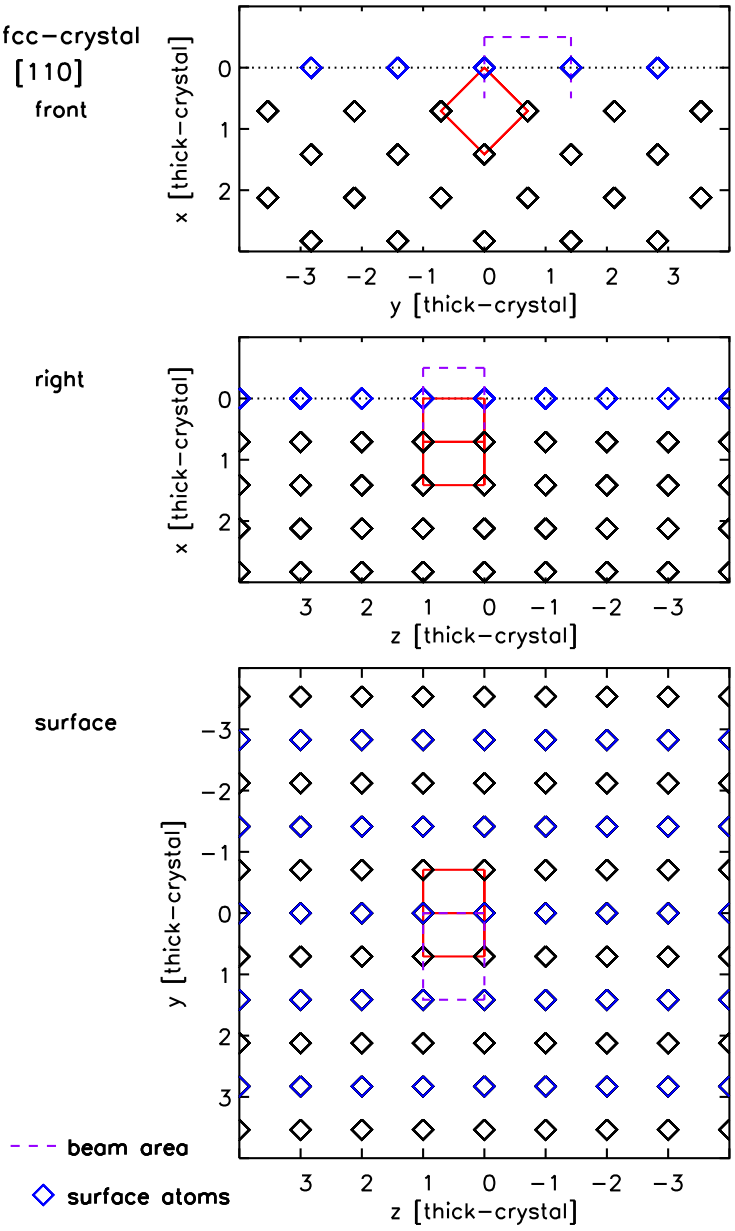

Figure 77: Projection of vertices fcc crystal [110] with beam-area for calculation

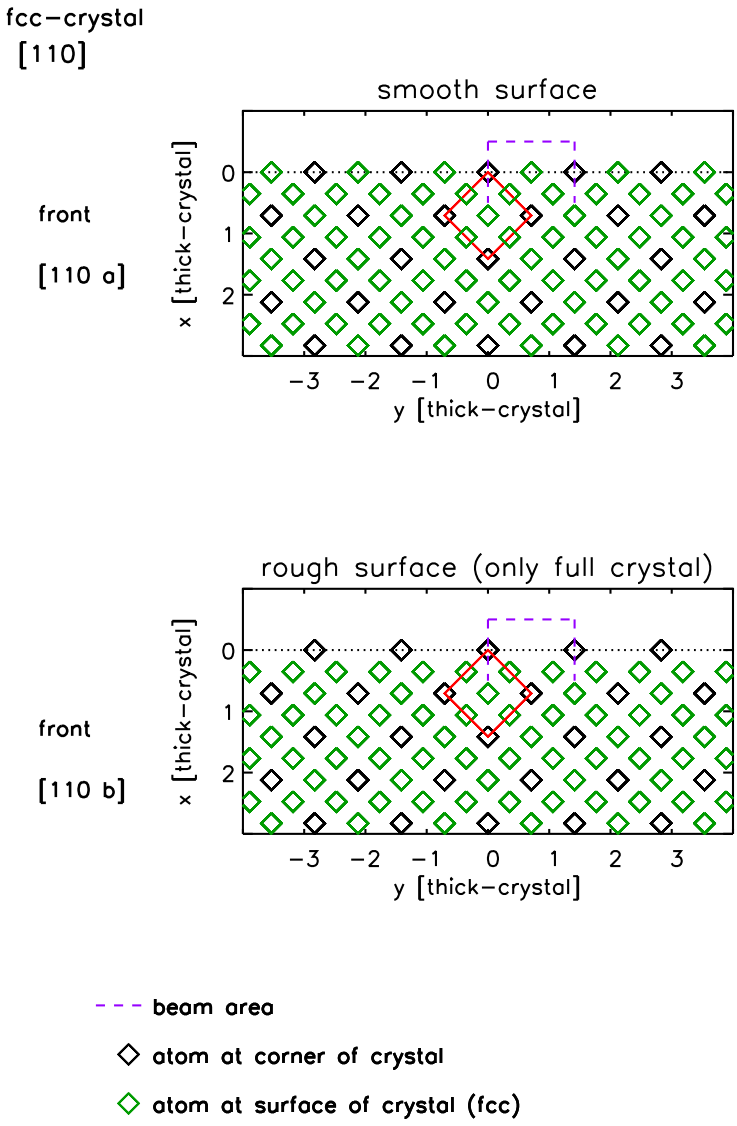

Figure 78: Projection of all atoms fcc crystal [110a] and [110b] with beam-area for calculation (like Fig. 77)

7.7.4. fcc crystal [111]

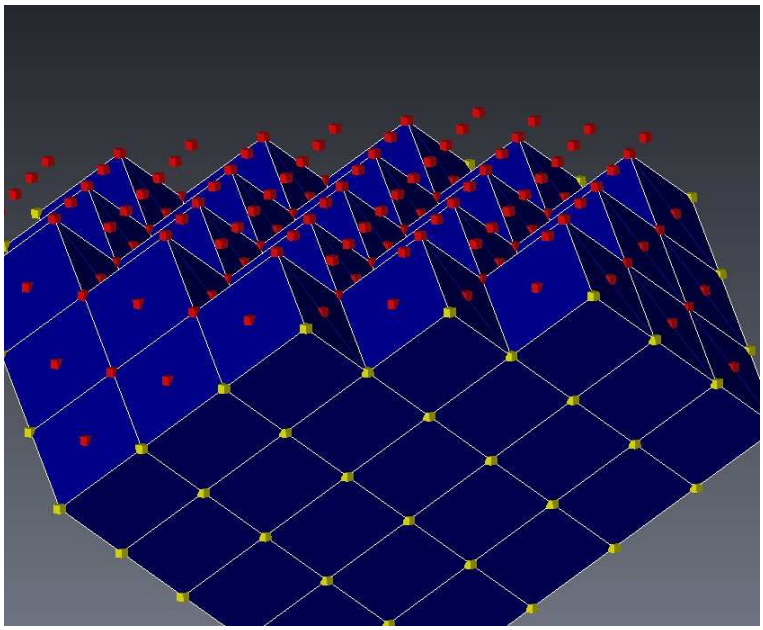

Figure 79: Cutout of fcc crystal [111 a] with smooth surface

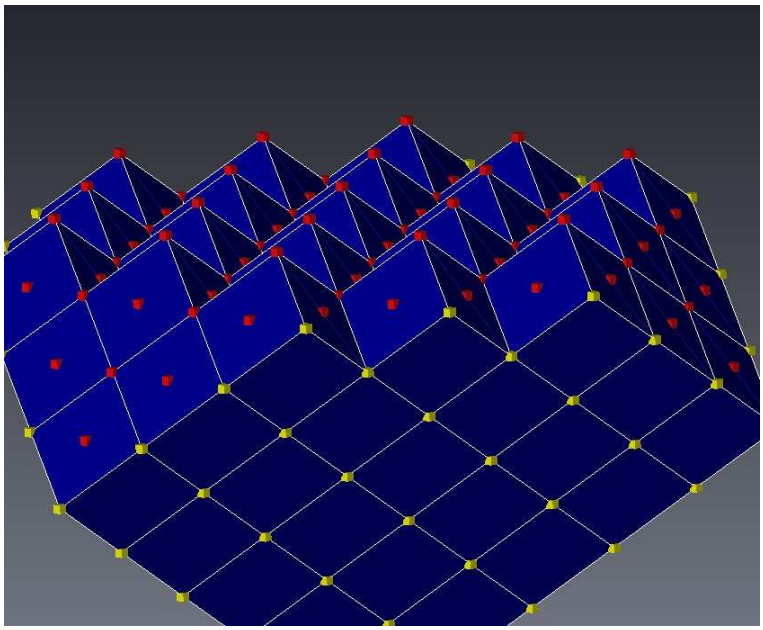

Figure 80: Cutout of fcc crystal [111 b] with rough surface (only atoms of full crystal)

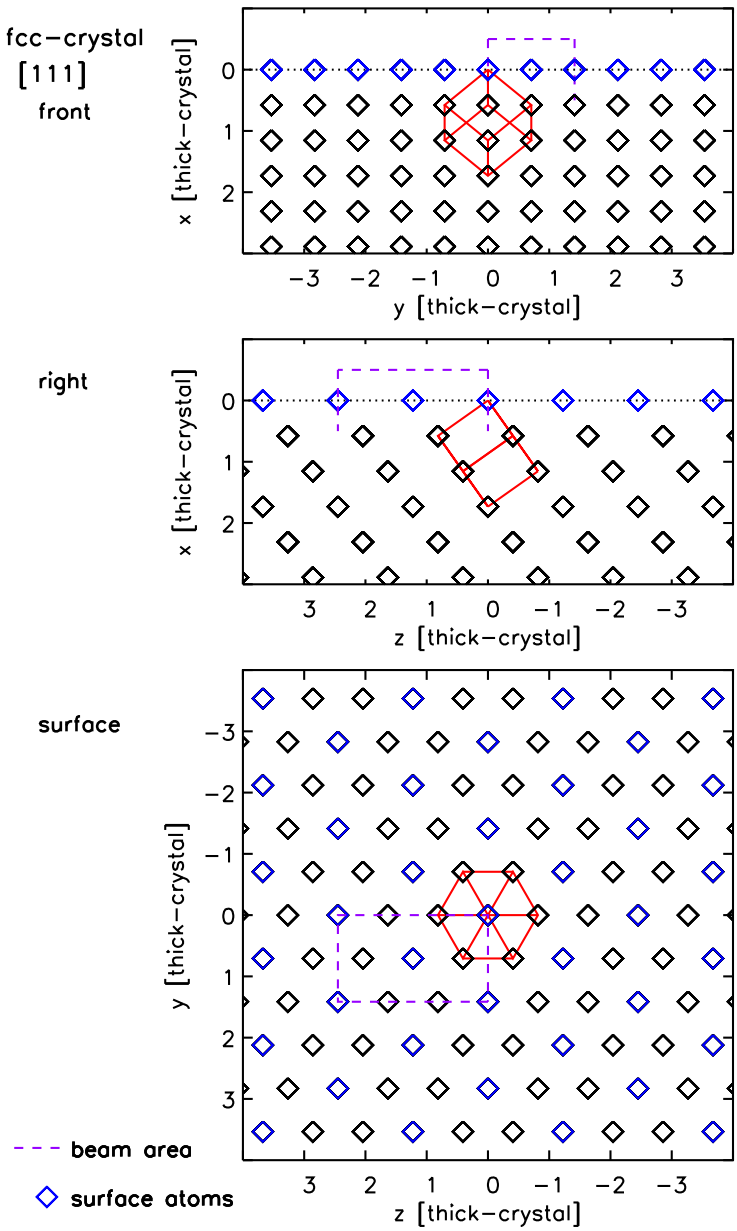

Figure 81: Projection of vertices fcc crystal [111] with beam-area for calculation

7.7.5. fcc crystal [310]

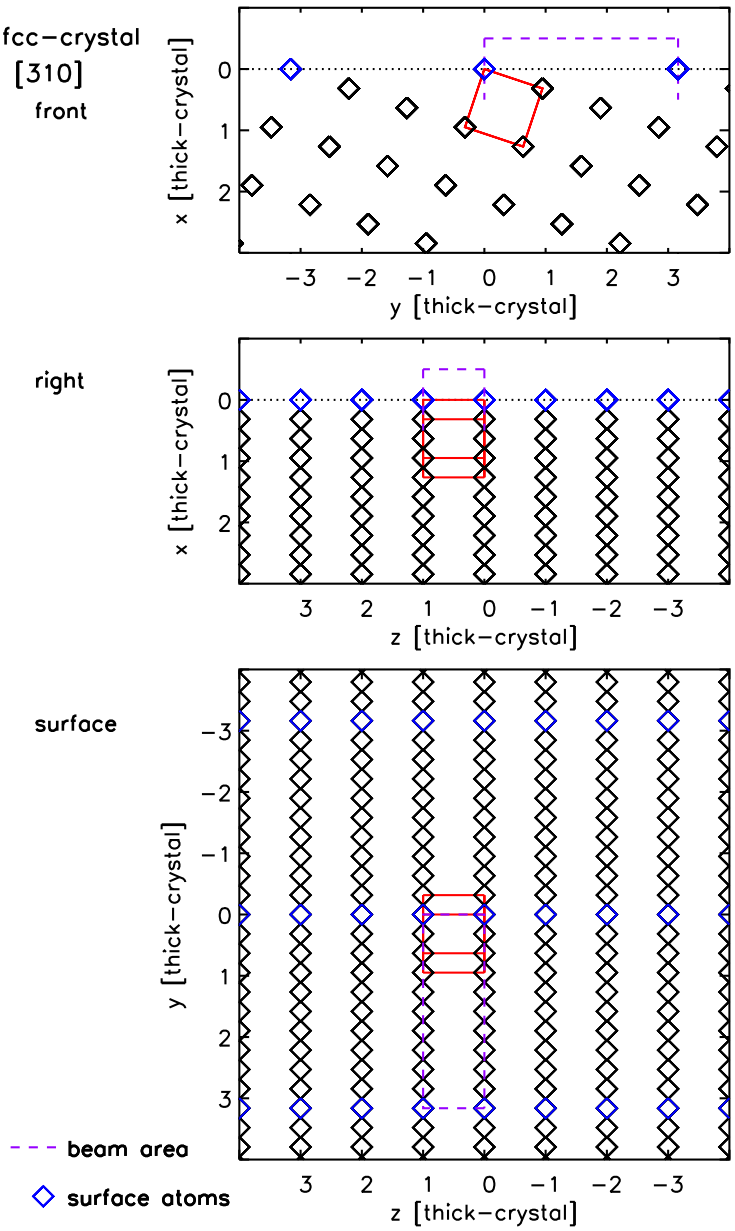

Figure 82: Projection of vertices fcc crystal [310] with beam-area for calculation

7.7.6. fcc crystal [321]

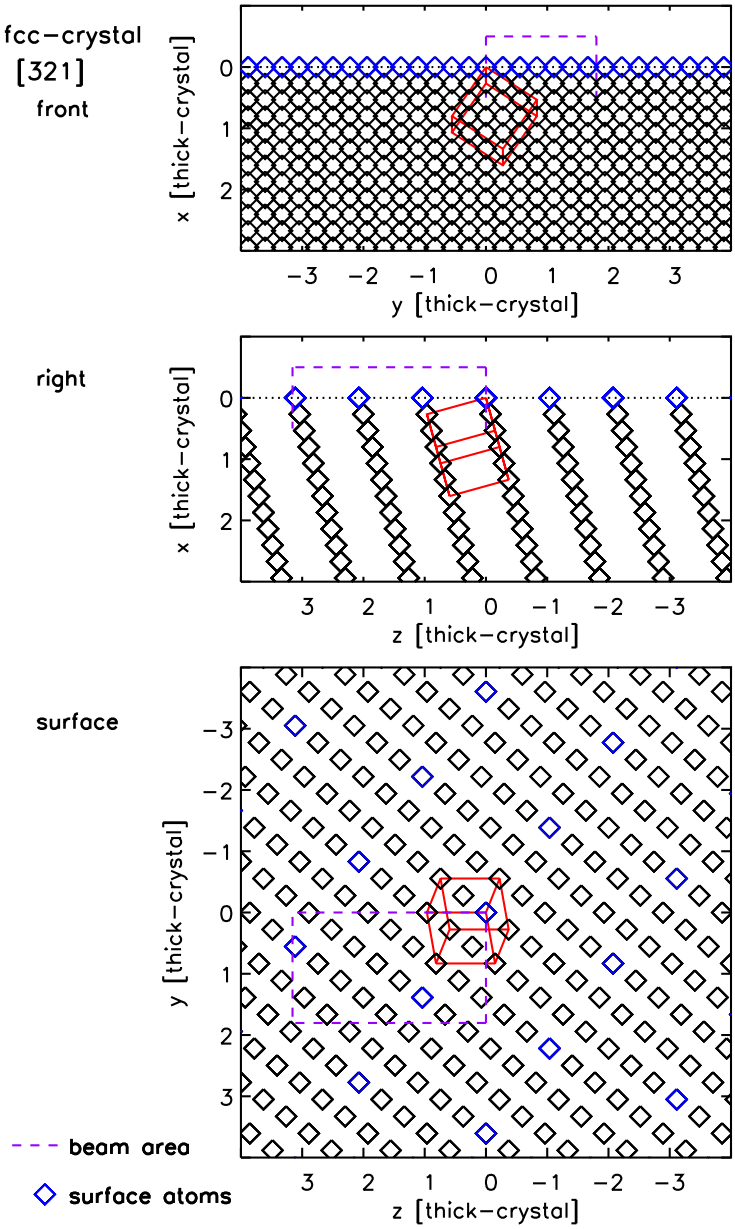

Figure 83: Projection of vertices fcc crystal [321] with beam-area for calculation

7.7.7. fcc crystal [311]

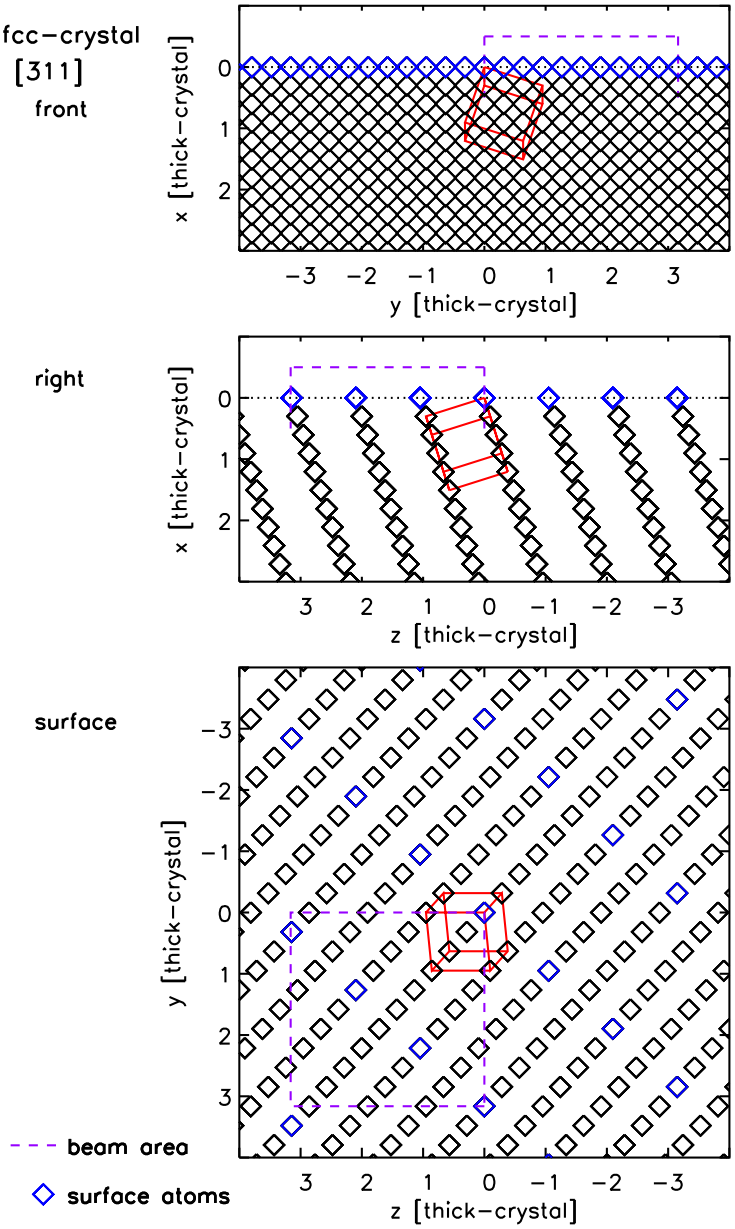

Figure 84: Projection of vertices fcc crystal [311] with beam-area for calculation

7.8. number incident projectiles

The accuracy of results of the yield is dependent on number of incident projectiles and their start-points. Fig. 85 shows the spread or range of local yield ($Y = 0...25$) dependent on start of incident projectile of a [111] fcc-crystal.

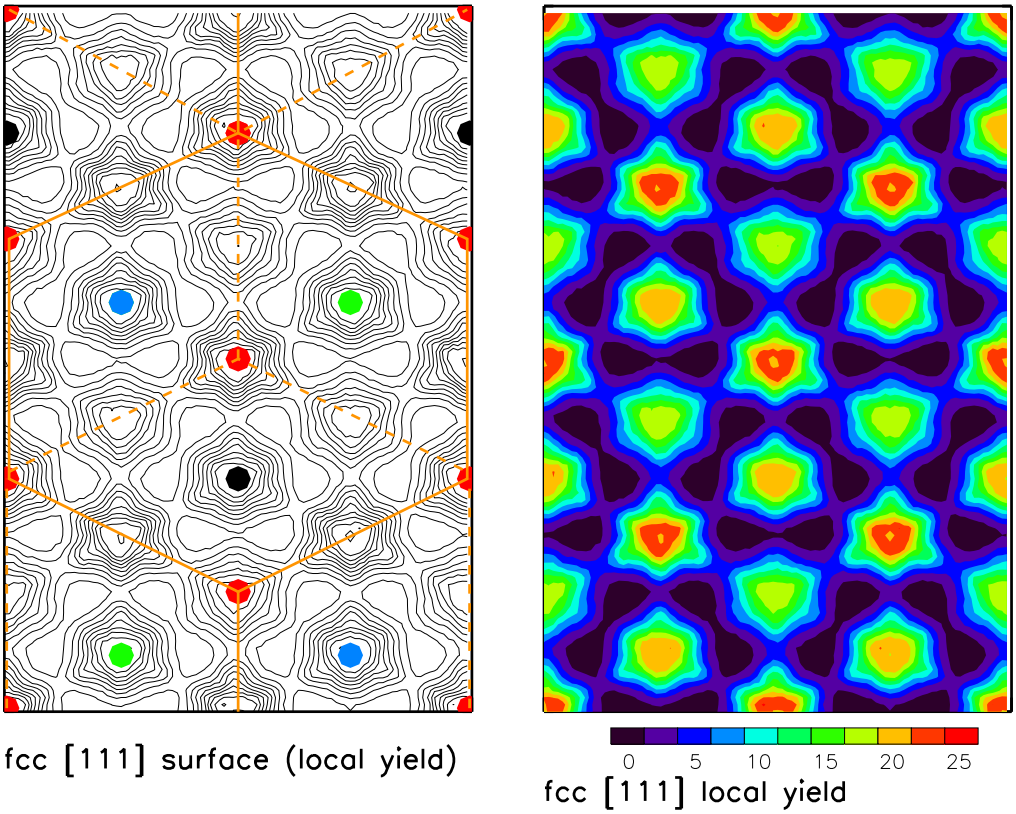

Figure 85: Distribution of yield dependent on start of incident projectile. Left the atoms of crystal (red,blue,green,black like Fig. 72) with contours, right the same in color (without atoms)

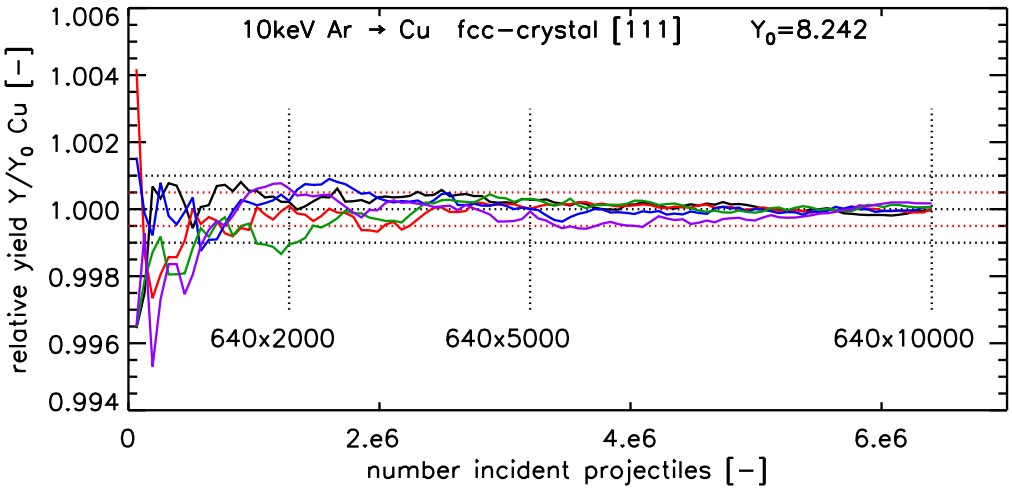

Figure 86: Accumulated accuracy of the yield as a function of the number of projection with different start-random-seed

7.9. beam-area

$\vec{m}$ is the Miller Indices, for example $m = [1, 0, 0]$. The crystal rotates around the z-axis with the angle φ and around the y-axis with the angle ϑ. The rotation-matrix is $\vec{a}$, see 7.7.
The y period:

$$\begin{aligned} m(2) = 0 \quad &: \quad dy_{beam} = dy_{crystal} \\ m(2) > 0 \quad &: \quad dy_{beam} = \frac{dx_{crystal}}{sin(\varphi)} \end{aligned}$$

The z period:

$$m(3) = 0 \quad : \quad dz_{beam} = dz_{crystal}$$

if $m(3) > 0$:

$$\vec{v} = \begin{bmatrix} 0 & 0 & 1 & 1 \\ 0 & 1 & 1 & 0 \end{bmatrix} \quad vertices\ of\ the\ crystal$$

$$\begin{aligned} \vec{s}(:,1) &= v(:,1) * cos(\varphi) + v(:,2) * sin(\varphi) \quad (x - component\ of\ \vec{a}, \vartheta = 0\ ) \\ dx &= max[\vec{s}(:,1)] - min[\vec{s}(:,1)] \\ dz_{beam} &= \frac{dx}{sin(\vartheta)} \end{aligned}$$

For $\vec{m}$=[1,1,1] :

$$\begin{aligned} dy_{beam} &= \sqrt{2} \cdot d_{crystal} \\ dz_{beam} &= \sqrt{6} \cdot d_{crystal} \end{aligned}$$

7.10. Compare yield(α) and yield(φ) fcc crystal direction [100]-[110]

The direction of incident projectile relative to the orientation of the crystal can be realized through the change of incident angle α or the rotation of crystal around the z-axes with angle φ.
The yield is only the same at the angle $\alpha = 0$ and $\varphi = 0$.

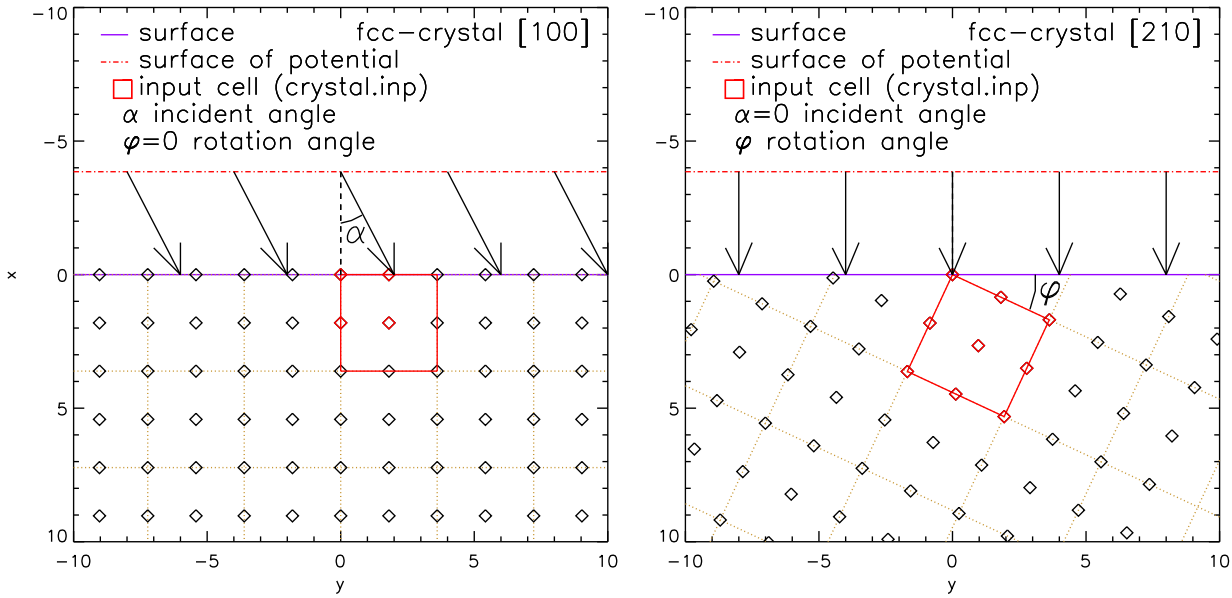

Figure 87: Two possibilities to realize the direction [210] of projectiles

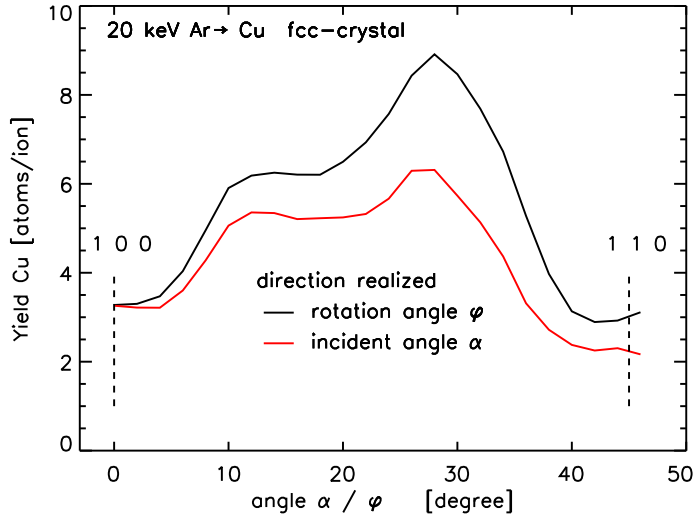

Figure 88: Yield of two possibilities to realize the direction [100]-[110] of projectile (compare yield(φ) with measurements see Fig. 96)

7.11. Compare trajectories of fcc crystal [100] with amorphous target (tunnel effect)

The comparison of trajectories in crystalline (Fig. 89, left) and amorphous target (Fig. 89, right) shows the tunnel effect in the crystal. The penetration depth of incident particles may be bigger in a crystal.

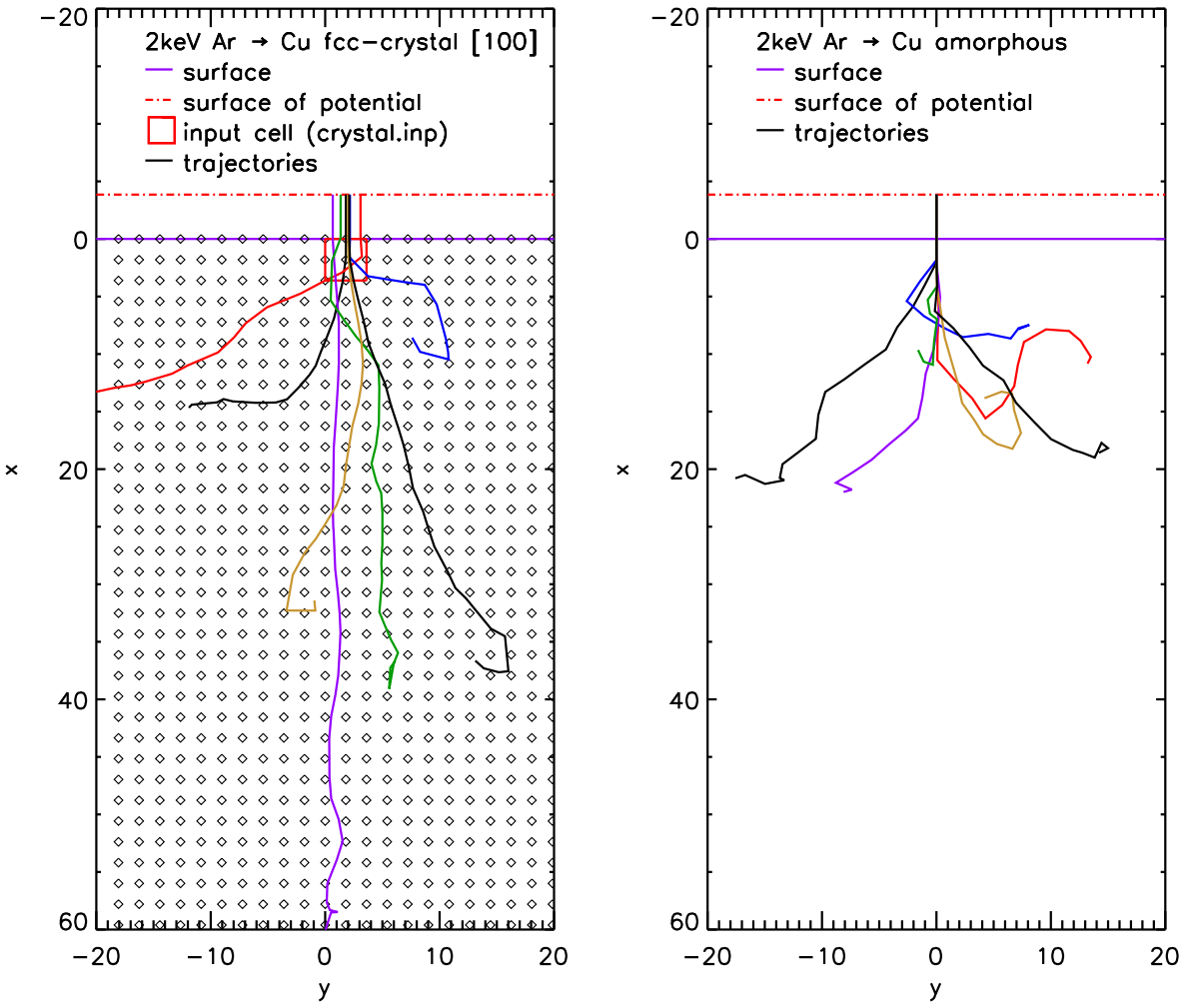

Figure 89: Some possible trajectories of Ar in fcc crystal and in amorphous target

7.12. Amorphization (dynamic) calculation of mono- and poly-crystalline profiles

During the bombardment parts of targets transform into amorphous (dyn). If there are enough vacancies 85 % of stopped atoms ($E_{start} > E_{displ}$) will replace to the crystal state. The absolute value is dependent on fluence.

$$0.85 \cdot Si_{stopped} \rightarrow Si_{crystalline}$$
$$0.15 \cdot Si_{stopped} \rightarrow Si_{amorphous}$$

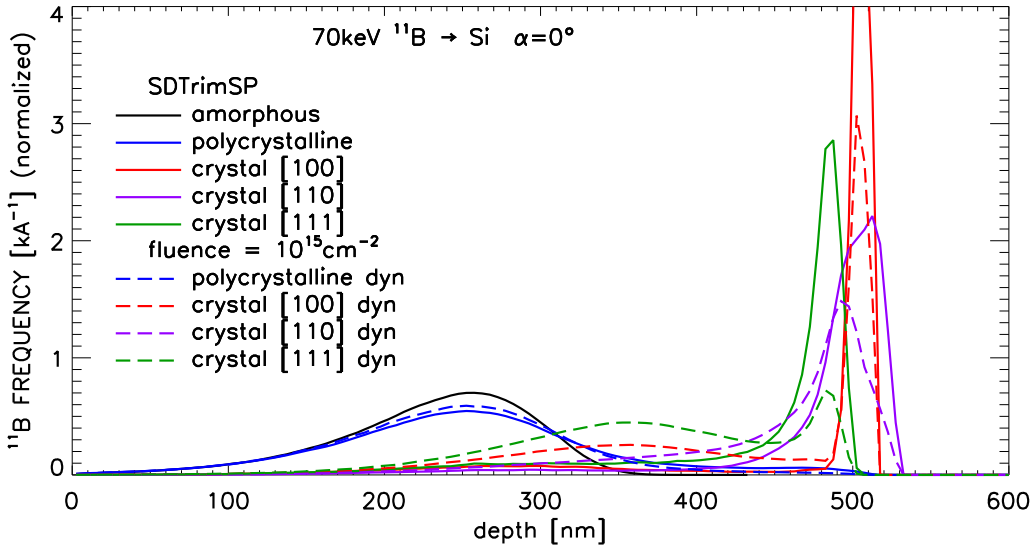

Figure 90: Calculated profile of B^{11} on Si-target amorphous, mono- and poly-crystalline with and without amorphization (dyn)

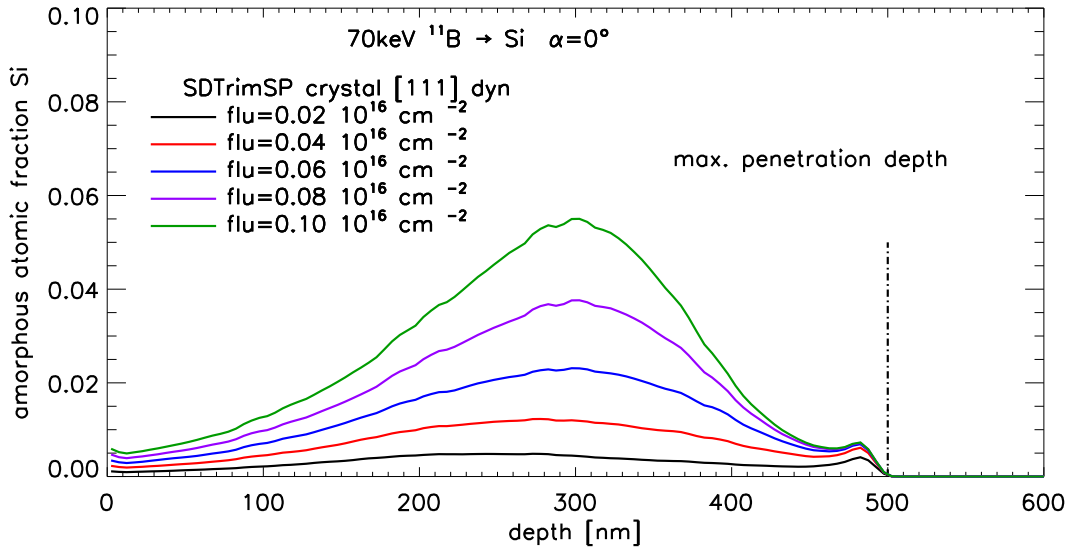

Figure 91: Atomic fraction of amorphous Si during bombardment dependent on fluence

8. Comparison of calculated and measured value of crystal-target

8.1. Compare yields of different crystal orientation with measurements Ga on Cu (fcc) and Ga on W(bcc)

Poly-crystalline target is a mix of crystals with different directions. The yield of a poly-crystalline target is the average of all directions.

The range of calculated directions in normalized form is: [1 , 0...1 , 0...1]

Example of normalization : [3 , 2 , 1] → [1 , 2/3 , 1/3]

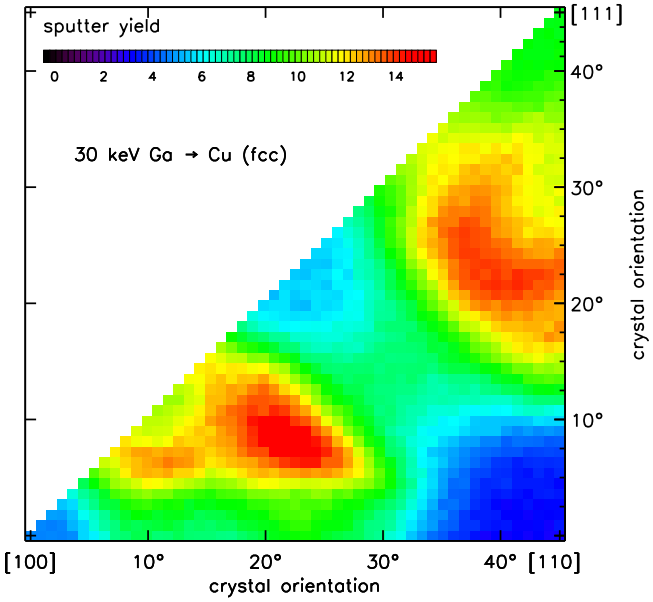

Figure 92: Calculated yields of different directions 30 KeV Ga on Cu, average of all yields is the yields of poly-crystalline target

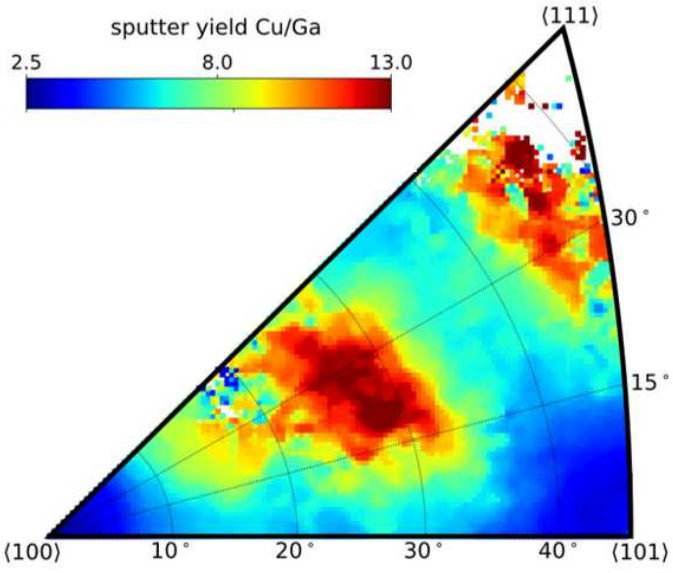

Figure 93: Measured yields of different directions 30 KeV Ga on Cu [75]

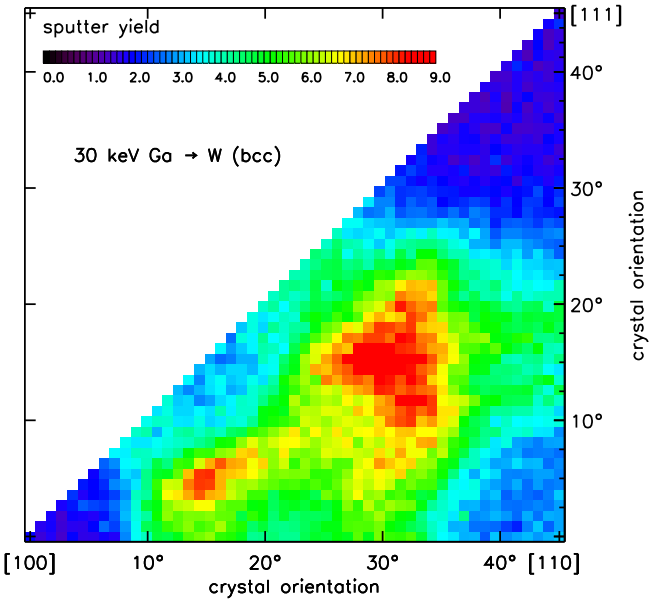

Figure 94: Calculated yields of different directions 30 KeV Ga on W, average of all yields is the yields of poly-crystalline target

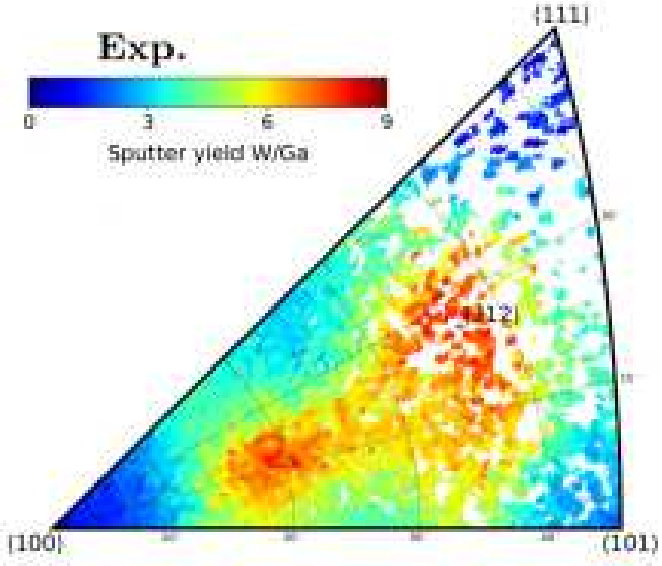

Figure 95: Measured yields of different directions 30 KeV Ga on W [75]

8.2. Compare calculated sputtered yield with measurement of Ar on Cu fcc-crystal

Inputfile '*crystal.inp*' for a face centered cubic (fcc) crystal:

```
Ar on Cu crystal fcc
1          lattice_id
2          number of species like tri.inp
"Ar"       first species
"Cu"       second species
3.6123153 0.0 0.0      base vector a1 : dx,dy,dz [A]
0.0 3.6123153 0.0      base vector a2 : dx,dy,dz [A]
0.0 0.0 3.6123153      base vector a3 : dx,dy,dz [A]
4                      number of atoms
0.0    0.0    0.0 2    relative x,y,z, number of species (red)
0.0    0.5    0.5 2    relative x,y,z, number of species (red)
0.5    0.0    0.5 2    relative x,y,z, number of species (red)
0.5    0.5    0.0 2    relative x,y,z, number of species (red)
3.0000                 p_max of crystal
0.0000 0.0000          dy_beam dz_beam if = 0 ... is calculated automatically
3                      matrix_id =5...5x5x5    =3...3x3x3
```

parameter of Inputfile '*tri.inp*' for crystal [100]:

```
ncp = 2
symbol = "Ar", "Cu"
l_crystal = .true.
miller_ind= 1.0 , 0.0 , 0.0
```

For dynamical calculation (mix of crystalline and amorphous) the second species is crystalline-Cu and the the third species is amorphous-Cu

parameter of Inputfile '*tri.inp*' for polycrystalline with dynamic:

```
ncp = 3
symbol = "Ar", "Cu", "Cu"
l_crystal = .true.
miller_ind= 0.0 , 0.0 , 0.0
l_crystal_dyn=.true.
```

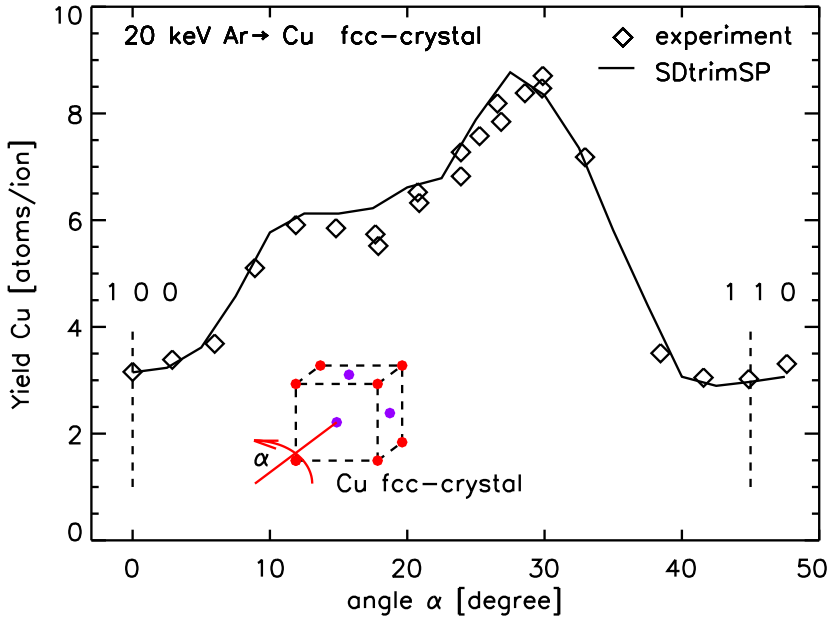

Figure 96: Compare calculated sputtered yield $Y_{(100)}$ with measurement [71] (found in [72]) for incidence of 20 keV Ar on Cu crystal (the crystal was turned around the [001] axis, the calculation was make with variable incident angle α)

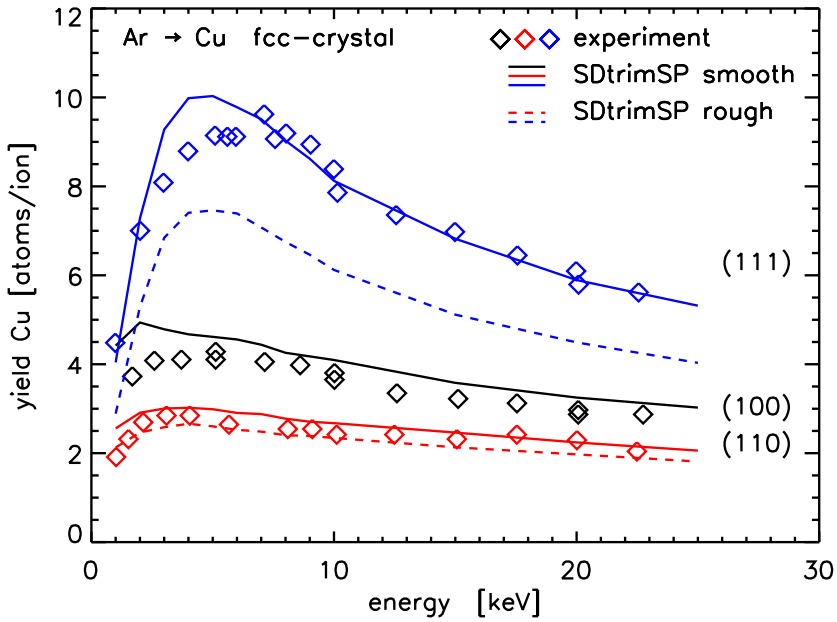

Figure 97: Compare calculated sputtered yield with measurement [73] for normally incidence onto low index planes of Cu crystal (smooth: Fig.79 and rough: Fig.80)

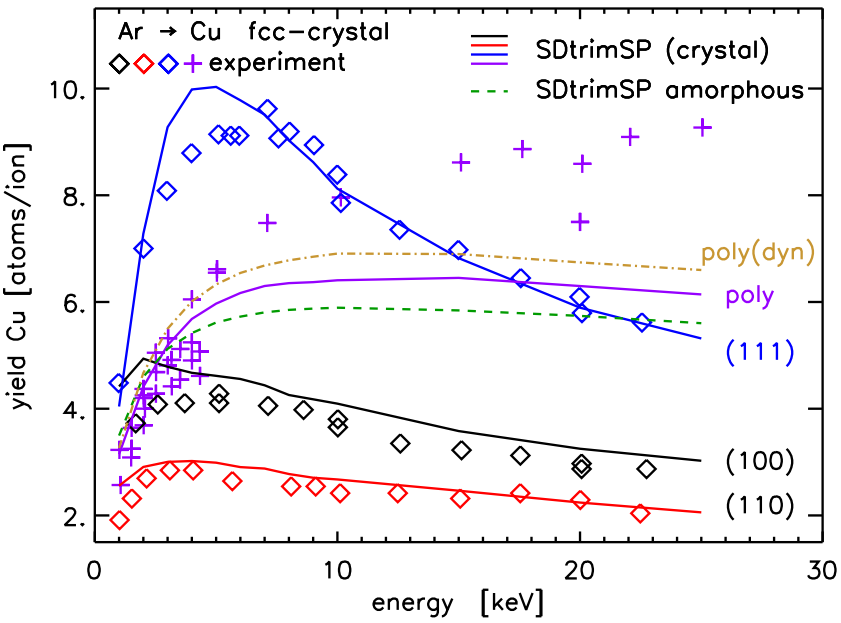

Figure 98: Compare calculated sputtered yield with measurement [73] for normally incidence onto low index planes of Cu crystal, add experimental polycrystalline and calculated amorphous and calculate dynamical polycrystalline at $fluence = 10^{-15} atoms/cm^2$

8.3. Compare experimental profiles with calculated profiles B on Si-crystal (diamond structure) and amorphous Si

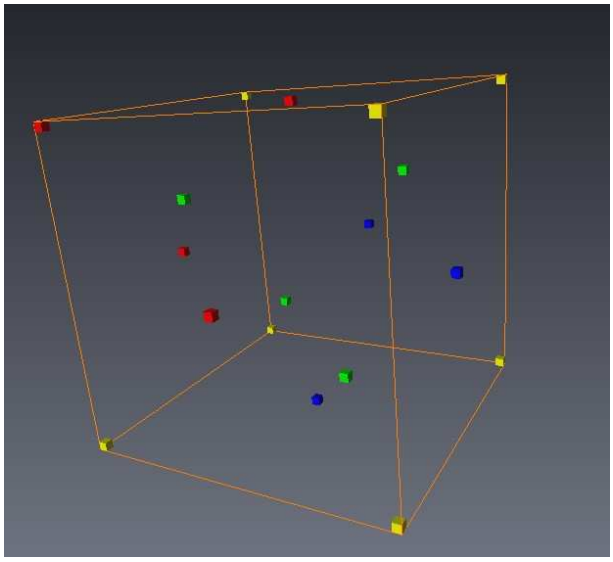

Figure 99: Atoms-position of a Si-crystal with diamond-structure, corner atoms (yellow/red), surface atoms (blue/red), inside atoms (green), input of inputfile '*crystal.inp*' (red/green)

Inputfile '*crystal.inp*':

```
Si crystal (diamond-structure)
1          lattice_id
2          number of species like tri.inp
"B11"      first species
"Si"       second species
5.4310 0.0 0.0              base vector a1 : dx,dy,dz [A]
0.0 5.4310 0.0              base vector a2 : dx,dy,dz [A]
0.0 0.0 5.4310              base vector a3 : dx,dy,dz [A]
8                           number of atoms
0.00   0.00   0.00 2       relative x,y,z, number of species (red)
0.00   0.50   0.50 2       relative x,y,z, number of species (red)
0.50   0.00   0.50 2       relative x,y,z, number of species (red)
0.50   0.50   0.00 2       relative x,y,z, number of species (red)
0.25   0.25   0.25 2       relative x,y,z, number of species (red)
0.25   0.75   0.75 2       relative x,y,z, number of species (red)
0.75   0.25   0.75 2       relative x,y,z, number of species (red)
0.75   0.75   0.25 2       relative x,y,z, number of species (red)
3.0000                      p_max of crystal
0.0000 0.0000               dy_beam dz_beam if = 0 ... is calculated automatically
3                           matrix_id =5...5x5x5    =3...3x3x3
```

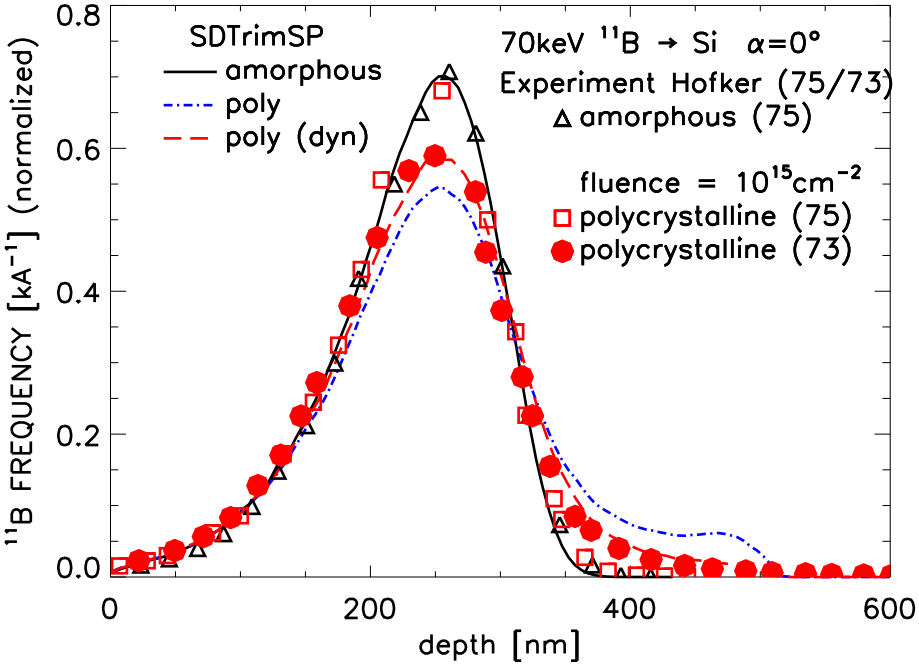

Figure 100: Comparison calculated profile with measurements [68] B^{11} on Si

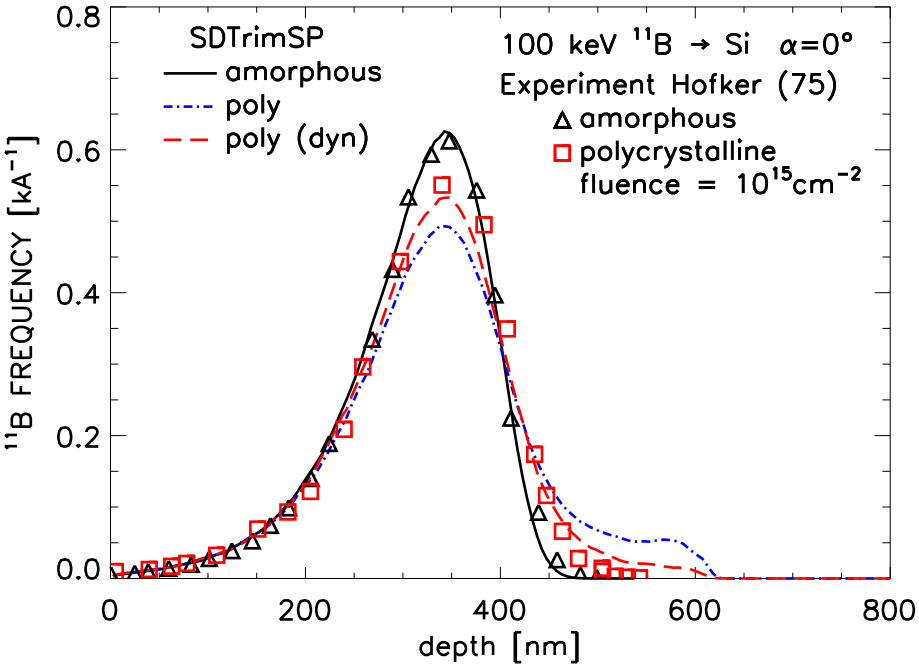

Figure 101: Comparison calculated profile with measurements [68] B^{11} on Si

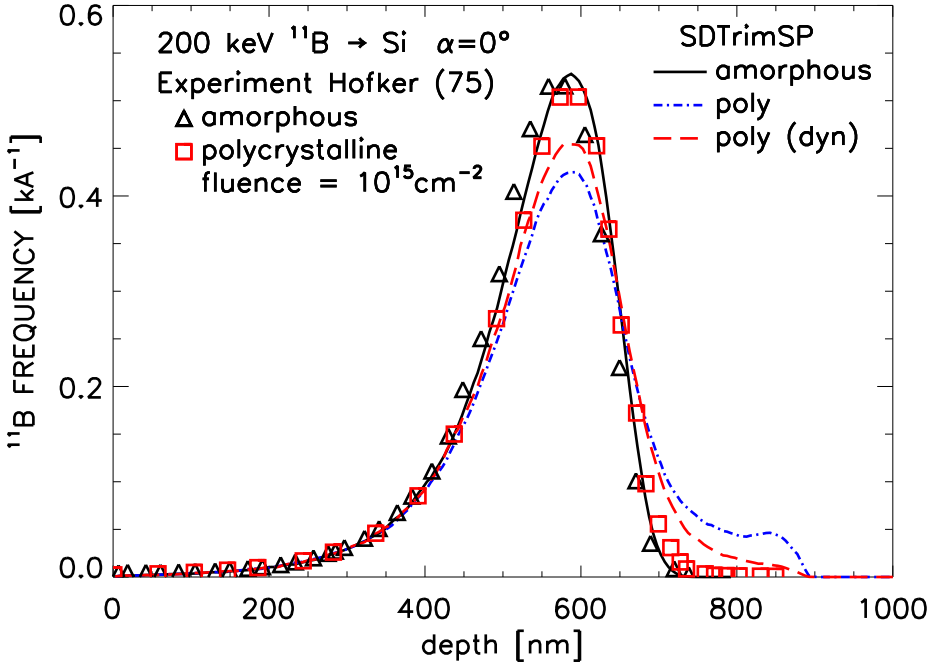

Figure 102: Comparison calculated profile with measurements [68] B^{11} on Si

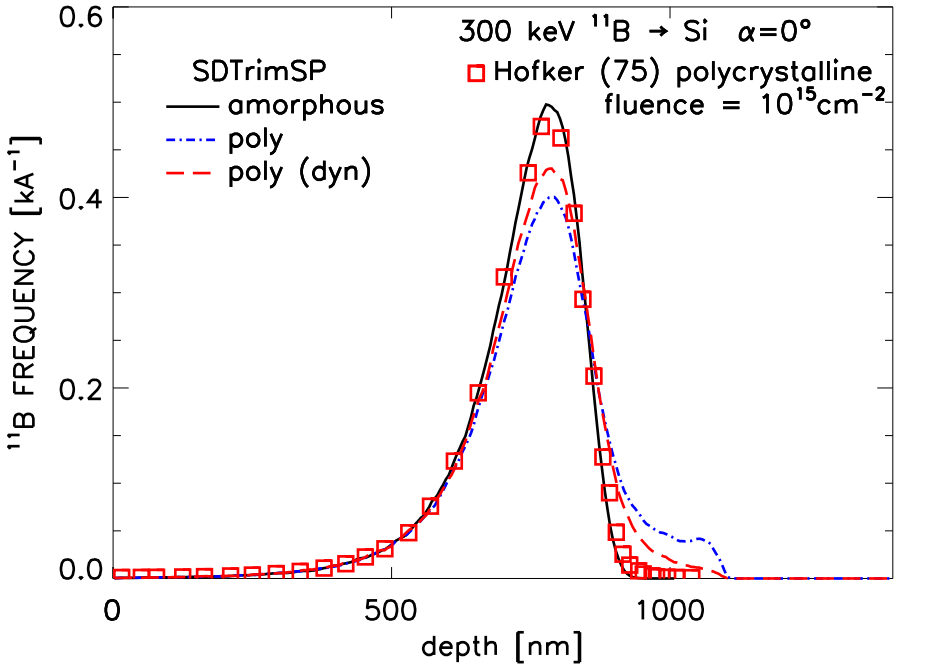

Figure 103: Comparison calculated profile with measurements [68] B^{11} on Si

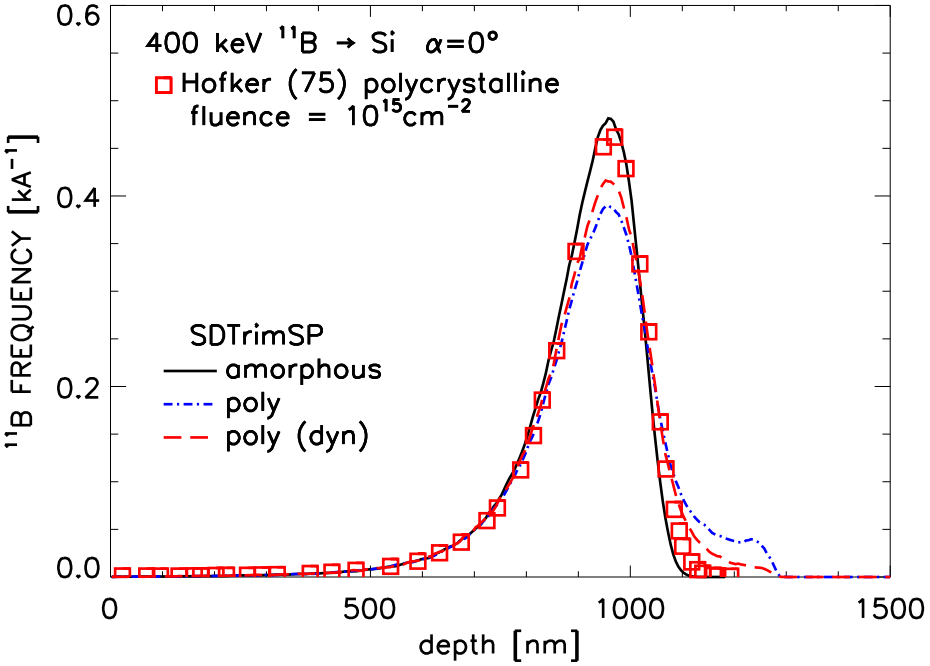

Figure 104: Comparison calculated profile with measurements [68] B^{11} on Si

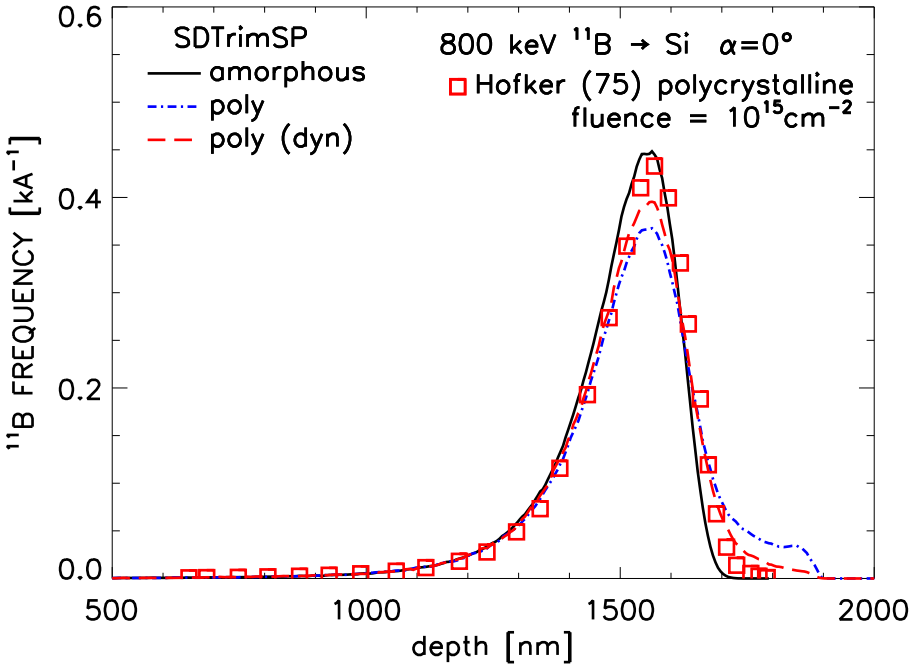

Figure 105: Comparison calculated profile with measurements [68] B^{11} on Si

8.4. Compare experimental with calculated profiles He on Fe bcc-crystal

If all incident atoms stop in the target the integral of the measured He-profile should be the fluence. It was use adjusted values of fluence to better compare the measured profiles with calculation (Statement of the author: $fluence = 1.0\ 10^{16} cm^{-2}$).

$$\begin{aligned} fluence &\geq \int He_{number\ density}\, dx \\ &\approx 1.15\ 10^{16} cm^{-2} \quad Fig.\ 106 \\ &\approx 1.05\ 10^{16} cm^{-2} \quad Fig.\ 107 \end{aligned} \tag{8.82}$$

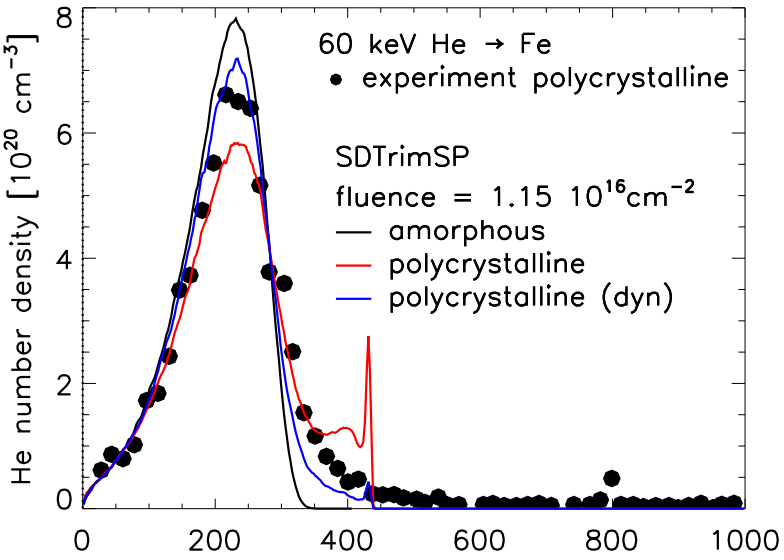

Figure 106: Comparison calculated profile with measurements [74] He on Fe

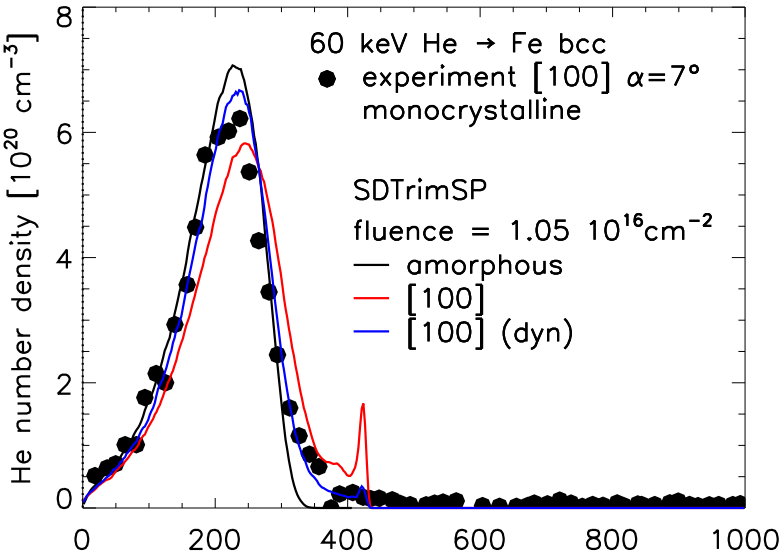

Figure 107: Comparison calculated profile with measurements [74] He on Fe

9. Comparison of calculated and measured values of amorphous-target

9.1. Z on B (yield)

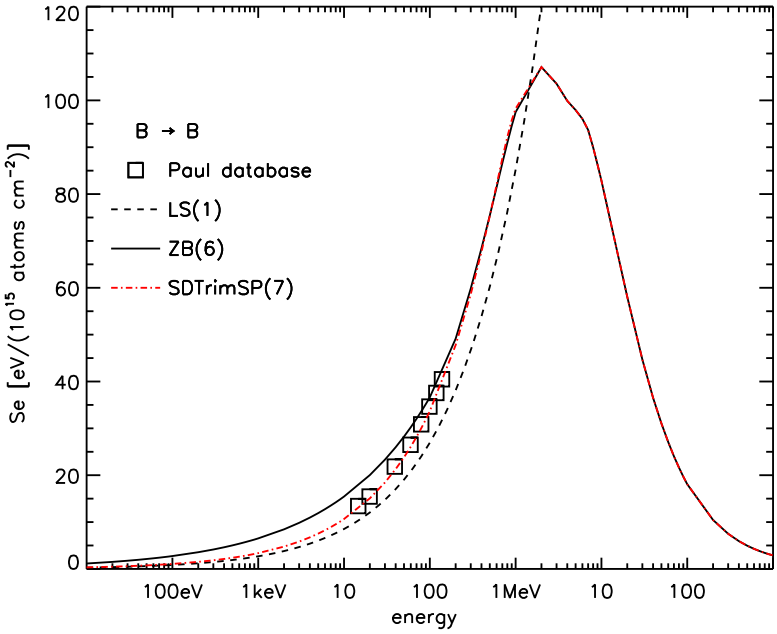

Figure 108: Electronic stopping power dependent on energy B on B with measurements [65], $ck_{elec} = 1.25$

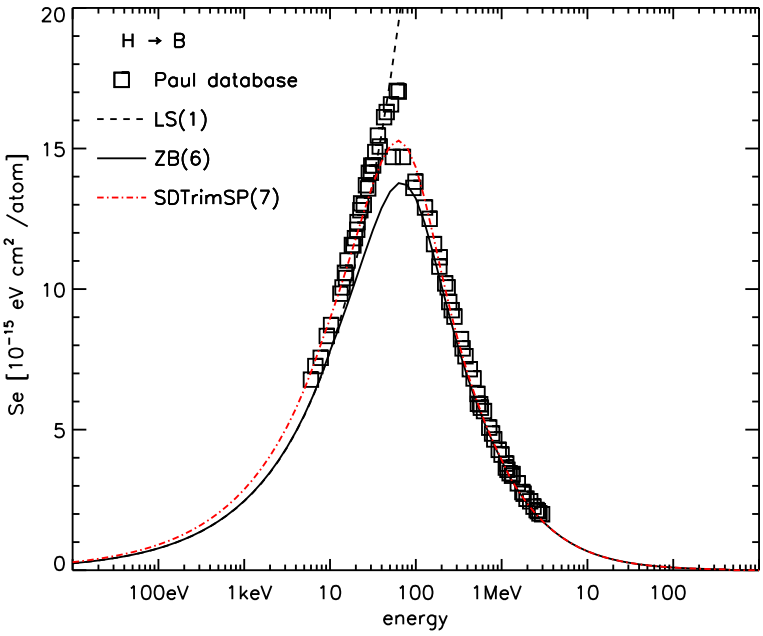

Figure 109: Electronic stopping power dependent on energy H on B with measurements [65], $ck_{elec} \cdot LS_{fak} = 2.886$, $a_2 = 3.236$

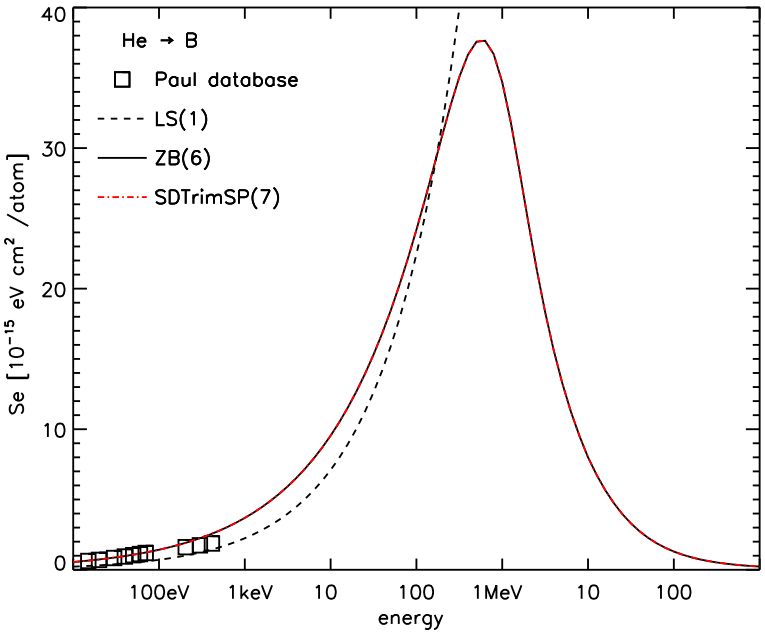

Figure 110: Electronic stopping power dependent on energy He on B with measurements [65]

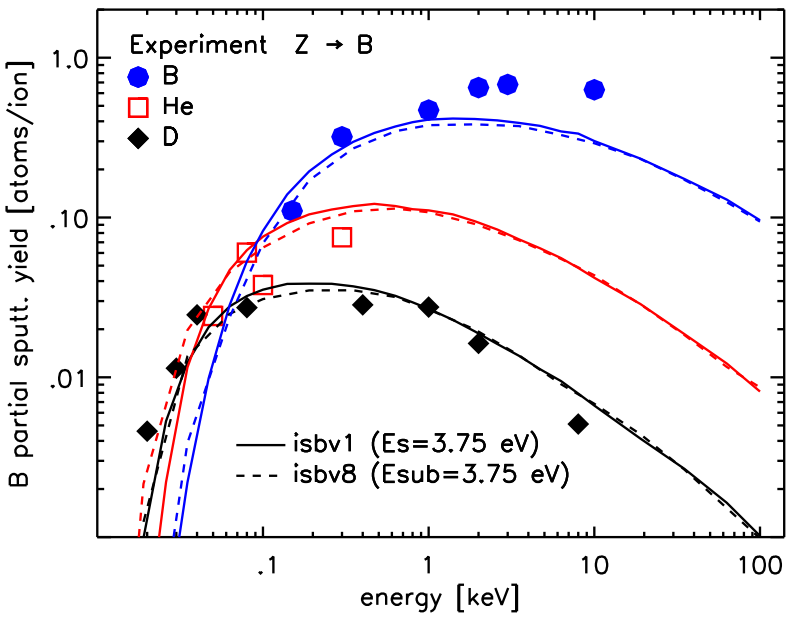

Figure 111: Comparison calculated yield with measurements [28] B on B, He on B and D on B

9.2. Z on C (yield)

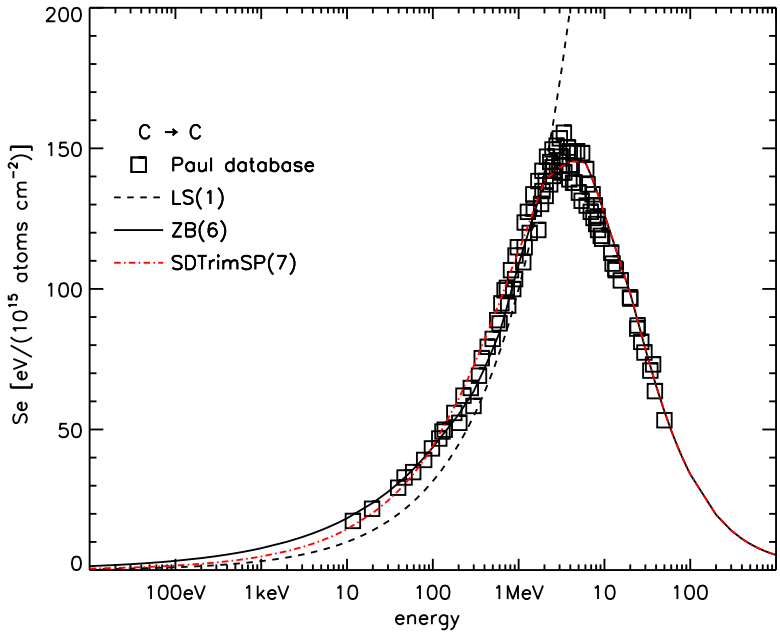

Figure 112: Electronic stopping power dependent on energy C on C with measurements [65], $ck_{elec} = 1.75$, $a_2 = 0.48$

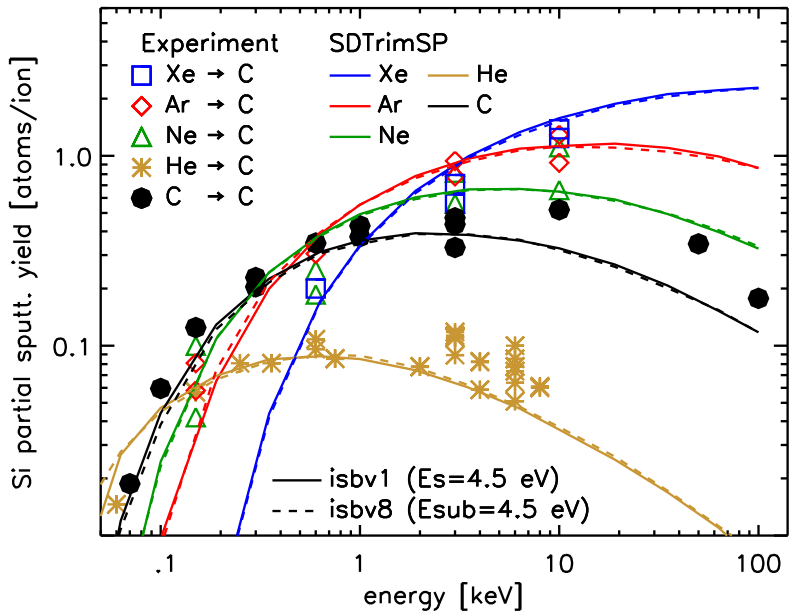

Figure 113: Comparison calculated yield with measurements [28],[76],[51] Z on C incident angle $\alpha = 0°$

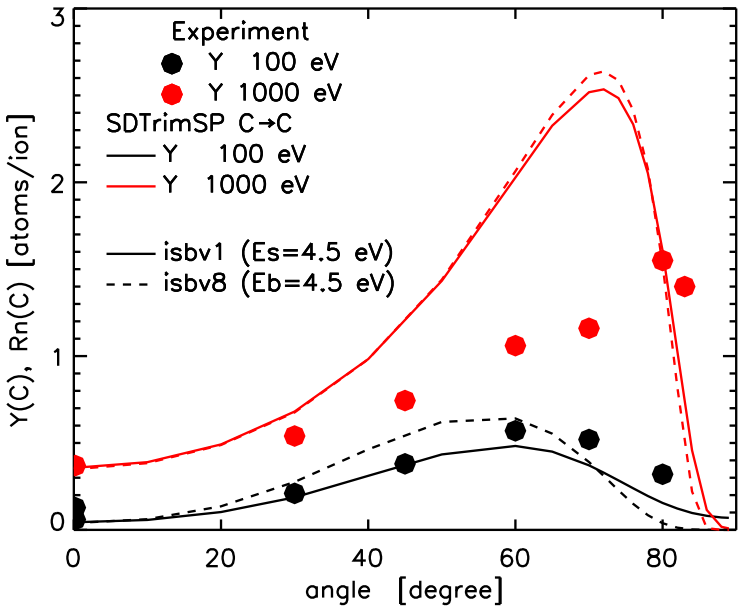

Figure 114: Comparison calculated yield with measurements [28] C on C dependent on incident angle α

9.3. Z on Al (yield)

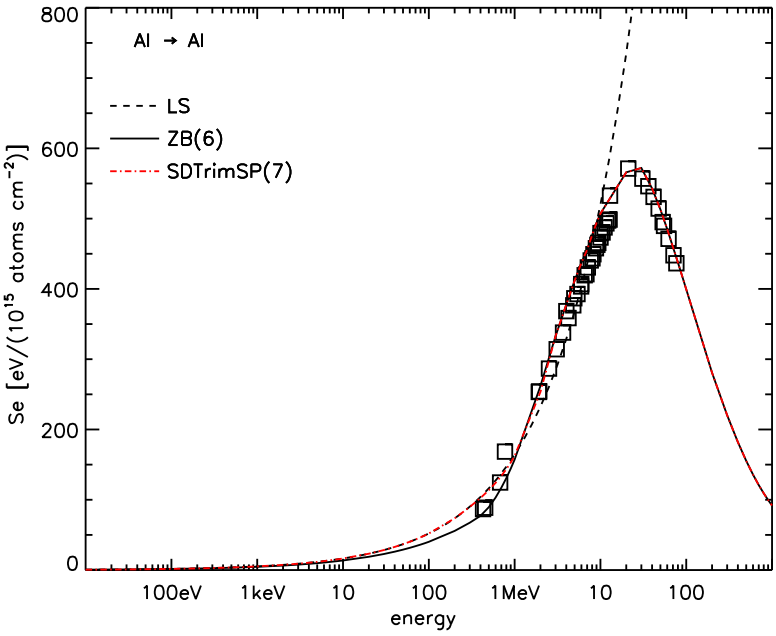

Figure 115: Electronic stopping power dependent on energy Al on Al with measurements [65]

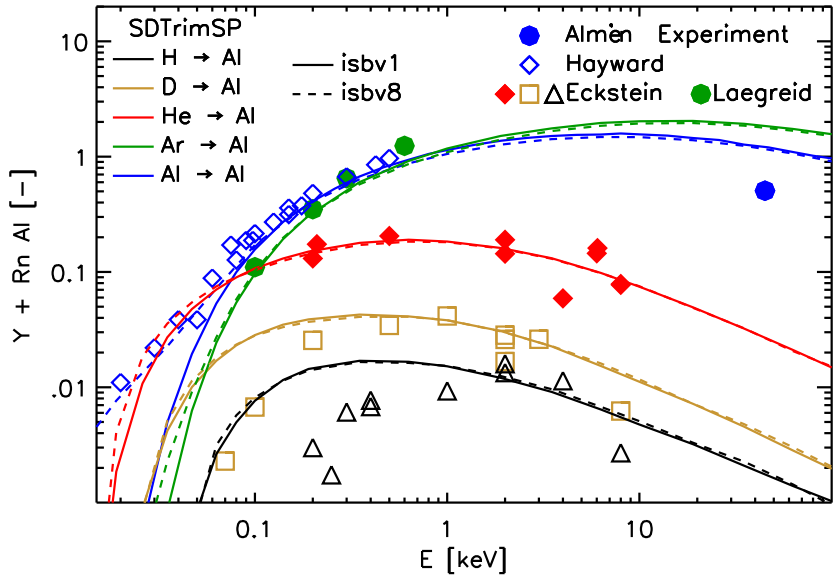

Figure 116: Comparison calculated yield with measurements [28], [51], [77] Al, Ar, He, D and H on Al incident angle $\alpha = 0°$, inel0(H)=4, inel0(He)=5, inel0(Al,Ar)=7 (note of [28]: value of H and D to small 'might be due to oxide formation during sputtering of Al')

9.4. Z on Si (yield, mean depth, implanted profile)

Electronic stopping of $Si \rightarrow Si$ and $B^{11} \rightarrow Si$ see Fig. 51 and Fig. 52.

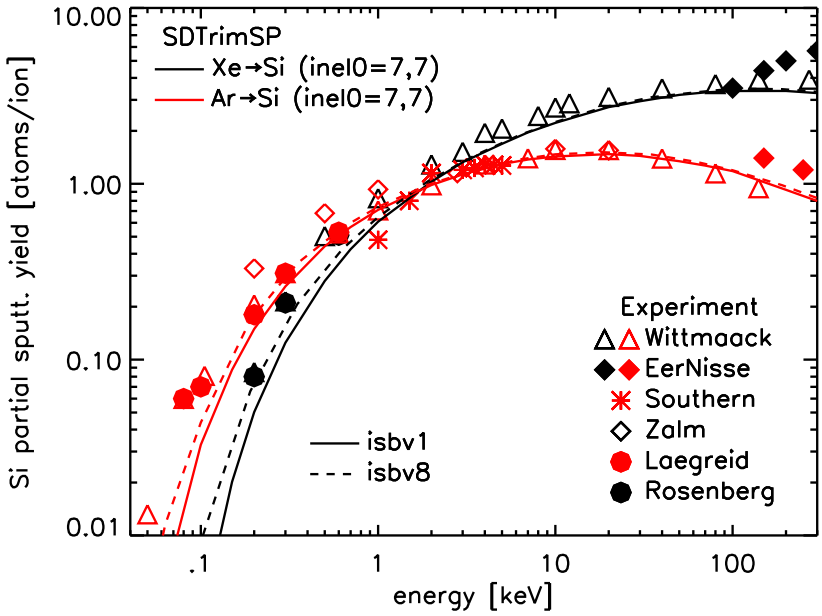

Figure 117: Comparison calculated yield with measurements [31],[32], [78], [46], [79], [82], [83] Ar and Xe on Si incident angle $\alpha = 0°$

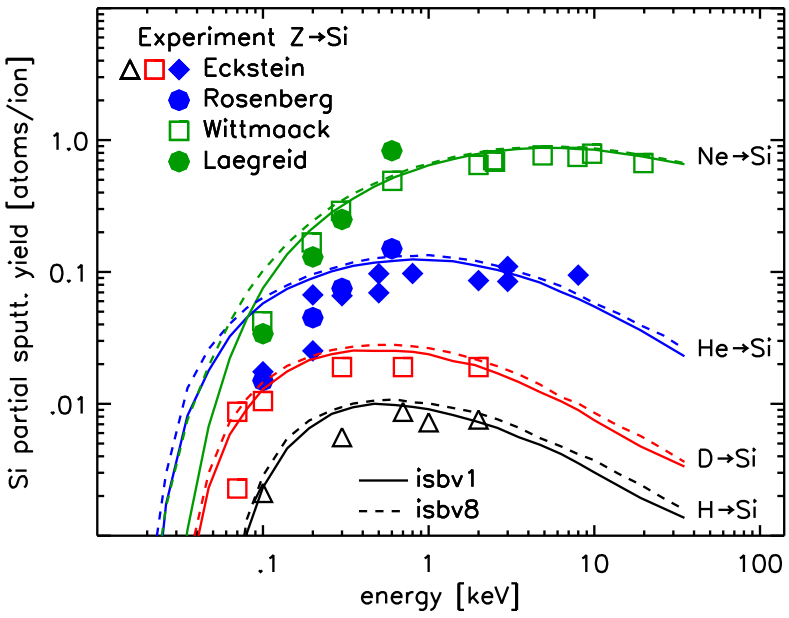

Figure 118: Comparison calculated yield with measurements [28], [32], [82], [83] Z on Si

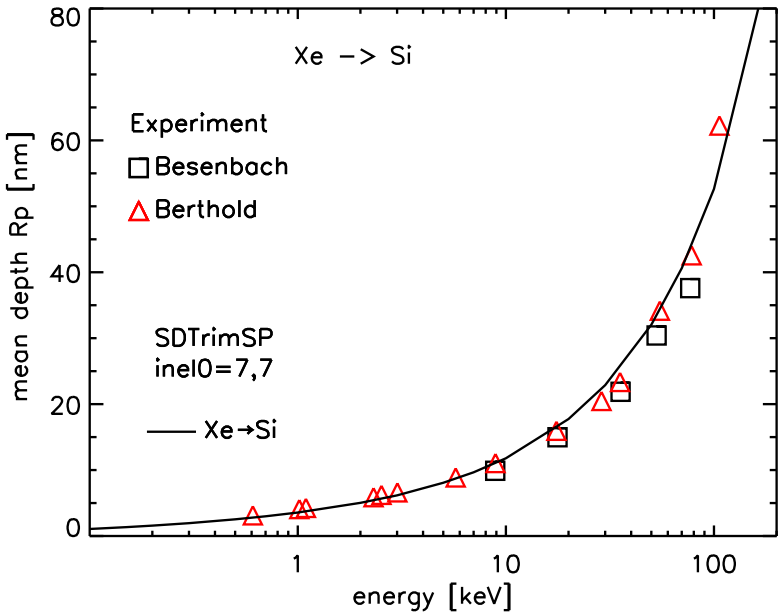

Figure 119: Comparison calculated mean depth R_p with measurements [80], [81] Xe on Si incident angle $\alpha = 0°$

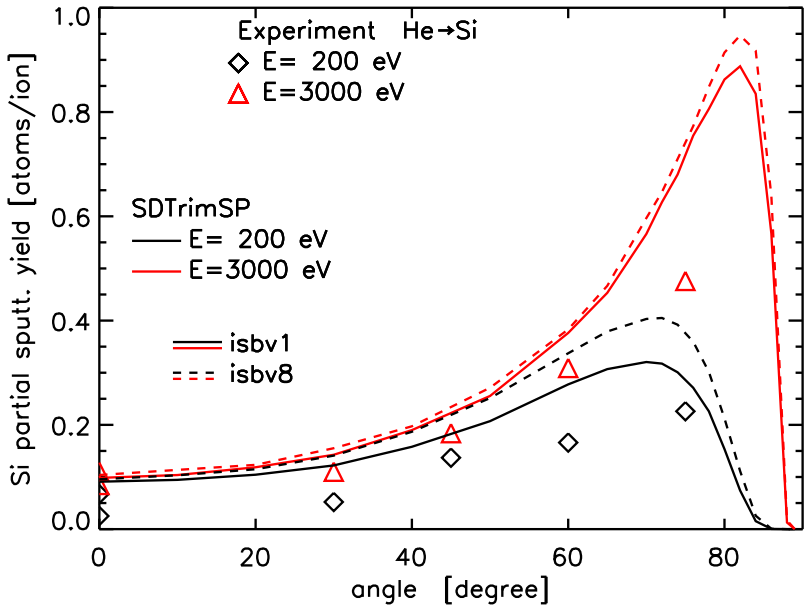

Figure 120: Comparison calculated yield with measurements [28], He Si dependent on incident angle α, inel0(He)=5, inel0(Si)=7

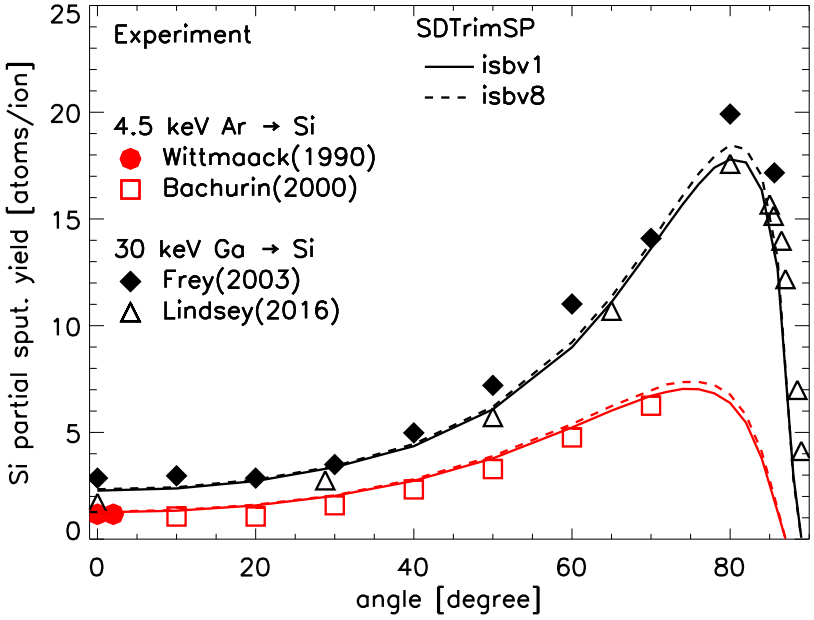

Figure 121: Comparison calculated yield with measurements [84], [85], [86], [84] Ar and Ga on Si dependent on incident angle α

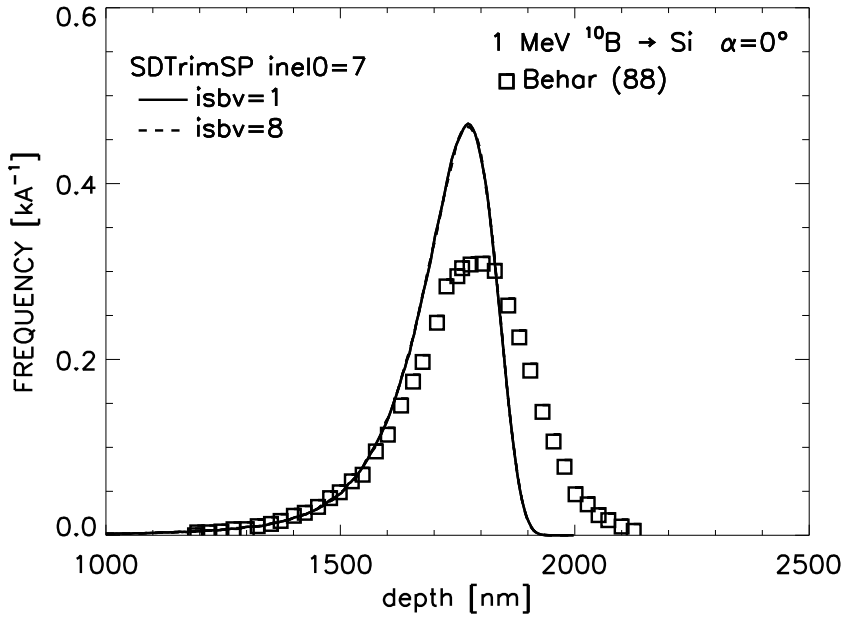

Figure 122: Comparison of calculated boron distributions with measurements [69] 1 MeV B10 on Si

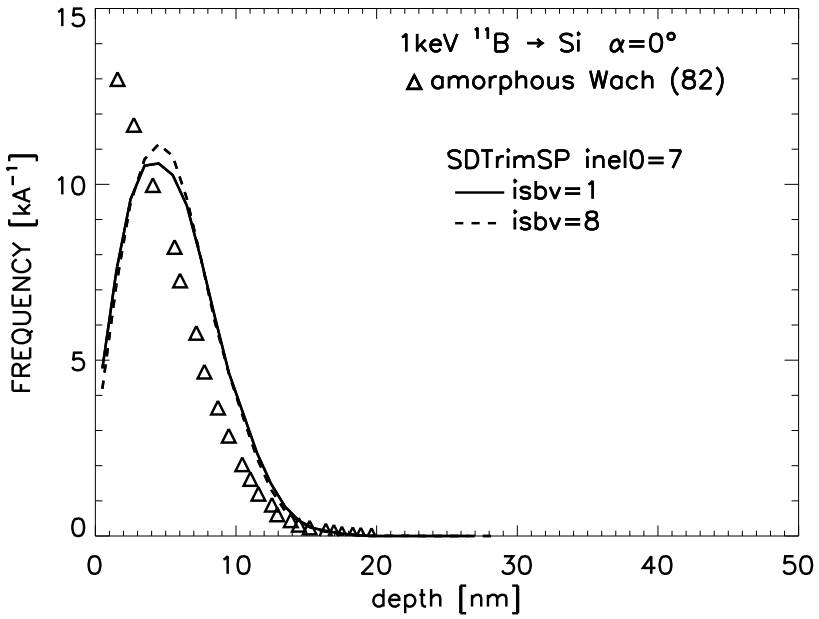

Figure 123: Comparison of calculated boron distributions with measurements [88] 1 keV B11 on Si

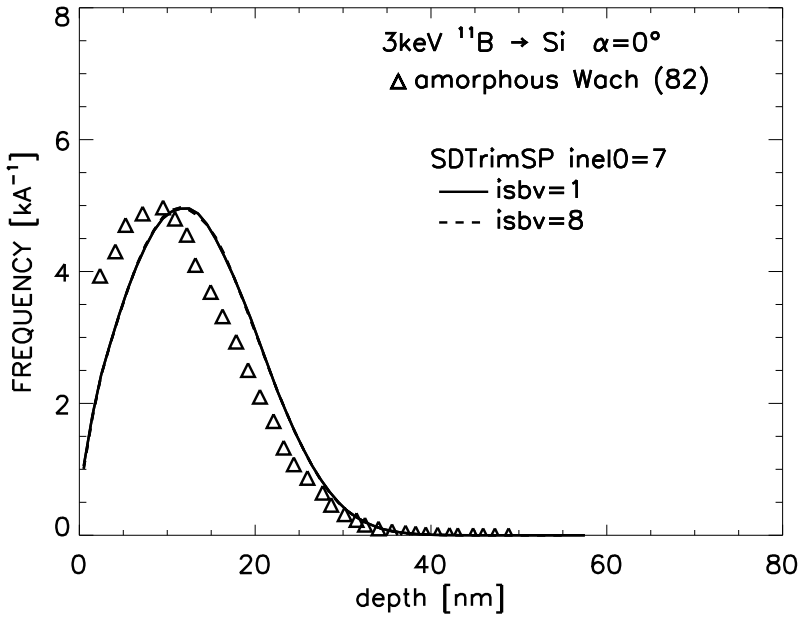

Figure 124: Comparison of calculated boron distributions with measurements [88] 3 keV B11 on Si

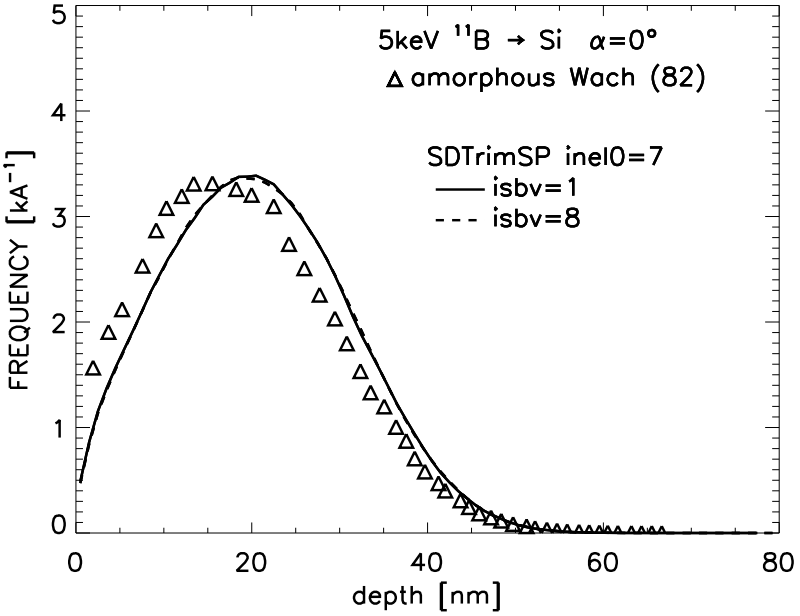

Figure 125: Comparison of calculated boron distributions with measurements [88] 5 keV B11 on Si

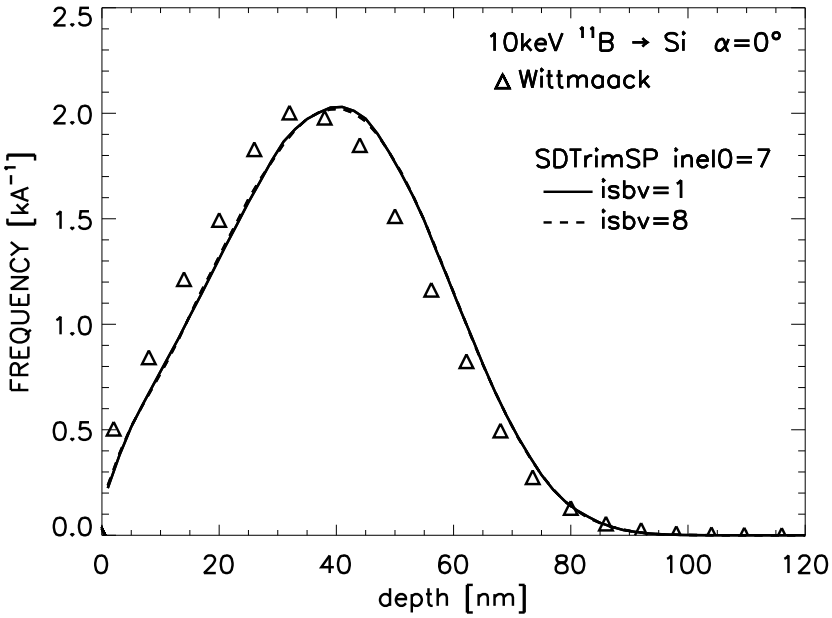

Figure 126: Comparison of calculated boron distributions with measurements 10 keV B11 on Si

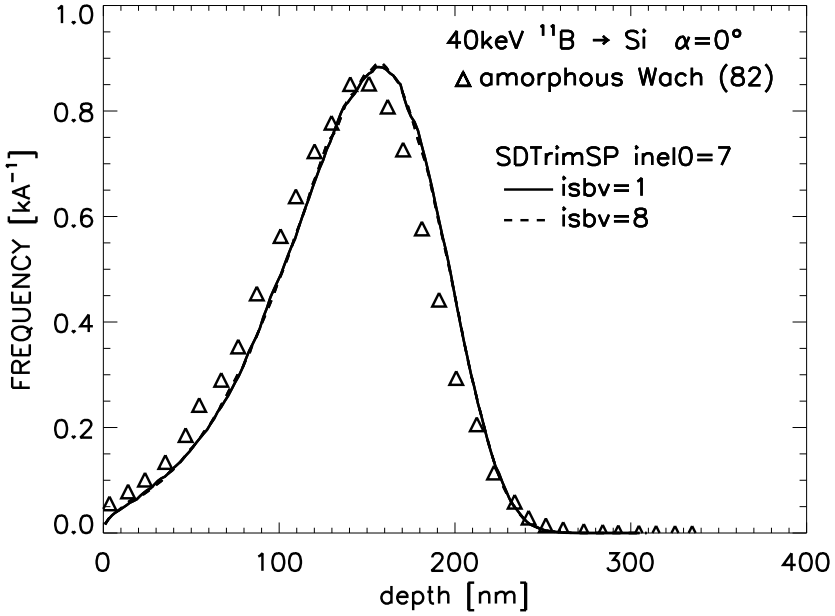

Figure 127: Comparison of calculated boron distributions with measurements [88] 40 keV B11 on Si

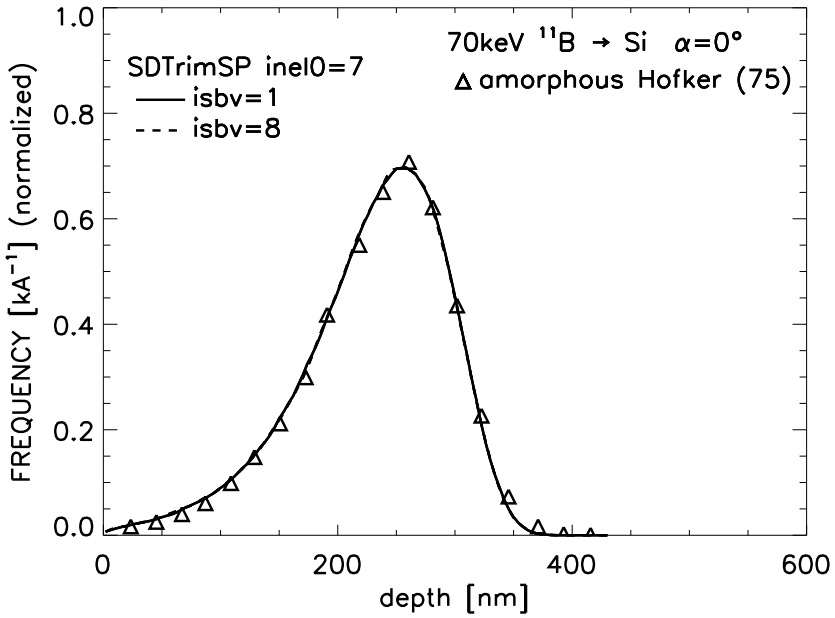

Figure 128: Comparison of calculated boron distributions with measurements [68] 70 keV B11 on Si

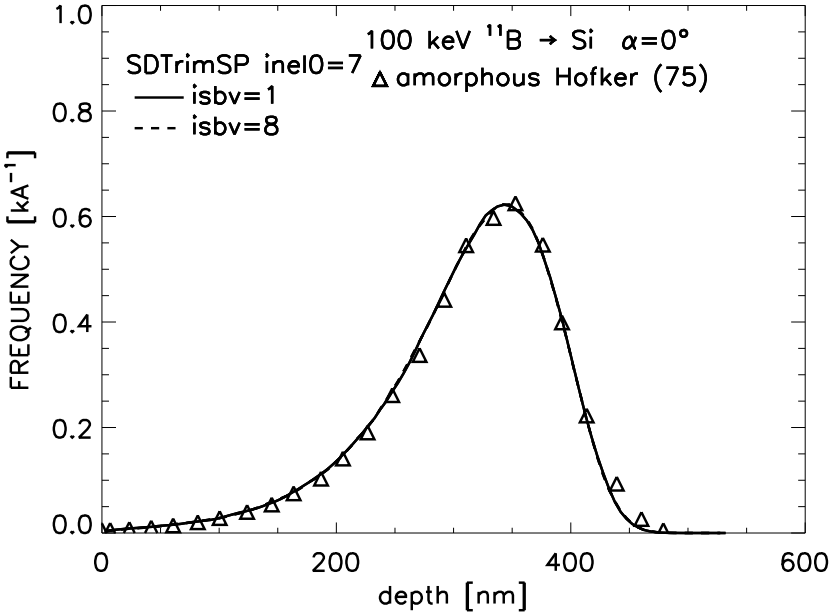

Figure 129: Comparison of calculated boron distributions with measurements [68] 100 keV B11 on Si

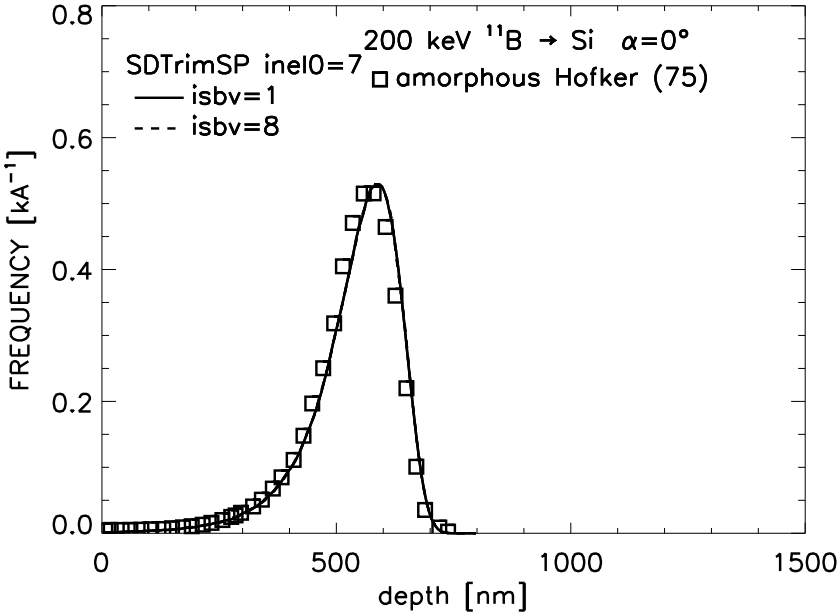

Figure 130: Comparison of calculated boron distributions with measurements [68] 200 keV B11 on Si

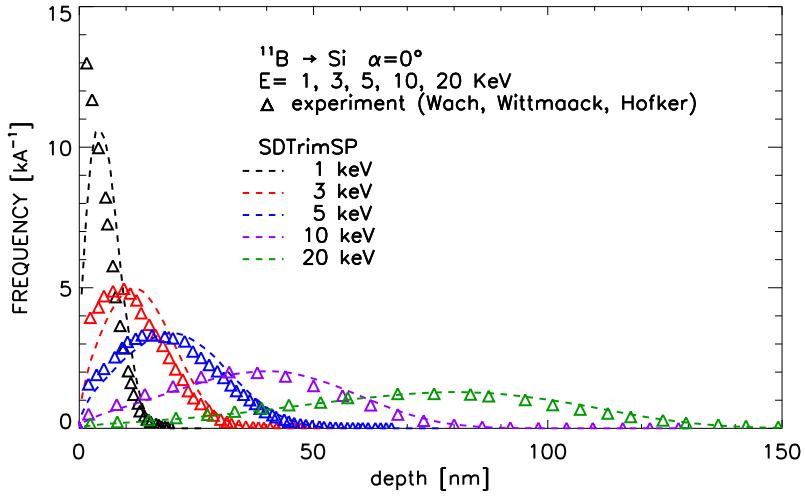

Figure 131: Comparison calculated profile with measurements B11 on amorphous Si, small incident energy (summary Fig. 123 - 126 + 20keV)

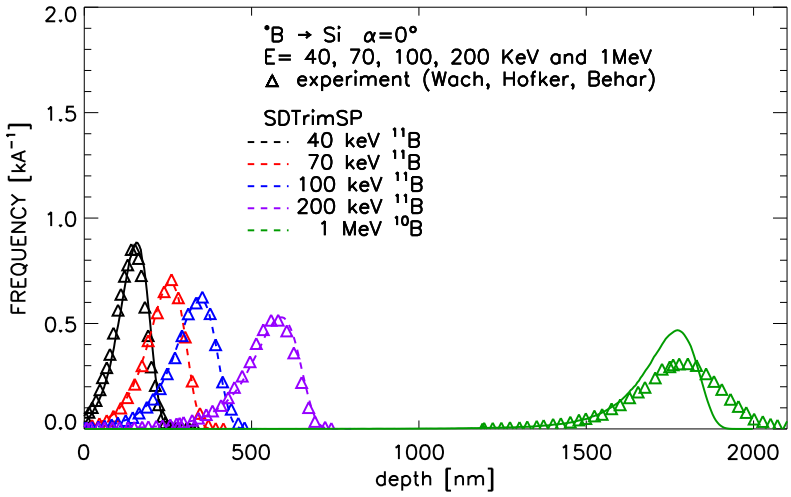

Figure 132: Comparison calculated profile with measurements B11/B10 on amorphous Si, high incident energy (summary Fig. 127 - 130 + Fig. 122

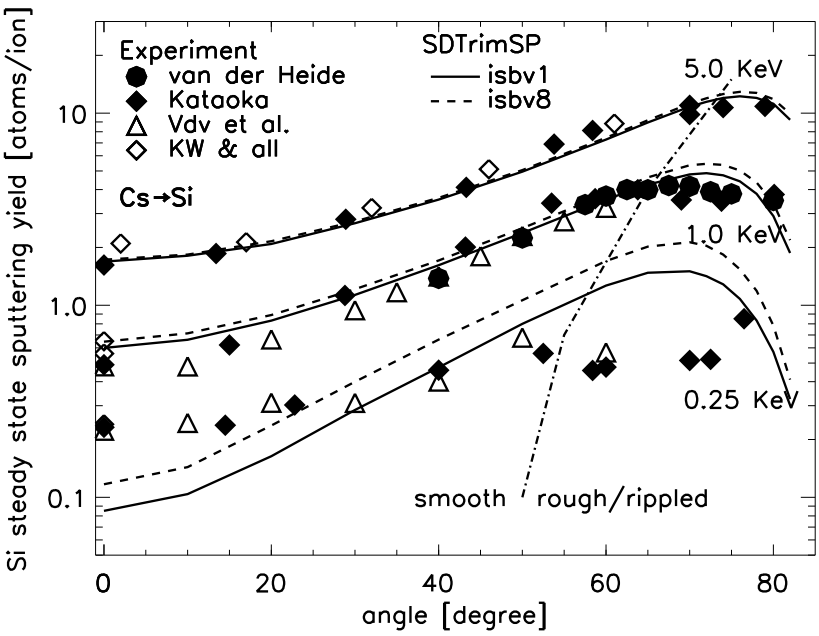

Figure 133: Comparison calculated yield with measurements [89],[90],[91] Cs on Si depend on different incident angle α

9.5. Z on Ti (yield)

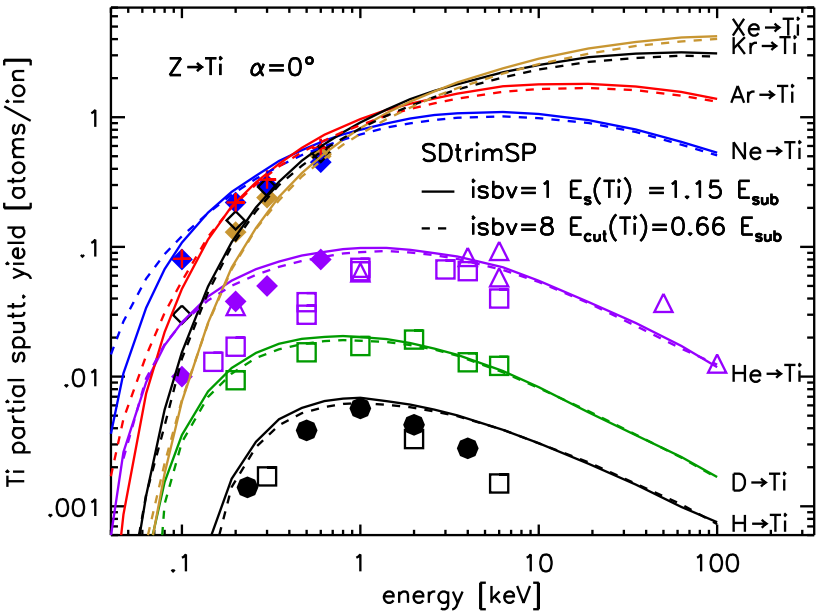

Figure 134: Comparison calculated yield with measurements [28], [92], [82], [83] Xe, Kr, Ne, He, D, H on Ti incident angle $\alpha = 0°$, inel0(Xe,Kr,Ar,Ne)=7, inel0(He)=5, inel0(D,H)=4

9.6. Z on Ni (yield)

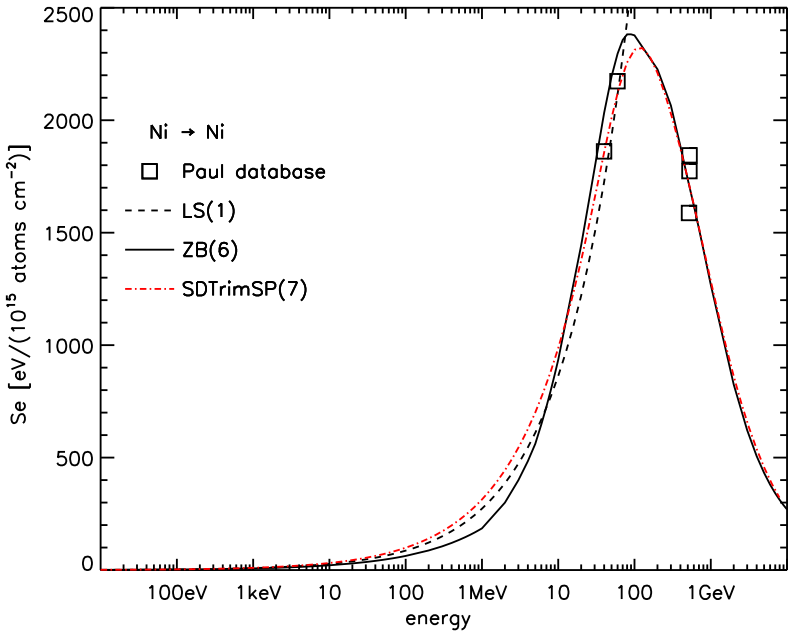

Figure 135: Electronic stopping power dependent on energy Ni on Ni with measurements [65]

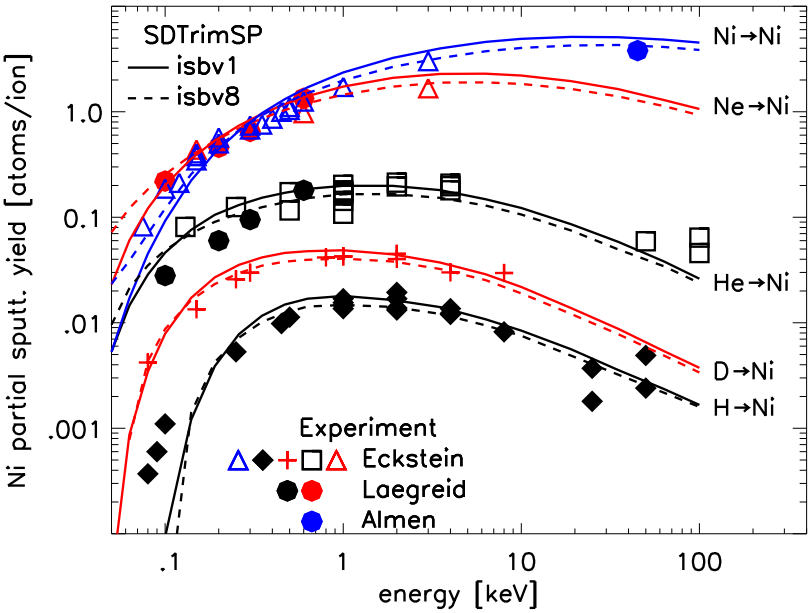

Figure 136: Comparison calculated yield with measurements [28], [82], [83] Ni, Ne, He, D and H on Ni incident angle $\alpha = 0°$, inel0(H)=4, inel0(He)=5, inel0(Ni,Ne)=7, Note: if Ni on Ni (Y+Rn) was drawn

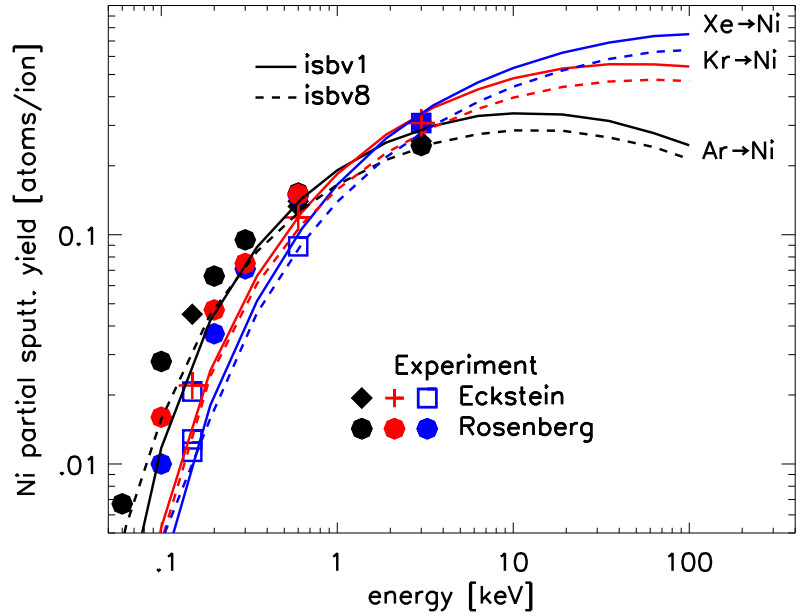

Figure 137: Comparison calculated yield with measurements [28], [82], Xe, Kr, Ar on Ni incident angle $\alpha = 0°$, inel0(Xe,Kr,Ar,Ni)=7

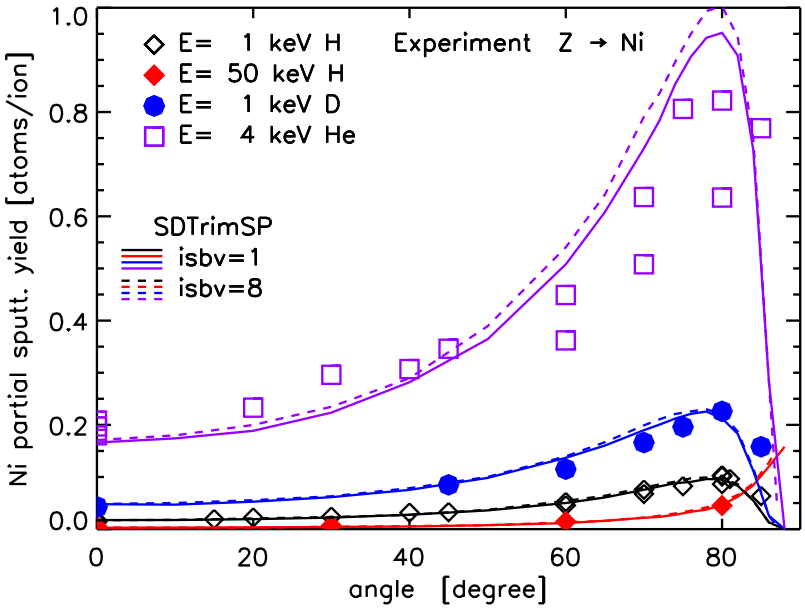

Figure 138: Comparison calculated yield with measurements [28], H, D, He on Ni dependent on incident angle α, inel0(H,D)=4, inel0(He)=5, inel0(Ni)=7

9.7. Z on Cu (yield)

The electronic stopping power of Cu-Cu dependent on energy see Fig. 49.

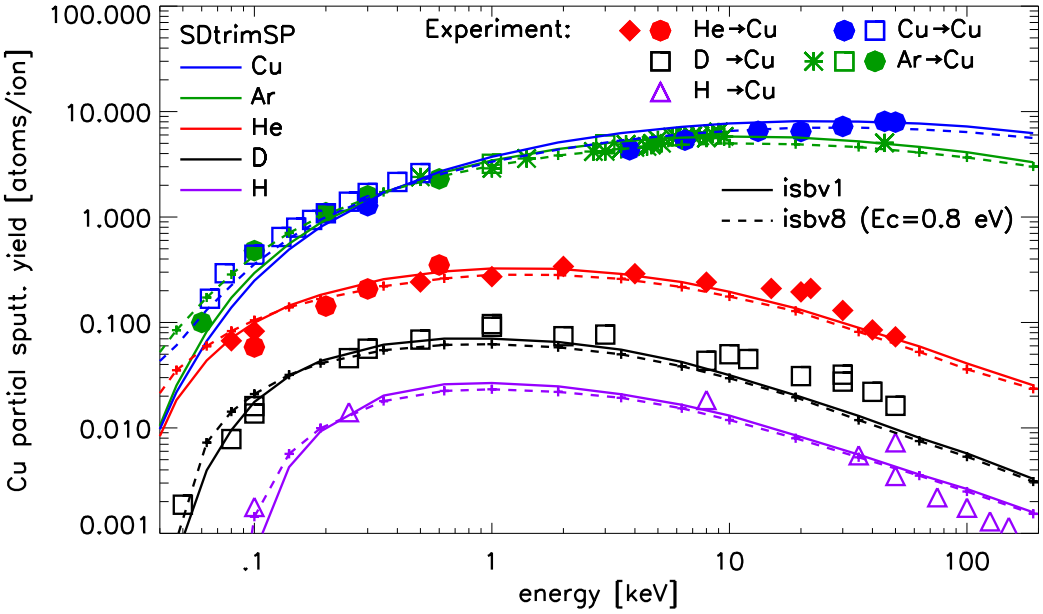

Figure 139: Comparison calculated yield with measurements [28], [51], [52], [77], [83], [98] Cu, Ar, He, D and H on Cu incident angle $\alpha = 0°$, inel0(Cu,Ar)=7, inel0(He)=5, inel0(H,D)=4

9.8. Z on Mo (yield and reflection coefficient Rn)

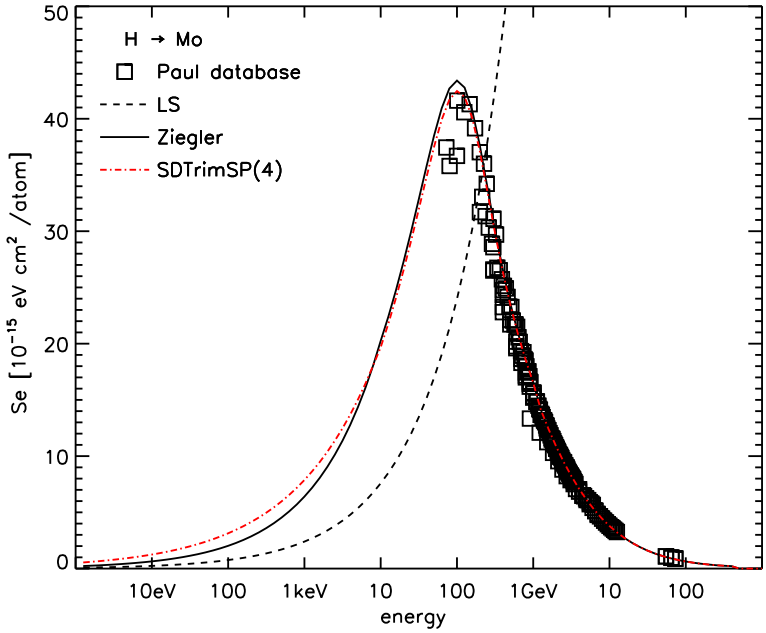

Figure 140: Electronic stopping power dependent on energy H on Mo with measurements [65], $a_1 = 7.900$, $a_2 = 0.40$

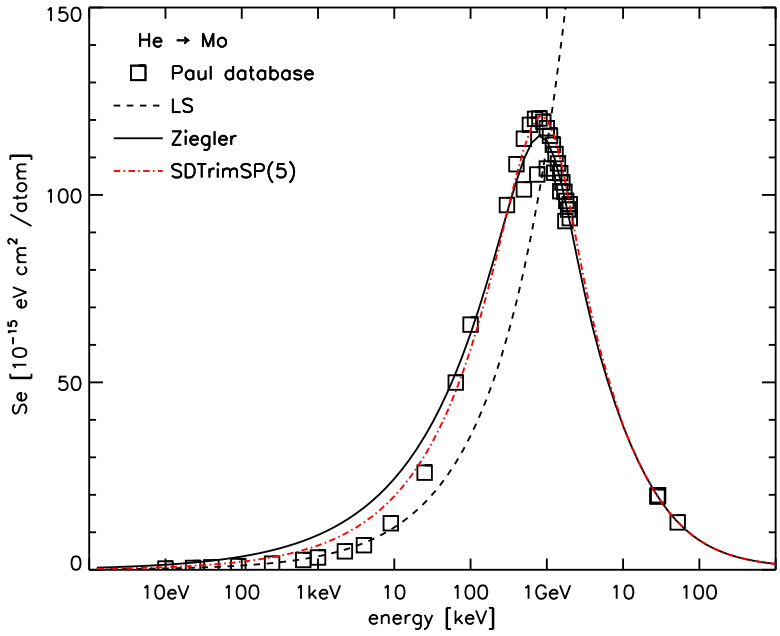

Figure 141: Electronic stopping power dependent on energy He on Mo with measurements [65], $a_1 = 6.50$, $a_2 = 0.50$

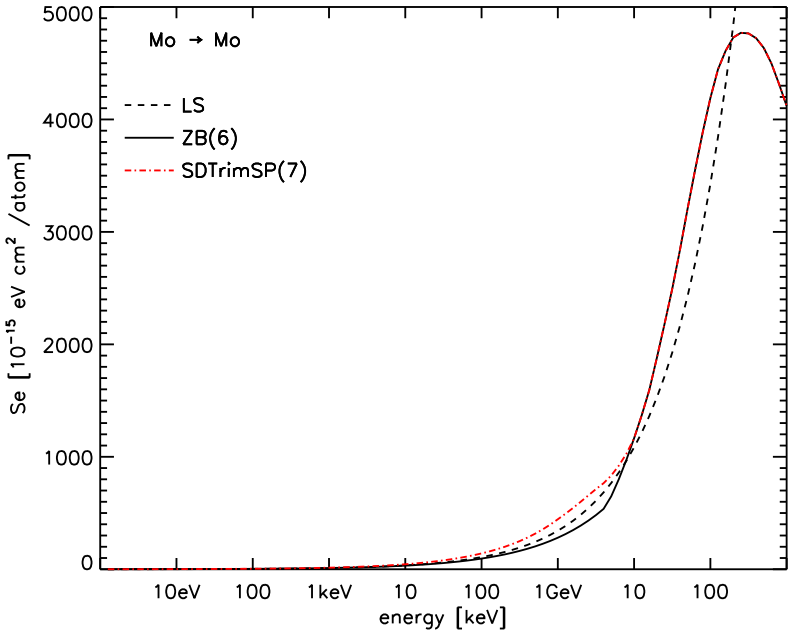

Figure 142: Electronic stopping power dependent on energy Mo on Mo, $ck_{elec} = 1.30$, $a_2 = 0.50$

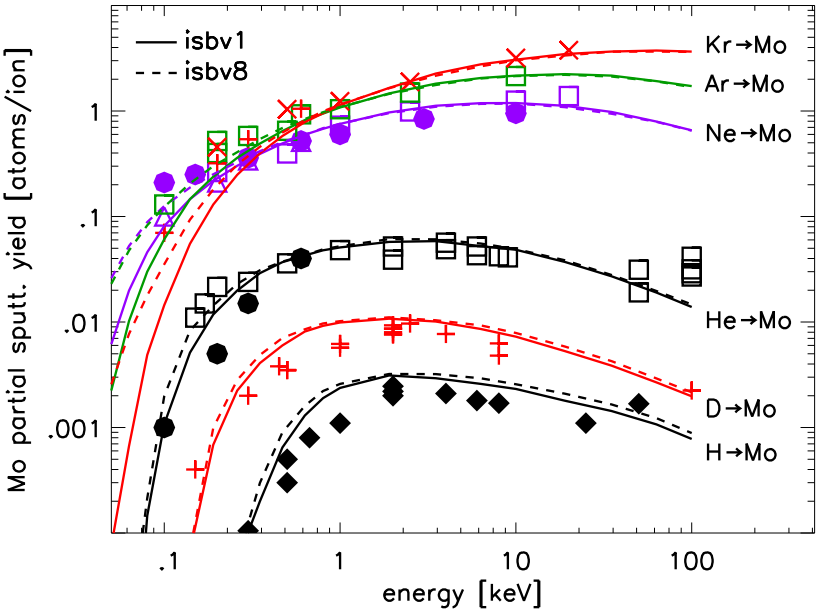

Figure 143: Comparison calculated yield with measurements [28], [92], [82],[83], [79], Kr, Ar, Ne, He, D and H on Mo incident angle $\alpha = 0°$, inel0(Kr,Ar,Ne,Mo)=7, inel0(He)=5, inel0(H)=4

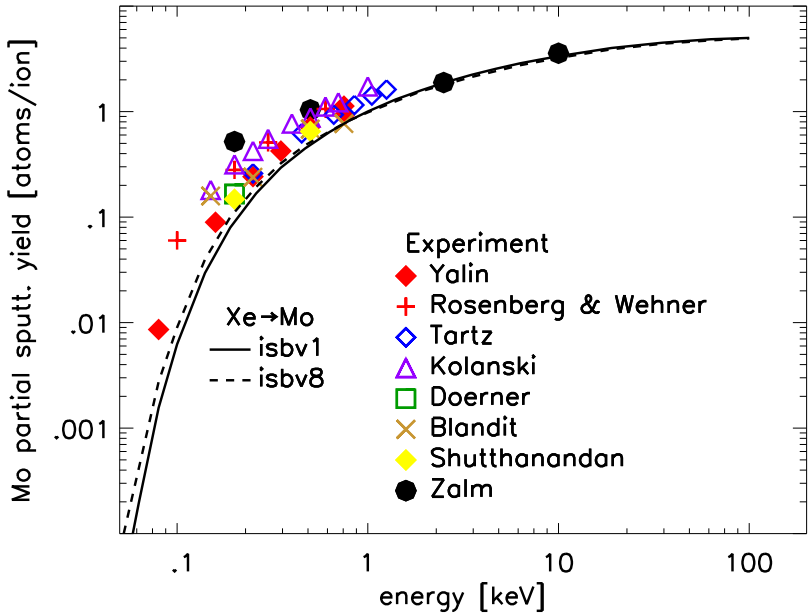

Figure 144: Comparison calculated yield with measurements [93], [82], [79], Xe on Mo incident angle $\alpha = 0°$, inel0(Xe)=7

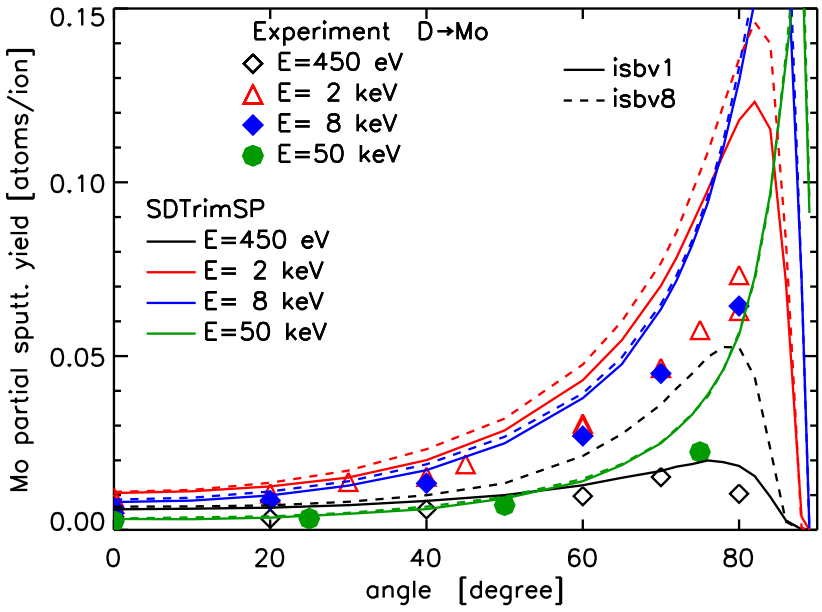

Figure 145: Comparison calculated yield with measurements [28], D on Mo dependent on incident angle α, inel0(Mo)=7, inel0(D)=4

9.9. K on Mo (reflection coefficient Rn)

Reflection coefficient (Rn) K on Mo dependent on energy see Fig. 40

9.10. Z on Ta (yield)

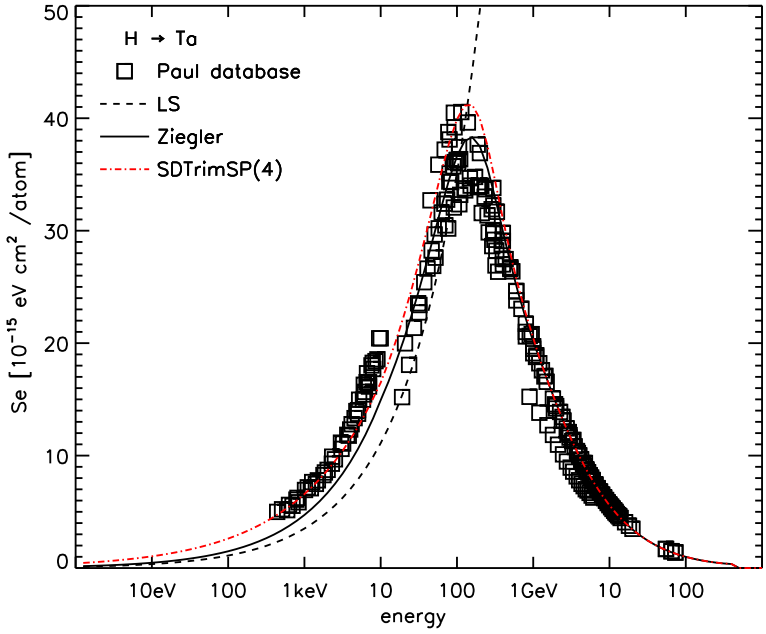

Figure 146: Electronic stopping power dependent on energy H on Ta with measurements [65], $a_1 = 6.60$, $a_2 = 0.40$,

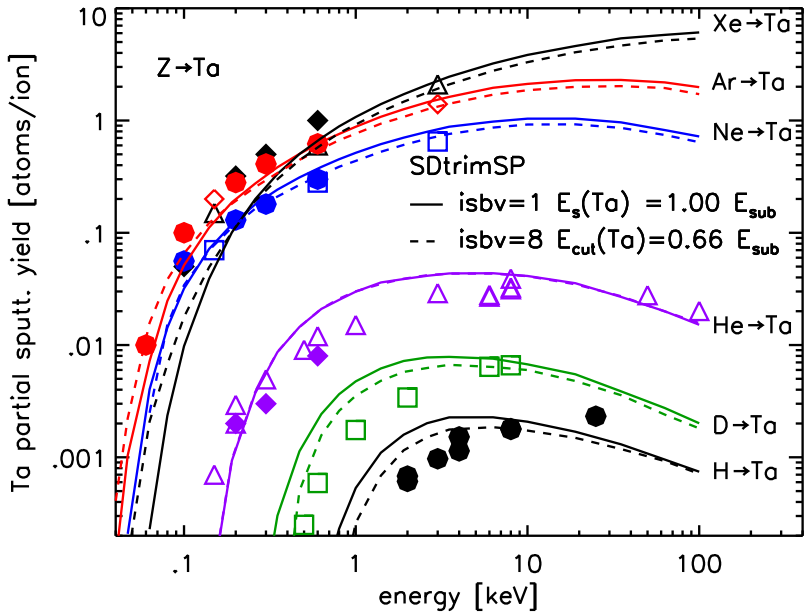

Figure 147: Comparison calculated yield with measurements [28], [82],[83] Xe, Ar, Ne, He, D and H on Ta incident angle $\alpha = 0°$, inel0(Xe,Ar,Ne,Ta)=7, inel0(He)=5, inel0(H,D)=4

9.11. Z on W (yield)

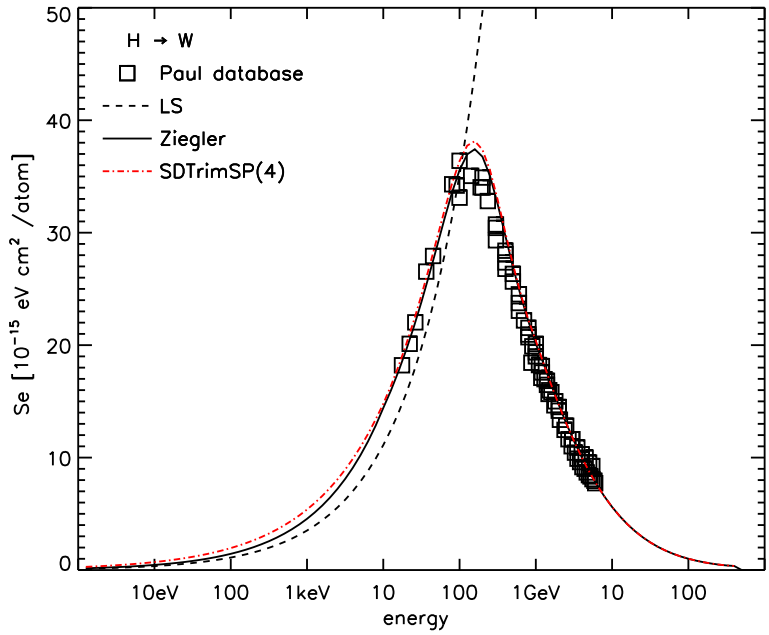

Figure 148: Electronic stopping power dependent on energy H on W with measurements [65], $a_1 = 5.400$, $a_2 = 0.44$

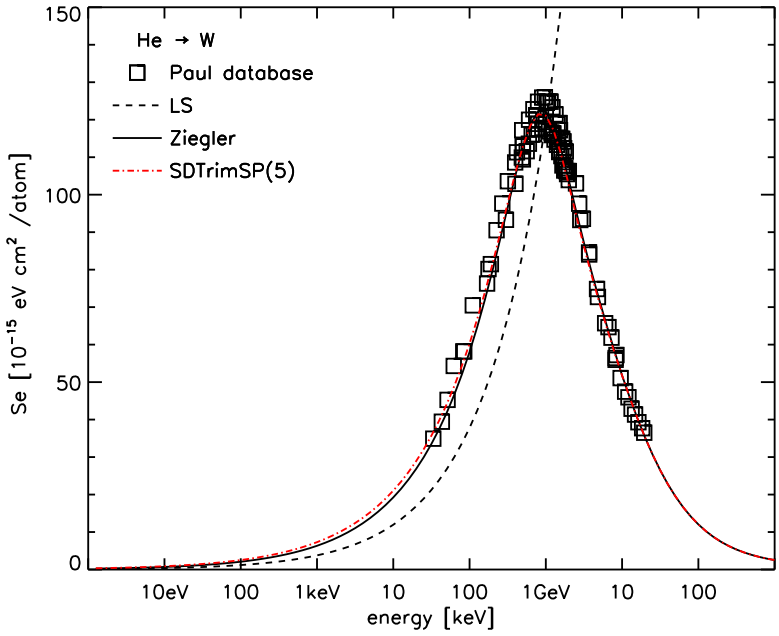

Figure 149: Electronic stopping power dependent on energy He on W with measurements [65], $a_1 = 7.30$, $a_2 = 0.46$

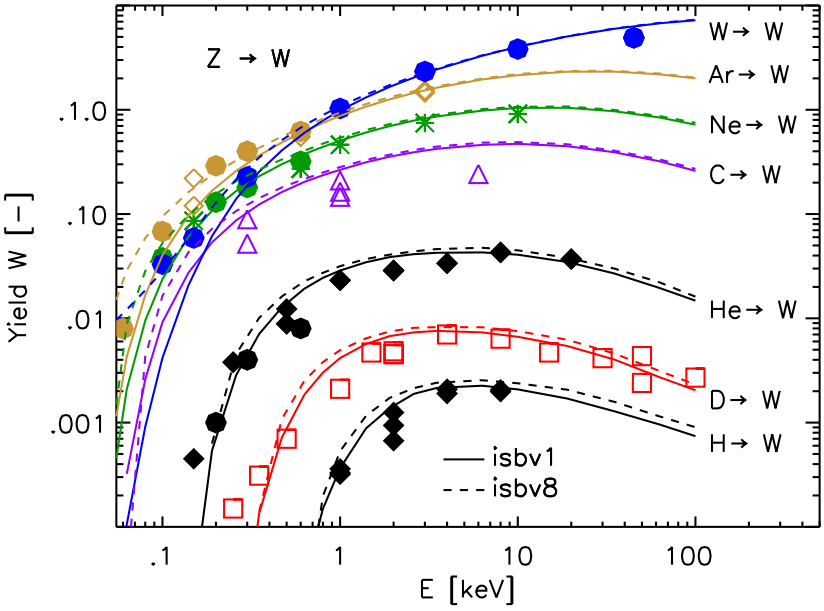

Figure 150: Comparison calculated yield with measurements [28], [92], [82], [83], [51] W, Ar, Ne, C, He, D and H on W incident angle $\alpha = 0°$, inel0(W,Ar,Ne,C)=7, inel0(He)=5, inel0(H)=4

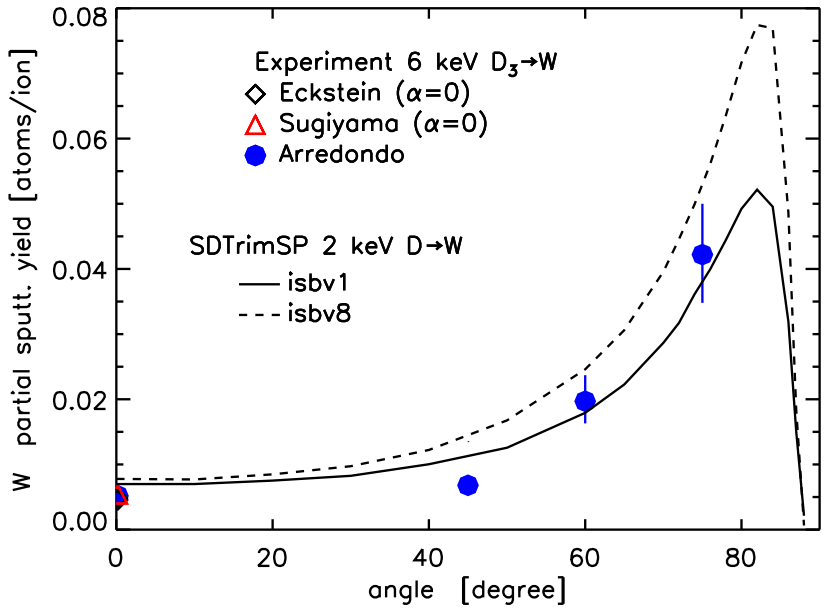

Figure 151: Comparison calculated yield with measurements [28], [94], [95] D on W dependent on incident angle α, inel0(W)=7, inel0(D)=4

9.12. D on W (reflection coefficient Rn)

See Fig. 42 and Fig. 43

9.13. Z on Au (yield)

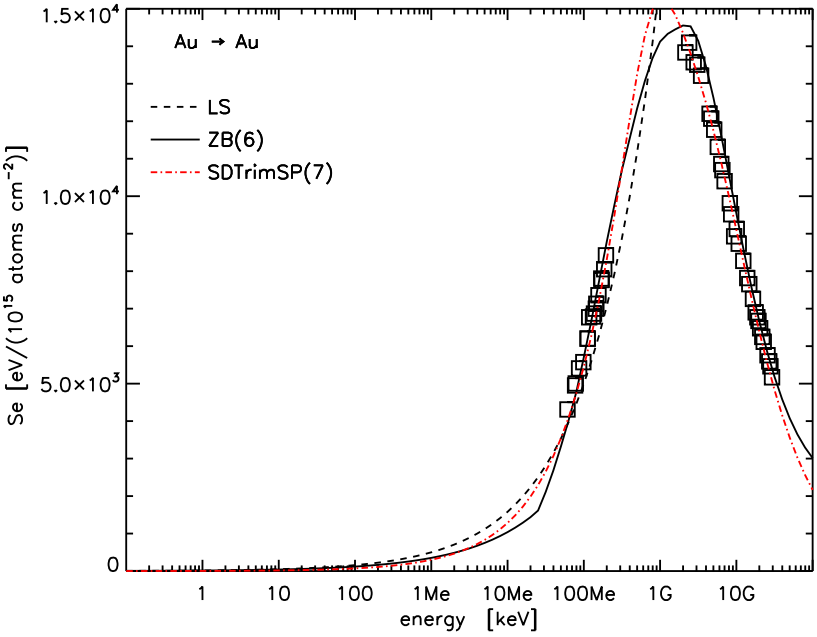

Figure 152: Electronic stopping power dependent on energy Au on Au with measurements [65], $ck_{elec} == 0.10$, $a_2 = 0.63$,

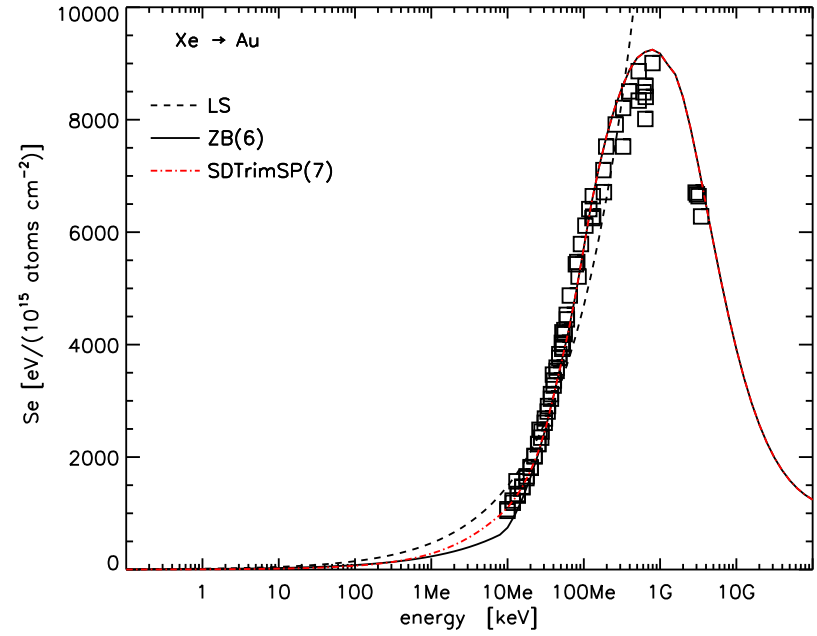

Figure 153: Electronic stopping power dependent on energy Xe on Au with measurements [65], $ck_{elec} = 0.10$, $a_2 = 0.63$,

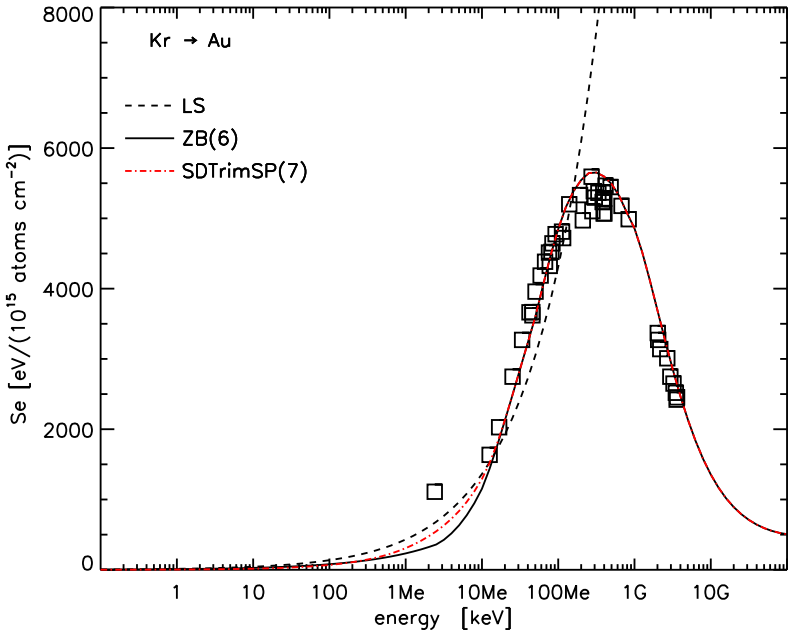

Figure 154: Electronic stopping power dependent on energy Kr on Au with measurements [65], $ck_{elec} = 0.10$, $a_2 = 0.63$,

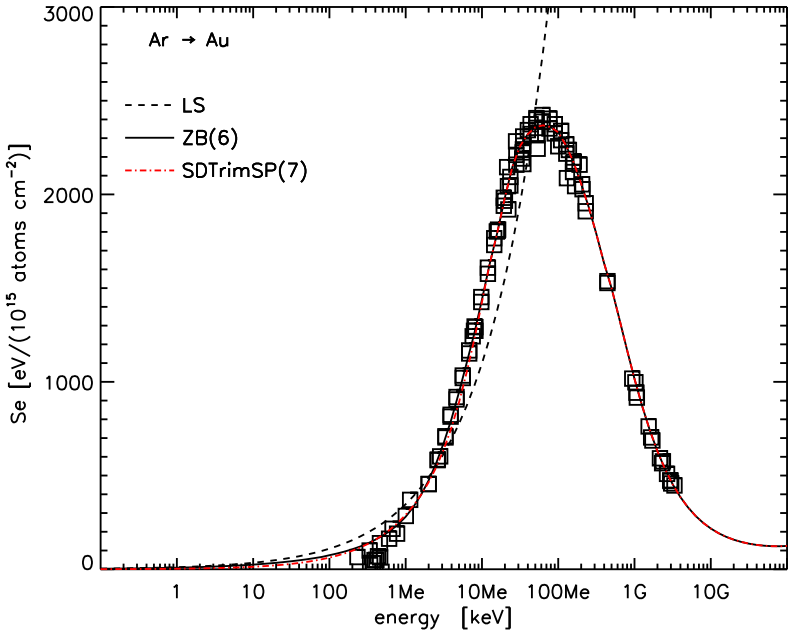

Figure 155: Electronic stopping power dependent on energy Ar on Au with measurements [65], $ck_{elec} = 0.09$, $a_2 = 0.65$,

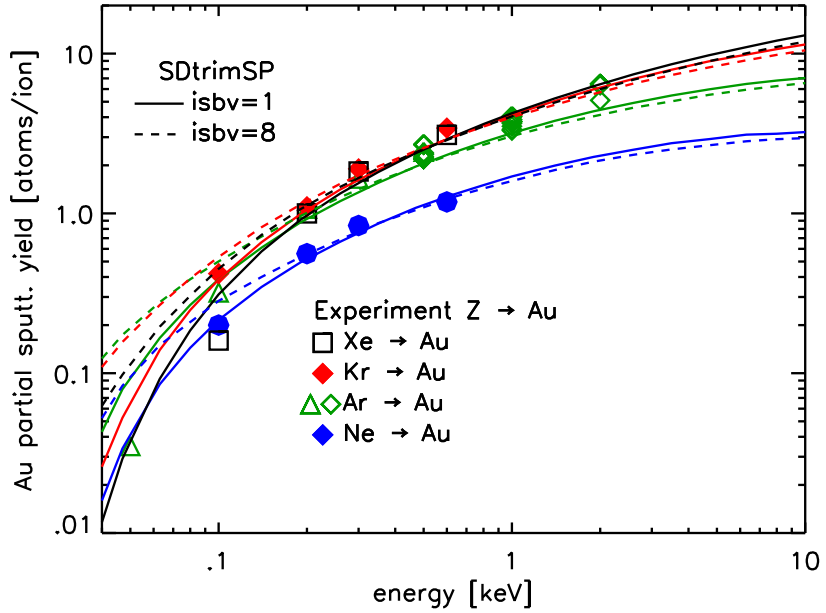

Figure 156: Comparison calculated yield with measurements [82], [83], [96] Xe, Kr, Ar and Ne on Au incident angle $\alpha = 0°$,inel0=7

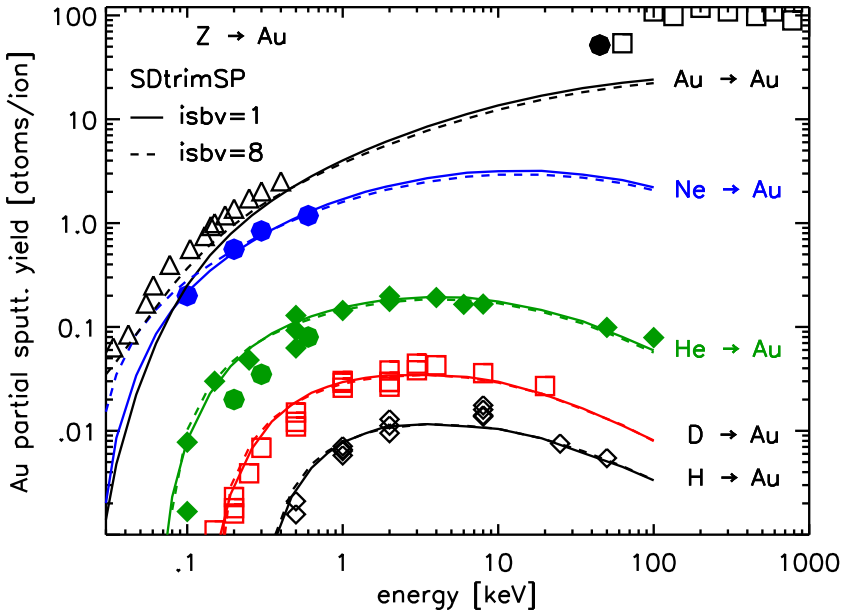

Figure 157: Comparison calculated yield with measurements [28], [82], [83], [77], [97] Au, Ne, He, D and H on Au incident angle $\alpha = 0°$, inel0(Au,Ne)=7, inel0(He)=5, inel0(H,D)=4

9.14. K on Au (reflection coefficient Rn)

Reflection coefficient (Rn) K on Au dependent on energy see Fig. 41

9.15. Sputter yield of low and high fluence Z-projectiles on Cu

The next example is the determination of sputter yields of Cu under impact of 45 keV ions of various atomic number Z for small and high fluence.

Fig. 159 shows the comparison of measured and calculated yields Z on Cu for low fluence. The fluence are $0.5 \cdot 10^{16}$ $atoms/cm^2$, $1.0 \cdot 10^{16}$ $atoms/cm^2$ and near zero in the static mode. The agreement of the calculated values with the experimental data are very good.

Fig. 160 shows the comparison of measured and calculated yields Z on Cu for high fluence. The fluences are $10{\cdot}10^{16}$ $atoms/cm^2$, $100{\cdot}10^{16}$ $atoms/cm^2$ and $500{\cdot}10^{16}$ $atoms/cm^2$.

In most cases for projectiles with $Z > 23$ the steady state has already been reached for a fluence of $10 \cdot 10^{16}$ $atoms/cm^2$. The agreement of calculated yields with the experimental data is qualitatively good. In some cases the exact value is reached. In the case where the yields decreases to zero, e.g. for B and C, the build-up of a solid layer of the collected projectiles was calculated, which prevents any sputtering of the backing material.

Note that the formation of chemical compounds due to O, F, Cl or other elements implantation into materials are not considered. The surface-binding energies were not changed during the calculation. This means that the composition of the surface has no influence on the value of the surface-binding energies (isbv=1). Also, the changes in the structure of the surface layer due to gas agglomeration and bubbling for inert gas were ignored in the model SDTrimSP. Formation of roughness has also not been considered.

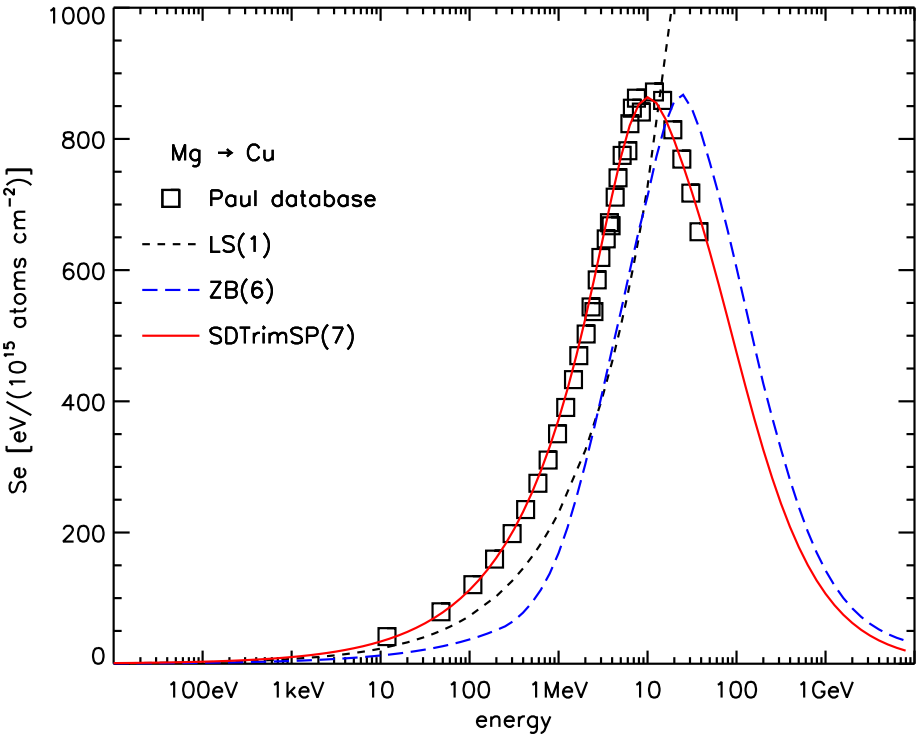

Figure 158: Electronic stopping power dependent on energy Mg on Cu with measurements [65]

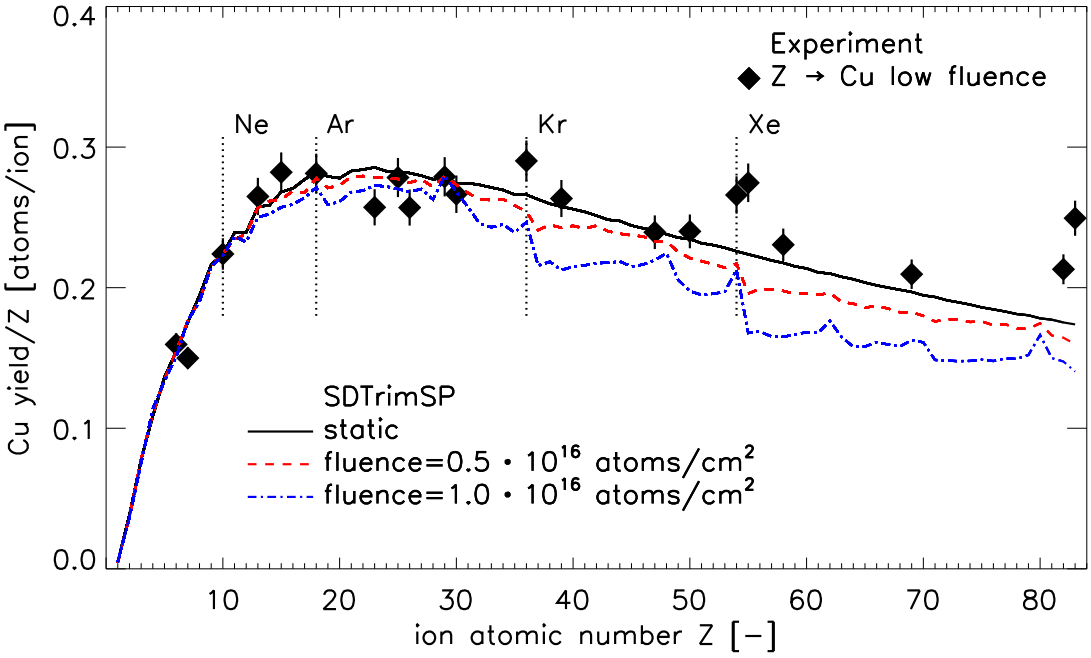

Figure 159: Comparison of calculated sputtered yields low fluence with experimental results [52], Z on Cu.

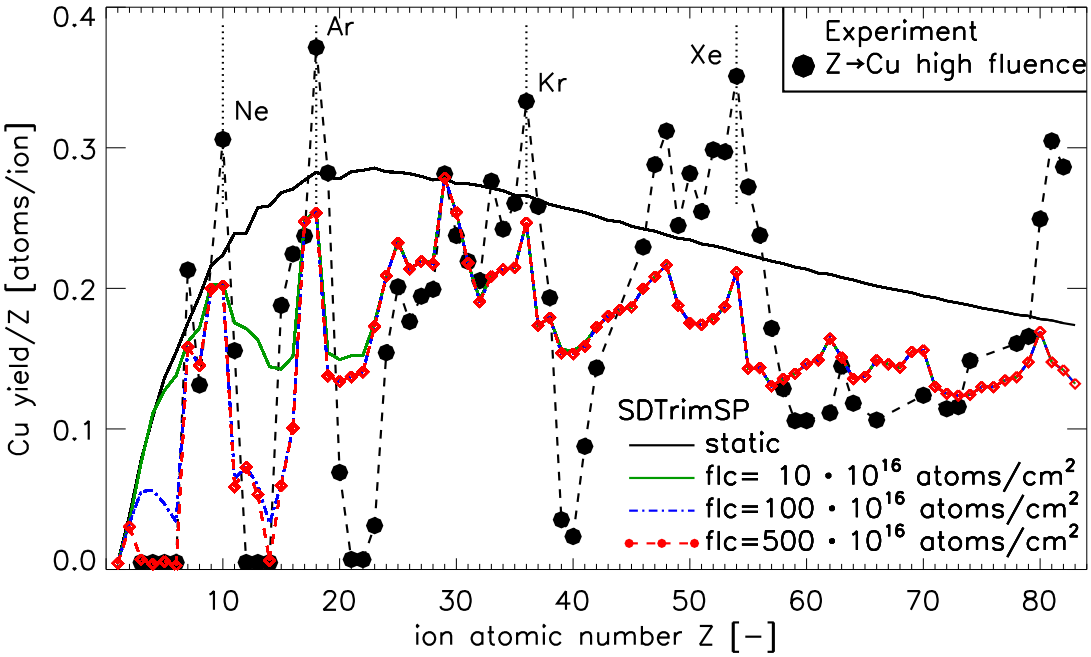

Figure 160: Comparison of calculated sputtered yields high fluence with experimental results [51], Z on Cu. Note Li and Be are calculated for $1000{\cdot}10^{16} atoms/cm^2$

10. Comparison of calculated and measured values of compound-target

10.1. Electronic stopping H on O

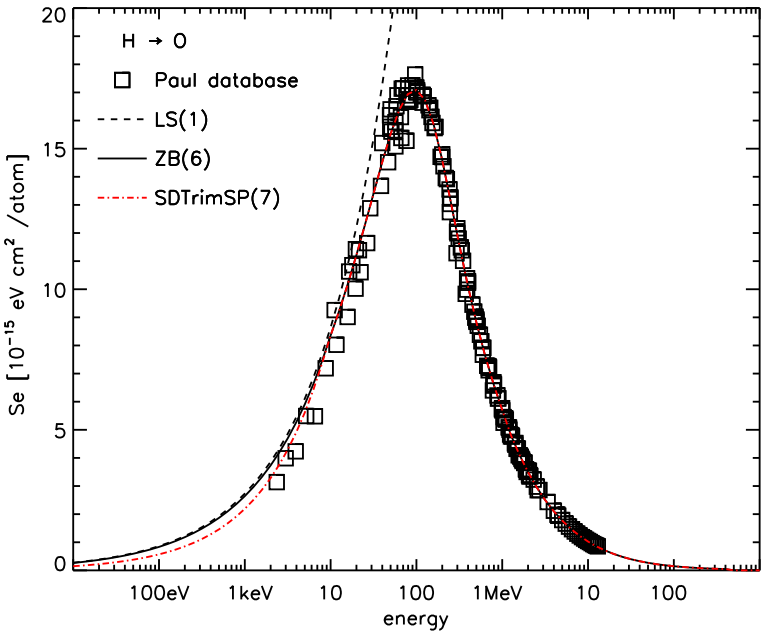

Figure 161: Electronic stopping power dependent on energy H on O with measurements [65], $a_1 = 2.2$, $a_2 = 2.9989$,

10.2. He on BeO (yield(

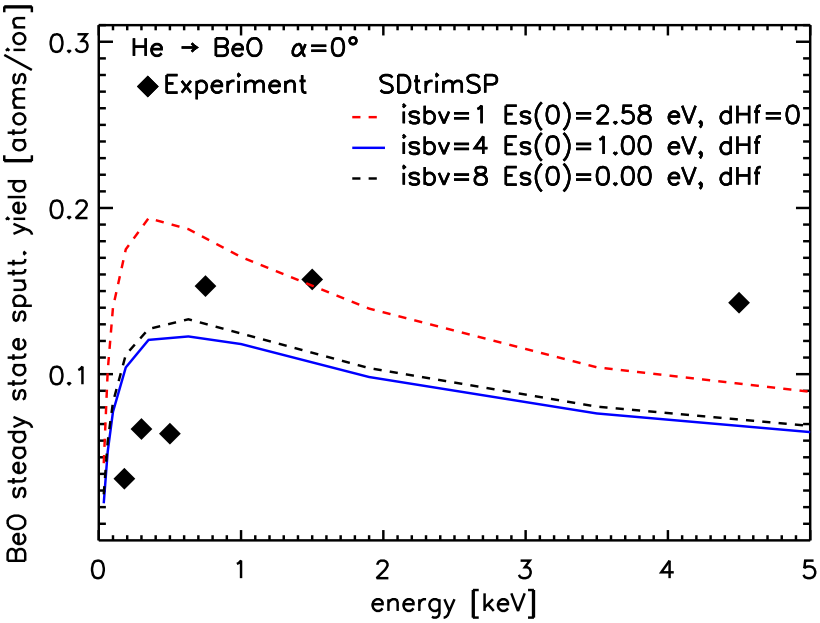

isbv		E_{surf}	E_{bulk}	E_{cut}
1	Be_f	3.310	0	1.103
	O_f	2.580	0	0.860
	Be_b	3.310	0	1.103
	O_b	2.580	0	0.860
4	Be_f	3.310	0	1.103
	O_f	1.000	0	0.860
	Be_b	3.310	3.153	1.103
	O_b	1.000	3.153	0.860
8	Be_f	0	3.310	1.103
	O_f	0	0.860	0.860
	Be_b	0	6.463	1.103
	O_b	0	4.013	0.860

Figure 162: Comparison calculated yield of three binding models with measurements [28] He on BeO incident angle $\alpha = 0°$ (f...free, b...bounded, dHf=6.306 eV)

10.3. H and He on Al_2O_3 (yield)

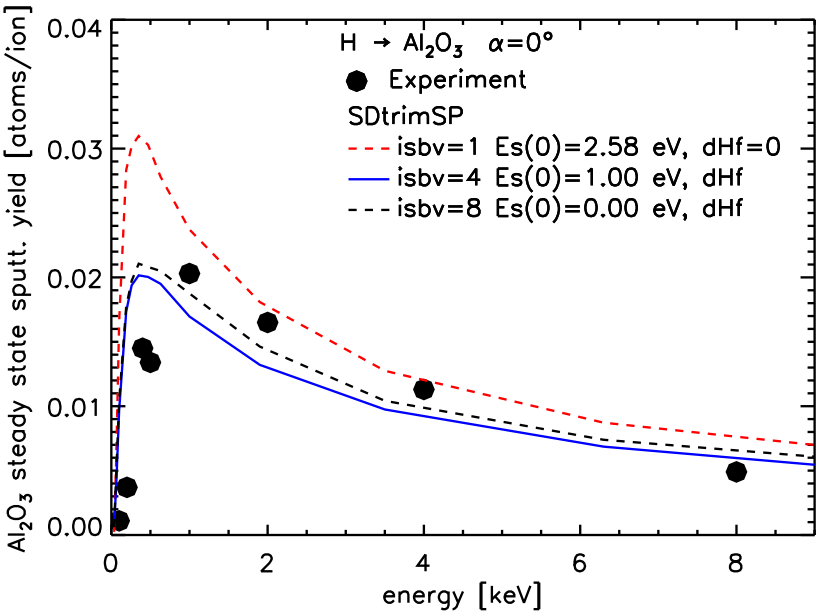

Figure 163: Comparison calculated yield of three binding models with measurements [28] H on Al_2O_3 incident angle $\alpha = 0°$

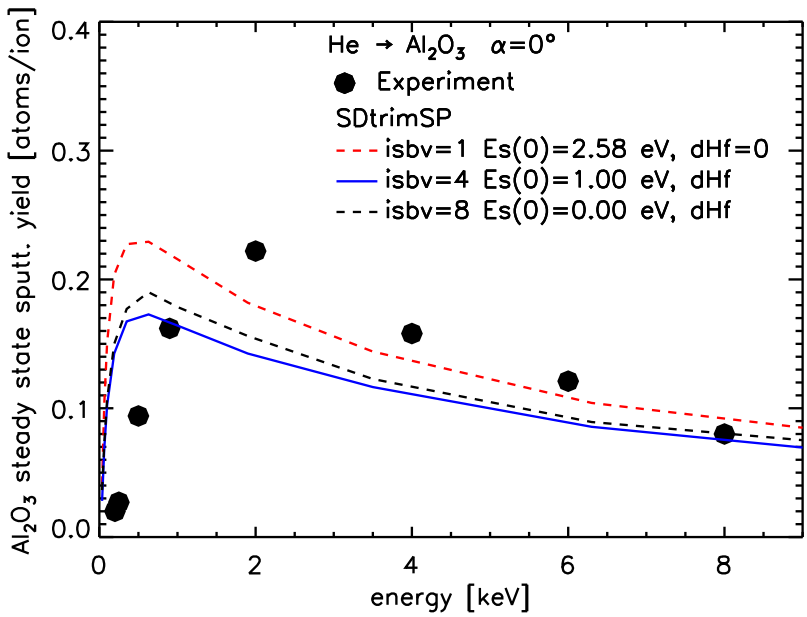

Figure 164: Comparison calculated yield of three binding models with measurements [92] He on Al_2O_3 incident angle $\alpha = 0°$

10.4. Ar on SiO_2 and He on SiO_2 (yield)

10.4.1. Calculation without dimers (l_two_comp1)

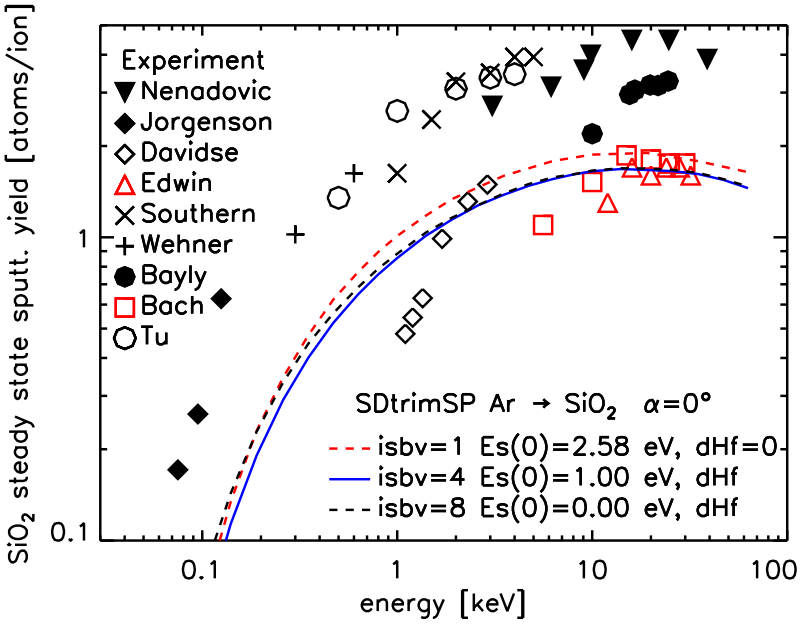

Figure 165: Comparison calculated yield with measurements [42],[43],[44],[45],[47],[48], [49],[50],[46] Ar on SiO_2 incident angle $\alpha = 0°$

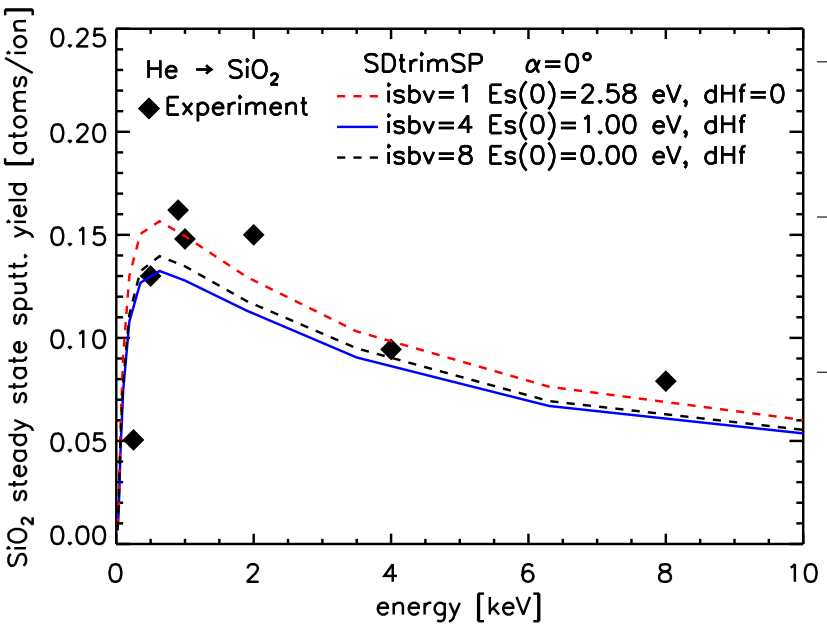

isbv		E_{surf}	E_{bulk}	E_{cut}
1	Si_f	4.720	0	1.573
	O_f	2.580	0	0.860
	Si_b	4.720	0	1.573
	O_b	2.580	0	0.860
4	Si_f	4.720	0	1.573
	O_f	1.000	0	0.860
	Si_b	4.720	3.147	1.573
	O_b	1.000	3.147	0.860
8	Si_f	0	4.720	1.573
	O_f	0	0.860	0.860
	Si_b	0	7.867	1.573
	O_b	0	4.007	0.860

Figure 166: Comparison calculated yield with measurements [92] He on SiO_2 incident angle $\alpha = 0°$

10.4.2. Calculation with dimers SiO and $SiO2$ (l_two_comp2)

collision:

$$\begin{aligned} n \cdot SiO_2 &\rightarrow n \cdot Si_f + 2n \cdot O_f \\ n \cdot SiO &\rightarrow n \cdot Si_f + n \cdot O_f \end{aligned}$$

chemical reaction:
$(m \leq n)$:

$$n \cdot Si_f + m \cdot O_f \rightarrow m \cdot SiO + (n-m) \cdot Si_f$$

$(m > n)$:

$(2n \geq m)$:

$$\begin{aligned} n \cdot Si_f + m \cdot O_f &\rightarrow n \cdot SiO + (m-n) \cdot O_f \\ &\rightarrow (m-n) \cdot SiO_2 + (2n-m) \cdot SiO \end{aligned}$$

$(2n < m)$:

$$\begin{aligned} n \cdot Si_f + m \cdot O_f &\rightarrow n \cdot SiO + (m-n) \cdot O_f \\ &\rightarrow n \cdot SiO_2 + (m-2n) \cdot O_f \end{aligned}$$

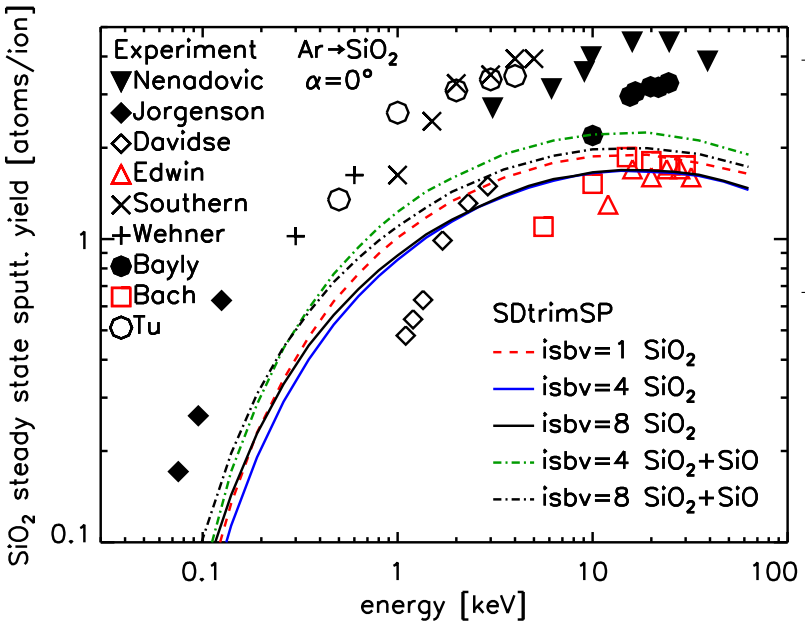

isbv		E_{surf}	E_{bulk}	E_{cut}
4	Si_f	4.720	0	1.573
	O_f	1.000	0	0.860
	Si_{b1}	4.720	3.147	1.573
	O_{b1}	1.000	3.147	0.860
	Si_{b2}	4.720	0.520	1.573
	O_{b2}	1.000	0.520	0.860
8	Si_f	0	4.720	1.573
	O_f	0	0.860	0.860
	Si_{b1}	0	7.867	1.573
	O_{b1}	0	4.007	0.860
	Si_{b2}	0	5.240	1.573
	O_{b2}	0	1.380	0.860

Figure 167: Comparison calculated yield with measurements [42],[43],[44],[45],[47],[48], [49],[50],[46] Ar on SiO_2 incident angle $\alpha = 0°$ (b1...SiO_2 b2...SiO)

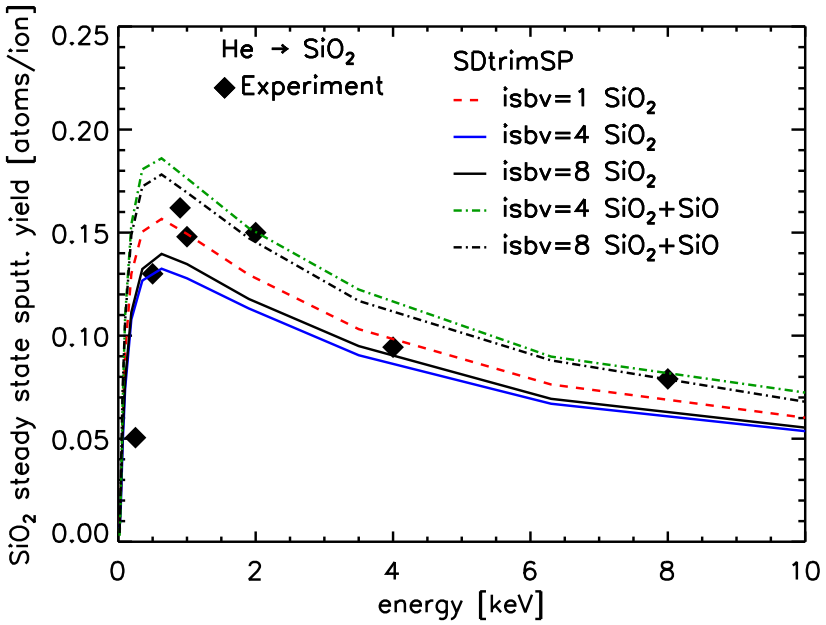

Figure 168: Comparison calculated yield with measurements [92] He on SiO_2 incident angle $\alpha = 0°$ (b1...SiO_2 b2...SiO)

10.5. W and He on WC (yield and implanted profile)

10.5.1. W on C

See Fig. 15

10.5.2. He on WC

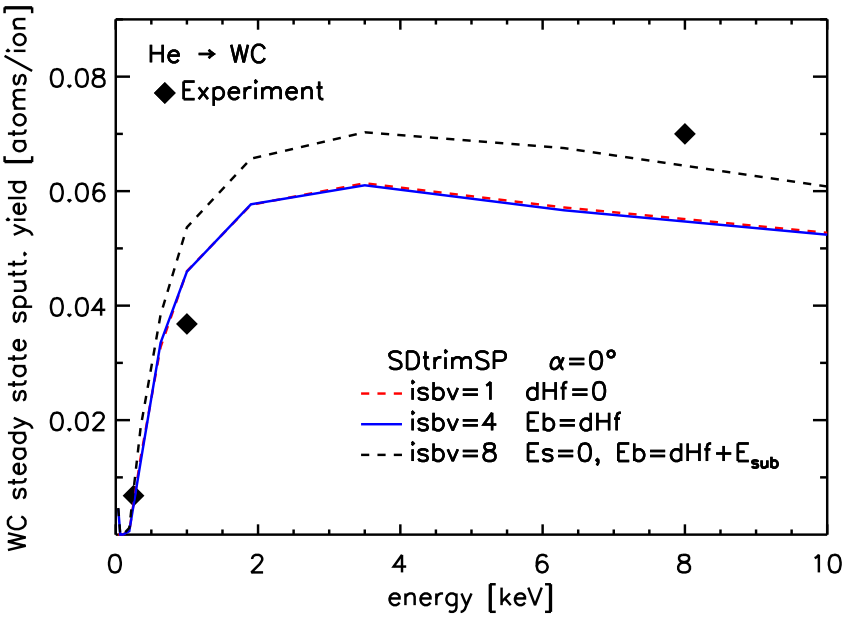

Figure 169: Comparison calculated yield of three binding models with measurements [28] He on CW incident angle $\alpha = 0°$

10.6. D, He and Ne on TiC (yield)

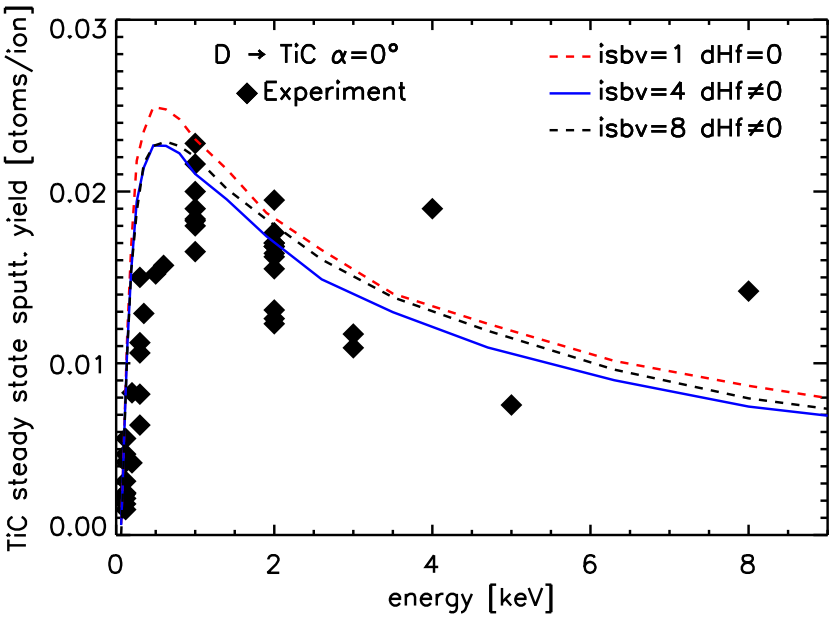

Figure 170: Comparison calculated yield with measurements [28] D on TiC incident angle $\alpha = 0°$

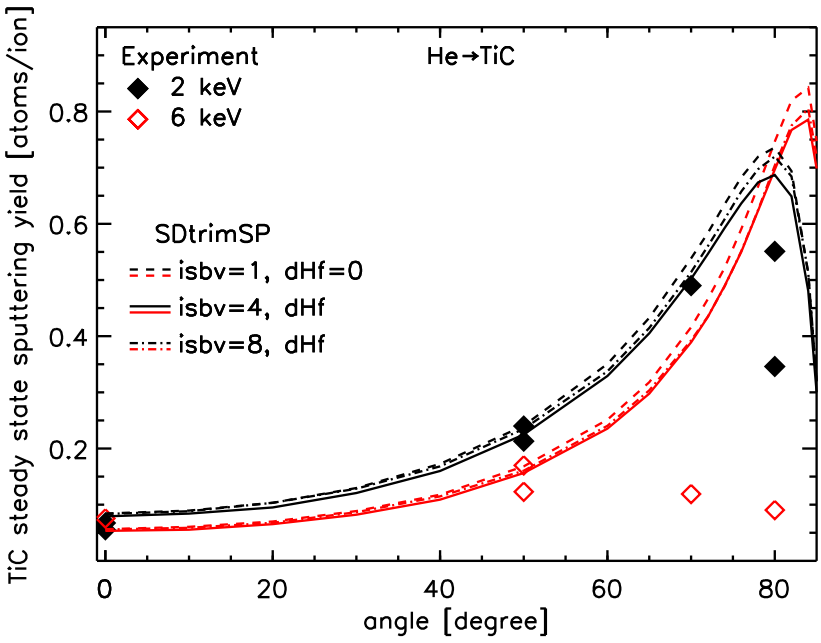

Figure 171: Comparison calculated yield with measurements [28] He on TiC depend on angle α

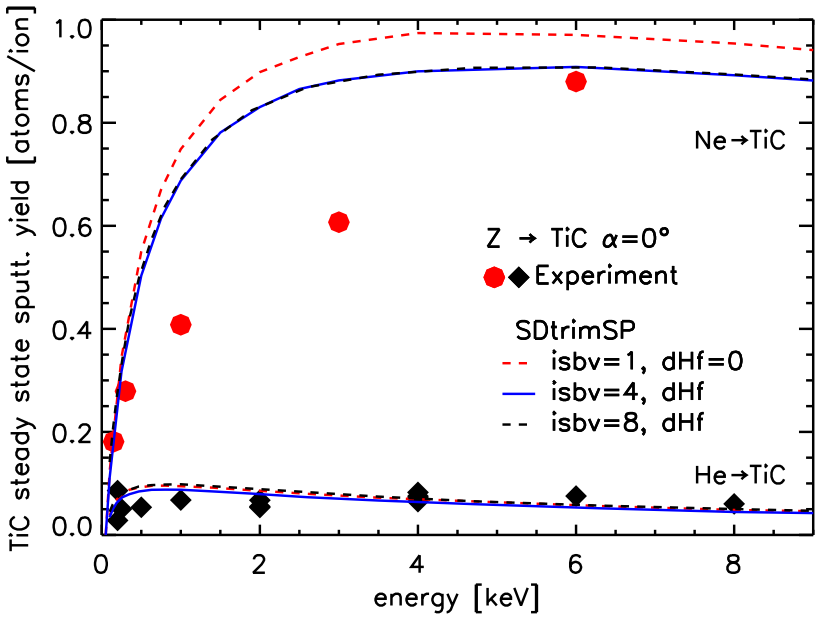

Figure 172: Comparison calculated yield with measurements [28] Ne, He on TiC incident angle $\alpha = 0°$

10.7. D on TaC (yield)

Steady state sputtering coefficients (yields) D on TaC dependent on energy see Fig. 47.

10.8. Ar and He on Ta_2O_5 (yield, profile)

10.8.1. Calculation without dimers (l_two_comp1)

Ar on Ta_2O_5: see Fig. 45 and Fig. 46

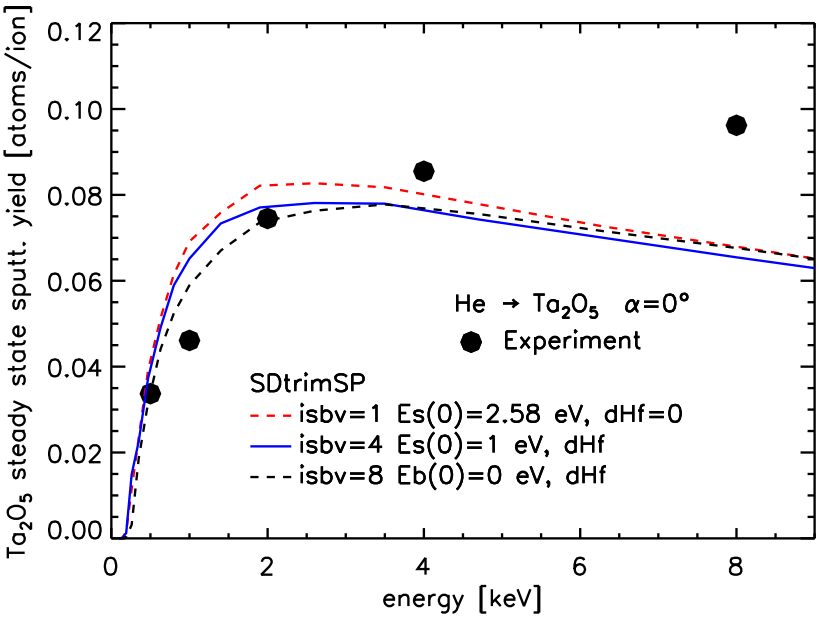

Figure 173: Comparison calculated yield with measurements [28] He on Ta_2O_5 incident angle $\alpha = 0°$

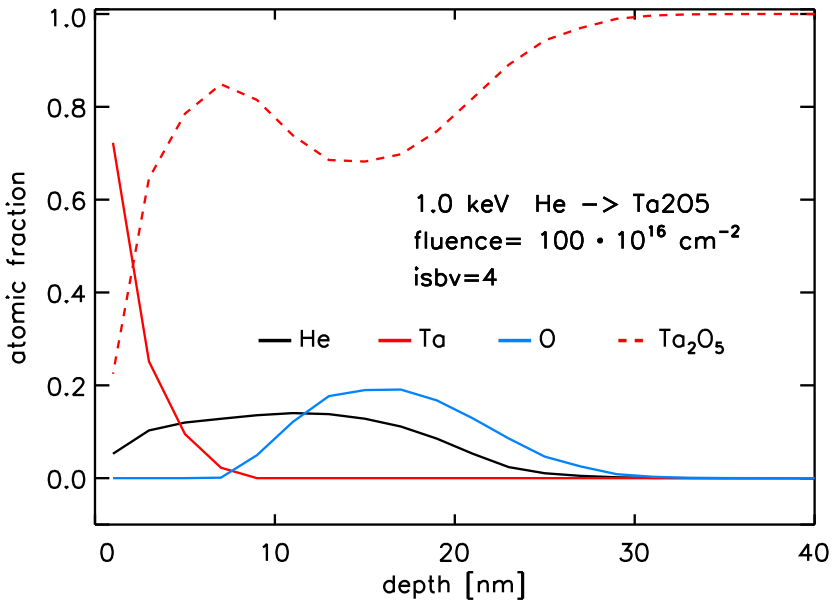

Figure 174: Calculated steady state profile of atomic fraction 1keV He on Ta_2O_5 incident angle $\alpha = 0°$

10.8.2. Calculation with dimers TaO_2 and Ta_2O_5 (l_two_comp2)

collision:

$$\begin{aligned} n_1 \cdot Ta_2O_5 &\rightarrow 2n_1 \cdot Ta_f + 5n_1 \cdot O_f \\ n_2 \cdot TaO_2 &\rightarrow n_2 \cdot Ta_f + 2n_2 \cdot O_f \\ n &= 2n_1 + n_2 \\ m &= 5n_1 + 2n_2 \end{aligned}$$

chemical reaction:

$$(n = 1,\ m > 1): \quad n \cdot Ta_f + m \cdot O_f \rightarrow 1 \cdot TaO_2 + (m-2) \cdot O_f$$

$$(n > 1,\ m = 3): \quad n \cdot Ta_f + m \cdot O_f \rightarrow 1 \cdot TaO_2 + (n-1) \cdot Ta_f + 1 \cdot O_f$$

$k = n \ mod \ 2$

$(m \geq 2n + (n-k)/2)$:

$$\begin{aligned} n \cdot Ta_f + m \cdot O_f &\rightarrow n \cdot TaO_2 + (m-2n) \cdot O_f \\ &\rightarrow (n-k)/2 \cdot Ta_2O_5 + k \cdot TaO_2 + (m-2n-(n-k)/2) \cdot O_f \end{aligned}$$

$(2n \leq m < 2n + (n-k)/2)$:

$$\begin{aligned} n \cdot Ta_f + m \cdot O_f &\rightarrow n \cdot TaO_2 + (m-2n) \cdot O_f \\ &\rightarrow (m-2n) \cdot Ta_2O_5 + (n - 2(m-2n)) \cdot TaO_2 \end{aligned}$$

$k = m \ mod \ 2$

$(m < 2n,\ m \neq 3)$:

$$\begin{aligned} n \cdot Ta_f + m \cdot O_f &\rightarrow (m-k)/2 \cdot TaO_2 + (n - (m-k)/2) \cdot Ta + k \cdot O_f \\ &\rightarrow k \cdot Ta_2O_5 + ((m-k)/2 - 2k) \cdot TaO_2 + (n - (m-k)/2) \cdot Ta_f \end{aligned}$$

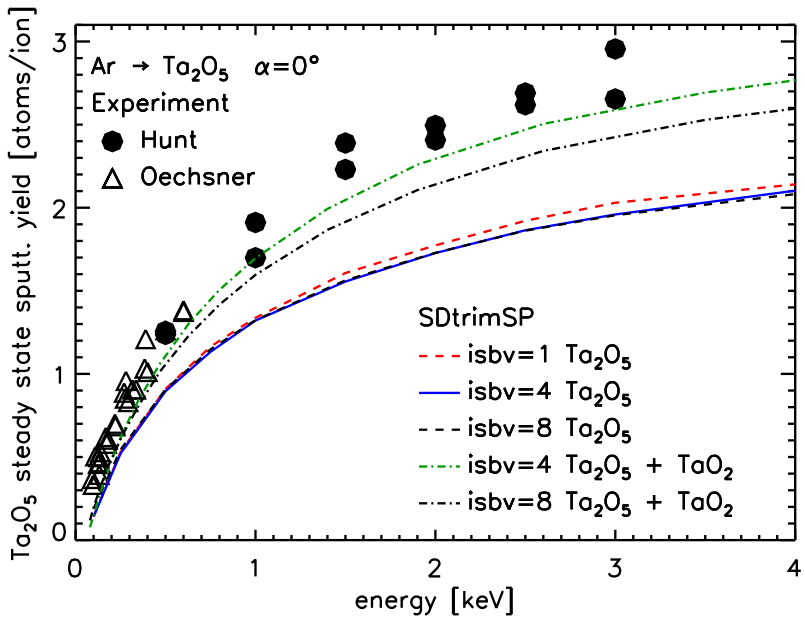

isbv		E_{surf}	E_{bulk}	E_{cut}
1	Ta_f	8.100	0	1.573
	O_f	2.580	0	0.860
	Ta_{b1}	8.100	0	1.573
	O_{b1}	2.580	0	0.860
4	Ta_f	8.100	0	5.400
	O_f	1.000	0	0.860
	Ta_{b1}	8.100	3.029	5.400
	O_{b1}	1.000	3.029	0.860
	Ta_{b2}	8.100	0.593	5.400
	O_{b2}	1.000	0.593	0.860
8	Ta_f	0	8.100	5.400
	O_f	0	0.860	0.860
	Ta_{b1}	0	11.129	5.400
	O_{b1}	0	3.889	0.860
	Ta_{b2}	0	8.693	5.400
	O_{b2}	0	1.453	0.860

Figure 175: Comparison of sputtered yields of compound calculated with Different surface binding models with reduced Es of O and experimental results [41], [60], Ar on Ta_2O_5.

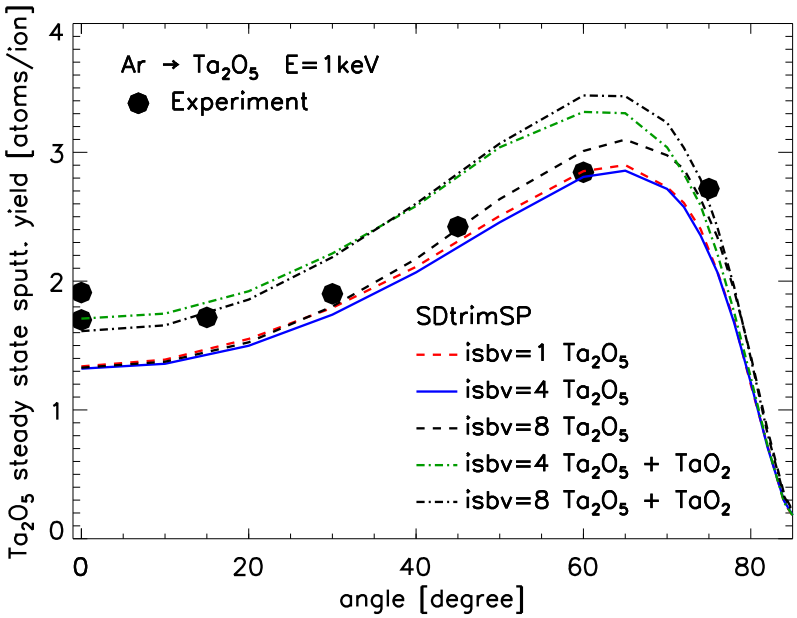

Figure 176: Comparison of sputtered yields of compound calculated with Different surface binding models with reduced Es of O and experimental results [28], *Ar* on Ta_2O_5.

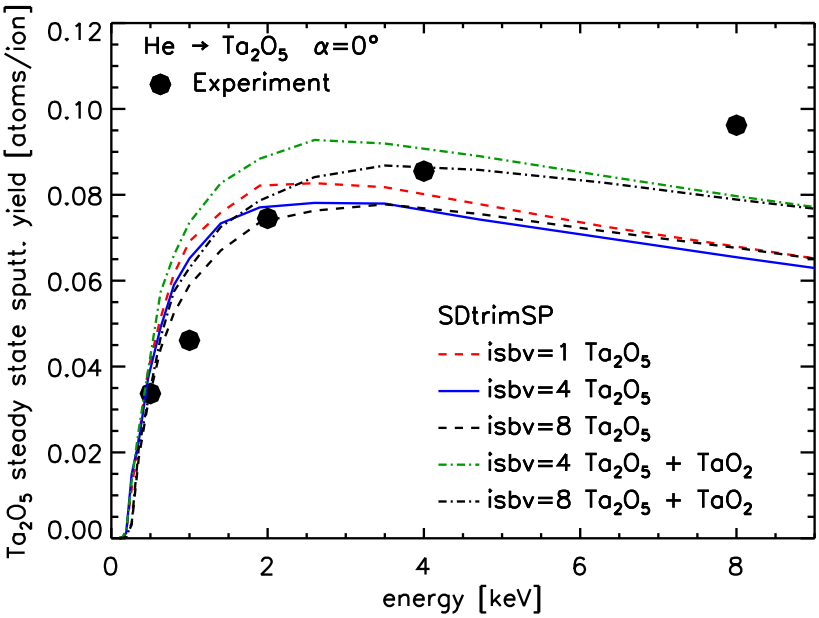

Figure 177: Comparison calculated yield with measurements [28] He on Ta_2O_5 incident angle $\alpha = 0°$

10.8.3. H and He on $CaSiO_3$ as combine of two compounds CaO and SiO_2 (l_two_comp2)

Assumption is that $CaSiO_3$ can be considered as CaO + SiO_2

	atomic density	ΔH_f/atom
$CaSiO_3$	0.07548	3.375
CaO	0.07238	3.290
SiO_2	0.07969	3.146

Because $\Delta H_f(CaO)$ is larger than $\Delta H_f(SiO_2)$:
collision:

$$\begin{aligned} n \cdot CaO &\rightarrow n \cdot Ca_f + n \cdot O_f \\ k \cdot SiO_2 &\rightarrow k \cdot Si_f + 2k \cdot O_f \\ m &= n + 2k \end{aligned} \tag{10.83}$$

chemical reaction:
$(m <= n)$

$$n \cdot Ca_f + m \cdot O_f + k \cdot Si_f \rightarrow m \cdot CaO + (n-m) \cdot Ca_f + k \cdot Si_f \tag{10.84}$$

$(m > n)$

$$n \cdot Ca_f + m \cdot O_f \rightarrow n \cdot CaO + (m-n) \cdot O_f \tag{10.85}$$

$(m-n) > 2k$

$$k \cdot Si + (m-n) \cdot O_f \rightarrow k \cdot SiO_2 + (m-n) - 2k \cdot O_f \tag{10.86}$$

$(m-n) <= 2k$

$$k \cdot Si + (m-n) \cdot O_f \rightarrow (m-n)/2 \cdot SiO_2 + k - (m-n)/2 \cdot Si_f \tag{10.87}$$

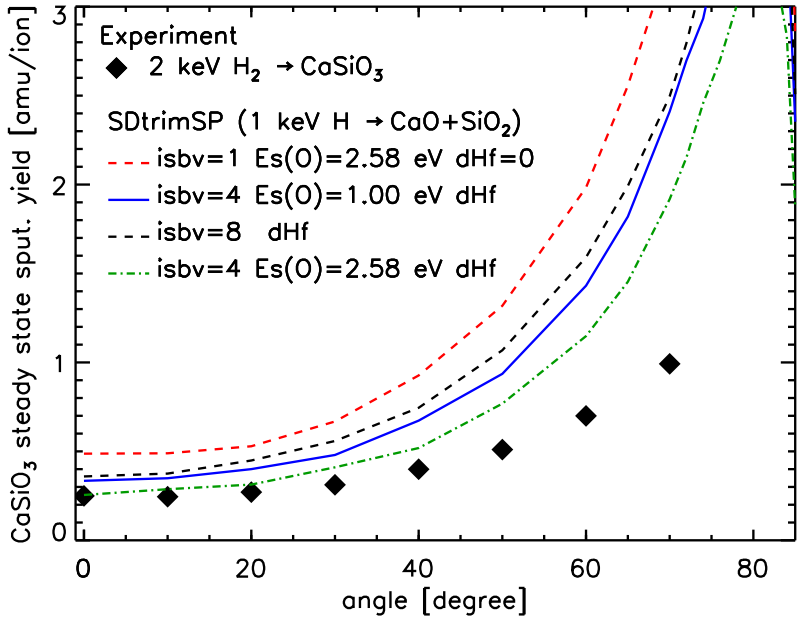

Figure 178: Comparison of calculated sputtered yields of complex compound with experimental results [99] 2keV H2 on $CaSiO_3$

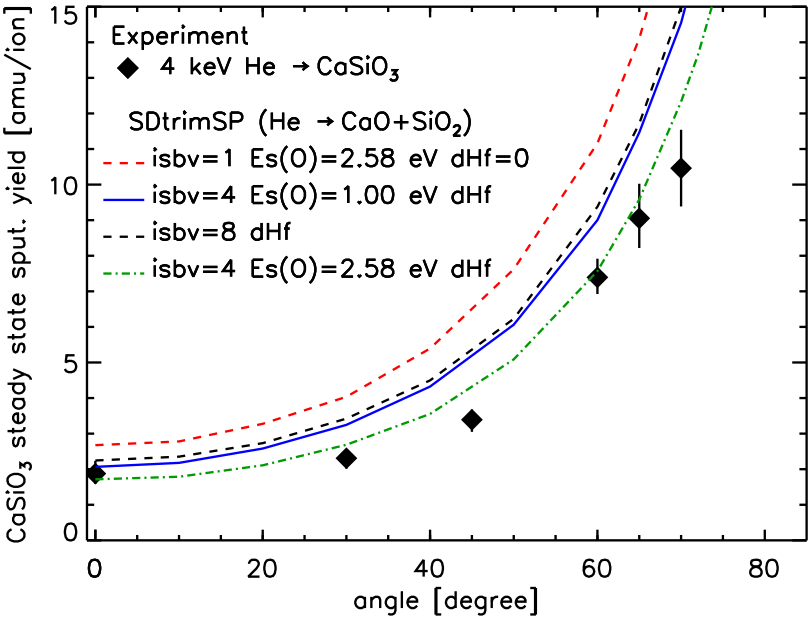

Figure 179: Comparison of calculated sputtered yields of complex compound with experimental results [96] He on $CaSiO_3$

10.9. Calculation with natural isotope mixture He on B

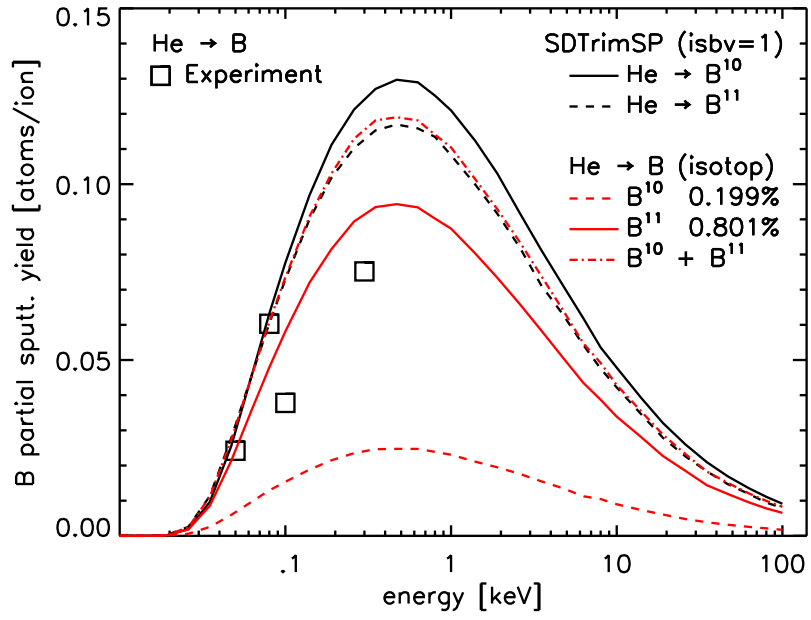

Figure 180: Comparison of sputtered yields with natural isotope mixture of B

References

[1] W. Eckstein,*Computer Simulation of Ion-Solid Interactions*, Springer Series in Material Science, Vol. 10, Springer Berlin, Heidelberg 1991

[2] J. P. Biersack, W. Eckstein, Appl. Phys. A 34 (1984) 73

[3] W. Möller, W. Eckstein, Nucl. Instrum. Meth. B 2 (1984) 814

[4] W. Möller, W. Eckstein, J. P. Biersack, Comput. Phys. Comm. 51 (1988) 355

[5] H. H. Andersen, J. F. Ziegler: In Hydrogen Stopping Powers and Ranges in All Elements, The Stopping and Range of Ions in Matter, Vol.3, ed. by J. F. Ziegler (Pergamon, NewYork, 1977)

[6] J. F. Ziegler: In Helium Stopping Powers and Ranges in All Elements, The Stopping and Range of Ions in Matter, Vol.4, ed. by J. F. Ziegler (Pergamon, NewYork, 1977)

[7] W. D. Wilson, L. G. Haggmark, J. P. Biersack, Phys. Rev. 15 (1977) 2458

[8] J. F. Ziegler, J. P. Biersack, U. Littmark: The Stopping and Range of Ions in Solids, The Stopping and Range of Ions in Matter, Vol.1, ed. by J. F. Ziegler (Pergamon, NewYork, 1985)

[9] G. Molière, Z. Naturforsch. A2 (1947) 133

[10] W. Eckstein, S. Hackel, D. Heinemann, B. Fricke, Z. Phys. D 24 (1992) 171

[11] J. P. Biersack, L. G. Haggmark, Nucl. Instrum. Meth. 174 (1980) 257

[12] K. Mehler, J. Reine Angew. Math. 63 (1864) 152

[13] Z. Kopal, *Numerical Analysis*, Chapman and Hall, London 1961, p. 367 ff.

[14] H. G. Schlager, W. Eckstein, IPP-Report 9/69, Garching 1991

[15] M. T. Robinson: Tables of Classical Scattering Integrals, Oak Ridge Natl. Lab., Oak Ridge, Tennessee (1970)

[16] W. Eckstein, R. Dohmen, Nucl. Instrum. Meth. B 129 (1997) 327

[17] R. Becerra-Acevedo, J. Bohdansky, W. Eckstein and J. Roth, Nucl. Instrum. Meth. B 2 (1984) 631

[18] W. Eckstein, Nucl. Instrum. Meth. B 27 (1987) 78

[19] S. T. Nakagawa, Y. Yamamura, Radiat.Eff.105, 239(1988)

[20] S. T. Nakagawa, Radiation Effects and Defects in Solids, Vol.116 (1991), page 21-28

[21] A. Mutzke, W. Eckstein, Nucl. Instr. and Meth. B 266(2008) 872

[22] K. Wittmaack, Nucl. Instr. and Meth. B 267(2009) 2846-2857

[23] N. Menzel and K. Wittmaack, Nucl. Instr. and Meth. in Phys. Res. B7/8 (1985) 366-370

[24] P. Blank, K. Wittmaack and F. Schulz, Nucl. Instr. and Meth. 132 (1976) 387-392

[25] W. Eckstein, R. Dohmen, A. Mutzke, R. Schneider, Report IPP-Report 12/3, Garching, (2007)

[26] W. Möller, W. Eckstein, Report IPP-Report 9/64, Garching, (1988)

[27] R.A. Zuhr, J. Roth, W. Eckstein, U. von Toussaint, J. Luthin, J. of Nucl. Mater. 290-293 (2001) 162-165

[28] W. Eckstein, C. García-Rosales, J. Roth, and W.Ottenberger, Sputtering Data, IPP-Report 9/82, 1993

[29] J. Roth, J. Bohdansky and W.Ottenberger, Data on low energy, IPP-Report 9/26, 1979

[30] J. F. Ziegler, J. P. Biersack, U. Littmark, *The Stopping and Range of Ions in Solids, The Stopping and Range of Ions in Matter*, Vol.1, Pergamon, New York, 1985

[31] P. Blank, K. Wittmaack, J. Appl. Phys. 50, (1979) 1519

[32] K. Wittmaack, Phys. Rev. B 68, 235211 (2003)

[33] J. Roth, C. Garcia-Rosales, Nuclear Fusion 36 (1996) 1647

[34] C. Hopf, A. von Keudell, W. Jacob, J. Appl. Phys. 94 (2003) 2373-2380

[35] B. V. Mech, A. A. Haasz and J. W. Davis, J. Appl. Phys. 84 (1998) 1655-1669

[36] A. Rai, A. Mutzke and R. Schneider, Nucl. Instr. Meth. B 268 (2010) 2639-2648

[37] J. W. Davis, A. A. Haasz, P. C. Stangeby, J .Nucl. Mater 145-147 (1987) 417-420

[38] W. Eckstein, V.I. Shulga, J. Roth, Nucl. Instr. and Meth. B 153 (1999) 415-421

[39] Y. Kudriavtsev, A. Villegas, A. Godines, R. Asomoza, Appl. Surface Science, 239 Issues 3-4 (2005)

[40] W. Möller, M. Posselt, Report FZR-317, Forschungszentrum Rossendorf, Dresden, (2002)

[41] C. P. Hunt and M. P. Seah, (1983) Surf. Interface Anal. 5 (1983) 199-209

[42] T.Nenadovic, B. Perraillon, Z. Bogdanov,Z. Djordjevi and M. Mili, Nucl. Instrum. Meths. B 48 (1990) 538-543

[43] G. V. Jorgenson and G. K. Wehner, J. Appl. Phys. 36 (1965) 2672-2674

[44] P. D. Davidse and L. I. Maissel, J. Vac. Sci. Technolog. 4 (1967) 33-36

[45] G. K. Wehner, Genaral Mills Report No. 2309, unpublished (1962)

[46] A. L. Southern, W. R. Willis and M. T. Robinson, J. Appl. Phys. 34 (1963) 153

[47] A. R. Bayly and P. D. Townsend, Opt. Laser Technol. (1970) 117-121

[48] H. Bach, Nucl. Instrum. Meths. 84 (1970) 4-12

[49] R. P. Edwin, J. Phys. D 6 (1973) 833-841

[50] Y. Y. Tu, T. J. Chuang and H. F. Winters, Phys. Rev. B 23 (1981) 823-835

[51] O. Almèn and G. Bruce, Nucl. Instrum. Meths. II (1961) 279-289

[52] H. H. Andersen and H. Bay, radiation effects 1972, Vol. 13, pp. 67-74

[53] M.J. Norgett and M.T. Robinson and I.M. Torrens, Nuclear Engeneering and Design 1975, Vol. 33, pp. 50-54

[54] R.E. Stoller, M.B. Toloczko, G.S. Was, A.G. Certain, S. Dwaraknath, F.A. Garner, Nucl. Instr. Meth. B 310, p. 75-80 (2013)

[55] ASTM Standard E521, 2016, ASTM International, West Conshohocken, PA, 2016, DOI: 10.1520/E0521-16

[56] A. Mutzke, R. Schneider, G. Bandelow, SDTrimSP-2D: Simulation of Particles Bombarding on a Two Dimensional Target Version 2.0, IPP-Report 12/11, 2013

[57] R. Arredondoa, M. Oberkofler, T. Schwarz-Selinger, U. von Toussaint, V.V. Burwitza, A. Mutzke, E. Vassallo, M. Pedroni, Nuclear Materials and Energy, 2019 Vol. 18, pp. 72-76

[58] Brunnée, Zeitschrift fuer Physik, Bd. 147, S. 161-183 (1957)

[59] J. Bøttiger and J. A. Davies, radiation effects 1971, Vol. 11 , pp. 61-67

[60] H. Oechsner, H. Schoof and E. Stumpe, Surface Science 76 (1978) 343-354

[61] J. Lindhard and M. Scharff, Phys. Rev. 124 (1961) 128

[62] H. H. Andersen, J. F. Ziegler, Hydrogen Stopping Powers and Ranges in All Elements, The Stopping and Range of Ions in Matter, Vol.3, ed.by J. F. Ziegler, Pergamon, New York, 1977

[63] J. F. Ziegler, Helium Stopping Powers and Ranges in All Elements, The Stopping and Range of Ions in Matter, Vol.4, ed.by J. F. Ziegler, Pergamon, New York, 1977

[64] J. F. Ziegler, J. P. Biersack, U. Littmark, The Stopping and Range of Ions in Solids, The Stopping and Range of Ions in Matter, Vol.1, ed.by J. F. Ziegler, Pergamon, New York, 1985

[65] H. Paul, Collection of graphs, data and comments, http://www.uni-linz.ac.at/fak/TNF/STOPPING/welcome.htmt, https://www-nds.iaea.org/stopping/stopping_heav.html

[66] M. Hou and T. Robinson Nucl. Instrum. Meth. 132 (1976) 641

[67] D. Rosenberg, G.K. Wehner J. Appl. Phys. 33 5 (1962) 1842-1845

[68] K. Hofker, D.P. Oosthoek, N.J. Koeman, H.A.M. De Grefte, Radiat.Eff. Vol.24, 67-74 (1975)

[69] M. Behar, M. Weiser, S. Kalbutzer, D. Fink, F.L. Grande, Nucl.Instr.Meth. in Phys Res. B34 (1988) 316-320

[70] V.V. Bandurko, N.N. Koborov, V.A. Kumaev, V.M. Sotnikov and O.V. Zabeyda, J. of Nucl. Mat. 176 / 177 (1990) 630-634

[71] D. Onderdelinden, Can. J. Phys. 46. 739 (1968)

[72] R. Behrisch, Sputtered by Particle Bombardment I, Springer-Verlag Berlin Heidelberg New York, 1981

[73] D. Onderdelinden, Appl. Phys. Lett 8, 8, 189 (1966)

[74] H. Lefaix-Jeuland, S. Moll, F. Legendre, F. Jomard, Nucl.Instr.Meth. in Phys Res. B 295 (2013) 69-71 316-320

[75] K. Schlueter, K. Nordlund, G. Hobler, M. Balden, F. Granberg, O. Flinck, T. F. da Silva, R. Neu, Physical Review Letters 125, 225502 (2020) and PFMC-19, 22-26 May 2023, Bonn, Germany

[76] J. Roth, J. Bohdansky and W. Ottenberger, J. Nucl. Mat. 165 (1989) 193-198

[77] W. H. Hayward, A.R. Wolter J. Appl. Phys. 40 2911(1969) 1842-1845 ,doi.org/10.1063/1.1658100

[78] E.P. EerNisse, J. Appl. Phys. 42 480 (1971)

[79] P.C. Zalm, J. Appl. Phys. 54 2660 (1983) doi:10.1063/1.332340

[80] J. Berthold and S. Kalbitzer, Nucl.Instr.Meth. 209/210 1983 13-18

[81] F. Besenbacher, J.Bottinger, T.Laursen, P. I. Oftager W. Moeller, Nucl. Instrum. 170 (1980) 183-188

[82] D. Rosenberg, G.K. Wehner J. Appl. Phys. 33 5 (1962) 1842-1845

[83] N. Laegreit, G.K. Wehner J. Appl. Phys. 32 3 (1961) 365-369

[84] K. Wittmaack, D.B. Poker, Nucl. Instrum. Methods Phys. Res. B 47 (1990) 224-235.

[85] V.I. Bachurin, P.A. Lepshin, V.K. Smirnov, Vacuum 56 (2000) 241-245.

[86] L. Frey, C. Lehrer, H. Ryssel, Appl. Phys. A 76 (2003) 1017-1023.

[87] S. Lindsey, G. Hobler, Nucl. Instrum. Methods Phys. Res. B 303 (2013) 142-147.

[88] W. Wach and K. Wittmaack, Nucl.Instr.Meth. 194 1982 223-231

[89] Klaus Wittmaack, Surface ScienceReports 68(2013)108-230

[90] P.A.W. van der Heide, M.S. Lim, S.S. Perry, J. Bennett, NIMB 201 (2003) 413-425

[91] B. Berghmans, B. Van Daele,, L. Geenen, T. Conard, A. Franquet, W. Vandervorst, Applied Surface Science 255 (2008) 1316-1319

[92] J. Roth, J. Bohdansky and W. Ottenberger, Data on low energy, IPP-Report 9/26, 1979

[93] A. P. Yalin, V. Surla, C. Farnell, M. Butweiller, J. D. Williams 42nd AIAA/ASME/SAE/ASEE Joint Propulsion Conference & Exhibit, July 2006, Sacramento, California

[94] R. Arredondo, M. Balden, A. Mutzke, U. von Toussaint, S. Elgeti, T. Höschen, K. Schlueter, M. Mayer, M. Oberkofler, W. Jacob, Nucl. Mat. and Eng. 20(2020)100749

[95] K. Sugiyama, et al, Nucl. Mat. and Eng. 8 (2016)1-7

[96] Szabo P., Private communication (2022)

[97] Y.Yamamura, Nucl. Instrum. Meths. 194 (1982) 512-522

[98] H. Schirrwitz, Beitraege aus der Plasmaphysik, 2 (1962) 188-204.

[99] P. S. Szabo, , R. Chiba, H. Biber, R. Stadlmayr, B. M. Berger, D. Mayer, A. Mutzke, M. Doppler.c, M. Sauer, J. Appenroth, J. Fleig, A. Foelske-Schmitz, H. Hutter.c, K. Mezger, H. Lammer, A. Galli, P. Wurz, F. Aumayr, Icarus 314 (2018) 98-105

[100] P. S. Szabo, H. Biber, N. Jäggi, M. Brenner, D. Weichselbaum, A. Niggas, R. Stadlmayr, D. Primetzhofer, A. Nenning, A. Mutzke, M. Sauer, J. Fleig, A. Foelske-Schmitz, K. Mezger, H. Lammer, A. Galli, P. Wurz, F. Aumayr The Astrophysical Journal, 891:100 (12pp), 2020 March 1

A. Global parameters

parameter	value	description	program
ncpm	8	maximum number of elements	param.F90
nqxm	5000	maximum number of depth intervals	param.F90
pemax	128	maximum number of PEs	work.F90
ntqmax	100000	size of local task queue	default_init.F90

Table 8: Global parameters (set in programs)

B. Input variables in 'tri.inp'

B.1. Necessary input variables

The sequence of the input values in the input file is arbitrary (namelist)

variable	description
alpha0(ncp)	polar angle of incidence (degree) of ncp species in case_alpha=0,5
e0(ncp)	energies (eV) of projectiles (qubeam $> 0.$) for case_e0=0,5
	e0=ttemp $\cdot$ boltzm (e0 < 0) of projectiles for case_e0=2,3
	temperature (eV) (kT) (e0 > 0) of projectiles for case_e0=2,3
flc	incident fluence ($10^{16} atoms/cm^2$ or $atoms/A^2$)
ipot	interaction potential: $= 1$: KrC
	$= 2$: Moliere
	$= 3$: ZBL
	$= 4$: Nakagawa-Yamamura
	$= 5$: Si-Si
	$= 6$: power

Table 9: Necessary input variables (no default values)

variable	description
isbv	atoms binding model, determines the composition dependent surface-binding-energy sbv(ncp,ncp) from the elemental surface binding energies e_surfb(ncp) and bulk-binding-energy e_bulkb(ncp) of target atoms = 1 : sbv(ip,jp)=e_surfb(jp) for ip=jp, =0 else e_bulkb(1:ncp)=0.0 e_surfb taken from table1 = 2 : sbv(ip,jp)=e_surfb(jp) for all ip, jp e_bulkb(1:ncp)=0.0 e_surfb taken from table1 = 3 : sbv(ip,jp)=0., if e_surfb(ip)=0 or e_surfb(jp)=0 sbv(ip,jp)=0.5*(e_surfb(ip)+e_surfb(jp)) else e_bulkb(1:ncp)=0.0 e_surfb taken from table1 = 4 : sbv(ip,jp)=e_surfb(jp) for ip=jp, =0 else (like isbv=1) e_bulkb(1:ncp)=0.0 e_surfb taken from table1 only for compound-atoms (ip): e_bulkb(ip)=e_bulkb(ip)+$\Delta H_f(ip)$/nm ΔH_f taken from table.compound = 6 : input of given matrix of the surface-binding-energy input-file: mat_surfb.inp = 8 : sbv(1:ncp,1:ncp)=0.0 (e_surfb=0.0) e_bulkb(1:ncp)=ΔH_{sub} e_cutoff(1:ncp)=$1/3 \cdot \Delta H_{sub}$ e_bulkb and e_cutoff taken from table1a only for compound-atoms (ip): e_bulkb(ip)=ΔH_{sub}+ΔH_f/nm ΔH_f taken from table.compound
ncp	number of species (projectiles + target species) more than one projectile species is allowed
nh	number of histories (projectiles)
nqx	number of depth intervals of the target (discretization)
qubeam(ncp)	projectile atomic fractions (in incident beam) of ncp species, qubeam $> 0.$, Note: sum(qubeam(1:ncp))=1 qubeam $\leq 1.$ for projectiles qubeam $= 0.$ for target atoms
qu(ncp)	initial target atomic fractions of ncp species in case of homogeneous initial composition (iq0 = 0)
symbol(ncp)	ncp chemical symbols of elements according to table1 (special symbol: 'H','D','T','He3','He','P_w','P_r', carbon with different density: 'C_a','C_g','C_f','C_d', hybridization state of carbon Sp2,Sp3,Sp3H)

Table 10: Necessary input variables (no default values) (continued)

B.2. Optional input variables

These values have default values (see default_init.txt). If values different from the default values are needed, then these values have to be given explicitly in the input file.

variable	default value	description
angleinp	'./'	directory of input-file 'angle.inp' (see also: layerinp, tableinp, energyinp)
a_mass(ncp)	table	mass (in amu) of ncp elements; default from table1
beta0(ncp)	0	azimuthal angle of incidence (degree) of ncp species (in case_alpha=1 2 or 3 beta0=random distribution)
case_alpha	0	flag for the choice of the polar angle of incidence = 0 : polar angle of incidence (degree) counted from the surface normal alpha0 =0°...90° (starting above surface) alpha0 =90°...180° (starting in solid, only static mode) = 1 : random distribution of angles of incidence (only from above surface) (alpha0 and beta0 random) alpha0 = 0°..90°, beta0 = 0°...360° = 2 : cosine distribution of angles of incidence (only from above surface) cos(alpha0) =$\sqrt{0...1}$, beta0 = 0°...360° = 3 : cosine distribution of angles of incidence cos(alpha0) =$\sqrt{1-(0...1)^2}$, beta0 = 0°...360° = 4 : input of a given incident polar angular distribution from input-file: 'angle.inp', beta0 from: 'tri.inp' = 5 : series of calculations with different polar angles (alpha= $(i-1)\cdot$alpha0; i = 1, number_calc) output : output.* dat default set :lmatrices = .false. ltraj_p = .false., ltraj_r = .false. lparticle_r = .false., lparticle_p = .false. case_e0 = 0 (note: all *.dat outputfile from last calculation) = 6 : distribution of alpha and energy input-file: 'ene_ang.inp', beta0 from: 'tri.inp'

Table 11: Optional input variables with default values

variable	default value	description
case_e0	0	flag for the choice of the incident energy = 0 : fixed incident energies(eV) of projectiles (qubeam>0) = 1 : input of a given energy distribution from file energy.inp = 2 : temperature (eV) of a Maxwellian velocity distribution of projectiles = 3 : temperature (eV) of a Maxwellian energy distribution of projectiles = 5 : series of calculations with different projectile energies e0(1)>0: linear energy= $i \cdot e0$; i = 1, number_calc e0(1)<0: logarithmic energy= $10^{(i-1)} \cdot e0$; i = 1, number_calc output: output.*dat default set: lmatrices = .false. ltraj_p = .false., ltraj_r = .false., lparticle_r = .false., lparticle_p = .false., case_alpha = 0 (note: all *.dat file from last calculation) = 6 : distribution of alpha and energy, input-file: 'ene_ang.inp', beta0 from: 'tri.inp'
case_layer_thick	0	mixing schema of target = 0 mixing layer with neighbour layer, if thick: 150% or 50% = 1 mixing the whole target to constant layer thick, if one layer thick: 105% or 95% = 2 mixing only the penetration depth and mix with 1/3 method, if one layer thick: 105% or 95%
ca_scre(ncp,ncp)	1.	correction factor for the screening length in the interaction potential (not applicable for KrC and ZBL potentials)
charge(ncp)	0	charge of species if case_e0=2,3 and sheath>0 (plasma) $\geq$ 1. for qubeam>0 (projectiles) = 0. for qubeam=0 (target atoms)

Table 12: Optional input variables with default values (continued)

variable	default value	description
ck_elec(ncp,ncp)	1.	correction factor for the inelastic energy loss; correction factors for hydrogen (below 25 keV) are given in table3
deltahf		heat of formation (eV) of a molecular target default from table.compound
diff_koeff1(ncp)	0.0	damage-diffusion-coefficient if loutgas true $[A^4/ion]$ (see also: loutgas)
diff_koeff2(ncp)	0.0	pressure-transport-coefficient if loutgas true $[A^3/ion]$ (see also: loutgas)
dist_nx	60	x-size of the matrix of energy distribution in target
dist_ny	60	y-size of the matrix of energy distribution in target
dist_nz	60	z-size of the matrix of energy distribution in target
dist_delta	2.0	distance between the matrix points of energy distribution in target
dns0(ncp)		atomic density $(atoms/A^3)$ of ncp elements; default from table1
dsf	5.	average depth (A) for surface composition
e_bulkb(ncp)	0.	bulk binding energy; if e_bulkb<0. read from table1 e_bulkb is subtracted from the transfer energy
e_cutoff(ncp)		cutoff energy (eV) of ncp species if not set or -1 in tri.inp set default: 0.5 eV for noble gases and for H, D, T; minimum of e_surf(1:ncp) - 0.05 eV but maximum of 1/3 heat of sublimation if isbv=8 read from table1a
e_displ(ncp)		displacement energy (eV); default from table1
e_surfb(ncp)		surface binding energy (eV) (heat of sublimation); default from table1 if isbv=8 e_surfb(1:ncp)=0.0
energyinp	'./'	directory of input-file 'energy.inp' (see also: layerinp, tableinp, angleinp)
flux	1.0	flux of incident atoms $(atoms/A^2/s = 10^{20} atoms/m^2/s)$
idrel	1	mode of simulation $= 0$: full dynamic calculation (TRIDYN) > 0 : suppression of dynamic relaxation (TRIM), full static calculation < 0 : suppression of dynamic relaxation and cascades static calculation (TRIM) only projectiles (no recoils) are followed

Table 13: Optional input variables with default values (continued)

variable	default value	description
idout	-1	control output, determines the outputfiles: E0_31_target.dat, E0_34_moments.dat, partic*.dat, trajec*.dat and restart_file = -1 : output after each fluence step of nh/100, 100 fluence steps = 0 : output only after the last fluence step > 0 : output after each idout'th fluence step and last step
iintegral	2	integration method = 0 : MAGIC, only valid for KrC, ZBL, Moliere = 1 : Gauss-Mehler quadrature, ipivot ≥ 8 recommended = 2 : Gauss-Legendre quadrature, ipivot ≤ 16
imcp	2	flag indicating whether (flib)-moments of distributions are calculated = 0 : no moment calculation = 1 : moments of depth distributions for all projectiles (qubeam>0.)
i_num_z(ncp)	table	atomic number of ncp elements; default from table1
inel0(ncp)	7,4,5	inelastic loss model = 1 : Lindhard-Scharff; necessary condition: $E < 25 \cdot Z^{4/3} \cdot M$ (in keV) where E, Z, M are the energy, the atomic number and the atomic mass of the moving particle = 2 : Oen-Robinson; necessary condition:$E < 25 \cdot Z^{4/3} \cdot M$ (in keV) = 3 : equally distributed of 1 and 2 = 4 : hydrogen (H,D,T): values from 'table3' = 5 : helium (He3,He): values from 'table4' = 6 : values is calculated for each element use values from 'table6a' and 'table6b' = 7 : values is calculated for each element with help of mix of 1 (low energy), 6 (high energy) and correctur-factors from 'table7_ck' and 'table7_a3a4a5' = 8 : use manual tabularised stopping power from database 'tbsp.db', to be found in tables-directory

Table 14: Optional input variables with default values (continued)

variable	default value	description
ioutput_hist(6)	10	number of traced trajectories for: stopped, back-scattered and transmitted projectiles, stopped, back-sputtered, transmission sputtered recoils (see also: ltraj_p, ltraj_r)
ioutput_part(6)	10	number of traced particles for: stopped, back-scattered and transmitted projectiles, stopped, back-sputtered, transmission sputtered recoils (see also: lparticle_p, lparticle_r)
ipivot	8	number of pivots in the Gauss-Mehler and Gauss-Legendre integration, the minimum number is 4 (larger numbers increase the computing time)
iq0	1	initial composition flag < 0 : initial depth dependent composition taken from file layer.inp $= 0$: initial composition homogeneous, one layer with constant depth intervals
irand	1	random seed
irc0	-1	flag for subthreshold recoil atoms < 0 : subthreshold recoil atoms free ≥ 0 : subthreshold atoms bound, if $E_{start} < E_{displ}$ then replace
isot(ncp)	0	flag for isotope mass $= 0$: natural isotope mixture (mass from table1) $= 1$: isotope masses and natural abundances from table2 (valid for projectiles as well as for target species)
i_two_comp	1	method to determine the densities dns0(:) from the compound density in a two-component target (table.compound) =1 : dns0 for the first target species is set equal to the elemental density; necessary if the second element is a gas (e.g. Ta2O5) =2 : dns0 for the second target species is set equal to the elemental density =3 : iterative determination of both dns0(:); recommended if the elemental densities are different
it_diff	200	outgasing steps

Table 15: Optional input variables with default values (continued)

variable	default value	description
i_diff_algo	2	flag for method of diffusion =0 : simple diffusion =1 : explicit (lambda=0) =2 : implicit (lambda=1) =3 : Crank-Nicolson (lambda=0.5) =4 : Crank-Nicolson with lambda=lambda_cn=[0,1]
iwc	2	number of ring cylinders for weak simultaneous collisions for projectiles; for high energies (MeV H or He) iwc can be reduced to 1 or 0 to reduce computing time
iwcr	2	number of ring cylinders for weak simultaneous collisions for recoils
k_start	0	start counter intern
layerinp	'./'	directory of input-file 'layer.inp' (see also: iq0, tableinp, angleinp, energyinp)
l_crystal	.false.	calculate crystal, see also miller_ind
l_crystal_dyn	.false.	if l_crystal=true calculate amorphization of crystal
lenergy_distr	.false.	output of energy distribution in target in E_distr_stop.dat (energy of stop, electric loss and elastic nuclear loss)
lmatrices	.false.	.true. : output of matrices, if idrel /= 0 .false. : no matrix output
lmatout_log_energ	.false.	energy spacing = .false. : linear energy intervals = .true. : logarithmic energy intervals
lmatout_cos_angle	.false.	angular spacing = .false. : angle in degree intervals = .true. : cosine intervals
lmoments	.true.	output of moments for energy distributions (linear and logarithmic) of projectiles and recoils and for range distributions (linear) of projectiles .true. : moments are written .false. : moments are not written
loutgas	.false.	calculation with outgasing diffusion(DDF) and transport (PDF) (see also: diff_koeff1, diff_koeff2)
lparticle_p	.false.	.true. : output of projectile information .false. : no output of projectile information (see also: ioutput_part)
lparticle_r	.false.	.true. : output of recoil information .false. : no output of recoil information (see also: ioutput_part)

Table 16: Optional input variables with default values (continued)

variable	default value	description
lpart_r_ed	.true.	.true. : output of stop recoil information only grater e_displ .false. : output of all stop recoil information
l_pot_thick	.true.	.true. : thickness of surface potential is a function of N .false.: thickness of surface potential is a function of N,iwc,iwcr
lrestart	.false.	.true. : output of restart-file after each idout .false. : no restart-files
ltableread	.true.	.true. : read from table1, table2, table3, table4 or table.compound .false. : no table read, a_num_z, a_mass, dns0, e_surfb e_displ have to be given *table*1 : chemical symbol (symbol), nuclear charge (a_num_z), atomic mass (a_mass), mass density, atomic density (dns0), surface binding energy (e_surfb), displacement energy (e_displ), cutoff energy (e_cutoff) *table*2 : chemical symbol, nuclear charge, isotope mass, atomic weight (in amu), natural abundance *table*3 : inelastic stopping coefficients for hydrogen: symbol, nuclear charge, inelastic stopping coefficients a1 to a12 (ch_h), ck *table*4, 5 : inelastic stopping coefficients for helium: symbol, nuclear charge, inelastic stopping coefficients a1 to a9 (ch_he) *table*6*a* : only for inel=6,7 coefficients inelastic stopping *table*6*b* : only for inel=6,7 coefficients inelastic stopping *table.compound* : symbol of two-component target and physical values *table*7_*ck* : only for inel=7, correction of inelastic stopping *table*7_*a*3*a*4*a*5 : only for inel=7, correction of inelastic stopping
lterm_dif	.false.	.false. : nothing calculate .true. : calculation of thermal diffusion input of given matrix a_0 and e_act input-files: a0_tdiff.inp, eact_tdiff.inp

Table 17: Optional input variables with default values (continued)

variable	default value	description
ltraj_p	.false.	.true. : output of projectile trajectories .false. : no output of projectile trajectories (see also: numb_hist, ioutput_hist)
ltraj_r	.false.	.true. : output of recoil trajectories .false. : no output of recoil trajectories (see also: numb_hist, ioutput_hist)
l_two_comp	.false.	.true. : calculation density of one two-compound (eg. SiO2)
l_two_comp2	.false.	.true. : calculation density of two two-compound (eg. SiO2+CaO)
l_two_comp3	.false.	.true. : calculation density of three two-compound (eg. FeO+SiO2+CaO)
matrix_e_min_p	0	minimum of lin. energy distribution of the projectile in matrices
matrix_e_min_r	0	minimum of lin. energy distribution of the recoil in matrices
matrix_e_max_p	max(e0)	maximum of lin. energy distribution of the projectile in matrices
matrix_e_max_r	max(e0)	maximum of lin. energy distribution of the recoil inmatrices
miller_ind	1,0,0	miller index of crystal direction, for example [1,1,1] [0,0,0] calculation of polycrystalline target
nm	-1	=-1 : not a molecular target > 1 : number of atoms in a two-component molecule (nm=nm1+nm2)
nm1	-1	number of first atoms in a two-component molecule
nm2	-1	number of second atoms in a two-component molecule
nr_pproj	10	number of projectiles between two target updates (idrel = 0)
numb_hist	20	number of traced trajectories of projectiles and recoils
number_calc	1	number of calculations if a series of calculations is carried out (case_e0 = 5 or case_alpha = 5)
nx_mat	1000	interval of depth origin nx_mat= 100 interval depth origin: input target ' nx_mat=1000 interval depth origin: 1 A ' nx_mat=1001 interval depth origin: 0.5 A '

Table 18: Optional input variables with default values (continued)

variable	default value	description
qu_int	.false.	linear interpolation of atomic fractions between the depth intervals
qumax(ncp)	1.	maximum atomic fractions in the target for ncp species, if idrel=0
rr_displ	0.	distance of count re-displace for frenkel pair computation (only statistic)
rhom		atomic density of a two-component target; default from table.compound $[g/cm^3]$
rhom2		atomic density of a second two-component target; default from table.compound $[g/cm^3]$
sfin	0	$= 0$: no inelastic energy loss outside the target surface ($x = 0.$) $= 1$: inelastic energy loss outside the target surface ($-su > x > 0.$)
shth	0.	$= 0$: no sheath potential > 0 : sheath potential (eV), usually $= 3 \cdot \|e0\|$, only if case_e0=2,3 (Maxwellian distribution, plasma)
tableinp	'../../tables'	directory of input-file for tables (see also: layerinp, angleinp, energyinp)
text		comment in NAMELIST
ttarget		total target thickness in Angstrom (A)
ttemp	300.	target temperature, only for thermic diffusion and high temperatures, it reduces the surface binding energy according to a Maxwellian energy distribution
two_comp	'???'	name of first compound "SiO2" Note: only selected compounds in table.compound
two_comp2	'???'	name of second compound "CaO" Note: only selected compounds in table.compound
two_comp3	'???'	name of third compound "TaO2" Note: only selected compounds in table.compound
x0(ncp)	0.	starting position of projectile $\leq 0.$: outside the surface at $x = xc = -su$ $> 0.$: inside the solid

Table 19: Optional input variables with default values (continued)

C. Compiler information

The program needs FORTRAN-90 compiler and use for compile the program 'make'.
It turned out that the results are consistent for all three available fortran-compilers (GCC, NAG, INTEL) in the sequential setting, as well as the code results using 'use mpi' or 'use mpi_f08' for the parallel versions of intel and gcc/gfortran.
The Makefile in /src the mk-script in /bin/* and the run-script in case/ is more an example. You must modify these file according to your compiler and your computer-machine.

C.1. Makefile

Example of compiler options (set in /src/Makefile):

GCC:
gfortran -c -O2 -Wextra -I ../../src -DSEQ -DRAND2

INTEL:
ifort -c -w -FR -O2 -xP -I ../../src -DSEQ -DRAND2

NAG:
nagfor -c -O0 -g -C=undefined -mtrace -gline -quiet -ieee=stop -I ../../src -DSEQ -DRAND2

C.2. mk

The script 'mk' call 'make' and use as input the option from Makefile. Example for GCC sequential (set in /bin/gnu_GCC.SEQ) is:

#! /bin/sh -x
SRC_DIR=../../src
if [! -L Makefile]; then
ln -s $SRC_DIR/Makefile Makefile fi
make SRC_DIR=$SRC_DIR MODE=SEQ RAND=RAND2 COMPILER=GCC DEBUG=NO DEBUG2=NO -e -f $SRC_DIR/Makefile

option are: MODE= SEQ (sequential) or PPROJ (parallel)
RAND= RAND2 (32 bit) or CRAY (64 bit only intel)
COMPILER= GCC or INTEL or NAG
MPIMODE=MPI_90_8 (standard use mpi_f08) or MPI (use mpi)

C.3. run

The start of program in sequential mode from /case-directory is:
/SDTrimSP/bin/gnu_GCC.SEQ/SDTrimSP.exe

The start of the program in parallel mode is very dependent on the computer-system and the organisation of queue system.
Example: salloc -n 64 -t 72:00:00
srun /SDTrimSP/bin/gnu_GCC.PRO/SDTrimSP.exe
or: mpirun -n 64 /SDTrimSP/bin/gnu_GCC.PRO/SDTrimSP.exe

D. Output format

D.1. Output format of energy distribution in the target

The option *lenergy_distr* enables the calculation of the distribution of the energy input in the target. The total input energy is divided into the contribution of stopped atoms, inelastic energy loss and elastic energy loss.

option: lenergy_distr = .true.

parameter: dist_nx
dist_ny
dist_nz
dist_delta

output: E_distr_all.dat (output of total input energy)
E_distr_inel.dat (output of inelastic energy loss)
E_distr_nucl.dat (output of elastic energy loss)
E_distr_stop.dat (output of energy from implanted particle)

The default values are:

variable	number	interval [Å]	distant [Å]	description
dist_nx	60	2	0 to 120	depth
dist_ny	60	2	-61 to 59	width
dist_nz	60	2	-61 to 59	length

Table 20: Default values for the option lenergy_distr

D.2. Output format of the depth of origin and penetration depth

In the static mode the output of the depth of origin and penetration depth are possible.

option: lmatrices =.true.

optional option: lmatout_log_energ=.true.

output: morigin_ex_bs.dat ...depth of origin of back-sputtered atoms dependent on energy
morigin_ex_ts.dat ...depth of origin of transmitted sputtered atoms dependent energy
mpe_ex_p.dat ...maximum of penetration of back-scattered atoms
mepb.dat ...path-length of back-scattered atoms dependent energy
mept.dat ...path-length of back-scattered atoms dependent energy

D.3. Output format of energy- and angle-distribution of scattered and sputtered atoms

D.3.1. Output-matrix-file

The option *lmatrices* initiates output of the energy and angular distributions into four files.

option:	lmatrices =.true.	
optional option:	lmatout_cos_angle=.true.	
output:	meagb_p.dat	...output of back-scattered particles (projectiles)
	meagb_s.dat	...output of all back-sputtered particles (recoils)
	meagt_p.dat	...output of all transmitted scattered particles (projectiles)
	meagt_s.dat	...output of all transmitted sputtered particles (recoils)

D.3.2. Post-processing of output-matrix-file with readmatrix4.F90

The FORTRAN program *readmatrix*4.*F*90 in the directory *post* splits the four matrices into individual matrices.

post program :	/post/readmatrix4.F90
input files:	meagb_p.dat
	meagb_s.dat
	meagt_p.dat
	meagt_s.dat

outputfiles:

name of outputfile	x-axis	y-axis	values
matrix__ag..	polar(lin)	azimuth(lin)	number of particles
matrix_Sag..	polar(lin)	azimuth(lin)	number of particles per solid angle
matrix__ea..	energy(lin)	polar(lin)	number of particles
matrix__eg..	energy(lin)	azimuth(lin)	number of particles
matrix__ee..	polar(lin)	azimuth(lin)	energy
matrix_lea..	energy)(log)	polar(lin)	number of particles
matrix_leg..	energy)(log)	azimuth(lin)	number of particles
matrixc_ag..	polar(cos)	azimuth(lin)	number of particles
matrixc_ea..	energy(lin)	polar(cos)	number of particles
matrixcSag..	polar(cos)	azimuth(lin)	number of particles per solid angle
matrixc_eg..	energy(lin)	azimuth(lin)	number of particles
matrixc_ee..	polar(cos)	azimuth(lin)	energy
matrixclea..	energy(log)	polar(cos)	number of particles
matrixcleg..	energy(log)	azimuth	number of particles

file extension:

..b_p..	back-scattered projectiles
..t_p..	transmitted projectiles
..b_s..	back-sputtered recoil
..t_s..	transmitted-sputtered recoil
..1.dat	number species

a ...polar angle
b ...back (-scattered/-sputtered)
p ...projectile
l ...log(e)
S ...values per solid angle
g ...azimuthal angle
t ...transmitted
s ...sputtered recoil
c ...cosine interval of polar angle

An example for the naming convention used is matrix__agb_p1.dat (number of 1. back-scattered-projectile dependent on polar- and azimuthal-angles)

D.4. Output format of depth_proj.dat, depth_recoil.dat and depth_damage.dat

depth_proj.dat stores interaction information of projectiles dependent on depth in columns:

Column name	Description
DEPTH/LENGTH	Center of layer or particle trajectory length, [A]
STOPS	Number of stopped projectiles in layer, [number]
PATHLENGTH	Number of particles with a trajectory of this length, [number] (sampled on same scale as target thickness → If path-length > ttarget poor sampling)
NUCL.LOSS	Sum of transferred energy at this depth by elastic collisions, [MeV]
ELECT.LOSS	Energy deposited at this depth by inelastic interaction with electrons, [MeV]
NUC.LOSS < ED	Sum of transferred energy by elastic collisions where transferred energy < displacement-energy, [MeV]
NUC.LOSS > ED	Sum of transferred energy by elastic collisions where transferred energy > displacement-energy, [MeV]
FRENKEL P.	Kinchen Pease based DPA, [number]
NUM.COLL.	Not used
NRT-DPA	Norgett-Robinson-Torrens [53] model based DPA, [number]

depth_recoil.dat stores interaction information of recoil dependent on depth in columns:
Columns:

Column name	Description
DEPTH/LENGTH	Center of layer particle trajectory length, [A]
STOPS	Number of stopped recoils in layer, [number]
PATHLENGTH	Number of particles with a trajectory of this length, [number] (sampled on same scale as target thickness → If path-length > ttarget poor sampling)
NUCL.LOSS	Sum of transferred energy at this depth by elastic collisions, [MeV]
ELECT.LOSS	Energy deposited at this depth by inelastic interaction with electrons, [MeV]
NUC.LOSS < ED	Sum of transferred energy at this depth of elastic collisions where transferred energy < displacement-energy, [MeV]
NUC.LOSS > ED	Sum of transferred energy at this depth of elastic collisions where transferred energy > displacement-energy, [MeV]
STOPS< ED	Number of stopped recoils at this depth with start-energy < displacement-energy, [number]

depth_damage.dat stores interaction information of damages dependent on depth in columns:

Column name	Description
DEPTH	Center of layer , [A]
STOPS	Number of stopped recoils in layer, [number]
STOPS< ED	Number of stopped recoils at this depth with start-energy < displacement-energy, [number]
DISPL	Number of created recoils at this depth, [number]
DISPL< E	Number of created recoils at this depth with start-energy < displacement-energy, [number]
SUBS	Number of created recoils with start-energy > displacement-energy, which substituted by topped projectile or recoil with energy < displacement-energy, [number]
REPL	Number of created recoils with start-energy > displacement-energy, which replaces by topped projectile or recoil of same species with energy < displacement-energy, [number]
d ATOMS	change of the number of atoms in this layer, [number]
VACANCIES	vacancies in this layer, [number]

If parameter $irc0 = 1$ then self-replacement:
Self-replacement of Z_2 with Z_2 after collision $Z_1 \rightarrow Z_2$:

$$E_{start}(Z_2) < Ed(Z_2) \;\; and \;\; Z_2 \; not \; sputtered \tag{D.88}$$

SUBS:
Substitution of Z_2 with Z_1 after collision $Z_1 \rightarrow Z_2$:

$$E_{start}(Z_2) > Ed(Z_2) \;\; and \;\; E(Z_1) < Ed(Z_1) \;\; , \text{with} Z_1 \neq Z_2 \tag{D.89}$$

REPL:
Replacement of Z_2 with Z_1 after collision $Z_1 \rightarrow Z_2$:

$$E_{start}(Z_2) > Ed(Z_2) \;\; and \;\; E(Z_1) < Ed(Z_1) \;\; , \text{with} Z_1 = Z_2 \tag{D.90}$$

E. Inputfile 'layer.inp'

number depth interval	thick-ness	composition of target (2:ncp) qu_2
1	0.10000E+02	0.94061E+00
1	0.10000E+02	0.89911E+00
1	0.10000E+02	0.88149E+00
1	0.10000E+02	0.86192E+00
3	0.10000E+02	0.85698E+00
3	0.10000E+02	0.84040E+00
1	0.10000E+02	0.83929E+00
1	0.10000E+02	0.82595E+00
1	0.10000E+02	0.82483E+00
1	0.10000E+02	0.81702E+00
1	0.10000E+02	0.81551E+00
1	0.10000E+02	0.81049E+00
100	0.10000E+02	0.80643E+00
0	0	0

Table 21: Inputfile 'layer.inp' for two components (ncp=2), $qu\_1 = 1 - qu\_2$

number of layer	thick-ness	composition of qu_2	target (2...ncp) qu_3
200	5.0	0.3	0.7
300	5.0	0.7	0.3
0	0	0	0

Table 22: Inputfile 'layer.inp' for three components (ncp=3), $qu\_1 = 1 - sum(qu(2:ncp)) = 0.0$

F. Inputfiles 'energy.inp' and angle.inp

energy(eV)	distribution[-]
100	1
200	2
300	2
500	5
600	8
700	12
800	20
900	25

Table 23: Inputfile 'energy.inp'

angle(degree)	distribution[-]
30	10
60	20
70	20
90	70

Table 24: Inputfile 'angle.inp'

The name of inputfile for qubeam(1) is energy.inp.
The name of inputfile for qubeam(2) is energy02.inp.
The name of inputfile for qubeam(3) is energy03.inp and so on.

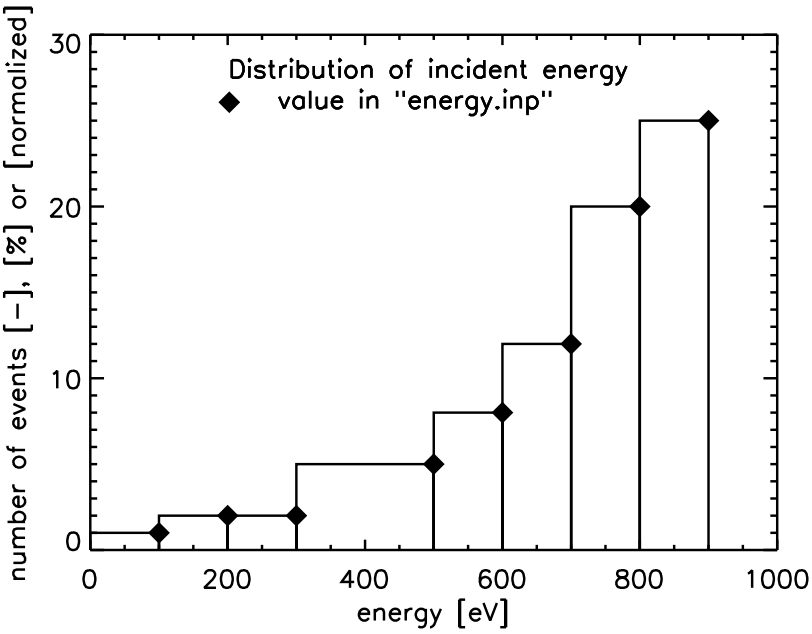

Figure 181: Distribution of incident energy according to Tab. 23

G. Inputfiles 'ene_ang.inp'

0.000000			: help	value		
0.000000			: help	value		
9			: columns	Angles		
10.0000	80.00000	10.00000	: Min Max	dAngle	[degrees]	
13			: rows	Energy		
10.0000	140.0000	10.00000	: Min Max	dE	[eV]	
2.39560	2.728417	9.982015	4.214628	1.330935	4.436451	3.327338
1.55830	5.512290	1.098021	2.994604	2.218225	1.109112	0.000000
3.56800	5.079736	3.438249	4.436451	2.218225	1.109112	0.000000
3.32730	2.218225	1.109112	1.109112	1.109112	0.000000	0.000000
0.00000	0.000000	0.000000	0.000000	0.000000	0.000000	0.000000
0.00000	0.000000	0.000000	0.000000	0.000000	0.000000	0.000000
0.00000	0.000000	0.000000	0.000000	0.000000	0.000000	0.000000
0.00000	0.000000	0.000000	0.000000	0.000000	0.000000	0.000000
0.00000	0.000000	0.000000	0.000000	0.000000	0.000000	0.000000
0.00000	0.000000	0.000000	0.000000	0.000000	0.000000	0.000000
0.00000	0.000000	0.000000	0.000000	0.000000	0.000000	0.000000
0.00000	0.000000	0.000000	0.000000	0.000000	0.000000	0.000000

Table 25: Inputfile 'ene_ang.inp'

H. Example of Inputfile 'tri.inp'

Inputfile 'tri.inp' of first static example He − > Ni

```
2 keV He − > Ni
&TRI_INP

    text='—elements—'
       ncp = 2
       symbol = "He", "Ni"

       flc = 1.0
       nh = 1
       idout = 1
       nr_pproj = 1

       idrel = 1
       isbv = 1
       ipot = 1

    text='—beam—'
       qubeam = 1.000, 0.000
       qumax = 0.000, 1.000
       case_e0 = 0
       e0 = 2000, 0.00
       case_alpha = 0
       alpha0 = 0.000, 0.000

    text='—target—'
       ttarget = 5000.
       nqx = 500
       qu = 0.0 , 1.0

       ltraj_p = .true.
       ltraj_r = .true.
       numb_hist = 1
       ioutput_hist = 1, 1, 0, 1, 1, 0
       lparticle_r = .true,
       lparticle_p = .true.
       ioutput_part = 100, 100, 0, 100, 100, 0
/
```

Inputfile 'tri.inp' of second static example Ar − > Ni

```
1 keV Ar − > Ni
&TRI_INP

   text='—elements—'
       ncp = 2
       symbol = "Ar", "Ni"

       flc = 10.0
       nh = 100000
       idout = 10000
       nr_pproj = 64
       idrel = 1
       ipot = 1
       isbv = 1

   text='—beam—'
       qubeam = 1.000, 0.000
       qumax = 0.000, 1.000
       case_e0 = 0
       e0 = 1000, 0.00
       case_alpha = 0
       alpha0 = 60.000, 0.000
       beta0 = 30.000, 0.000

   text='—target—'
       ttarget = 5000.
       nqx = 500,
       qu = 0.0 , 1.0

       lmatrices = .true.
/
```

Inputfile 'tri.inp' of first dynamic example Ni − > WC

```
10 keV Ni − > WC
&TRI_INP

   text='—elements—'
      ncp = 3
      symbol = "Ni", "W", "C_g"

      flc = 15.00
      nh = 45000
      idout = 500
      nr_pproj = 64

   text='—beam—'
      qubeam = 1.000, 0.000, 0.000
      qumax = 1.000, 1.000, 1.000
      case_e0 = 0
      e0 = 10000, 0.00 , 0.00
      case_alpha = 0
      alpha0 = 0.00, 0.00, 0.00

      ipot = 1
      isbv = 4

   text='—target—'
      l_two_comp=.true'
      two_comp='WC'
      idrel = 0
      case_layer_thick = 2

      ttarget = 500
      nqx = 100
      qu = 0.0, 0.5, 0.5
/


note: new values will set during calculation
      ncp = 5
      symbol ="Ni","W","C_g","W_1","C_g_1"
```

Inputfile 'tri.inp' of second dynamic example W − > C

```
5 keV W − > C
&TRI_INP

   text='—elements—'
       ncp = 2
       symbol = "W", "C_g"

       flc = 50.00
       nh = 1000000
       idout = 500
       nr_pproj = 64

   text='—beam—'
       qubeam = 1.000, 0.000
       qumax = 1.000, 1.000
       case_e0 = 0
       e0 = 5000, 0.00
       case_alpha = 0
       alpha0 = 0.00, 0.00

       ipot = 1
       isbv = 1

   text='—target—'
       idrel = 0
       ttarget = 1000
       nqx = 100
       qu = 0.0, 1.0
       qu_int = .true.
       case_layer_thick = 2
       l_two_comp=.true'
       two_comp='WC'
/


note: new values will set during calculation
       ncp = 4
       symbol ="W","C_g","W_1","C_g_1"
```

Inputfile 'tri.inp' of third dynamic example Ar − > Si Ta

```
3 keV Ar − > Si Ta
&TRI_INP
   text='—elements—'
       ncp = 3
       symbol = "Ar", "Si", "Ta"

       flc = 50
       nh = 50000
       idout = 500
       nr_pproj = 32
       ipot = 1
       isbv = 1

   text='—beam—'
       qubeam = 1.000, 0.000, 0.000
       qumax = 0.000, 1.000, 1.000
       case_e0 = 0
       e0 = 3000, 0.00
       case_alpha = 0
       alpha0 = 0.000, 0.000 ,0.000

   text='—target—'
       idrel = 0
       case_layer_thick = 2
       ttarget = 1815
       nqx = 363
       qu = 0.0, 0.5, 0.5
       iq0 = -1
/
```

Inputfile 'layer.inp' of third dynamic example Ar − > Si Ta

number of layer	thick-ness	target composition 2...ncp qu_2	qu_3	name of layer
40	5.00	1.0000	0.0000	Si 1
15	5.00	0.0000	1.0000	Ta 1
21	5.00	1.0000	0.0000	Si 2
15	5.00	0.0000	1.0000	Ta 2
21	5.00	1.0000	0.0000	Si 3
15	5.00	0.0000	1.0000	Ta 3
21	5.00	1.0000	0.0000	Si 4
15	5.00	0.0000	1.0000	Ta 4
200	5.00	1.0000	0.0000	Si 5
0	0	0	0	end

Inputfile 'tri.inp' of sputtering with noble gas ions Xe − > Si

```
10 keV Xe − > Si
&TRI_INP
   text='—elements—'
       ncp = 2
       symbol = "Xe", "Si"

   text='—beam—'
       case_e0 = 0
       e0 = 10000, 0.00
       qubeam = 1.00, 0.000
       case_alpha=0
       alpha0 = 0.0 , 0.000

   text='—control—'
       flc = 10
       nh = 10000
       nr_pproj = 64
       idout = 1000
       idrel = 0
       ipot = 1

   text='—target—'
       ttarget = 5000
       nqx = 500
       isbv = 1
       qu = 0.0, 1.00
       qumax = 1.00, 1.000
       qu_int= .true.
       case_layer_thick=2
       loutgas = .true.
       diff_koeff1 = 1.65e06 , 0.0
       diff_koeff2 = 95 , 0.0
/
```

Inputfile 'tri.inp' of sputtering with chemical erosion H − > C

```
200 eV H − > C
&TRI_INP
   text='—elements—'
      ncp = 4
      symbol ="H","Sp2","Sp3","Sp3H"

      flc = 50
      nh = 5000
      idout = 1000
      nr_pproj = 640

      idrel = 0
      isbv = 1
      ipot = 1

   text='—beam—'
      qubeam = 1.00 , 0.00 , 0.00, 0.00
      case_e0=0
      e0 = 200 ,0.00, 0.00, 0.00
      case_alpha=0
      alpha0 = 0.00, 0.00, 0.00, 0.00

   text='—target—'
      ttarget = 5000
      nqx = 1000
      qumax = 1.0, 1.00, 1.00, 1.00
      qu = 0.0, 1.00, 0.00, 0.00
      ttemp = 800
      qu_int = .true.
      case_layer_thick=2
      loutgas = .true.
      diff_koeff1 = 1.00e06, 0.0, 0.0, 0.0
      diff_koeff2 = 100, 0.0, 0.0, 0.0
      lchem_ch = true
      flux = 1.00
/
```

Inputfile 'tri.inp' of sputtering with thermal diffusion C − > WC

```
1 eV C − > CW with diffusion
&TRI_INP
   text='—elements—'
       ncp = 2
       symbol ="C_g","W"

       flc = .1
       nh = 1000
       idout = 10
       nr_pproj = 8

   text='—beam—'
       qubeam = 1.00 , 0.00
       qumax = 1.0, 1.00
       case_e0=0
       e0 = 1.0, 0.00
       case_alpha=0
       alpha0 = 0.00, 0.00

       ipot = 1
       isbv = 1

    text='—target—'
       idrel = 0
       ttarget = 5000
       nqx = 1000
       qu = 0.0, 1.00
       iq0 = -1
       ttemp = 873
       irc0 = 1
       qu_int = .true.
       case_layer_thick=0
       lterm_dif = .true.
       flux = 0.0001
/
```

Inputfile 'a0_tdiff.inp' of example C − > WC

```
a0 [m**2/s]
2   number of elements
6   C Z-symbol for check of input
74   W Z-symbol for check of input

        C          W
 8.91e-6        0.0     a0 for C
      0.0    8.91e-6    a0 for W
```

Inputfile 'eact_tdiff.inp' of example C − > WC

```
a_act [eV]
2   number of elements
6   C Z-symbol for check of input
74   W Z-symbol for check of input

    C     W
 2.32  0.00     a_act for C
 0.00  2.32    a_act for W
```

Inputfile 'tri.inp' natural isotope mixtur of B, He $->$ B

```
100 eV He -> B (natural isotope mixtur)
&TRI_INP
   text='—elements—'
       ncp = 2
       symbol ="He","B"

       isot = 0 , 1

    text='—beam—'
       qubeam = 1.00, 0.000
       case_e0=0
       e0 = 100 ,0.00
       case_alpha=0
       alpha0 = 0.00, 0.00

    text='—controll—'
       flc = 1
       nh = 200
       nr_pproj = 960
       idout = 100

       idrel = 1
       ipot = 1

    text='—target—'
       ttarget = 50000
       nqx = 2500
       isbv = 1
       qumax = 1.0, 1.00
       qu = 0.0, 1.00
       qu_int = .true.
       case_layer_thick=2
/


note: new values will set during calculation
       ncp = 3
       symbol ="He","B10","B11"
       qu = 0.0, 0.1990 0.8010
```